Research Toward Laser Spectroscopy of Trapped Atomic Hydrogen

by

Jon Carl Sandberg

Submitted to the Department of Physics
in partial fulfillment of the requirements for the degree of

Doctor of Philosophy in Physics

at the

MASSACHUSETTS INSTITUTE OF TECHNOLOGY

May 1993

Author ....
Department of Physics
May 14, 1993

Certified by ....
Daniel Kleppner
Professor of Physics
Thesis Supervisor

Accepted by ....
George F. Koster
Chairman, Department of Physics Graduate Committee

Research Toward Laser Spectroscopy of Trapped Atomic Hydrogen

by

Jon Carl Sandberg

Submitted to the Department of Physics
on May 14, 1993, in partial fulfillment of the
requirements for the degree of
Doctor of Philosophy in Physics

Abstract

An apparatus has been designed and constructed to perform laser spectroscopy on magnetically trapped atomic hydrogen. Earlier experiments demonstrated the feasibility of magnetic trapping and evaporative cooling of atomic hydrogen. The current apparatus has been designed to explore two areas of research: high resolution laser spectroscopy of hydrogen, and the possible production and detection of Bose condensation. The $1S-2S$ two-photon transition was chosen for study because of its extremely narrow natural linewidth. The techniques developed here should ultimately permit laser spectroscopy with a resolution approaching 1 part in 10^{15} and should be well suited to the detection of Bose condensation.

The apparatus consists of two subsystems: a cryogenic apparatus for magnetically trapping hydrogen, and a laser source for producing the ultraviolet light necessary to excite the $1S-2S$ transition. The two subsystems have independently demonstrated exceptional performance. The magnetic trap has produced gas densities approaching 10^{14} cm^{-3} at temperatures as low as 100 μK, the closest approach to Bose condensation achieved to date with atomic hydrogen. The continuous wave laser source has produced 20 mW of 243 nm light with an estimated spectral linewidth of 2 kHz.

The optimum experimental conditions for excitation and detection of the $1S-2S$ transition in trapped hydrogen have been identified. Initial trials with the apparatus revealed an unexpected operational problem, however several strategies have been proposed that should allow observation of the transition. The expected features of the $1S-2S$ transition lineshape with magnetically trapped hydrogen have been calculated. The possibilities for future research with laser spectroscopy of magnetically trapped hydrogen are described, and a promising strategy for the detection of Bose condensation is proposed.

Thesis Supervisor: Daniel Kleppner
Title: Professor of Physics

To My Wife and My Parents

Acknowledgments

My deepest acknowledgment goes to my wife, Sheri. Without her love, patience, and support, I never would have made it this far.

I owe a great debt to the entire hydrogen group. I have enjoyed a very rewarding (both personal and professional) relationship with John Doyle. I hope someday to be able to repay the friendship and support I have received from Mike Yoo in the later stages of this thesis. Albert Yu and Claudio Cesar have both put alot of work into this experiment and have been great to work with. The recent additions to the group of Dale Fried and Adam Polcyn make me optimistic for the future of this experiment.

My thesis advisor, Dan Kleppner, has been exceptionally supportive and understanding throughout the course of a very challenging thesis project. I have also received valuable support and encouragement from Tom Greytak. It is my sincere hope for them that the potential of this experiment is soon realized.

I thank the following people for making my time at MIT more enjoyable: Reiko Oda, Janet Sahlstrom, Carol Costa, Peggy Berkovitz, and Frank Payne. I also thank two of my especially close friends, Mike Folsom and Claus Zimmermann, for helping me keep things in perspective.

I gratefully acknowledge financial support in the form of a graduate fellowship from the National Science Foundation and from AT&T Bell Laboratories.

Contents

List of Figures

Chapter 1

Introduction

Atomic hydrogen is currently the subject of vigorous research on two heretofore separate fronts. The study of a cold, dense gas of atomic hydrogen is advancing rapidly toward observation of the long sought Bose-Einstein transition. High resolution laser spectroscopy of the hydrogen atom is pushing forward the frontiers of precision and yielding improved values for fundamental constants. This thesis describes research that is a synthesis of these two areas and that offers possibilities of significant advances on both fronts.

1.1 Overview of Interest

1.1.1 Spin-polarized Atomic Hydrogen

Atomic hydrogen can be stabilized in gaseous form by polarizing the electron spins of the hydrogen atoms. The resulting gas is predicted to have many unique properties. Among the most interesting is that the gas will never condense into a conventional liquid or solid, even at zero temperature. Instead, it is predicted that the gas will undergo a transition to a weakly interacting Bose condensate under conditions where the thermal deBroglie wavelength of the atoms is comparable to the mean interparticle spacing. The transition temperature, T_0, for a gas of density n is given by

$$T_0 = \frac{h^2}{2\pi k_B m}\Big(\frac{n}{2.612}\Big)^{2/3} \tag{1.1}$$

where h is Planck's constant, k_B is Boltzmann's constant, and m is the mass of the atom.

The possibility of observing Bose-Einstein condensation (BEC) in atomic hydrogen has been the subject of intense research for more than 10 years (see, for example, review articles by Greytak and Kleppner[1] or Silvera and Walraven[2]). The first experimental milestone was reached with the stabilization of spin-polarized atomic hydrogen by Silvera and Walraven[3] in 1980. This experiment accumulated atomic hydrogen in a low temperature vessel with superfluid helium coated walls. Further advances were made by Bell, et al.[4] who compressed a sample of atomic hydrogen and ultimately reached a density of 1.4×10^{18} cm^{-3} at a temperature of 190 mK. Closer approach to BEC either by increasing the sample density or by decreasing the sample temperature was not possible with this experimental approach. Increases in density were prohibited by a three-body recombination mechanism, while decreases in temperature were prohibited by excessive adsorption of the hydrogen atoms on the superfluid helium coated walls of the containment vessel.

A significant advance was made by Hess[5], who suggested that the lower limit to the gas temperature present in earlier experiments could be removed by wall-free confinement of the gas in a magnetic trap. The confinement mechanism in this case is the force applied to the magnetic moment of the hydrogen atom by an inhomogeneous magnetic field. Hess also proposed that evaporative cooling could be used to cool the trapped hydrogen gas to reach BEC. Magnetic trapping of atomic hydrogen was first demonstrated by Hess, et al.[6] in 1987. Evaporative cooling was demonstrated shortly thereafter by Masuhara, et al[7].

Recent experiments[8][9] in this laboratory have demonstrated significant progress toward BEC using the techniques of magnetic trapping and evaporative cooling of atomic hydrogen. A hydrogen gas with a density of 8×10^{13} cm^{-3} at a temperature of 100 μK has been produced, which represents the closest approach to BEC to date with atomic hydrogen. At this density the transition temperature is only a factor of 3.5 lower. There appears to be no fundamental limitation in extending these techniques to reach BEC. The immediate limitation is due to the detection technique used in these experiments (this is discussed in Chap. 2). An improved detection technique should make it possible to observe and study a weakly interacting Bose condensate.

1.1.2 High Resolution Laser Spectroscopy of Atomic Hydrogen

The second aspect of this research is ultra-high resolution spectroscopy of hydrogen. As will be shown, trapped atomic hydrogen provides a unique medium for this goal. Because of its simplicity, the structure of the hydrogen atom can be treated theoretically with an extremely high degree of precision. Precise comparison between theory and experiment for the transition frequencies of the hydrogen atom can either test the content of the theory, or use the theory to determine better values for the fundamental constants.

Of particular interest for ultra-precise spectroscopy is the metastable $2S$ state, which has a lifetime of 1/8 of a second. This long lifetime is a consequence of the fact that radiative decay of the $2S$ state via single photon emission is forbidden. The dominant decay channel is via two-photon spontaneous emission. A corollary to this is that the $2S$ state cannot be directly excited from the ground state by single photon absorption. Instead, a transition from the ground state to the $2S$ state (hereafter called the $1S-2S$ transition) must take place by absorption of *two* photons, the sum of whose energies is equal to the $1S-2S$ energy interval.

Currently, high resolution laser spectroscopy of the hydrogen $1S-2S$ transition is an area of active research. Recent experiments using the technique of two-photon Doppler-free spectroscopy have yielded improved values for the Rydberg constant[10] and the hydrogen-deuterium isotope shift[11]. In these experiments the $1S-2S$ transition was observed by longitudinal excitation of a cooled (80 K) atomic beam, and a resolution of 2 parts in 10^{11} was achieved. The resolution was limited by the second order Doppler effect and time-of-flight broadening in the atomic beam. This resolution was sufficient to modestly exceed the other sources of uncertainty in the current measurements, but it is four orders of magnitude larger than the intrinsic resolution of the transition. As techniques for optical metrology advance, there will likely be an incentive for improved resolution. Further cooling of the atomic beam allows some room for improvement, but a substantial advance would seem to require a different approach. An atomic hydrogen fountain has been proposed[12], but formidable technical challenges may prevent its realization in the near future.

Magnetically trapped atomic hydrogen should allow a substantial increase in the resolution of the $1S{-}2S$ transition. Confinement of the atoms by the trap provides a way to overcome the interaction time limitations inherent with atomic beam experiments. The low temperatures obtained with magnetically trapped hydrogen reduce the second order Doppler shift to a negligible level. The ultimate resolution achievable with this system appears to be due to the small perturbation of the $1S{-}2S$ transition frequency by the trapping fields. The current $1S-2S$ resolution is 30 kHz[11]; a resolution on the order of 30 Hz appears feasible with the conditions already achieved in the laboratory.

1.2 Overview of the Experiment

The focus of this work is observation of the $1S{-}2S$ two-photon transition in magnetically trapped atomic hydrogen. The main goals of this effort are the development of laser excitation of the $1S-2S$ transition as a probe of the macroscopic properties of a trapped hydrogen gas, and the development of magnetically trapped hydrogen as a sample for high resolution laser spectroscopy of the $1S-2S$ transition.

Our experimental approach is illustrated in the schematic diagram in Figure 1-1. Atomic hydrogen, cooled by a dilution refrigerator, is loaded into a magnetic trap. The trapped hydrogen is then evaporatively cooled to submillikelvin temperatures.

To excite the $1S$–$2S$ transition, continuous-wave radiation at 243 nm is generated by frequency doubling of a frequency stabilized dye laser and introduced along the axis of the magnetic trap. The 243 nm beam is then retro reflected to produce a standing wave radiation field suitable for Doppler-free excitation of the $1S-2S$ transition in the trapped hydrogen. The excitation of the $2S$ state is detected by electric field induced L_α fluorescence.

The magnetic trap is a modified version of the apparatus described by Doyle[9]. A 0.55 K deep magnetic potential for ground state hydrogen atoms in the $F = 1, m_F = 1$ hyperfine level is produced by a set of superconducting coils. A dense hydrogen gas is loaded into the magnetic trap by thermal accommodation with the superfluid helium coated walls of an experimental cell. The experimental cell is cooled to temperatures below 0.3 K by a dilution refrigerator. Once loaded into the trap, the hydrogen atoms are evaporatively cooled to temperatures as low as 100 μK. The presence of trapped hydrogen is verified by releasing it from the trap and allowing it to recombine into molecular hydrogen. A fraction of the energy released in the recombination is detected as heat by a bolometer located in the experimental cell. This apparatus and the principles behind its operation are discussed in more detail in Chapter 2.

The source of 243 nm radiation is a frequency doubled continuous-wave dye laser (Coherent 699-21). This laser has been extensively modified to reduce its spectral linewidth by more than three orders of magnitude, to an estimated 2 parts in 10^{12}. The dye laser output at 486 nm is frequency doubled in the nonlinear crystal beta barium borate (BBO) to produce 243 nm radiation. We have developed specialized techniques to optimize the efficiency of the frequency doubling, and are able to generate 20 mW of 243 nm radiation from 400 mW of 486 nm radiation. This system is thoroughly described in Chapter 4.

The 243 nm beam is introduced along the axis of the trap and retro reflected to produce a standing wave radiation field in the trapping region. The standing wave field excites Doppler-free $1S-2S$ two-photon transitions in the trapped atoms. The excitation of the $2S$ state is detected by applying an electric field to the sample. The electric field mixes the $2S$ and $2P$ states, opening a channel for one-photon radiative

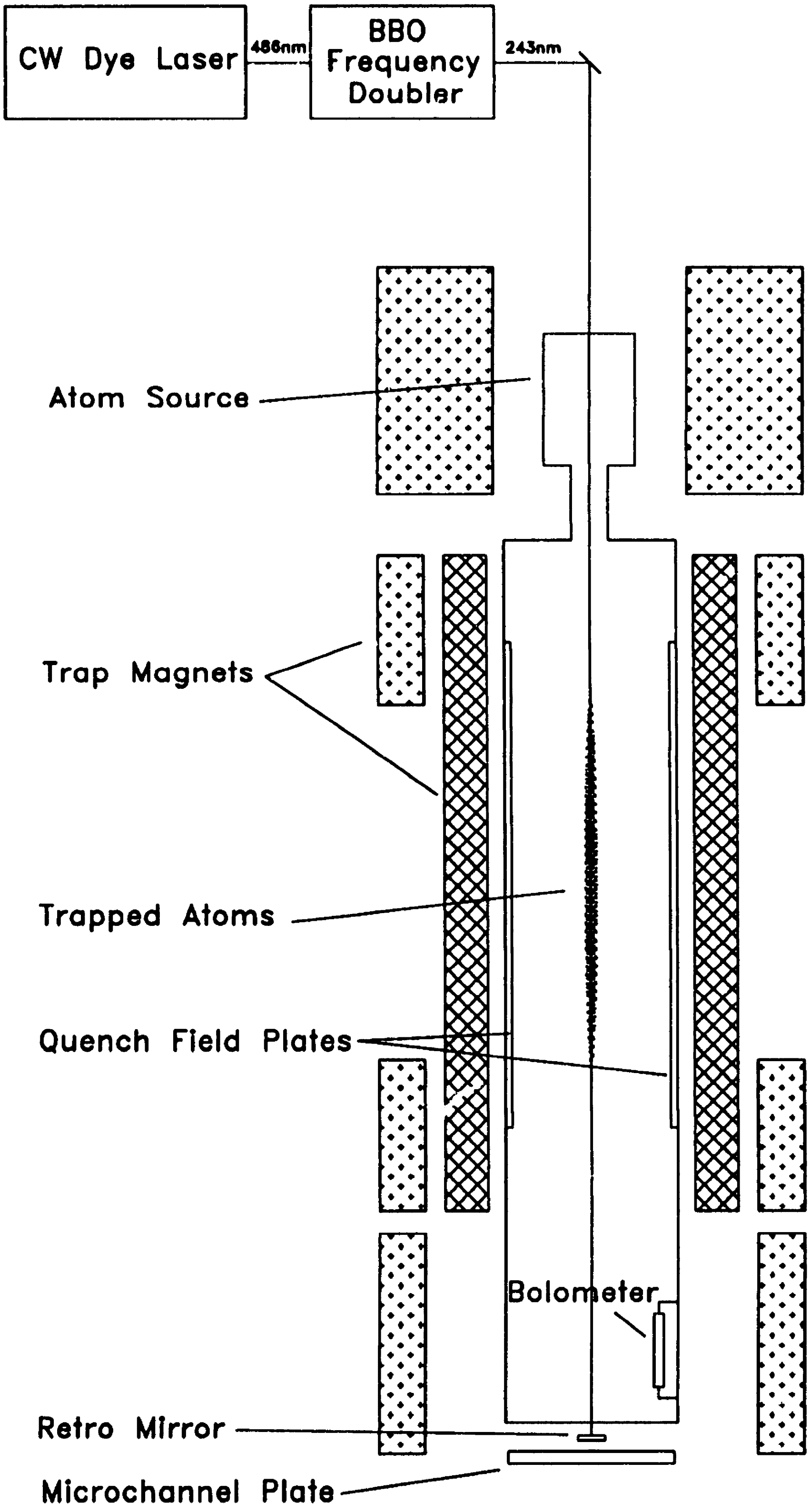

Figure 1-1: Schematic diagram of the apparatus.

decay of the perturbed $2S$ state via emission of a L_α photon. The L_α photons are transmitted out of the experimental cell and detected with a microchannel plate detector. These aspects of the apparatus are described in Chapter 5.

Significant progress has been made toward observation of the $1S-2S$ transition in magnetically trapped atomic hydrogen. We have developed an apparatus that allows optical access for excitation and detection of the $1S-2S$ transition with trapped hydrogen. This apparatus has been successfully used to further develop the techniques of evaporative cooling, and demonstrate significant progress toward observation of Bose condensation in trapped hydrogen. A specialized laser source has been developed for excitation of the $1S-2S$ transition. This source has demonstrated state-of-the-art performance in terms of spectral linewidth and output power in this spectral region. Diagnostic trials with the apparatus have been performed to explore its operational limitations. Several strategies have been identified that should allow successful observation of the $1S-2S$ transition.

We conclude in Chapter 6 with a discussion of the anticipated properties of a $1S-2S$ resonance signal, and how the signal may be used to measure the density and temperature of our trapped hydrogen. We also discuss the potential of ultra-high resolution laser spectroscopy of trapped atomic hydrogen. Finally, we introduce a promising new technique for detection of a Bose condensate using the $1S-2S$ transition in atomic hydrogen.

In the Appendix we present three papers by the author of this thesis and co-workers. These papers summarize the contributions of the author to recent work in magnetic trapping and evaporative cooling of atomic hydrogen. This work is fundamental to the feasibility of the continuing efforts toward observation of the $1S-2S$ transition in trapped atomic hydrogen.

Chapter 2

Magnetic Trapping of Spin-Polarized Atomic Hydrogen

Most of this thesis work was devoted to developing techniques for magnetic trapping and evaporative cooling of atomic hydrogen. The goal of this work was to produce cold, dense magnetically confined atomic hydrogen. Such a gas is of interest for possible observation of Bose condensation and for high resolution laser spectroscopy of the $1S-2S$ transition in hydrogen.

Important aspects of the work has been described in the thesis work of Doyle[9], and the reader is referred there for a more complete discussion of the material of this chapter. We present here a brief description to provide a context for the discussion in later chapters.

2.1 Background

2.1.1 Magnetic Trapping

The confinement of neutral atoms by magnetic fields can be understood by considering the interaction between the magnetic moment of the atom and the magnetic field.

The interaction energy is given by

$$U = -\vec{\mu} \cdot \vec{B} \tag{2.1}$$

where $\vec{\mu}$ is the magnetic moment of the atom and $\vec{B}$ is the magnetic field. We may write the interaction energy as $U = -\mu_z B$, where μ_z is the projection of the magnetic moment along the magnetic field axis and B is the magnitude of the field. If the field is inhomogeneous then the atom will feel a force

$$\vec{F} = -\nabla U = \mu_z \vec{\nabla} B. \tag{2.2}$$

If the atom is in a quantum state with $\mu_z > 0$ then it feels a force in the direction of $\vec{\nabla} B$, or toward regions of stronger magnetic fields. Atoms in these states are called strong field seekers. Atoms in states with $\mu_z < 0$ feel a force in the opposite direction and are called weak field seekers.

The behavior of a hydrogen atom in an inhomogeneous field can be understood with reference to Fig. 2-1, which shows the hyperfine energy levels of the electronic ground state in a magnetic field. The four hyperfine states are conventionally label a through d in order of increasing energy. In low magnetic fields, the state a is a $F = 0$ hyperfine singlet and the states b through d belong to a $F = 1$ hyperfine triplet. From Fig. 3-4 we see that the energies of the a and b states decrease with increasing magnetic field making them strong field seekers. The energies of the c and d states behave oppositely, hence these states are weak field seekers.

Free space confinement of strong field seeking atoms would require a local maximum in the magnetic field magnitude. Maxwell's equations forbid a local maximum for a static magnetic field in a current free region of space, so confinement of strong field seeking atoms is not possible with static magnetic fields. It is possible to produce a local *minimum* in the magnetic field strength in free space, therefore atoms in weak field seeking states may be confined solely with magnetic fields.

A simple estimate for the strength of the confinement may be obtained as follows. A hydrogen atom in the d hyperfine state has a magnetic moment of approximately

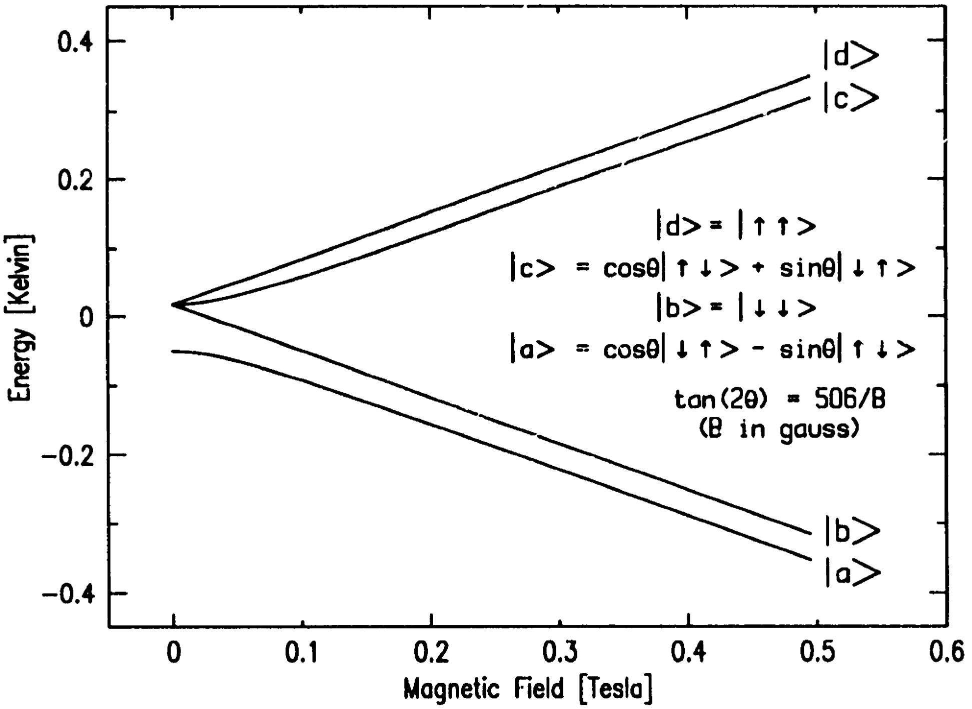

Figure 2-1: Hyperfine structure of the ground state of the hydrogen atom.

one Bohr magneton. If we construct a magnetic field geometry with a minimum field strength B_{min} and maximum field strength B_{max}, then the depth of this potential for a *d* state hydrogen atom is

$$\Delta E = \mu_B \Delta B \tag{2.3}$$

where $\Delta B = (B_{max} - B_{min})$. If $\Delta B = 1$ T, then the trap depth is 0.67 K. Therefore, the confinement is relatively weak and the atoms must be quite cold before they may be held in an experimentally practical magnetic trap.

2.1.2 Collisions between Trapped Atoms

If a magnetic trap is loaded with a sample at a sufficiently high density, then interactions between the atoms will dominate the behavior of the sample. Three different collisional processes are important to understand the trap dynamics: spin-exchange collisions, elastic collisions, and dipolar relaxation collisions.

The magnetic trap stably confines both the *c* and *d* hyperfine states. However, the c state atoms undergo spin-exchange collisions of the form $c + c \rightarrow b + d$. The b state atoms produced in this collision are ejected from the trap. Spin-exchange collisions proceed until all c state atoms have been depleted from the trap, leaving a trapped gas of pure d state atoms (which is stable against spin-exchange collisions). In practice, this process goes to completion rapidly, in the first few seconds after the trap is loaded.

Elastic collisions occur between trapped atoms. In an elastic collision the kinetic energy and momentum of the colliding atoms are changed, but their internal states are not. The primary effect of elastic collisions is to drive the sample toward a state of internal thermal equilibrium. Collisions between trapped atoms occur at a mean collision energy much less than the trap depth. At such energies we can neglect all elastic collision channels with the exception of the s-wave channel. In considering s-wave collisions, the interatomic potential may be treated as a hard sphere interaction with scattering length $a = 0.7$ Å[13].

A gas of d state atoms is an energetically inverted population. Transitions to other hyperfine states are energetically favored and can be induced by the interaction between the magnetic moments of two colliding atoms. Transitions of this type are referred to as dipolar relaxation collisions. In our context the dominant dipolar relaxation channel is $d + d \rightarrow a + a$, with the resulting a state atoms being ejected from the trap. Dipolar relaxation collisions are the dominant loss mechanism for an otherwise stable gas of d state atoms. Dipolar relaxation is a two-body process, therefore its rate is proportional to the density. This results in a density dependent trap lifetime. In our experimental conditions this limits the trap lifetime to tens of seconds at densities of 10^{14} cm^{-3}.

2.1.3 Forced Evaporative Cooling

A sample of trapped hydrogen will evolve toward a state of internal thermal equilibrium due to elastic collisions between the atoms. This allows us to consider the sample as a thermodynamic system and in most cases to define a temperature for the sample. However, for a finite temperature the equilibrium energy distribution

(Maxwell-Boltzmann) will contain atoms with energies that exceed the depth of the trap. These atoms escape the trapping potential. Collisions between lower energy atoms regenerate the high energy portion of the energy distribution, which are again lost due to escape over the finite depth of the trap. The process of escape of the high energy atoms is called evaporation. Typically the escaping atoms have a total energy that greatly exceeds the average energy of the sample. The loss of such an atom reduces the average energy of the remaining atoms and therefore can be thought of as a cooling process.

Dipolar relaxation collisions also affect the thermodynamics of the trapped gas. The two-body dipolar relaxation happens preferentially in the high density regions of the trap where the potential energy is lowest. This process preferentially removes atoms with low potential energy, independent of their kinetic energy. Therefore, atoms lost to dipolar relaxation have a lower than average total energy. The loss of atoms with a lower than average total energy raises the average energy of the remaining atoms and can be thought of as a heating process.

The effects of evaporation and dipolar relaxation are illustrated in Fig. 2-2. The cooling due to evaporation and the heating due to dipolar relaxation are competing mechanisms that ultimately balance to yield to a well defined equilibrium temperature for the trapped gas. This can be understood by considering the temperature dependence of the cooling and heating rates. The rate of evaporation from the trap is strongly dependent on the sample temperature, decreasing exponentially with the ratio of the sample temperature to the trap depth. The dipolar relaxation rate is also dependent on the temperature, but in the opposite sense. A low sample temperature means a high density at the trap center and a correspondingly high dipolar relaxation rate. The equilibrium temperature of the gas is reached when the cooling rate equals the heating rate. The equilibrium temperature depends on the elastic collision rate, the dipolar relaxation rate, and the trap geometry. In our experimental conditions the equilibrium temperature corresponds to approximately one tenth of the trap depth.

The evaporation process can be used to cool a trapped gas in a controlled manner. Consider a gas confined in a trap at its equilbrium temperature. If the depth of

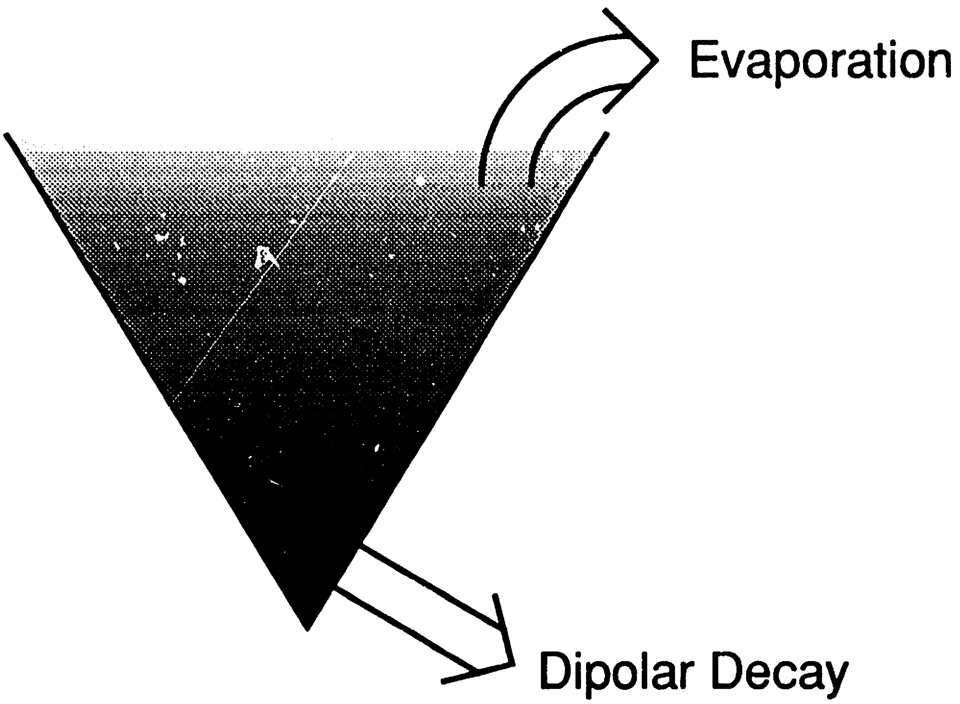

Figure 2-2: Decay processes in trapped hydrogen.

the trap is lowered slightly the evaporation rate will increase. The increase in the evaporation rate will cause an increased cooling and the sample temperature will drop. If the trap depth is lowered continuously (at a rate slow enough for the sample to maintain internal thermal equilbrium), then the sample temperature will continue to drop. This technique is called forced evaporative cooling.

Forced evaporative cooling allows one to cool a trapped gas at the cost of a loss of atoms. This process is optimized by controlling the time variation of the trapping potential to obtain the largest temperature decrease with the smallest loss in atoms. A thermodynamic model of the trapped gas that quantitatively accounts for heating, cooling, and atom loss mechanisms allow one to predict the sample conditions at the end of a given evaporative cooling process. These models can be used to evaluate different cooling paths and find the optimum evaporative cooling process to produce a chosen set of sample conditions.

It is important to appreciate that, although a decrease in sample number is inevitable in evaporative cooling, a decrease in sample density is not. If the trapping potential is such that the depth and effective volume of the trap can be independently varied, then a decrease in trapping volume can more than overcome the loss in atom number, and the sample density can increase. An example of this is discussed in the next section.

2.2 Apparatus and Method

A diagram of the trapping apparatus is shown in Fig. 2-3. This apparatus and its operation are described in detail in Ref. [9]. We give a brief description here of the aspects that are important to understand the discussion of later chapters.

The main functional components of this apparatus are the magnet system, the atom source, and the experimental cell. The magnet system is a set of superconducting coils that produce the fields that confine the trapped hydrogen. The atom source produces atomic hydrogen by dissociation of molecular hydrogen in a low temperature radio frequency discharge. The experimental cell surrounds the trapping region and is important in the trap loading process. The superconducting trap magnets are immersed in a bath of liquid helium. The atom source and the experimental cell are vacuum isolated from the liquid helium bath and cooled by a dilution refrigerator.

Trapping Field Geometry

As discussed in Section 2.1.1, a static magnetic trap consists of a magnetic field distribution that possesses a local minimum in the magnitude of the field. However, the confinement provided by experimentally practical traps is relatively weak (0.68 K for a 1 T deep trap). Therefore, a significant technological effort is required to produce a magnetic trap deep enough to confine hydrogen with currently available cooling techniques.

The trapping potential is illustrated in Figure 2-4. It has approximate cylindrical symmetry, and is most easily understood by considering axial and radial confinement separately. Radial confinement is provided by a linear quadrupole magnet. This magnet produces a field whose magnitude is zero along the axis of the trap, and

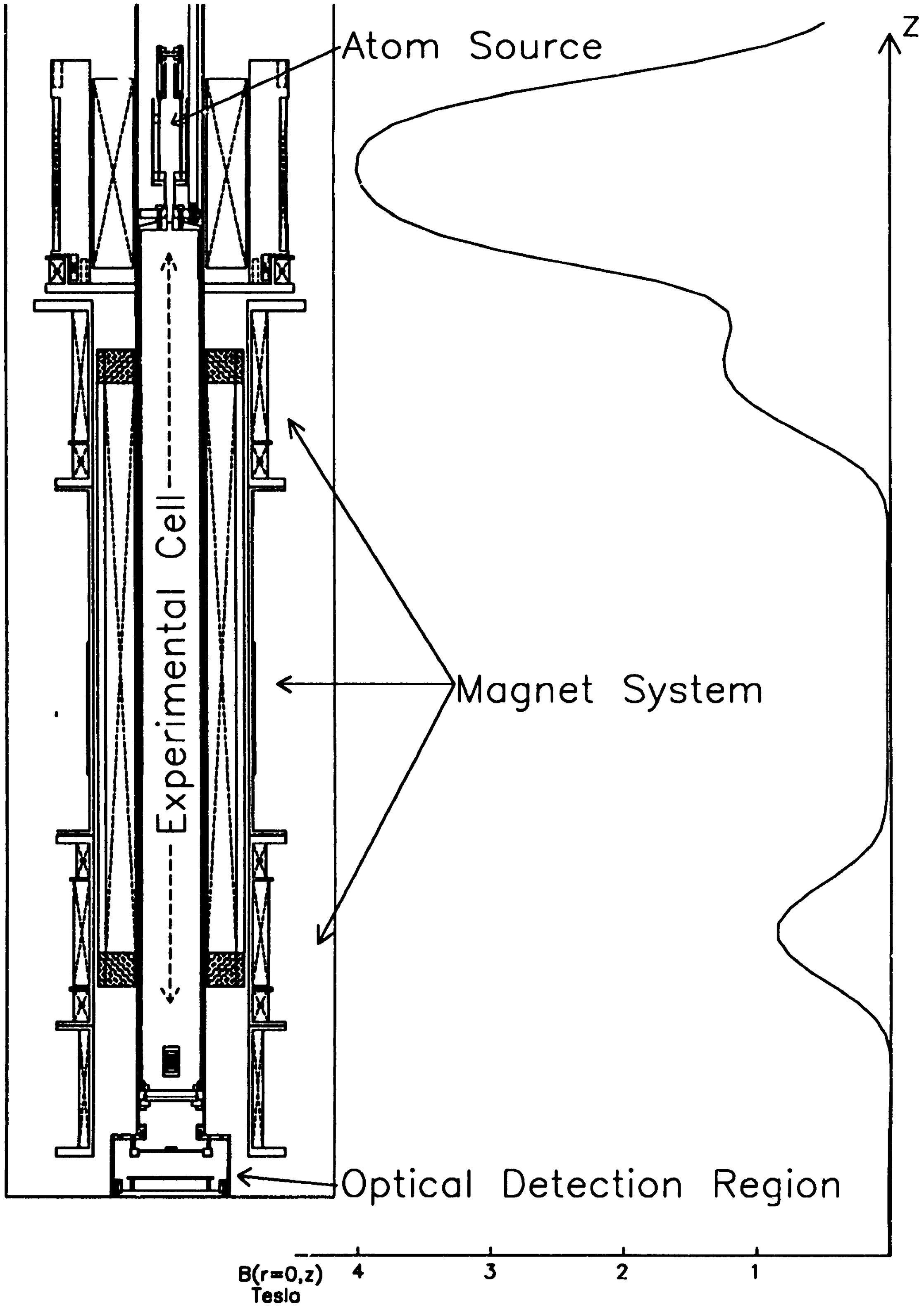

Figure 2-3: Diagram of trap apparatus. The curve at the right shows the magnetic field along the axis of the apparatus.

increases linearly with radius away from the axis. Axial confinement is provided by two solenoids (called the pinch magnets) placed at opposite ends of the quadrupole magnet. The far field profiles of the pinch magnets are compensated by counterwound coils to produce a box-like confining potential (approximately 26 cm in length) in the axial direction. A low field solenoid (the bias solenoid) allows application of a uniform field in the axial direction to the trapping region. This field prevents the magnitude of the field from vanishing at any point inside the trap and avoids atom loss due to nonadiabatic spin-flips that would occur in a zero field region.

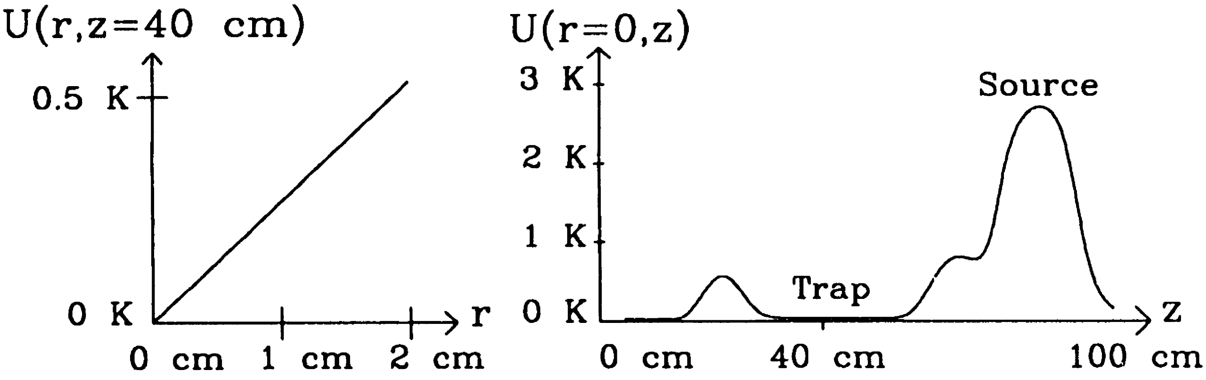

Figure 2-4: Shape of trapping potential.

A hydrogen gas confined in this potential will form a pencil-like sample. When the trap magnets are fully energized, the equilibrium hydrogen sample temperature (see Sec. 2.1.3) is approximately 50 mK. The radius of the sample is 2 mm and its length is 260 mm.

Trap Loading

Hydrogen atoms are produced in a low temperature radio frequency discharge (the atom source) by dissociation of molecular hydrogen. The atom source is located in a region of high magnetic field, and atoms in the weak field seeking hyperfine states are expelled from this high field region into the low field trapping region. Once in the trapping region, they are cooled by thermal accommodation with the walls of the experimental cell. The walls of the experimental cell are coated with a film of superfluid helium (^{4}He). The helium film is necessary to provide a surface with a low (1 K) binding energy that permits thermal accommodation at sub-Kelvin temperatures without complete adsorption of the gas onto the surface.

Elastic collisions between hydrogen atoms produce a thermal distribution of atom density and energies in the trapping region. The temperature of this distribution is determined by the temperature of the experimental cell, typically 0.3 K in this phase of the apparatus operation. Since this temperature is lower than the 0.55 K trap depth, a significant fraction of the atoms have insufficient energy to escape the trap potential. The final step in the trap loading consists of stopping the input flux of atoms and permitting high energy atoms to escape the trapping region. The remaining low energy atoms now have no thermal contact to the rest of the apparatus and evolve toward the internal equilibrium temperature discussed in Sec. 2.1.3.

Evaporative Cooling

After the atoms are loaded into the trap they are evaporatively cooled by controlled lowering of the trap magnets. The pinch magnets and the quadrupole magnet are energized with separate power supplies and their currents may be varied independently in the evaporative cooling process. The pinch magnets control the trap depth (independent of the trap length), and therefore, to a good approximation, the sample temperature. The quadrupole magnet current controls the gradient of the radially confining potential. Since this gradient will control the radial extent of a fixed temperature sample, the quadrupole magnet can be thought of as controlling the sample volume. The choice for the time variation of these independent magnets depends on the goal of the evaporative cooling process.

The different paths possible in an evaporative cooling cycle are illustrated in Fig. 2-5. The "High Compression" path is followed by lowering the pinch current more quickly than the quadrupole current. As the sample cools, its radial extent decreases and its density increases in spite of the atom loss inevitable with evaporative cooling. This type of path is suitable for producing high density, low temperature samples of interest for approaching the Bose-Einstein transition. The "Low Compression" path is followed by lowering the pinch current and quadrupole current at comparable rates. Here, the gradient of the potential in the radial direction is lowered as the sample cools, and the sample volume remains roughly constant. The sample density decreases as atoms are lost in the evaporative cooling process. This type of path is of interest when large sample sizes are desirable to relax the constraints on alignment between the sample and an optical beam.

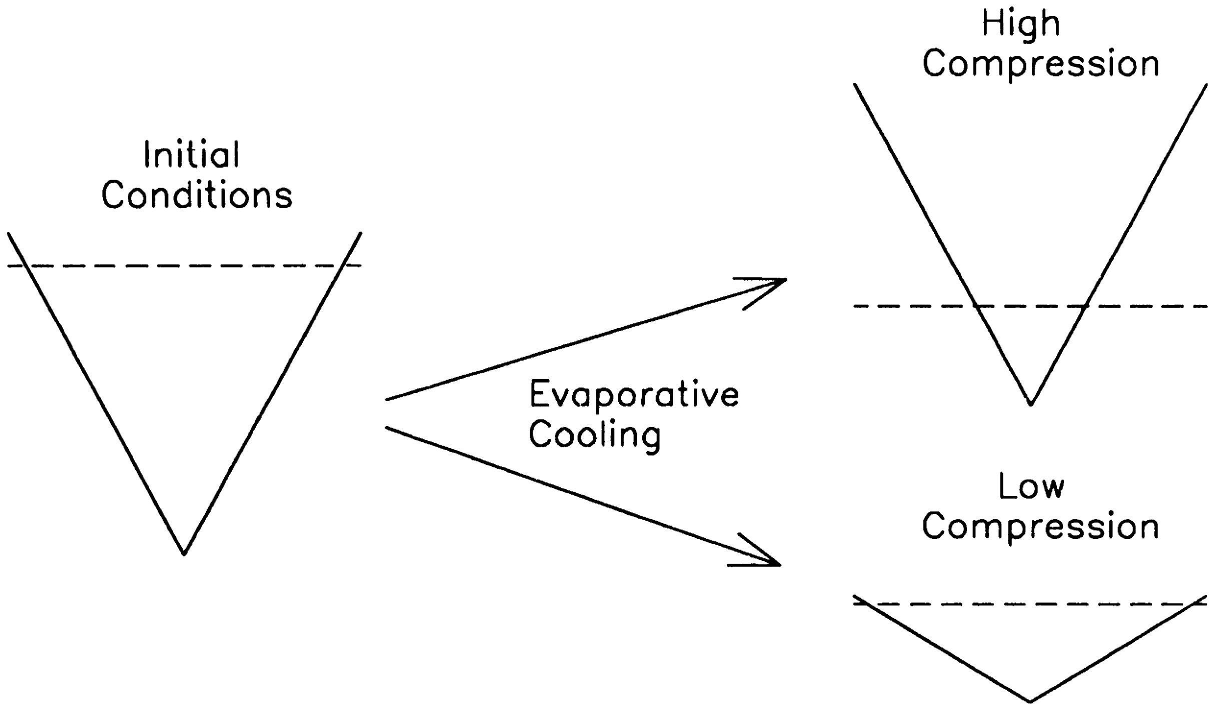

Figure 2-5: Possible paths for evaporative cooling.

The ability to control the radial compression in the evaporative cooling process is important for the optical experiments discussed in later chapters. A low compression cooling path would be best suited to initial observation of an optical signal. The large sample size reduces the constraints on the alignment between the sample and the optical beam. After the signal has been first observed the signal size may be used to optimize the alignment. Once the alignment has been optimized the smaller sample sizes resulting from high compression cooling paths could be used.

Energy Distribution Measurements

The trapped hydrogen is detected by releasing it from the trap. Once released from the trap, the hydrogen collides with and sticks to the walls of the experimental cell, where it eventually recombines into molecular hydrogen. A fraction of the energy released in the recombination process is detected as heat by a bolometer that is located in the experimental cell.

The detection process is illustrated in Fig. 2-6. The trap is dumped by lowering one of the pinch magnets linearly to zero. The time scale for this is much faster than for evaporative cooling, and the sample does not maintain internal thermal equilibrium during the dump. As the energy barrier that defines the trap depth is lowered, atoms with total energies higher than the barrier escape the trap. The time scale for escape and detection (through recombination) is short compared to the time scale of the trap dump. If the bolometer signal is plotted as a function of the barrier height during the trap dump, the energy distribution of the sample is obtained. The measured energy distributions can be compared to calculated distributions with an assumed temperature. The shape of the trap potential must be known in order to calculate an energy distribution. An example of this type of comparison is shown in Fig. 2-7. This method is used to determine the temperature of the sample.

The total amount of heat detected by the bolometer during a trap dump is proportional to the number of atoms released from the trap. The bolometer is calibrated by measuring the decay time of a sample. The sample decay is due to dipolar relaxation, which occurs with a known rate constant[14]. Since the dipolar relaxation rate is density dependent, a measurement of the sample decay rate allows one to determine the sample density Knowledge of the sample density and the sample temperature allows one to calculate the total number of trapped atoms.

The sample decay rate is measured by performing a series of identical trap loading and evaporational cooling sequences, and then holding the sample for varying lengths of time after completion of the cooling sequence. Plotting the size of the bolometer signal as a function of the holding time yields the sample decay time.

The techniques described in this chapter have yielded the closest approach yet

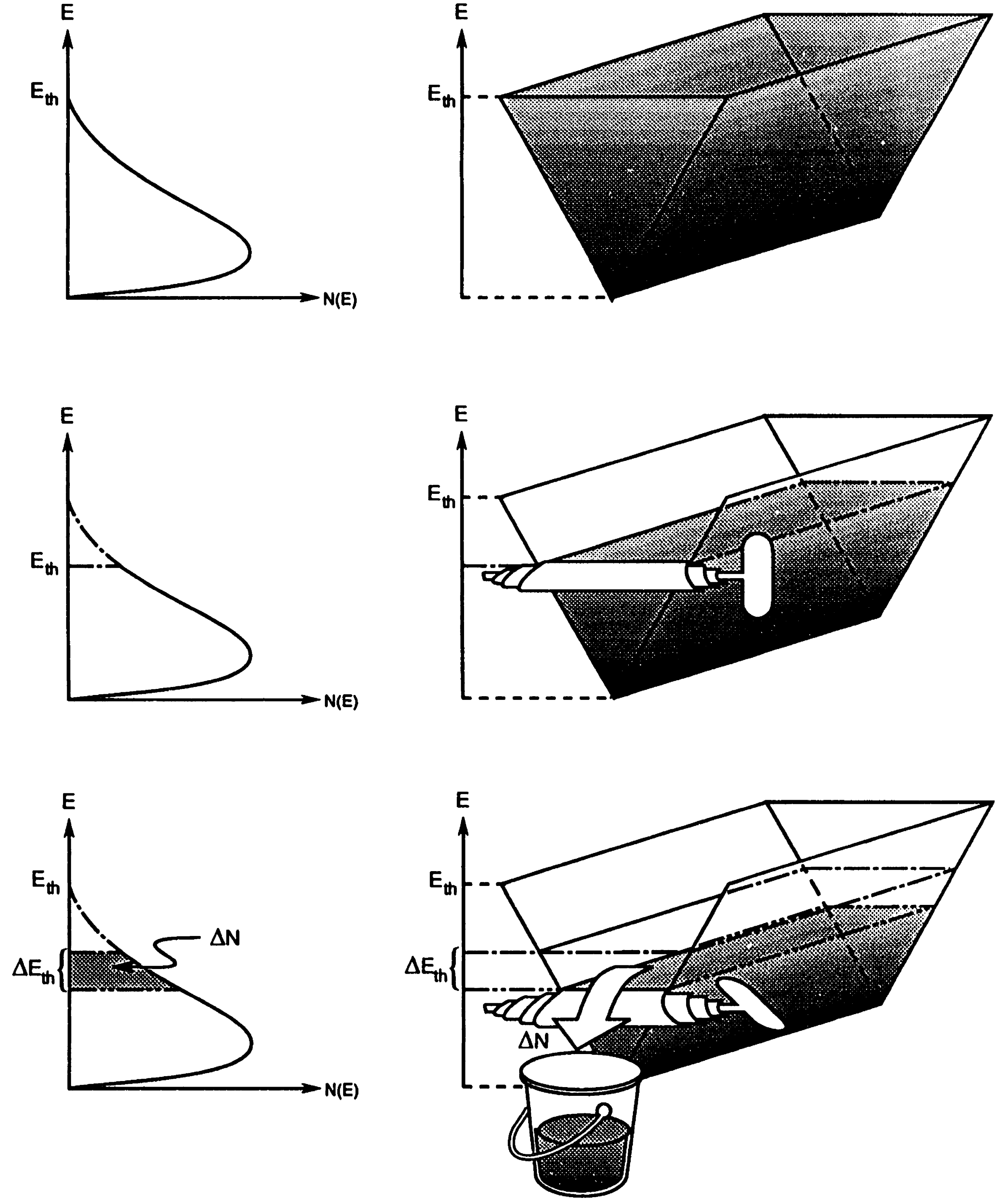

Figure 2-6: Method for energy distribution measurement. Adapted from N. Masuhara.

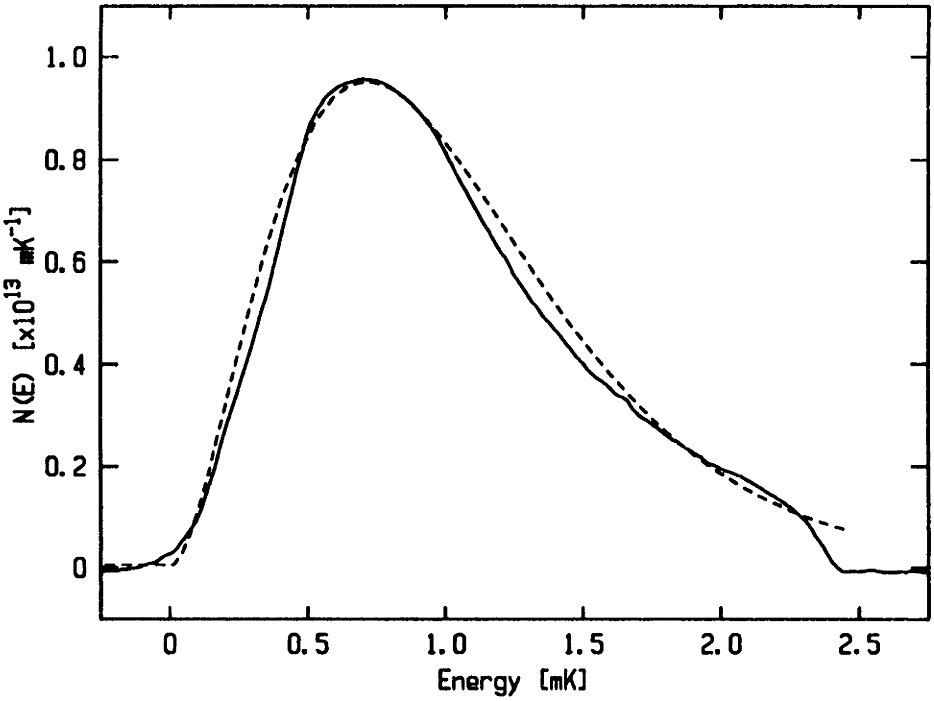

Figure 2-7: Example of energy distribution. The solid line is a measured energy distribution, the dashed line is a calculated distribution with a temperature of 275 μK. The number of atoms in this sample is 1×10^{13}, and the central density is 4×10^{13} cm^{-3}.

observed to the Bose-Einstein with atomic hydrogen. Samples have been produced with a temperature of 100 μK and a density of 8 × 10^{13} cm^{-3}. At this density the Bose-Einstein transition is expected to occur at a temperature of 30 μK, only a factor of 3.5 lower than has been achieved. This progress in relation to other research is illustrated in Fig. 2-8.

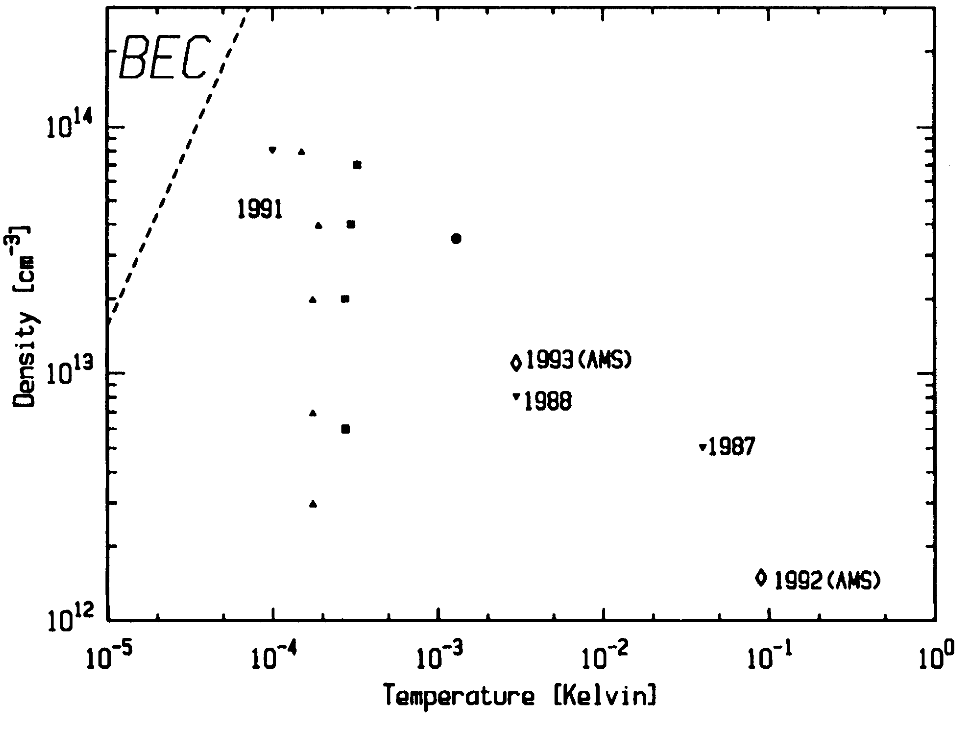

Figure 2-8: Progress toward the Bose-Einstein transition with magnetically trapped hydrogen. The solid symbols are from experiments at MIT[9]. The open symbols are from experiments in other groups[1ᶠ].

2.3 Need for a New Detection Technique

There appears to be no fundamental obstacle to further progress toward Bose condensation. The primary difficulty in extending these results is due to the limitations of our technique for detecting the atoms. This technique cannot be effectively applied to samples of either significantly higher density or lower temperature.

The limitation to higher densities can be understood as follows. We recall that the sample energy distribution (and therefore temperature) is determined by releasing the atoms from the trap and monitoring the escaping atom flux as a function of the barrier height. There are three important time scales in this process. The first is τ_{esc}, the escape time. τ_{esc} is the time necessary for an atom that has an energy above the barrier height to escape the trap *and* be detected by the bolometer. The second time scale is τ_{lower}, or the trap lowering time. The third time scale is τ_{therm}, or the sample thermalization time.

In order for this technique to accurately measure the energy distribution these time scales must satisfy the conditions

$$\tau_{esc} \ll \tau_{lower} \tag{2.4}$$

$$\tau_{lower} \ll \tau_{therm}. \tag{2.5}$$

We must have $\tau_{esc} < \tau_{lower}$ so that an atom with an energy high enough to escape the trap does so quickly compared to the trap lowering time. Only in this case does the instantaneous bolometer signal represent the number of atoms with an energy equal to the instantaneous barrier height. Also, we must have $\tau_{lower} < \tau_{therm}$ so that the trap lowering time is shorter than the sample thermalization time. If this is not the case, then the distribution will change as the trap is lowered, causing difficulty in interpretion of the measurement.

Clearly, if $\tau_{esc} \approx \tau_{therm}$ then these conditions cannot be satisfied. These times may be estimated as follows. τ_{esc} is roughly given by

$$\tau_{esc} \approx L/v \tag{2.6}$$

where L is the distance between the trap center and the detection region ($\approx$ 30 cm), and v is the thermal velocity for the sample. We estimate τ_{therm} as the elastic collision rate at the center of the trap. This gives

$$\tau_{therm} \approx (n\sigma v)^{-1}. \tag{2.7}$$

where n is the density at the trap center, σ is the elastic scattering cross section, and v is the thermal velocity. The ratio of these times is given by

$$\frac{\tau_{esc}}{\tau_{therm}} \approx Ln\sigma \approx 10^{-14} \ \ n \ \ \mathrm{cm}^3 \tag{2.8}$$

Thus, at densities much higher than 10^{14} cm^{-3} , the technique is no longer capable of straightforward measurement of the energy distribution.

The limitation to lower temperatures is due to the fact that it is necessary to know the shape of the trapping potential to determine the sample temperature. We recall that the sample temperature is determined by comparison of the measured energy distribution with a calculated distribution. The calculated distribution is obtained by convolving an assumed Boltzmann distribution of energies with the density of states determined by the shape of the trapping potential. If the trap shape has uncertainties on an energy scale comparable to the sample temperature, then this method cannot be used to determine the temperature with confidence.

Uncertainties in our trap shape exist due to residual magnetism in the superconducting trap magnets. Significant effort has been expended to minimize this effect, but uncertainties in the magnetic field in the trapping region do exist on the 0.1 mT level. A magnetic field of 0.1 mT corresponds to an atom energy of 68 μK. The magnetic field uncertainties therefore introduce difficulty in measurement of the sample energy distributions for sample temperatures less than 100 μK.

Another important consideration is that the bolometric detection technique is poorly suited to the study of Bose condensation because it is inherently destructive. The sample must be released from the trap and destroyed in order to be detected. It is conceivable that the onset of BEC could be detected, but a thorough study of the condensate would require a method of investigating it while still confined in the trap.

The main body of this thesis is devoted to a new detection technique designed to resolve these difficulties. The technique is based on laser excitation of the $1S$–$2S$ two-photon transition. In addition to providing enhanced detection capabilities that will assist the approach to Bose condensation, it will open the way for new experiments in high resolution laser spectroscopy of the $1S-2S$ transition.

Chapter 3

1S-2S Excitation and Detection in a Magnetic Trap

This chapter discusses the theoretical concepts necessary to understand the excitation and detection of the $1S$–$2S$ two-photon transition in the environment of our magnetic trap.

In Section 3.1 we review a treatment of the hydrogen $1S-2S$ transition due to Beausoleil and Hänsch[16]. The hydrogen atom is treated as an effective two-level system, with the two-photon interaction being expressed as an interaction Hamiltonian within the two-level manifold. In Section 3.2 we consider optimization of the transition rate and develop estimates for the transition rate and linewidth in our experimental conditions. In Section 3.3 we consider in detail the detection of the $1S$–$2S$ transition by electric field induced L_α fluorescence.

3.1 The 1S-2S Two-Photon Transition

Two-photon transitions obey the selection rules[17] $\Delta F = 0$, $\Delta m_F = 0$, so that transitions from a given hyperfine level in the $1S$ manifold involve only one hyperfine level in the $2S$ manifold. This allows us to consider the hydrogen atom as an effective two-level system when describing the $1S-2S$ two-photon transition. The presence of other states is necessary for the two-photon interaction to exist (as will be seen below), but they play no further role once an effective two-level Hamiltonian for the interaction has been determined.

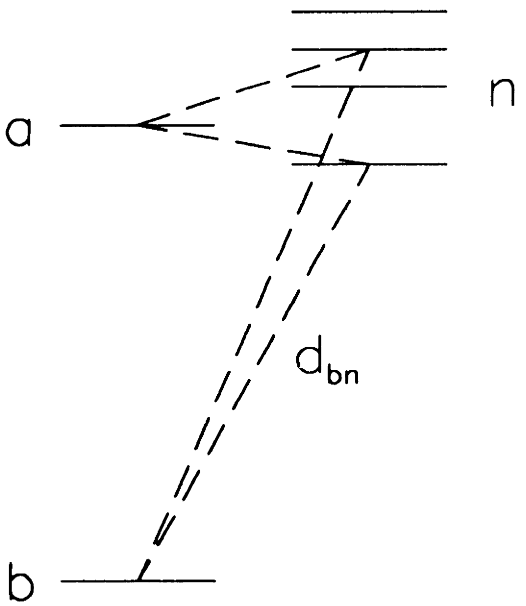

Figure 3-1: Relevant states for $1S-2S$ transition

Our model for the hydrogen atom is illustrated in figure 3-1. State b corresponds to one of the hyperfine levels of the ground ($1S$) state, and state a corresponds to the analogous hyperfine level of the excited ($2S$) state. Because states a and b have the same parity, one-photon electric dipole transitions between them are forbidden. Electric dipole matrix elements do exist between both a and b and a series of intermediate states n of opposite parity and satisfying the selection rules $\Delta J = 0, \pm 1$. The states n correspond to the P states of hydrogen. We consider the effect of an electric field that introduces a second order coupling between states a and b through the intermediate states n. The electric field is assumed to be produced by two nearly counterpropagating optical beams derived from the same laser. We write this field as the sum of two monochromatic fields with angular frequency ω:

$$\vec{E}(\vec{r},t) = \mathrm{Re}(\vec{E}_1(\vec{r},t)e^{-i\omega t} + \vec{E}_2(\vec{r},t)e^{-i\omega t}). \tag{3.1}$$

$\vec{E}_1(\vec{r},t)$ and $\vec{E}_2(\vec{r},t)$ are complex vector amplitude functions that describe the polarization, spatial dependence, and (slowly varying) time dependence of the field amplitude. Taking $\vec{E}_1(\vec{r},t)$ and $\vec{E}_2(\vec{r},t)$ to be paraxial optical beams, we write (for $j = 1,2$)

$$\vec{E}_j(\vec{r},t) = \hat{\epsilon}_j \, E_j(t) \, U_j(\vec{r}) \, e^{i(\vec{k}_j \cdot \vec{r} - \phi_j)} \tag{3.2}$$

where $\hat{\epsilon}_j$ is a complex polarization vector, $E_j(t)$ is a real, slowly varying envelope function with the dimensions of an electric field, $U_j(\vec{r})$ is a complex function describing the spatial dependence of the field, $\vec{k}_j$ is the propagation vector, and ϕ_j allows for an arbitrary phase. The envelope function $E_j(t)$ is not explicitly used in this analysis, but it is retained to permit straightforward generalization to different experimental conditions. The intensity of the field in Eq. 3.2 is given by $I_j(\vec{r},t) = \frac{1}{2}\epsilon_0 \, c \, E_j^2(t) \, |U_j(\vec{r})|^2$.

We write the Hamiltonian for this system as $H(t) = H_0 + V(t)$, where

$$H_0 = \begin{bmatrix} \hbar\omega_a & 0 \\ 0 & \hbar\omega_b \end{bmatrix} \tag{3.3}$$

is the unperturbed Hamiltonian, and

$$V(t) = \begin{bmatrix} \hbar\Delta\omega_a(t) & V_{ab}(t) \\ V_{ba}(t) & \hbar\Delta\omega_b(t) \end{bmatrix} \tag{3.4}$$

is the interaction Hamiltonian. The terms $\hbar\Delta\omega_j(t)$ correspond to energy shifts of the a and b levels by the perturbing fields. These are normally referred to as AC Stark shifts. The terms $V_{ab}(t)$ and $V_{ba}(t)$ are the coupling terms responsible for the two-photon transition between levels a and b. The terms of the interaction Hamiltonian are given by[12]

$$\frac{V_{ab}(t)}{\hbar} = \left[\frac{ea_0}{2\hbar}\right]^2 e^{-2i\omega t} \sum_n \frac{\vec{d}_{an} \cdot [\vec{E}_1 + \vec{E}_2] \quad \vec{d}_{nb} \cdot [\vec{E}_1 + \vec{E}_2]}{\omega_{bn} + \omega} \tag{3.5}$$

$$\Delta\omega_a(t) = \left[\frac{ea_0}{2\hbar}\right]^2 \sum_n \left[\frac{|\vec{d}_{an} \cdot [\vec{E}_1^* + \vec{E}_2^*]|^2}{\omega_{an} + \omega} + \frac{|\vec{d}_{an} \cdot [\vec{E}_1 + \vec{E}_2]|^2}{\omega_{an} - \omega}\right] \tag{3.6}$$

with an analogous expression for $\Delta\omega_b(t)$, and $V_{ba}(t) = V_{ab}^*(t)$. The sums in the above equations are over all states n that possess a nonzero electric dipole moment with both states a and b, and implicitely include an integral over the continuum states. The terms $\vec{d}_{jn}$ are the electric dipole moments in units of ea_0 given by

$$\vec{d}_{jn} = (1/a_0)\ \langle j|\vec{r}|n\rangle \tag{3.7}$$

The expression for $V_{ab}(t)$ contains four terms of the form $\vec{d}_{an} \cdot \vec{E}_i\ \vec{d}_{nb} \cdot \vec{E}_j$, with $i, j = 1, 2$. The spatial behavior of these terms is fundamentally different for $i = j$ and for $i \neq j$. The terms with $i = j$ possess a spatial dependence of $\exp(2i\vec{k}_i \cdot \vec{r})$, while the terms with $i \neq j$ have a dependence of $\exp(i(\vec{k}_1 + \vec{k}_2) \cdot \vec{r})$. If $\vec{E}_1(\vec{r}, t)$ and $\vec{E}_2(\vec{r}, t)$ are nearly counterpropagating, then we have $\vec{k}_1 \approx -\vec{k}_2$, and the spatial dependence of the $i \neq j$ terms nearly vanishes. This has significant consequences if we allow for motion of the atoms. The $i = j$ terms acquire a Doppler shift, while the $i \neq j$ terms do not. This has a profound effect on the lineshape and transition rate. In this discussion we neglect the Doppler broadened terms, and keep only the Doppler free terms. Under these assumptions Equation 3.5 simplifies to

$$\frac{V_{ab}(t)}{\hbar} = D_{ab}\tfrac{1}{2}\epsilon_0 c E_1(t) E_2(t) U_1(\vec{r}) U_2(\vec{r}) \exp i[(\vec{k}_1 + \vec{k}_2) \cdot \vec{r} - 2\omega t - (\phi_1 + \phi_2)] \tag{3.8}$$

where

$$D_{ab} = \frac{1}{\pi^2 \hbar c}\left[\frac{\alpha}{2R_\infty}\right]^3\ \tfrac{1}{3} M_{ab}^{12} \tag{3.9}$$

M_{ab}^{12} is a dimensionless two-photon transition amplitude defined as

$$M_{ab}^{12} = 3\pi c R_\infty \sum_n \frac{\hat{\epsilon}_1 \cdot \vec{d}_{an}\ \ \hat{\epsilon}_2 \cdot \vec{d}_{nb}\ +\ \hat{\epsilon}_2 \cdot \vec{d}_{an}\ \ \hat{\epsilon}_1 \cdot \vec{d}_{nb}}{\omega_{bn} + \omega}. \tag{3.10}$$

The value for M_{ab}^{12} has been calculated by Bassani et al.[18]. They find for linear polarization of $\vec{E}_1(\vec{r}, t)$ and $\vec{E}_2(\vec{r}, t)$

$$M_{ab}^{12} = 11.78 \cos\theta \tag{3.11}$$

where θ is the angle between the polarization directions. For $\theta = 0$, this

$$D_{ab} = 4.63 \ \ \mathrm{cm}^2/\mathrm{J} \tag{3.12}$$

The spatial dependence of $e^{i((\vec{k}_1+\vec{k}_2)\cdot\vec{r})}$ has been retained in Eq. 3.8 to allow for the case where $\vec{E}_1(\vec{r},t)$ and $\vec{E}_2(\vec{r},t)$ are not exactly counterpropagating.

The two-photon interaction has now been expressed as an effective Hamiltonian for a two level system. This allows straightforward application of familiar results for perturbed two level systems to describe the interaction. For example, the two-photon Rabi frequency for this system is

$$\omega_R = 2\left|\frac{V_{ab}(t)}{\hbar}\right| = 9.26 \ \ \sqrt{I_1\,I_2} \ \ \mathrm{cm}^2/\mathrm{Ws} \tag{3.13}$$

where I_1 and I_2 are the intensities of the two beams. We also recall the transition rate from state b to state a in the presence of a weak resonant excitation and a homogeneous linewidth $\Delta\omega$

$$R_a = \frac{\omega_R^2}{\Delta\omega} = \frac{85.7}{\Delta\omega} \ \ I_1 I_2 \ \ \mathrm{cm}^4/\mathrm{W}^2\mathrm{s} \tag{3.14}$$

If the unperturbed $2S$ state lifetime were the only broadening mechanism present, then $\Delta\omega = \gamma_s = 8.2 \ \mathrm{s}^{-1}$. Taking the saturation power to be such that $R_a = \gamma_s$, the $1S-2S$ transition would be saturated by 0.89 W/cm² of monochromatic 243 nm radiation.

3.2 1S-2S Excitation in a Magnetic Trap

In the previous section we calculated the two-photon transition rate as a function of the effective linewidth of the transition. In this section we discuss the contributions to the linewidth. We also consider optimization of the total sample transition rate, which is important for the first observation of a $1S-2S$ resonance signal.

The conditions that will be assumed in this discussion are based on the experiwhere θ is the angle between the polarization directions. For $\theta = 0$, this gives

$$D_{ab} = 4.63 \ \text{cm}^2/\text{J} \tag{3.12}$$

The spatial dependence of $e^{i((\vec{k}_1+\vec{k}_2)\cdot\vec{r})}$ has been retained in Eq. 3.8 to allow for the case where $\vec{E}_1(\vec{r},t)$ and $\vec{E}_2(\vec{r},t)$ are not exactly counterpropagating.

The two-photon interaction has now been expressed as an effective Hamiltonian for a two level system. This allows straightforward application of familiar results for perturbed two level systems to describe the interaction. For example, the two-photon Rabi frequency for this system is

$$\omega_R = 2\left|\frac{V_{ab}(t)}{\hbar}\right| = 9.26\ \sqrt{I_1\, I_2}\ \ \text{cm}^2/\text{Ws} \tag{3.13}$$

where I_1 and I_2 are the intensities of the two beams. We also recall the transition rate from state b to state a in the presence of a weak resonant excitation and a homogeneous linewidth $\Delta\omega$

$$R_a = \frac{\omega_R^2}{\Delta\omega} = \frac{85.7}{\Delta\omega}\ I_1 I_2\ \ \text{cm}^4/\text{W}^2\text{s} \tag{3.14}$$

If the unperturbed $2S$ state lifetime were the only broadening mechanism present, then $\Delta\omega = \gamma_s = 8.2\ \text{s}^{-1}$. Taking the saturation power to be such that $R_a = \gamma_s$, the $1S-2S$ transition would be saturated by 0.89 W/cm^2 of monochromatic 243 nm radiation.

3.2 1S-2S Excitation in a Magnetic Trap

In the previous section we calculated the two-photon transition rate as a function of the effective linewidth of the transition. In this section we discuss the contributions to the linewidth. We also consider optimization of the total sample transition rate, which is important for the first observation of a $1S-2S$ resonance signal.

The conditions that will be assumed in this discussion are based on the experimental results of earlier experiments described in Chapter 2. To a first approximation they represent the lowest temperatures and highest densities that have been achieved in conditions suitable for initial observation of a $1S$–$2S$ signal. They are summarized in Section 3.3.1.

We separate the contributions to the linewidth of the system into two categories: intrinsic contributions and instrumental contributions. The intrinsic contributions are ones that are inherently present in this type of experiment. Examples of intrinsic contributions are: Zeeman broadening, photoionization, the AC Stark effect, and, of course, the natural linewidth. The intrinsic contributions are described and estimated in Section 3.2.2. The instrumental contributions would not be present with an idealized apparatus. Some of these contributions are troublesome because they are not directly measurable (with our current capabilities) and are difficult to estimate with confidence. Examples of instrumental contributions are line broadening from stray electric fields and finite laser linewidth. These contibutions are described in Section 3.2.3. In Section 3.2.4 we consider optimization of the total sample transition rate with respect to the focus of the beam. We then calculate the expected transition rate given our current understanding of the intrinsic and instrumental linewidth contributions.

3.2.1 Trap Conditions

In Chapter 2 we described the experimental conditions that have been achieved with trapping and evaporative cooling of hydrogen. We recall that sample temperatures of 100 μK are achievable. Sample densities approaching 10^{14} cm^{-3} have been achieved at these temperatures, but this requires a large degree of sample compression in the radial direction. The resulting small radial extent of the sample would make initial alignment between the sample and the laser beam difficult to achieve. For the purposes of this discussion we will assume a sample density of 10^{13} cm^{-3}. We assume that the trapping fields have been adjusted so that the spatial extent of the sample is approximately 1 mm in the radial direction and 40 mm in the axial direction. The radius is chosen as the largest practical value to minimize the constraints on alignment of the beam and the sample. The length is adjusted to the minimum practical value to minimize the effects of radiation trapping. Radiation trapping is discussed in Sec. 3.3.4.

As explained in Chapter 2, the sample consists entirely of d state atoms. This, coupled with the hyperfine selection rules for two-photon transitions, means that the laser can only induce one transition. The quantum numbers of the two states involved in this transition are

$$|n=1, l=0, J=\tfrac{1}{2}, F=1, m_F=1> \;\rightarrow\; |n=2, l=0, J=\tfrac{1}{2}, F=1, m_F=1> \tag{3.15}$$

We note that in the $F=1, m_F=1$ hyperfine level, m_s and m_i are also good quantum numbers. In later discussion we restrict our attention to the transition indentified in Equation 3.15.

3.2.2 Intrinsic Linewidth Contributions

In this section we discuss the contributions to the linewidth that are inherent in this type of experiment. Wherever possible we shall state the size of the contributions as a function of the experimental conditions.

Natural Lifetime

Radiative decay via single photon emission is forbidden for an unperturbed $2S$ state atom. The dominant decay channel is by two-photon spontaneous emission, which occurs at a rate[19]

$$\gamma_s = 8.23 \ \text{s}^{-1}. \tag{3.16}$$

This decay rate gives a natural linewidth of

$$\Delta\nu_N = \gamma_s/2\pi = 1.3 \ \text{Hz}. \tag{3.17}$$

Zeeman Shift

A consequence of magnetic trapping is that the trapped atoms are subject to perturbing magnetic fields. The magnetic field seen by the sample has two components: a uniform bias field, B_0, and the inhomogeneous trapping fields. The bias field is essentially a free parameter chosen by the experimenter. The purpose of the bias field is to prevent Majorana spin flips near the bottom of the trap. The fields necessary for this are extremely small, but uncertainty in the trapping fields require one to be conservative in choosing a value. We assume a value of $B_0 = 0.3$ mT for this discussion. The field inhomogeneity necessary to confine the sample is determined by the sample temperature. Roughly speaking, the field inhomogeneity, ΔB, over the sample (or over a typical atom's trajectory) is given by

$$\Delta B \approx \frac{kT}{\mu_B} = 1.47 \ T \ \text{ T/K}. \tag{3.18}$$

The magnetic field shifts the $1S$ and $2S$ state energies, but it shifts them by nearly identical amounts. The magnetic moments of both states are nearly equal since in both states $m_s = m_i = +1/2$. There is, however, a small relativistic correction to the magnetic moment of a bound electron that depends on the bound state energy. The magnetic moment for an electron bound in the $nS_{1/2}$ state of a hydrogen atom is given (to order α^2) by[20]

$$\mu = \mu_e(1 - \frac{\alpha^2}{3n^2}) \tag{3.19}$$

where μ_e is the free electron magnetic moment and α is the fine structure constant. This leads to a first order frequency shift of the $1S-2S$ transition by an amount

$$\nu_B = \frac{\mu(2S) - \mu(1S)}{h} B = \frac{\alpha^2 \mu_B}{4h} B = 1.8 \times 10^5 \ B \ \text{ Hz/T}. \tag{3.20}$$

The uniform bias field, B_0, introduces a frequency shift to the transition that does not effect the linewidth and will be ignored. The inhomogeneous trapping fields introduce a frequency shift that depends on an atom's position in the trap, a source of inhomogeneous broadening. Using Eq. 3.18 for the field inhomogeneity, we find a spread in resonance frequencies for a sample at temperature T

$$\Delta\nu_B \approx \frac{\alpha^2 kT}{4h} = 2.8 \times 10^5\, T \text{ Hz/K}. \tag{3.21}$$

Photoionization

The $2S$ state can be photoionized by a single 243 nm photon. The photoionization cross section for the $2S$ state at 243 nm is[16]

$$\sigma_{pi} = 9.26 \times 10^{-18} \text{ cm}^2. \tag{3.22}$$

The photoionization rate can be obtained by multiplying σ_{pi} by the total photon flux in both counterpropagating beams

$$\gamma_{pi} = 11.4\, (I_1 + I_2) \text{ cm}^2/\text{Ws}. \tag{3.23}$$

This gives a photoionization linewidth of

$$\Delta\nu_{pi} = 1.8\, (I_1 + I_2) \text{ cm}^2/\text{Ws}. \tag{3.24}$$

AC Stark Effect

The presence of laser induced energy shifts for the $1S$ and $2S$ levels was noted in Section 3.1. The resulting frequency shift of the $1S$–$2S$ transition is an inhomogeneous broadening mechanism, since an atom's resonance frequency is laser intensity (and therefore position) dependent. Beausoleil[16] treats the evaluation of the sum in Equation 3.6 and finds a value for the net AC Stark shift of the transition

$$\Delta\nu_{AC} = 3.33\sqrt{I_1 I_2} \text{ Hz/W cm}^2. \tag{3.25}$$

Collisional Quenching

The metastable $2S$ state can be quenched by collisions with other atoms. In our situation the relevant collisions would be H($2S$) - H($1S$) collisions at submillikelvin energies. There is at present no good experimental data or theoretical predictions for the collisional quenching rates in this energy regime. Collisional quenching of H($2S$) has been investigated theoretically[21] and experimentally[22] for higher energy collisions ($T \geq 300$ K). Slocomb et al.[21] developed a simple model for quenching by a spherically symmetric species that predicted the quenching cross section should scale roughly as $(\alpha/v)^{1/3}$, where α is the polarizability of the quenching species and v is the collision velocity. Taking the experimental value for the quenching cross section for helium at 300 K and scaling it according to this model we find

$$\sigma_{CQ} = 5 \times 10^{-14}\, T^{-1/6} \ \mathrm{cm}^2\ \mathrm{K}^{1/6} \tag{3.26}$$

Using this value for σ_{CQ} we can calculate the collisional quenching rate as a function of sample density and temperature

$$\gamma_{CQ} = 5 \ \times \ 10^{-10}\, n \ \ T^{1/3} \ \ \mathrm{cm}^3/\mathrm{K}^{1/3}\mathrm{s} \tag{3.27}$$

However, this value is not meaningful because the assumptions made in the high temperature treatments are not satisfied in our case. In particular it was assumed that the collision energy was sufficiently large that the $2S$ and $2P$ levels could be considered degenerate. However, the Lamb shift interval corresponds to a temperature of 50 mK, and the $2S - 2P_{3/2}$ interval is 470 mK, which are much larger than the collision energy. Naively, one would expect this to reduce the value of the quenching cross section, since the nondegeneracy would suppress the $2S$ and $2P$ mixing responsible for the quenching. A full theoretical treatment of the collisional quenching process in the low temperature regime would obviously be desirable, but at present none is available.

Doppler Effect

The absence of the first order Doppler effect in two-photon absorption from counterpropagating beams was pointed out in Section 3.1. Here we consider the "residual" first order Doppler effect due to small misalignments of the counterpropagating beams, and the second order Doppler effect.

Consider an atom moving with velocity $\vec{v}$ through a field produced by two infinite plane waves with propagation vectors $\vec{k_1}$ and $\vec{k_2}$. In the rest frame of the atom, the sum frequency of the two fields will be shifted by an amount

$$\nu_{D1} = \frac{1}{2\pi}(\vec{k}_1 + \vec{k}_2) \cdot \vec{v}. \tag{3.28}$$

This frequency shift can be averaged over a Maxwellian velocity distribution at temperature T to yield a gaussian distribution with a FWHM of

$$\Delta\nu_{D1} = 8.8 \times 10^8 \sqrt{T}\, \Delta\theta \ \ \mathrm{Hz/K^{1/2}} \tag{3.29}$$

where the misalignment has been expressed as an angle $\Delta\theta$ given by

$$\Delta\theta = \frac{|\vec{k}_1 + \vec{k}_2|}{|\vec{k}_1|}. \tag{3.30}$$

The experimental constraints on $\Delta\theta$ are discussed in Chapter 5. In this discussion we assume $\Delta\theta \leq 10^{-4}$ radians, which gives

$$\Delta\nu_{D1} = 8.8 \times 10^4 \sqrt{T} \ \ \mathrm{Hz/K^{1/2}}. \tag{3.31}$$

In many circumstances the residual Doppler effect will be reduced even further by a form of Dicke narrowing. The wave vector responsible for the residual Doppler effect is

$$|\vec{k}_{res}| \ = \ |\vec{k}_1 + \vec{k}_2| \ \approx \ |\vec{k}_1|\Delta\theta, \tag{3.32}$$

which, for small misalignments ($\Delta\theta < 10^{-3}$), may be smaller than either the sample dimensions or the beam dimensions.

Even with perfect alignment of the beams, the second order Doppler effect is still present. The resonance frequency of an atom moving with velocity v is shifted by an amount

$$\Delta\nu_{D2} \ = \ -\nu_0 \, \frac{v^2}{2c^2} \tag{3.33}$$

where ν_0 is the transition frequency. If the atomic velocity is an rms thermal velocity of temperature T, then the second order Doppler shift can be written

$$\Delta\nu_{D2} = -341\,T \text{ Hz/K}. \tag{3.34}$$

3.2.3 Instrumental Contributions to the Linewidth

There are two significant contributions to our linewidth that result from practical limitations of our apparatus. These contributions are the Stark effect and the laser linewidth.

Stark Effect

The close proximity of the $2P$ levels to the $2S$ level makes the $2S$ level highly susceptible to electric fields. Application of an electric field causes a mixing of the $2S$ and the $2P$ states. This mixing causes a quenching of the metastability of the $2S$ state and introduces a Stark shift. Both effects are second order in the field strength. The decay rate of the $2S$ state in an electric field is[23]

$$\gamma_{SQ} = 2800\,E^2 \text{ cm}^2/\text{V}^2\text{ s}, \tag{3.35}$$

which gives a linewidth of

$$\Delta\nu_{SQ} = 440\,E^2 \text{ Hz cm}^2/\text{V}^2. \tag{3.36}$$

The Stark shift of the $2S$ level is (see Sec. 3.3)

$$\nu_{SS} = 3600\,E^2 \text{ Hz cm}^2/\text{V}^2. \tag{3.37}$$

The Stark shift and Stark quenching are discussed in detail in Sec. 3.3.

The broadening and line shifts due to the electric fields could in principle be made arbitrarily small in an idealized apparatus. In the design of our experimental cell (detailed in Chap. 5) we attempted to minimize the level of stray electric fields present in the trapping region. The degree to which we were successful is not well known. There is little experimental information available about the sources and levels of stray electric fields in cryogenic environments of this type and currently we have no direct measurement technique.

The degree of uniformity of any stray field is also important. If the stray fields are relatively uniform, then they are a source of homogeneous broadening through γ_{SQ}. Uniform fields introduce a frequency shift through ν_{SS} but they do not inhomogeneously broaden the resonance. Nonuniform fields (whose variation is comparable to their magnitude) introduce both homogeneous and inhomogeneous broadening, with the inhomogeneous broadening from the Stark shift being almost an order of magnitude larger than the homogenous broadening from Stark quenching. The nonuniform case is perhaps more relevant since the sample extends over a significant distance (>30 mm) in the axial direction. It is unlikely that a stray electric field would be uniform on that length scale.

Laser Linewidth

An exact description of the effect of laser frequency noise on a two-photon resonance signal is beyond the scope of this discussion, instead the interested reader is referred to Reference [24]. The performance of the laser system is discussed in Chapter 4. Here we assume a 243 nm laser linewidth of 2 kHz, giving a linewidth at the $1S-2S$ transition frequency of

$$\Delta\nu_{laser} = 4 \text{ KHz}. \tag{3.38}$$

It is noted that this is an estimate based on the performance of similar laser systems, not the result of a direct measurement.

Time-of-flight Broadening

Since the sample is confined by a trap, the interaction time between the laser field and the atoms could, in principle, be made as long as the trap lifetime. In practice our laser field is tightly focussed, so that the extent of the beam may be small compared to the size of an atom's trajectory. There are two scenarios in this case. If the coherence of the atom is lost between successive passages through the beam then there will be a time-of-flight linewidth contribution due to the finite interaction time with an atom as it passes through the beam. If the atom coherence is preserved, then a type of Ramsey interference will occur between successive passages through the beam, removing the time-of-flight contribution to the linewidth.

3.2.4 Optimizing the Transition Rate

We now consider the optimum choice of the adjustable experimental parameters in the context of the first observation of a $1S-2S$ resonance signal. The sample conditions most favorable for the first signal observation were outlined in Sec. 3.2.1. In this discussion we take the sample geometry, density, and temperature to be fixed quantities. The maximum laser power available is also a fixed quantity. Under these assumptions the only adjustable parameter is w_0, the minimum beam radius of the TEM_{00} mode used to excite the transition.

In Section 3.1 we calculated that the single atom excitation rate, R_a, should vary as $I^2/\Delta\omega$ where I is the laser intensity and $\Delta\omega$ is the effective linewidth due to all sources of line broadening. Maximizing the total signal requires maximizing the product of the single atom excitation rate and the total number of atoms being excited. The total number of excitations occurring in the sample per unit time, R_{TOTAL}, can be expressed as

$$R_{TOTAL} = \int d\vec{r}\ \ R_a(I(\vec{r}), \Delta\omega)\ \ n(\vec{r}) \tag{3.39}$$

where $n(\vec{r})$ is the sample density at position $\vec{r}$. The effective limits of the integral in Eq. 3.39 may depend on the extent of the sample through $n(\vec{r})$ or the extent of the laser beam through $I(\vec{r})$. Our goal is to maximize R_{TOTAL} with respect to the beam radius, w_0. Physically, w_0 affects three quantities of interest here, the laser intensity, the effective interaction volume, and the time-of-flight across the beam for a finite temperature atom.

To help understand the dependence of R_{TOTAL} on w_0, we introduce a simplified model for the sample density $n(\vec{r})$. We assume that the sample is a cylinder of radius r_s and length l_s, with a uniform density of n_0. Furthermore, we separate out the intensity dependence of R_a by writing $R_a = R_a^o I^2$. With these assumptions Eq. 3.39 can be expressed as

$$R_{TOTAL} = n_0 \; R_a^o(w_0, \Delta\omega) \; V_{int}(w_0, l_s) \; P_{laser}^2 \tag{3.40}$$

where P_{laser} is the laser power, and $V_{int}(w_0, l_s)$ is defined by

$$V_{int} = \frac{2\pi}{P_{laser}^2} \int_0^{r_s} r dr \int_{-l_s/2}^{l_s/2} dz \; I^2(r, z). \tag{3.41}$$

In Eq. 3.40 the dependence of R_{TOTAL} on w_0 has been separated into two types of contributions. $R_a^o(w_0, \Delta\omega)$ allows for a possible reduction in the single atom excitation rate due to time-of-flight broadening, while $V_{int}(w_0, l_s)$ includes the effect of w_0 on the beam intensity and interaction volume. This procedure is only valid if the effective linewidth does not depend on position within the trap. This is reasonable with the exception of time-of-flight broadening in a strongly focussed beam where the axial variation of the beam radius along the beam is not negligible. This case is discussed separately later. Evaluation of Eq. 3.41 is straightforward if we assume that the radial extent of the sample is much greater than the beam radius, i.e. $r_s \gg w_0$. This assumption is valid in most cases of interest. Using this assumption, and taking $I(\vec{r})$ for a TEM$_{00}$ beam, Eq. 3.41 gives

$$V_{int} \;=\; \frac{k}{\pi} \; \arctan\left(\frac{l_s}{kw_0^2}\right) \tag{3.42}$$

where $k = 2\pi/\lambda$ is the propagation constant for the beam. We note that $b = kw_0^2$ is the confocal parameter of the beam. Two useful approximations for V_{int} are

$$V_{int} \approx \tfrac{1}{2}k \qquad \text{for } l_s \gg kw_0^2 \tag{3.43}$$

$$V_{int} \approx \frac{l_s}{\pi w_0^2} \qquad \text{for } l_s \ll kw_0^2. \tag{3.44}$$

We note that V_{int} varies linearly with l_s up to $l_s \approx kw_0^2$, where it then levels off. This expresses the fact that in a two-photon transition (where the excitation rate varies as the square of the intensity) most of the excitation occurs within one divergence length of the focus.

The effect of time-of-flight broadening is taken into account by the function $R_a^o(w_0, \Delta\omega)$. At this stage in our analysis we assume a contribution to the linewidth due to time-of-flight broadening from a single pass of an atom across the beam. Possible coherence between multiple passes of a trapped atom through the beam is neglected. If the radial extent of the sample is much greater than the beam, then the variation in the trapping potential is negligible across the beam. Then the problem of time-of-flight broadening in our trap is equivalent to a free gas. Roughly speaking, one would expect a time-of-flight broadening on the order of $\Delta\omega_{tof} = v_o/w_0$, where v_o is the rms thermal velocity in the sample. In Chapter 6 we treat the problem of time-of-flight broadening in detail and find this expression to be accurate for the purposes of this discussion. We approximate the combination of the time-of-flight broadening with the linewidth from other sources, $\Delta\omega$, as a simple addition. This approximation is accurate for either $\Delta\omega_{tof} \ll \Delta\omega$ or $\Delta\omega_{tof} \gg \Delta\omega$, but may only be accurate to the order of unity for the case $\Delta\omega_{tof} \approx \Delta\omega$, depending on the exact nature of $\Delta\omega$. With this approximation, $R_a^o(w_0, \Delta\omega)$ can be written

$$R_a^o = \frac{4|D_{ab}|^2}{(\Delta\omega + \Delta\omega_{tof})}. \tag{3.45}$$

Combining the functions V_{int} and R_a^o we have

$$R_{TOTAL} = \frac{4n_0 k|D_{ab}|^2}{\pi(\Delta\omega + (v_0/w_0))} P_{laser}^2 \arctan(\frac{l_s}{kw_0^2}). \tag{3.46}$$

The dependence of R_{TOTAL} on w_0 can be more clearly understood by writing

$$R_{TOTAL} = \frac{4n_0 k|D_{ab}|^2}{\pi} P_{laser}^2 \frac{w_{div}}{v_0} f(\beta, \bar{w}) \tag{3.47}$$

where

$$\begin{aligned}
w_{div} &= \sqrt{l_s/k} && (3.48)\\
\bar{w} &= w_{div}/w_0 && (3.49)\\
\beta &= \Delta\omega/(v_0/w_{div}) && (3.50)\\
f(\beta,\bar{w}) &= \frac{1}{\beta+\bar{w}}\ \arctan(\bar{w}^2) && (3.51)
\end{aligned}$$

These quantities can be understood as follows. w_{div} is the beam radius for which the confocal parameter of the beam equals the length of the sample. $\bar{w}$ is a dimensionless parameter describing the strength of the focussing. β is the ratio of $\Delta\omega$ to the time-of-flight linewidth for $\bar{w} = 1$. $f(\beta, \bar{w})$ is the dimensionless function that describes the dependence of R_{TOTAL} on the beam radius. The inaccuracy of this treatment for time-of-flight broadening in a tightly focussed beam was mentioned earlier. This limits the validity of this treatment to values of $\bar{w} < \max[1, \beta]$. The problem of time-of-flight broadening is discussed in more detail in Chap. 6.

The function $f(\beta, \bar{w})$ is plotted versus $\bar{w}$ in Fig. 3-2. It has two different forms for $\beta \ll 1$ or $\beta \gg 1$. In either case R_{TOTAL} will be optimized for $\bar{w} \approx 1$, or $w_0 \approx \sqrt{l_s/k}$. We have chosen $w_0 = 38$ μm ($\sqrt{l_s/k} = 39$ μm).

All of the parameters that affect the transition rate and lineshape have now been fixed. Using the established values for the laser power, beam radius (and therefore intensity), sample density, and sample temperature, we can obtain values for the intrinsic linewidth contributions discussed in Section 3.2.2. These are summarized in Table 3.1. From Table 3.1 we see that the time-of-flight broadening is much larger than any of the intrinsic linewidth contributions. Since the other sources of instrumental broadening (Stark broadening and laser linewidth) are not well characterized, we combine these two contributions into one factor, $\Delta\omega_{inst}$, and treat separately the cases of $\Delta\omega_{tof} > \Delta\omega_{inst}$ and $\Delta\omega_{tof} < \Delta\omega_{inst}$.

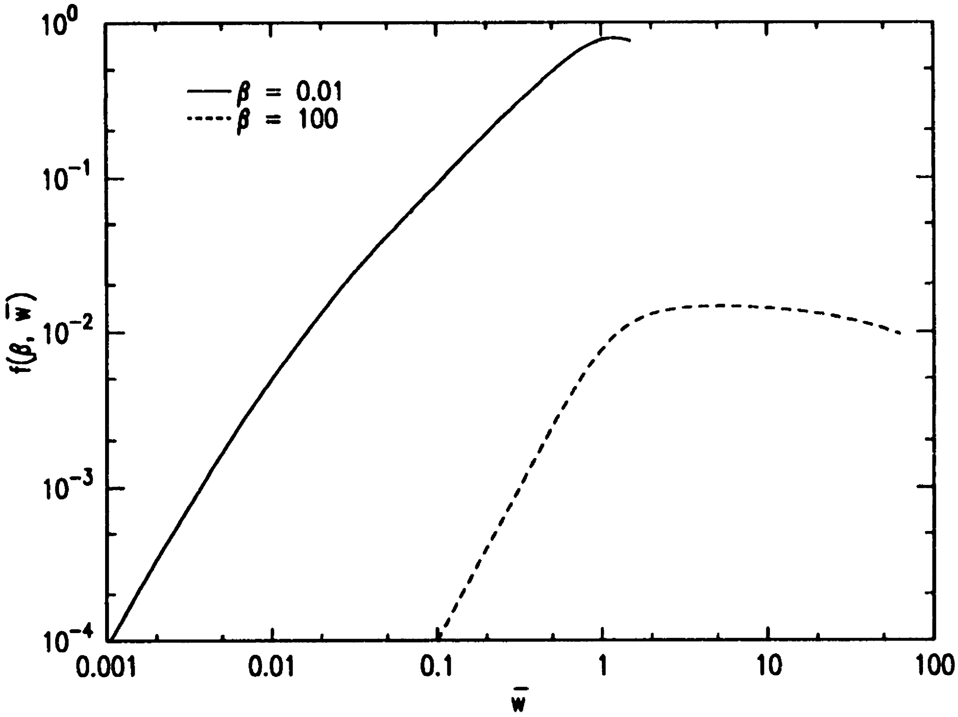

Figure 3-2: The variation of $f(\beta, \bar{w})$ versus $\bar{w}$ with two different values of β.

Table 3.1: Contributions to linewidth from various sources.

Linewidth contribution	Homogeneous linewidth (Hz)	Inhomogeneous linewidth (Hz)
Natural Linewidth	1.3	
Zeeman Shift		28
Photoionization	800	
AC Stark Effect		730
Collisional Quenching	230	
1st Order Doppler		880
2nd Order Doppler		2×10^{-2}
Time-of-flight	6.6×10^3	
Laser linewidth	4×10^3 (?)	
Stark quenching	?	
Stark shifts		?

$\Delta\omega_{tof} > \Delta\omega_{inst}$

When time-of-flight broadening dominates the linewidth, the transition rate is straightforward to estimate. Using Eq. 3.46, we find the resonant transition rate in the time-of-flight broadened regime

$$R_{TOTAL} = \frac{4n_0 k |D_{ab}|^2 w_0}{\pi v_0} P_{laser}^2 \arctan\left(\frac{l_s}{k w_0^2}\right). \tag{3.52}$$

Inserting the numerical values in the above equation, we can express the transition rate as a function of the sample density and temperature (assuming $P_{laser} = 10$ mW)

$$R_{TOTAL} = 1.7 \times 10^{-4}\, n_0 T^{-1/2} \ \mathrm{cm^3 K^{1/2}/s}. \tag{3.53}$$

For a sample density of 10^{13} cm^{-3} and temperature of 100 μK, we find a total transition rate of

$$R_{TOTAL} = 1.7 \times 10^{11} \ \mathrm{s^{-1}}. \tag{3.54}$$

$\Delta\omega_{tof} < \Delta\omega_{inst}$

If the linewidth is dominated by unknown instrumental contributions, then we must leave $\Delta\omega_{inst}$ as an undetermined parameter. Then Eq. 3.46 becomes

$$R_{TOTAL} = \frac{4n_0 k |D_{ab}|^2}{\pi \Delta\omega_{inst}} P_{laser}^2 \arctan\left(\frac{l_s}{k w_0^2}\right) \tag{3.55}$$

Inserting the numerical values in the above equation, we can express the transition rate as a function of the sample density and temperature (assuming $P_{laser} = 10$ mW)

$$R_{TOTAL} = \frac{1.0 \times 10^3}{\Delta\omega_{inst}} n_0 \ \mathrm{cm^3/s}. \tag{3.56}$$

For a sample density of 10^{13} cm^{-3} and temperature of 100 μK, we find a total transition rate of

$$R_{TOTAL} = \frac{1.0 \times 10^{16}}{\Delta\omega_{inst}} \ \mathrm{s^{-2}}. \tag{3.57}$$

3.3 2S State Fluorescence in a Magnetic Trap

Radiative decay via single photon emission is forbidden for an unperturbed $2S$ state atom. The dominant decay channel is by two-photon spontaneous emission. If the atom is subject to an electric field, this is no longer the case. The electric field destroys parity as a good quantum number and couples the S and P states. The admixture of the $2P$ state in the $2S$ state opens a channel for one-photon spontaneous decay to the ground state.

We propose to use this effect to detect the excitation of the $2S$ state. After a period of interaction with the 243 nm laser beam, an electric field is applied to the sample, inducing L_α fluorescence. The fluorescence is detected and assumed to be proportional to the $2S$ state population in the sample. In this section we address the feasibility of this technique. We first describe the properties of the emitted radiation (its polarization, angular distribution, and frequency), and then treat the problem of reabsorption of the radiation by ground state atoms in the sample.

3.3.1 $n = 2$ Level Structure of the Hydrogen Atom

To describe the excitation and detection processes of the $1S-2S$ transition we need to consider all of the $n = 2$ levels of the hydrogen atom. In this section we review the major features of the $n = 2$ level manifold and describe the naming convention for referring to the individual states.

Figure 3-3 illustrates the behavior of the $n = 2$ levels in a magnetic field. This diagram includes energy contributions from the fine structure and the Lamb shift, but neglects the hyperfine structure. The states are labeled with a convention set forth by Lamb: the P states ($L = 1$) are labeled a through f in order of decreasing energy, and the S states ($L = 0$) are labeled α and β. At low magnetic fields $\vec{L}$ and $\vec{S}$ are coupled, giving states of good J and m_j. States a through d correspond to the $2P_{3/2}$ level and states e and f correspond to the $2P_{1/2}$ level. At high fields $\vec{L}$ and $\vec{S}$ become decoupled, leaving m_l and m_s as good quantum numbers. For all fields $m_j = m_s + m_l$ is a good quantum number.

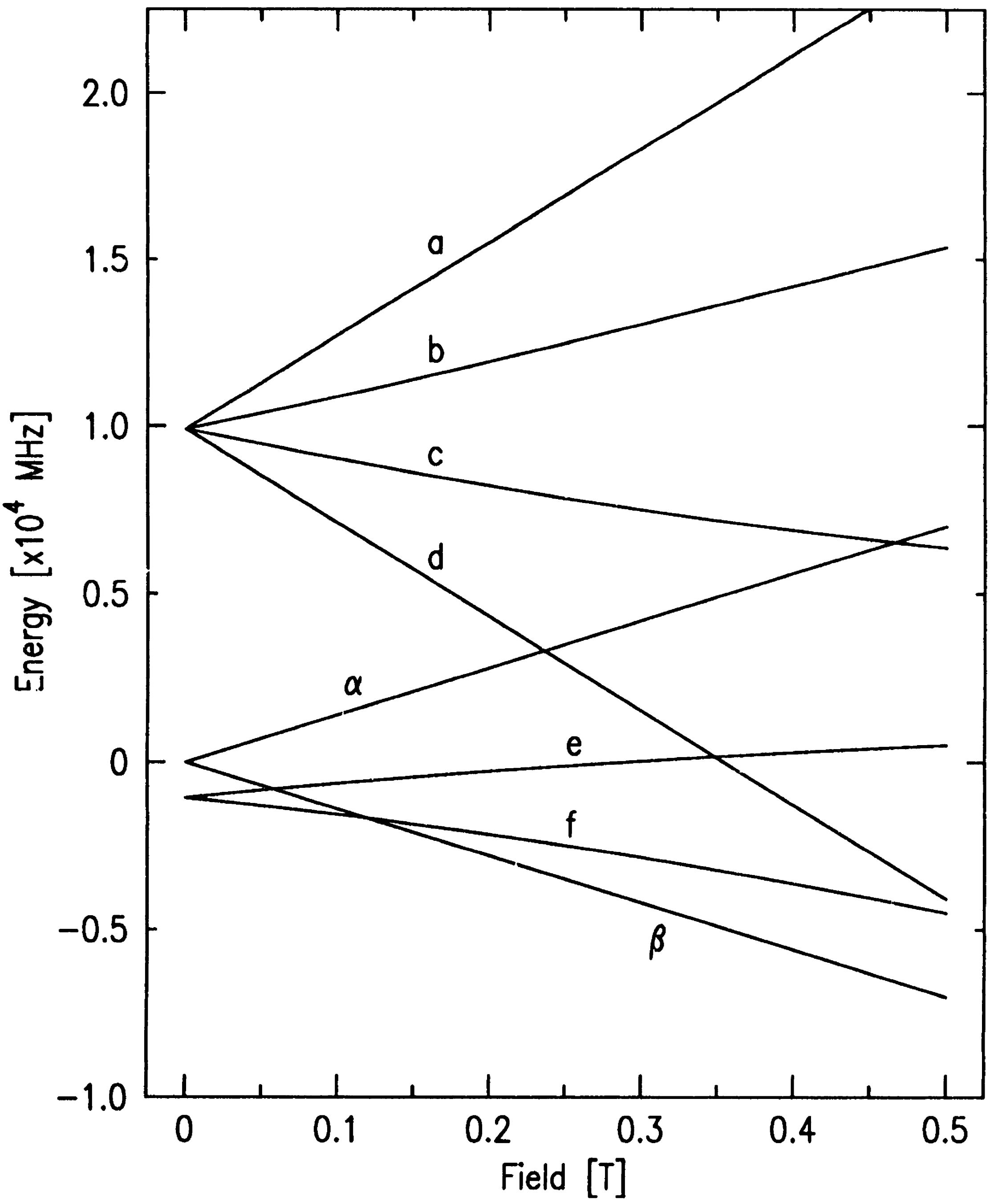

Figure 3-3: Fine structure of the $n = 2$ levels

In discussing the radiative properties of the states, it is useful to express the states a through f in the m_l, m_s basis. We define a dimensionless magnetic field strength parameter ξ,

$$\xi = \frac{\mu_B B}{E_{FS}} \tag{3.58}$$

where μ_B is the Bohr magneton, B is the field strength, and E_{FS} is the fine structure energy splitting. Then we have for states a through f [25]

$$\begin{aligned}
|a> &= \psi_{211}\,|\uparrow> \\
|b> &= \sqrt{\tfrac{1}{2}(1+\delta)}\,\psi_{210}\,|\uparrow> \;+\; \sqrt{\tfrac{1}{2}(1-\delta)}\,\psi_{211}\,|\downarrow> \\
|c> &= \sqrt{\tfrac{1}{2}(1+\delta)}\,\psi_{21-1}\,|\uparrow> \;+\; \sqrt{\tfrac{1}{2}(1-\delta)}\,\psi_{210}\,|\downarrow> \\
|d> &= \psi_{21-1}\,|\downarrow> \\
|e> &= \sqrt{\tfrac{1}{2}(1+\delta)}\,\psi_{211}\,|\downarrow> \;-\; \sqrt{\tfrac{1}{2}(1-\delta)}\,\psi_{210}\,|\uparrow> \\
|f> &= \sqrt{\tfrac{1}{2}(1+\delta)}\,\psi_{210}\,|\downarrow> \;-\; \sqrt{\tfrac{1}{2}(1-\delta)}\,\psi_{21-1}\,|\uparrow>
\end{aligned} \tag{3.59}$$

where ψ_{nlm} is the eigenfunction for the Coulomb Hamiltonian for a spinless electron and $|\uparrow>$ and $|\downarrow>$ represent the spinors describing the electron spin degrees of freedom. δ is defined as

$$\delta = \frac{\xi + \frac{2m_l}{3}}{\sqrt{1 + \frac{4m_l}{3}\xi + \xi^2}}. \tag{3.60}$$

These expressions will be of interest later in this section.

The effect of the hyperfine interaction has been neglected. Its effect on the $2S_{1/2}$ and $2P_{1/2}$ levels is shown in figure 3-4. In low magnetic fields, both levels are split into $F = 1$ triplets and $F = 0$ singlets. By analogy with the terminology for the ground state, we label the hyperfine components of the $2S$ state as $2S_d$ through $2S_a$ in order of decreasing energy.

Finally, we introduce a shorthand notation for describing the $n = 2$ levels in the n, l, m_l, m_s, m_i basis. For example, we write

$$|n = 2, l = 1, m_l = 0, m_s = -\tfrac{1}{2}, m_i = \tfrac{1}{2}> \quad \Rightarrow \quad |\rightarrow \downarrow \twoheaduparrow> \tag{3.61}$$

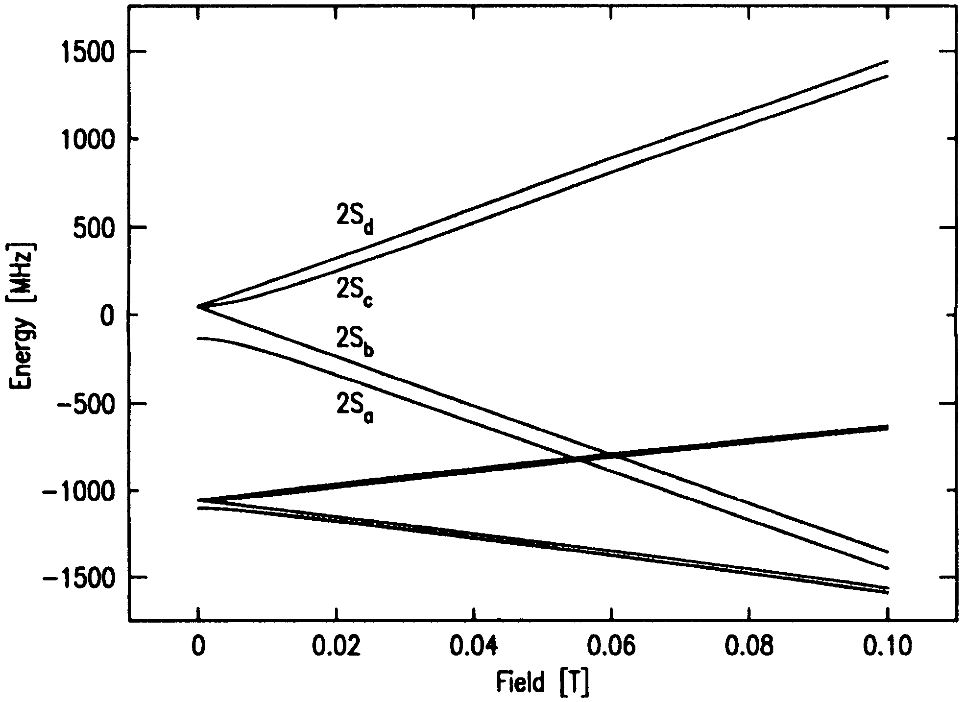

Figure 3-4: Hyperfine structure of the $2S_{1/2}$ and $2P_{1/2}$ levels

where the first arrow corresponds to m_l, the second to m_s, and the third to m_i. A 0 in the first position corresponds to an $l = 0$ state. In discussions that neglect the hyperfine structure we omit the third arrow.

3.3.2 $n = 2$ Eigenstates in Electric and Magnetic Fields

There are a total of 16 states in the $n = 2$ level manifold. It is a straightforward matter to write a complete Hamiltonian for these 16 levels that includes contributions from the fine structure, the Lamb shift, hyperfine structure, and external electric and magnetic fields. The Hamiltonian can then be numerically diagonalized to obtain the eigenstates and energies given arbitrary field values. This procedure has been employed and the main features of the results will be given later in this section. First we present a simple perturbation treatment that provides a qualitative understanding of the effect of electric fields on the $2S$ state. Hyperfine structure is neglected in this simple treatment.

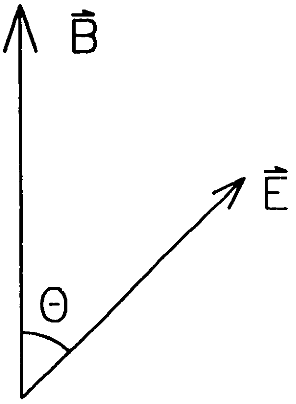

Figure 3-5: Geometry of perturbing fields

Consider an α state atom subject to the field configuration shown in figure 3-5. The magnetic field is due to the trap magnets, while the electric field is the applied quenching field. We choose the coordinate axes for this discussion such that:

$$\begin{aligned} \vec{B} &= B\hat{z} \\ \vec{\mathcal{E}} &= \mathcal{E}_z\hat{z} + \mathcal{E}_x\hat{x} = \mathcal{E}(\cos\theta\hat{z} + \sin\theta\hat{x}). \end{aligned} \tag{3.62}$$

The strengths of the fields are such that the magnetic field breaks the degeneracy of the m_j states, but does not break the $\vec{L}\cdot\vec{S}$ coupling, and shifts the energies a small amount compared to the Lamb shift energy splitting. The electric field is small enough that it can be considered as a perturbation to the (nondegenerate) eigenstates of J, m_j. For $T = 100\ \mu$K trapped hydrogen typical values for the field strengths would be $B \approx 0.5$ mT, and $E \leq 10$ V/cm. The Hamiltonian for this perturbation is given by

$$H = -e\vec{\mathcal{E}}\cdot\vec{r} \tag{3.63}$$

where $\vec{r}$ is the electron-nucleus position vector. We recognize this as the familiar electric dipole Hamiltonian. We then write this Hamiltonian as a sum $H = H_z + H_x$, where

$$\begin{aligned} H_z &= -e\mathcal{E}_z z = -e\mathcal{E}\cos\theta\ z \\ H_x &= -e\mathcal{E}_x x = -e\mathcal{E}\sin\theta\ x \end{aligned} \tag{3.64}$$

The first order correction to the eigenstate is given by simple perturbation theory:

$$|\alpha^{(1)}> = \sum_{p \neq \alpha} \frac{<p|H|\alpha>}{E_\alpha - E_p} |p> \tag{3.65}$$

where E_p is the energy of state p. The sum in Equation 3.65 is over all states, but only the states with $E_p \approx E_\alpha$ will contribute significantly because of the energy denominator. States with $n \neq 2$ can be neglected entirely. The matrix elements $<p|H|\alpha>$ can be easily evaluated if the states p are expressed in the m_l, m_s basis. In this basis the only relevant nonzero matrix elements are[26]

$$\begin{aligned} <\psi_{210}|H|\psi_{200}> &= 3ea_0\mathcal{E}_z && (3.66) \\ <\psi_{211}|H|\psi_{200}> &= -\tfrac{3}{\sqrt{2}}ea_0\mathcal{E}_x && (3.67) \\ <\psi_{21-1}|H|\psi_{200}> &= \tfrac{3}{\sqrt{2}}ea_0\mathcal{E}_x. && (3.68) \end{aligned}$$

The terms in the sum of Eq. 3.65 can be further reduced by neglecting the contribution from the $2P_{3/2}$ levels. This is justified because the $2P_{3/2}$-$2S_{1/2}$ energy interval is nearly an order of magnitude larger than the $2P_{1/2}$-$2S_{1/2}$ interval. Thus we need only consider states e and f in the sum. Using Equations 3.68, 3.65, and 3.59 we find

$$|\alpha^{(1)}> = -\sqrt{3}\,\frac{ea_0}{E_{LS}}(\mathcal{E}_z\,|e> + \mathcal{E}_x\,|f>) \tag{3.69}$$

where E_{LS} is the Lamb shift energy splitting. The discussion of the spontaneous emission properties of this state will be facilitated by expressing it in the m_l, m_s basis:

$$|\alpha^{(1)}> = |0\uparrow> - \frac{ea_0}{E_{LS}}\Big[\mathcal{E}_z\,(\sqrt{2}\,|\uparrow\downarrow> - |\rightarrow\uparrow>) + \mathcal{E}_x\,(|\rightarrow\downarrow> - \sqrt{2}\,|\downarrow\uparrow>)\Big]. \tag{3.70}$$

This treatment is also well suited to the evaluation of the Stark shift. The first order energy correction from the Hamiltonian of Eq. 3.63, $<\alpha|H|\alpha>$, is zero. The second order energy correction is given by

$$E_\alpha^{(2)} = \sum_{p\neq\alpha} \frac{|<p|H|\alpha>|^2}{E_\alpha - E_p}. \tag{3.71}$$

This sum can be straightforwardly evaluated over all of the $n = 2$ levels using the matrix elements of Eqs. 3.68. We find

$$\Delta E_{STARK} = (\frac{3}{E_{LS}} - \frac{6}{E_{FS} - E_{LS}})(ea_0)^2\, \mathcal{E}^2 \tag{3.72}$$

where E_{LS} is the Lamb shift energy interval, and E_{FS} is the fine structure energy interval. This result is independent of the field orientation. Introducing the numerical values for the constants and expressing the result as a frequency, we obtain a value for the second order Stark shift of the $2S$ level

$$\Delta\nu_{STARK} = 3600\, \mathcal{E}^2 \text{ Hz cm}^2/\text{V}^2. \tag{3.73}$$

The exact treatment of this problem based on numerical diagonalization of the complete Hamiltonian confirms the predictions of Eq. 3.70 (and Eq. 3.73). We find the major components of the $2P$ admixture to be the four states predicted by Equation 3.70, with modest changes to the coefficients. There are additional $2P$ states mixed in as well, but their contribution is at least a factor of 20 smaller. The results of the exact treatment are well represented by the empirical relation

$$\begin{aligned} |2S_d^{(1)}> = |0\uparrow \text{⤉}> \quad - \quad 10^{-3}\Big[&\mathcal{E}_z(1.82\,|\uparrow\downarrow \text{⤉}> - 0.90\,|\rightarrow\uparrow \text{⤉}>) \\ &+ \mathcal{E}_x(1.26\,|\rightarrow\downarrow \text{⤉}> - 1.51\,|\downarrow\uparrow \text{⤉}>)\Big] \end{aligned} \tag{3.74}$$

where $\mathcal{E}$ is expressed in V/cm. We note that this state is not normalized, but for the small electric fields assumed in this treatment, the deviation from normalization is small enough to be neglected.

3.3.3 Properties of $2S$ State Fluorescence

The results of the previous section allow us to determine the properties of the L_α radiation emitted via spontaneous emission. Determination of the polarization, angular distribution, and frequency of the radiation will allow us to estimate the fraction collected by our detector and to estimate the possible attenuation of the fluorescence due to radiation trapping effects. The frequency of the radiation will be stated in terms of the deviation from the zero-field $1S_d \rightarrow 2S_d$ resonance frequency. For the low values of the fields assumed in this discussion, the frequency shifts due to the fields can be neglected.

In Section 3.3.2 we found that there are four main components to the electric field induced $2P$ state admixture. The weighting of these components depends on the relative orientation of the $\vec{\mathcal{E}}$ and $\vec{B}$ fields. To simplify the discussion we will treat only the cases of $\vec{\mathcal{E}} \parallel \vec{B}$ and $\vec{\mathcal{E}} \perp \vec{B}$.

<u>$\vec{\mathcal{E}} \parallel \vec{\mathbf{B}}$</u>

The excited state eigenvector is

$$2S'_d \;=\; |0\uparrow \ddagger> \;-\; 10^{-3}\mathcal{E}(1.82\,|\uparrow\downarrow\ddagger> \;-\; 0.90\,|\rightarrow\uparrow\ddagger>) \tag{3.75}$$

where the subscript indicates the d hyperfine state of the $2S$ manifold and the prime indicates the electric field perturbed state. This state will radiate via 3 transitions:

transition	polarization	frequency	line strength
$2S'_d \rightarrow 1S_d$	π	0	0.20
$2S'_d \rightarrow 1S_c$	σ^+	0	0.40
$2S'_d \rightarrow 1S_a$	σ^+	$\nu_1 = 1420$ MHz	0.40

(3.76)

where ν_1 is the $1S$ hyperfine splitting. The line strength is the fraction of the total fluorescence intensity contained in the line.

$\vec{\mathcal{E}} \perp \vec{\mathbf{B}}$

The excited state eigenvector is

$$2S_d' = |0\uparrow \text{⤉}> - 10^{-3}\mathcal{E}(1.26\,|\rightarrow \downarrow \text{⤉}> - 1.51\,|\downarrow \uparrow \text{⤉}>). \tag{3.77}$$

This state will radiate via 3 transitions:

transition	polarization	frequency	line strength
$2S_d' \rightarrow 1S_d$	σ^-	0	0.59
$2S_d' \rightarrow 1S_c$	π	0	0.20
$2S_d' \rightarrow 1S_a$	π	$\nu_1 = 1420$ MHz	0.20

(3.78)

We recall the relationship between the fluorescence polarization and its angular distribution[27]

polarization	angular distribution
σ^+, σ^-	$\frac{1}{2}(1 + \cos^2\phi)$
π	$\sin^2\phi$

(3.79)

The angle ϕ denotes the angle of observation with respect to the magnetic field.

Observation Conditions

The data in Tables 3.76 and 3.78 allow us to predict the intensity, polarization, and frequency of the fluorescence in any direction. The observation direction is specified with respect to the coodinate axes defined by the field vectors (see Equation 3.63). The orientation of these axes with respect to the natural axes for describing the apparatus depends on the location of the fluorescing atom within the trap. We now discuss the factors that influence the position at which a typical atom fluoresces, making reference to the apparatus as described in Chapters 2 and 5.

Under the conditions outlined in Section 3.2, the atoms interact with the 243 nm beam near the axis of the trap. Along the trap axis, the magnetic field is relatively uniform and in the axial direction. As an atom moves away from the trap axis, the radial component of the magnetic field grows in relation to the axial component. The position at which fluorescence occurs depends on the time interval between when the atoms interact with the laser and when the quenching field is applied. The choice of this time interval is discussed in Chapter 5. For now we take it to be less than 100 μs. A 100 μK hydrogen atom moves approximately 0.13 mm in 100 μs, a small fraction of the effective trap radius of 1 mm. For the field configuration assumed in Section 3.2, the magnetic field direction is within 8 degrees of the axial direction at a radius of 0.13 mm. It is thus a reasonable approximation to consider the magnetic field to be in the $\hat{z}$ direction in the laboratory coordinate system. The electric field is a uniform field applied in the $\hat{x}$ direction in the laboratory coordinate system. Under these conditions, the laboratory coordinate system and the atom coordinate system can be taken to coincide. The angle θ that defines the electric field direction in Equation 3.63 is taken to be $\pi/2$, yielding the $\vec{\mathcal{E}} \perp \vec{B}$ case treated above to be the relevant case. The observation direction in this coordinate system is the $-\hat{z}$ direction ($\phi = \pi$ in Eq. 3.79).

Observing the radiation field of Table 3.78 along the $-\hat{z}$ direction permits detection of only the σ^- line. If we multiply the line strength of the σ^- line by its angular distribution function, we find that the fluorescence intensity along the $-\hat{z}$ direction is 90% of what would be observed if all lines radiated in a spherically symmetric distribution. The σ^- line is left-hand circularly polarized when observed in the $-\hat{z}$ direction.

It is noted that atoms that undergo spontaneous emission from the electric field perturbed $2S$ state to either the $1S_c$ state or the $1S_a$ state will be lost from the trap. Atoms that decay to the $1S_d$ state are confined by the trap, but in the decay process they receive a recoil energy of $E_{recoil} = h^2/2m_p k_B \lambda^2 = 670$ μK. However, the number of atoms undergoing excitation and spontaneous decay is small compared to the total number of atoms in the trap, so the recoil energy will have a negligible effect on the sample temperature.

3.3.4 Radiation Trapping

A L_α photon emitted by a trapped atom can be absorbed by another ground state atom in a single photon $1S - 2P$ transition. This phenomenon is referred to as radiation trapping. In this section we discuss the effect of radiation trapping on the detection of the L_α fluorescence.

A L_α photon emitted near the center of the trap must travel through a sample length of approximately 15 mm to reach the detector. The photon's path will lie close to the trap axis, where the magnetic field is relatively uniform and mostly in the axial direction. From the previous section we know that the photon will have σ^- polarization and a frequency within 20 MHz of the $2S_d \rightarrow 1S_d$ transition frequency. The ground state atoms in the sample populate only the d hyperfine state, leaving us to consider L_α absorption in transitions of the type $1S_d \rightarrow 2P_{3/2}$ and $1S_d \rightarrow 2P_{1/2}$.

We recall the familiar result for the absorption cross section for a resonant photon (for an $l = 0 \rightarrow l = 1$ transition)

$$\sigma_a = 6\pi \lambda\!\!\!^{-}{}^2 \tag{3.80}$$

where $\lambda = 2\pi\lambda\!\!\!^{-}$ is the transition wavelength. If the photon is detuned from resonance by an amount $\delta\nu$, then the cross section becomes

$$\sigma_{eff}(\delta\nu) = \sigma_a \frac{(\Gamma/4\pi)^2}{\delta\nu^2 + (\Gamma/4\pi)^2} \tag{3.81}$$

where Γ is the spontaneous decay rate of the excited state. In our case the excited state is a $2P$ level, giving $\Gamma/4\pi = 50$ MHz. This frequency detuning factor allows us to neglect the contribution of the $2P_{3/2}$ levels to the reabsorption cross section since they are nearly an order of magnitude further away from resonance than the $2P_{1/2}$ levels.

Given the σ^- polarization of the L_α photon, we can identify the relevant transitions within the $2P_{1/2}$ hyperfine structure. In the m_l, m_s, m_i basis the only nonzero matrix element is

$$< \downarrow \uparrow \mathrlap{\uparrow}{-} |(x - iy)| 1S_d > . \tag{3.82}$$

This leads to two possible transitions

$$\mathrm{A}:\ 1S_d \ \rightarrow\ 2P_{1/2}(F=1, m_F=0) \tag{3.83}$$

$$\mathrm{B}:\ 1S_d \ \rightarrow\ 2P_{1/2}(F=0, m_F=0) \tag{3.84}$$

The frequency detunings of these transitions are given by

transition	detuning	
A	$\nu_{LS} + \frac{1}{4}\nu_{HFS}(2S) - \frac{1}{4}\nu_{HFS}(2P_{1/2}) - 2\nu_{recoil} = 1060\ \mathrm{MHz}$	(3.85)
B	$\nu_{LS} + \frac{1}{4}\nu_{HFS}(2S) + \frac{3}{4}\nu_{HFS}(2P_{1/2}) - 2\nu_{recoil} = 1120\ \mathrm{MHz}$	

where ν_{HFS} corresponds to the hyperfine interval of the indicated state and $\nu_{recoil} = h/2m_p\lambda^2 = 14$ MHz is the recoil frequency shift.

A further reduction of the absorption cross section comes from the incomplete overlap of the matrix element identified in Eq. 3.82 with the eigenstates of J, F, m_F identified in Eqs. 3.83 and 3.84. The relevant matrix elements can be determined from the Clebsch-Gordon coefficients for the coupling of $\vec{L}$, $\vec{S}$, and $\vec{I}$. For magnetic fields less than the hyperfine decoupling field for the $2P_{1/2}$ level of 4 mT, these matrix elements are

$$< 2P_{1/2}(F=1, m_F=0)|\downarrow\uparrow\text{⇞}> = < 2P_{1/2}(F=0, m_F=0)|\downarrow\uparrow\text{⇞}> = \sqrt{\frac{1}{3}} \tag{3.86}$$

If we sum the cross sections of the two transitions and include the effect of the frequency detuning and incomplete overlap with the excited states, we find an effective absorption cross section of

$$\sigma_{eff} = 1.4 \times 10^{-3}\ 6\pi\lambda\!\!\!^{-}{}^2 = 9.8 \times 10^{-14}\ \mathrm{cm}^2. \tag{3.87}$$

This allows us to calculate an absorption length

$$l_a = \frac{1}{n\sigma_{eff}} = \frac{1.0 \times 10^{13}}{n}\ \mathrm{cm}^{-2}. \tag{3.88}$$

At a density of 10^{13} cm^{-3} this gives an absorption length of 1 cm, which is less than typical trap lengths. This compels us to consider what actually happens when a fluorescent photon is reabsorbed.

In the simplest scenario, a L_α photon that is absorbed by a ground state atom is reemitted in a random direction, with a polarization state and angular distribution determined by the particular $2P$ state that was excited in the absorption process. In the case of the transitions identified in Eqs. 3.83 and 3.84, a spherical distribution is a reasonable approximation. By energy conservation, the emitted photon will have the same energy as the absorbed photon (minus the recoil energy determined by the net momentum transfer to the atom). Any mechanism for nonradiative dissipation of the photon energy will be neglected in this discussion.

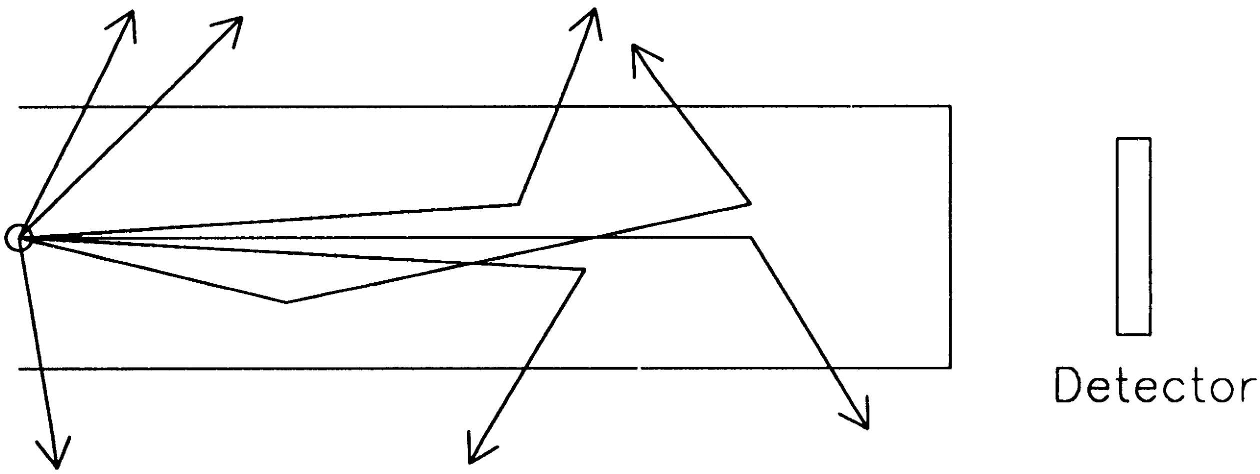

Figure 3-6: Effect of radiation trapping (drawing is not to scale).

The consequences of a single absorption-reemission event can be understood with reference to Figure 3-6. For simplicity we model the atom sample as a cylinder with radius r, length $2l$, and uniform density n. A L_α photon emitted at the center of the sample must travel through the length of the sample to reach the detector. The detector subtends a small solid angle ($\approx 10^{-3}$ steradians) for fluorescence collection (the solid angle subtended by the sample is approximately the same). In the low density limit, where $l_a > l > r$, no radiation trapping takes place and the photons leave the sample as they were emitted. As the density increases, we enter the regime where $l > l_a > r$. This regime has serious consequences for our detection technique. Photons that are initially emitted in the radial direction leave the sample with no absorption, while photons travelling near the axis are absorbed with high probability. If an otherwise detectable photon is absorbed and reemitted randomly, its probability for detection will be further reduced by the solid angle factor for the detector. This we treat as an effective loss of the photon. Thus, photons emitted more than l_a away from the edge of the sample are unlikely to reach the detector.

To minimize the loss of fluorescence due to radiation trapping we propose the excitation geometry illustrated in Fig. 3-7. The divergence length of the beam and the sample length are chosen to be comparable. Since most of the excitation occurs near the focus of the beam, the sample is restricted to this region. A sample extending further than a divergence length does not contribute significantly to the excitation rate, but reduces the signal due to radiation trapping.

The reduction in detected fluorescence in this geometry can be described with a transmission factor

$$S = \frac{1}{l_s} \int_0^{l_s} dz \, e^{-n\sigma z} = \frac{1}{n\sigma l_s}(1 - e^{-n\sigma l_s}). \tag{3.89}$$

Here we have integrated the fluorescence emitted at location z multiplied by an attenuation factor $e^{-n\sigma z}$. In writing this we have neglected the variation in the excitation rate over the length of the sample due to divergence of the beam. This is reasonable if l_s is comparable to (or less than) the divergence length of the beam.

We see that S drops with increasing density. However, the detected fluorescence level is proportional to $n\,S$, which monotonically increases with n. Thus, in this geometry, there is no possibility of a decrease in signal due to excessively high density.

Radiation trapping provides an incentive for working with short samples and tightly focussed beams. However, there are important practical limitations to keep in mind. The apertures on the optical system place a lower limit on the minimum divergence length for the beam. The current choice of $w_0 = 38$ μm for the beam radius corresponds to a divergence length of 19 mm, and is near the minimum value that

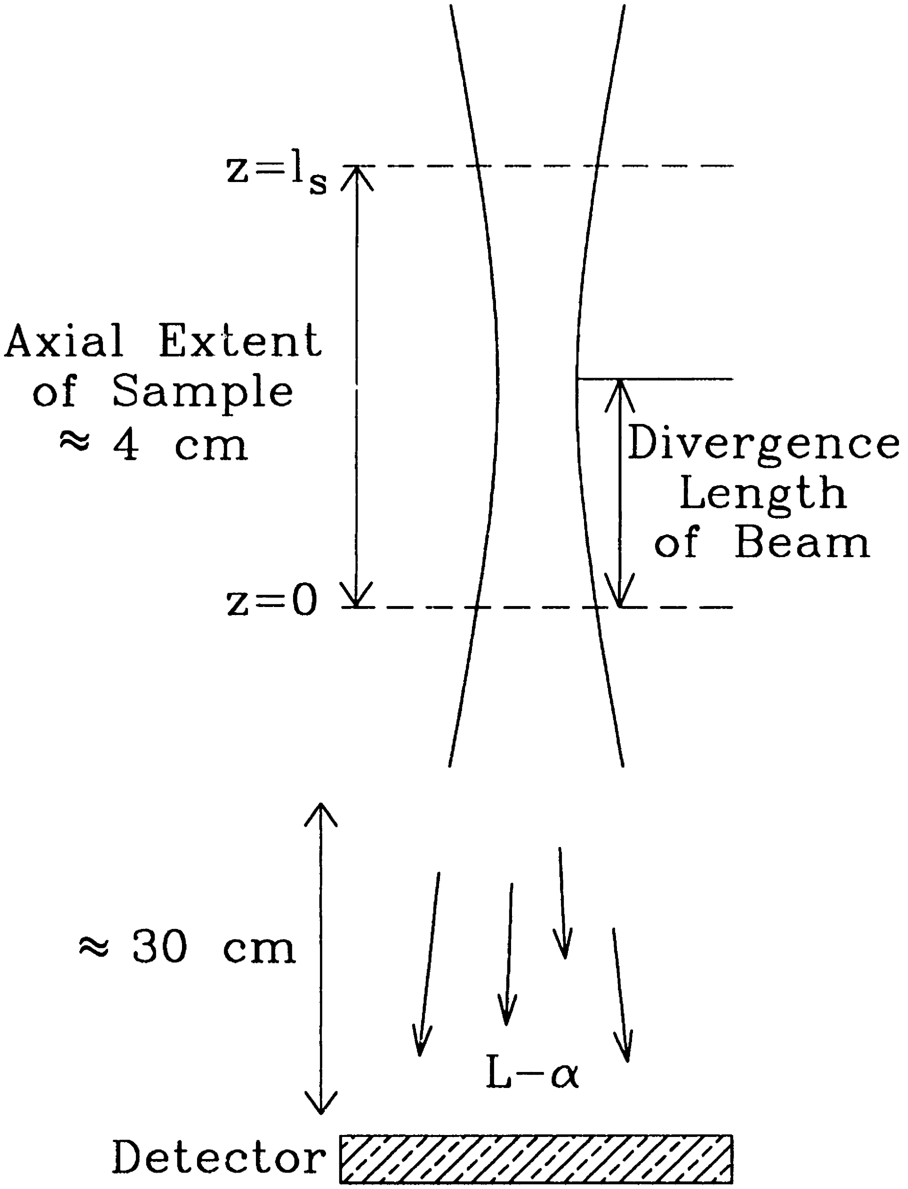

Figure 3-7: Excitation region geometry to minimize radiation trapping.

can be obtained within the constraints of the trap apparatus. This determines an optimum sample length of approximately 40 mm, which we have adopted. This value for the sample length is near the minimum that can be obtained without significant modifications to the trap magnet system.

With this value for l_s, we can evaluate Eq. 3.89 to find $S = 0.32$ at a sample density of 10^{13} cm^{-3}. Therefore, the detected fluorescence level is reduced by a factor of 3 due to radiation trapping. Thus, with this choice of geometry the effects of radiation trapping can be reduced to manageable levels.

Chapter 4

Laser System

Progress in laser spectroscopy of the $1S$–$2S$ transition has been closely tied to progress in producing 243 nm radiation to excite the transition. The combined constraints of deep ultraviolet output, high average power, and narrow spectral linewidth are not satisfied by commercial laser systems. This chapter describes the radiation source we have developed.

4.1 Overview

The discussion in Chapter 3 gives an idea of the requirements for a suitable radiation source for these experiments. The output wavelength must be tunable near 243 nm. The source must have a multimilliwatt power level to excite the weak $1S-2S$ transition. Finally, the spectral linewidth of the source should be less than the expected hydrogen signal (initially 10 kHz, ultimately much narrower).

The requirement for narrow spectral linewidth dictates the use of a continuous wave source. Since there is no source of laser radiation at 243 nm, one must start with a laser source in another spectral region and use nonlinear frequency conversion techniques to generate 243 nm radiation. The frequency conversion must be carried out with a relatively high degree of efficiency to generate a sufficient level of 243 nm power given the modest power of available tunable CW laser sources.

An overview of the laser system is shown in Figure 4-1. The system consists of three main components: a frequency stabilized 486 nm dye laser, a frequency doubling system, and a tellurium reference spectrometer. Each of these components is described in detail in a section of this chapter. The 486 nm dye laser is based on a commercial system, a Coherent 699-21 dye laser (using Coumarin 102 dye) pumped by a Coherent I-200 krypton ion laser. This commercial system has been extensively modified to stabilize its frequency to within 100 Hz of a Fabry-Perot reference cavity. The frequency doubling system uses an external enhancement cavity to generate 243 nm light via second harmonic generation in beta barium borate (BBO). The tellurium reference spectrometer is used to tune the system near the anticipated location of the hydrogen $1S-2S$ transition frequency.

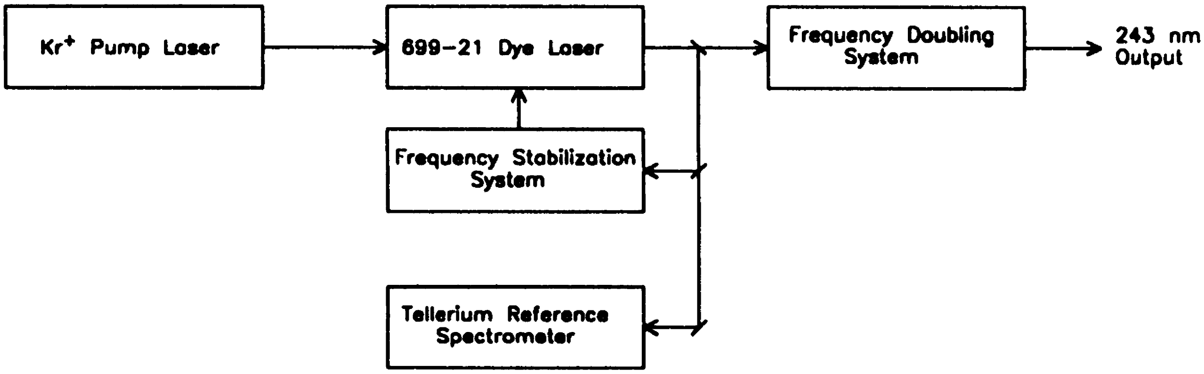

Figure 4-1: Overall diagram of laser system

The completed system has achieved state-of-the-art performance in terms of spectral linewidth and 243 nm output power. Many of the techniques employed in the development of the source, while not routine, were not originally developed in this laboratory. Much use has been made of recent literature on the subject of laser frequency stabilization. We have also benefitted from personal communication with several experts in the field, especially Jim Bergquist, Claus Zimmermann, and Reinald Kallenbach. We have found the thesis work of Dave McIntyre[28] to be especially useful in setting up our tellurium spectrometer.

4.2 Frequency Stabilized 486 nm Laser

4.2.1 Coherent 699-21 Laser

To fully understand the design and operation of the laser source described in this section one needs a detailed understanding of the commercial system on which it was based, namely the Coherent 699-21 dye laser (hereafter referred to as the 699). We will not describe every aspect of this laser, but only the systems that were directly involved or modified to achieve frequency stabilization. The two main systems we will be concerned with here perform the functions of mode selection and frequency stabilization.

The 699 is a unidirectional CW ring dye laser. The dye has an inherently broad gain profile that forms the basis for the tunability of the laser. The broad gain profile requires the laser to possess a sophisticated system of optics and electronics to ensure that the laser lases with a single, well defined, and predictably tunable frequency as is required in high precision spectroscopic experiments. Conceptually this problem can be considered as two (almost) separate issues: mode selection and frequency stabilization. If this laser is operated with only the minimum number of components to establish lasing, then it will, in general, lase in a large number of different longitudinal modes (at different frequencies), all near the maximum of the dye gain profile. Mode selection is the process of selecting a single mode to lase in the desired spectral region. Frequency stabilization is the process of comparing the frequency of the single lasing mode to a reference that possesses a high degree of frequency stability, and employing a servo system to lock the laser frequency to the frequency reference.

Mode selection is accomplished by three intracavity etalons. The coarsest tuning etalon is the birefringent filter. It consists of a stack of 3 etalons of differing thicknesses, all consisting of a birefringent material. The birefringent filter is placed at Brewster's angle inside the laser cavity and its spectral passband is controlled by rotating the filter about an axis normal to its face. As the filter is rotated the effective index of refraction for the etalons changes as a result of their birefringence, thereby changing the spectral passband of the entire filter. The birefringent filter selects 10 or so modes for lasing in the desired spectral region of the gain profile. Further mode selection is accomplished by inserting two intracavity etalons, the thin etalon and the thick etalon. These etalons are mounted in the cavity near normal incidence and are responsible for selection of a single mode for lasing. Both of these etalons are electronically tunable by varying the effective path length of the beam through the etalons. With the thin etalon this is accomplished by rotating the etalon around an axis perpendicular to the beam axis by means of a galvanometer. The thick etalon is constructed of two separated pieces that make up the etalon whose separation can be controlled by a piezoelectric element. The tunability of the etalons is required for scanning the laser frequency over wide ranges, as will be discussed later in the section.

The frequency stabilization of the laser is accomplished as follows. A small amount of the laser output is selected by a beamsplitter and directed to the frequency stabilizing optics. The frequency reference for the system consists of a temperature stabilized Fabry-Perot interferometer. The "fringe side" technique is used to generate an error signal for use in servo locking the laser to the reference. The 699 has two transducers on the laser frequency. The necessity for two transducers stems from the conflicting requirements for wide transducer bandwidth necessary for effective frequency stabilization and large transducer excursions encountered in laser frequency scans over wide ranges. The low frequency, large excursion transducer consists of a glass plate mounted on a galvanometer. The plate is mounted near Brewster's angle in the cavity and, by rotating it around an axis perpendicular to the beam, the optical path length through the glass changes, changing the effective cavity length for the laser and hence the laser frequency. The high frequency, small excursion transducer is made by mounting one of the cavity mirrors on a piezoelectric element (PZT). In this case, the laser cavity length is changed by physical translation of one of the cavity mirrors. The jargon terms for these two transducers are the "woofer" and "tweeter", respectively. The woofer is capable of providing frequency excursions of up to 30 GHz with a small signal bandwidth of approximately 50 Hz. The tweeter can provide excursions of up to 1 GHz in magnitude and has a small signal bandwidth of approximately 5 kHz. The servo loop electronics in the laser controller drive these transducers with a multiple pole loop and the appropriate crossover function for the two tranducers. The loop has a unity gain frequency of approximately 5 kHz, limited by the tweeter bandwidth, and is claimed by the manufacturer to be able to lock the laser frequency to within 500 kHz of the reference cavity frequency under the appropriate conditions.

Another important capability in a general purpose spectroscopic laser, beyond frequency stability, is the ability to scan a stabilized frequency over a wide range. This can often be one of the more difficult of features to implement in this type of system. It places serious constraints on both the frequency stabilization and mode selection systems and introduces some interdependence between them. We will not describe in detail these constraints but instead outline the solution that was chosen by the laser manufacturer. To tune a locked system such as this, one must either change the frequency of the reference, or introduce a frequency shift between the reference and the laser. The former approach has been adopted by introducing a galvonometer driven Brewster plate into the Fabry-Perot reference cavity. By tilting the Brewster plate the cavity resonance fringes can be shifted (relatively) smoothly over 30 GHz. The frequency stabilizing servo system controls the laser frequency to follow the tuning of the reference cavity. It is at this point that the mode selection system comes into the picture. If the mode selection optics were not involved in the tuning process, then the laser could never be tuned over a range greater than the free spectral range of the laser cavity. If such a feat were attempted, the laser would simply switch lasing modes, or "mode hop" as a new mode became the lowest loss mode. The only way around this problem is to vary the passband of the mode selection optics in concert with the tuning process. This is accomplished by feeding a portion of the frequency tuning signal that drives the reference cavity into the control circuitry for the thin and thick etalons. In this way, the etalons are swept along with the cavity mode in the tuning process, allowing a single cavity mode to be tuned over approximately 300 times the free spectral range of the laser cavity. A final point is the fine tuning of the thick etalon spacing. The thick etalon is the finest tuning element in the mode selection system and is responsible for the selection between the final two or three competing modes. It is important that it be carefully adjusted at all times to prevent the possibility of mode hops or significant power variations if its passband maximum does not exactly overlap with the desired cavity mode. Such a degree of adjustment would be impractical for the operator to maintain as it would require constant attention to compensate for drifts due to temperature variations, for example. Therefore, an additional servo system has been implemented to continuously optimize the thick etalon spacing with respect to the lasing mode. The details of the operation of this loop will not be discussed here, but its presence is important to keep in mind when modifying the laser.

The rest of this section will be devoted to the modifications to the 699 implemented in our program of frequency stabilization. Several modifications were made to the dye circulation system to decrease the laser frequency perturbations caused by the dye jet and to increase the output power of the dye laser. The original dye jet was replaced by a Radiant Dyes[29] RSD-6 dye jet. This jet allowed dye circulation at higher pressures without dye bubbling or foaming in the catch tube. The higher pressures gave a higher flow rate in the jet, allowing higher pump laser power to be used without deleterious effects on the dye laser frequency stability or beam profile. The higher pump powers gave correspondingly higher dye laser output powers. A dye accumulator was placed in the dye circulation line between the dye pump and the dye jet. The accumulator was designed with a trapped air volume to damp out pressure fluctuations caused by the dye pump. The original dye filter cartridges were replaced by paper based cartridges (Filterite[30] DFNT 0.45-4UN). The paper based cartridges are expected to trap fewer bubbles than the original wound string types, giving fewer bubble induced perturbations to the dye laser operation. These modifications required a change in volume and concentration (the new dye jet is thicker than the orignal) of the dye solution. The new dye solution is prepared by dissolving 1.0 g of Coumarin 102 dye in 100 ml of benzyl alcohol. This solution is then added to 1.6 l of ethylene glycol.

The only significant modification to the laser cavity was the introduction of an intracavity electo-optic modulator (EOM). The EOM (Gsänger[31] model PM 25) was introduced to provide a transducer on the dye laser frequency with a greater bandwidth than was available with the tweeter. Its use in this context will be discussed in the next section. The EOM was inserted in the collimated arm of the 699 between mirrors M4 and M5 (notation from the 699 manual). An aluminum mount was constructed to support the EOM from the invar frame of the laser and to allow adjustment of the EOM position and Brewster angle. The optical quality of the EOM was found to be quite good, causing only a 5-10 % reduction in laser output power upon insertion.

The electronics of the 699 were also modified. The error signal path for the frequency stabilization loop was broken at R17 on schematic 1A9 (manufacturer's notation) and the signals were routed to the back panel. With this modification, a signal from an external source could be used to control the servo transducers instead of the error signal generated by the 699. Additionally, the 699 error signal is available for monitoring on the back panel, a feature that was useful for the redundant locking scheme described in Section 4.2.3.

4.2.2 Frequency Stabilization System

Significant progress in narrowing the spectral linewidth of the 699 requires substantial effort in two directions: the frequency reference and the servo loop bandwidth. The reference cavity supplied with the 699 has not been designed to achieve the highest degree of short and long term stability possible with this type of frequency reference. Considerations such as cost and wide range tunability have dictated a design that is substantially more susceptible to environmental perturbations such as vibrations and temperature drifts than is desirable for a specialized laser source. Several research groups around the world (see, for example, Ref. [32]) have undertaken serious efforts to develop the Fabry-Perot interferometer as a frequency reference for laser stabilization. We have adopted techniques from these efforts to design a reference cavity that far surpasses the Coherent cavity in both short and long term stability. This reference cavity will be discussed in detail later in this section. The other main issue is that of servo loop bandwidth. The presence of a free flowing dye jet in the laser cavity introduces significant laser frequency noise that lies outside the bandwidth of the original servo loop. This noise has Fourier components up to the MHz range, requiring a loop bandwidth increase of almost 3 orders of magnitude to effectively cancel out the noise. This type of increase is not feasible using the original servo transducers alone. We have followed the approach of previous workers in the field [33] and inserted an EOM into the cavity of the laser. The EOM is inherently a wide bandwidth transducer, having essentially no mechanical constraints on its high frequency operation like the other transducers in the system. The relatively small servo excursions possible with the EOM neccessitate retaining the original transducers to handle large, slow perturbations. The rest of this section will be devoted to the description of this system, starting with an overview and following with a detailed description of each component.

A diagram of the frequency stabilization is shown in Figure 4-2. Briefly, the system operates as follows. A portion of the laser output is deflected by an acousto-optic modulator (AOM) and coupled into a single mode optical fiber. The frequency of the light exiting the fiber is compared to the resonant frequency of the reference cavity using the FM sideband technique [34]. The resulting error signal is used to drive the intracavity EOM and fed into the 699 electronics to control the tweeter and woofer, locking the laser frequency to reference cavity resonant frequency.

Frequency Reference

The primary short term (< 1 day) frequency reference for the system is a precision Fabry-Perot interferometer which is referred to as the external reference cavity. The cavity is constructed by optically contacting two mirrors to the ends of a Zerodur spacer. This type of construction was chosen for maximum structural rigidity and minimum thermal expansion coefficient in order to make the cavity less susceptible to environmental perturbations such as vibrations or temperature fluctuations. The spacer consists of a 103 mm OD, 250 ± 0.5 mm long cylinder with a 13 mm hole drilled along the cylinder axis. A 1 mm diameter radial hole vents the space between the

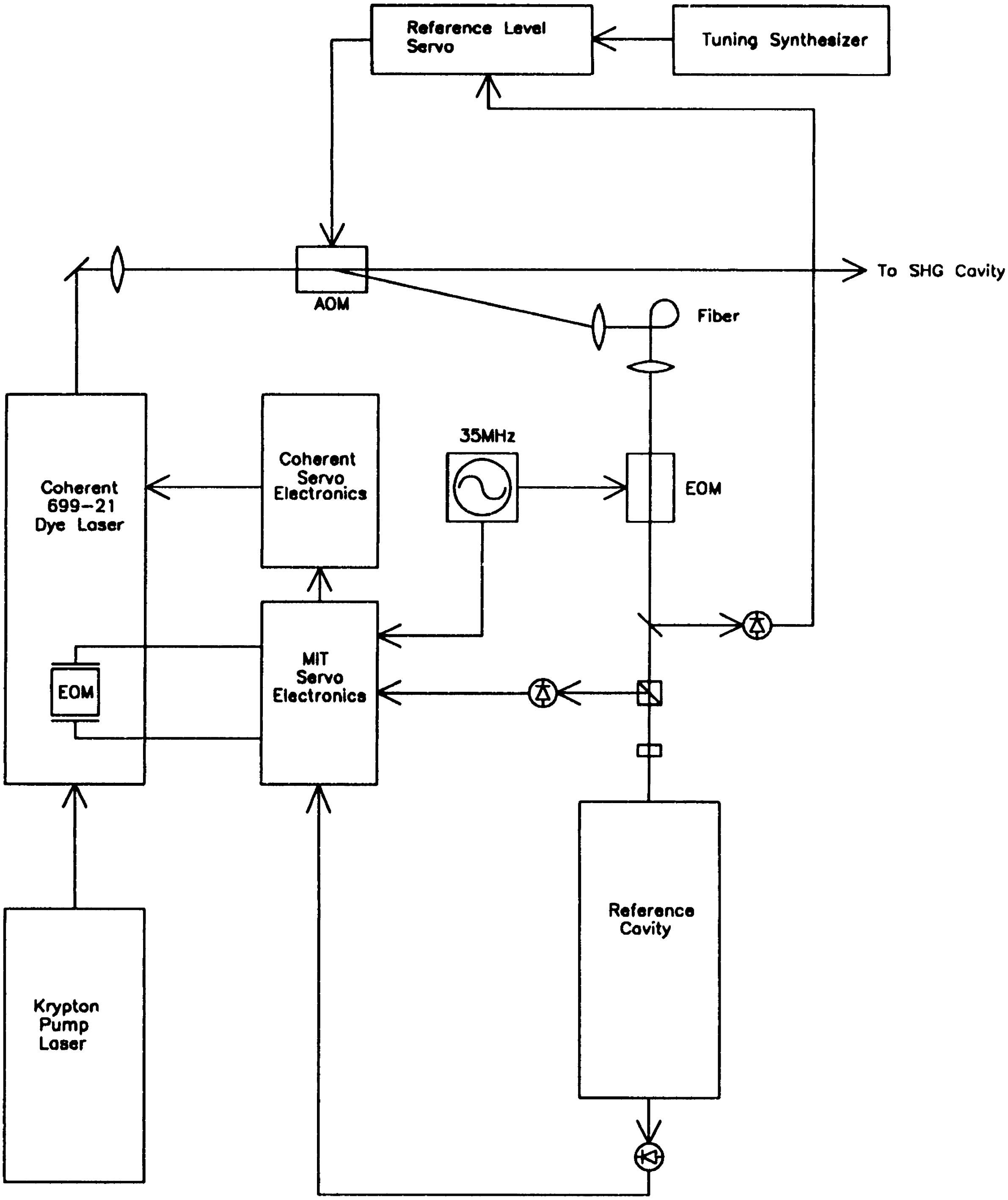

Figure 4-2: Laser frequency stabilization system

mirrors. The ends of the spacer were polished flat and parallel to within 1 mrad for optical contacting of the mirrors. The spacer was acid etched after it was machined to size to remove surface microcracks caused by the machining process. Failure to perform this etching procedure has been found to result in high drift rates[35].

The reference cavity mirrors had a radius of curvature of 400 mm and a reflectivity of 99.9%. The radius of curvature was chosen to maximize the spacing between the resonant frequencies of the TEM_{00} modes in the cavity and the higher order transverse modes. This arrangement is chosen to minimize the effect of unwanted excitation of higher order transverse modes of the reference cavity due to imperfect mode-matching of the input beam. The mirror reflectivity was chosen to provide a cavity finesse of 3000 and a cavity resonance linewidth of 400 kHz. These values were chosen to give a compromise between two extremes. A very narrow cavity resonance minimizes the effect of systematic errors in determining the center of the cavity resonance on the laser frequency, but it also gives a narrow frequency range over which a linear error signal exists. This makes it more difficult to initially obtain and maintain a lock to the cavity resonance in the presence of perturbations. A wide cavity resonance makes locking easier, but the finite signal to noise ratio with which the center of the cavity resonance can be determined corresponds to a larger absolute frequency uncertainty.

The optical structure of the reference cavity was placed inside a housing designed to minimize environmental perturbations to the reference cavity frequency. The housing is a 300 mm diameter by 500 mm long aluminum cylinder, sealed on both ends with aluminum plates. The end plates hold 50 mm diameter fused silica windows (with a 3 degree wedge) on the axis of the cylinder. The housing is evacuated and continuously pumped with a 25 l/s ion pump that maintains the housing pressure at 2×10^{-6} torr. All of the housing vacuum seals are made by Viton O-rings. A temperature control system maintains the housing temperature at a constant value to within 10 mK. The housing temperature is monitored with a precision thermistor and controlled by copper heater wires wrapped on the cylinder and end plates. The outside of the housing is thermally insulated from the surrounding environment by a layer of 25 mm thick foam rubber. The temperature setpoint can be varied between

35 C and 70 C.

The degree of vibration isolation that can be obtained in the support system for the reference cavity is one of the most critical factors in determining the final linewidth of the locked laser system. We chose an approach that was relatively simple to implement and, based the experience of others[35], would give a level of performance that was adequate for our initial needs. A stainless steel cradle was supported in the housing on teflon pads. The cradle supported a set of two 25 mm diameter fused silica rods. The rods were supported in two places by Viton O-rings placed around the rounds and resting in V-grooves in the cradle. Two O-rings were placed around the OD of the reference cavity spacer at the nodal points of the lowest order bending mode of the cavity. The cavity was then placed on the fused silica support rods, making contact through the O-rings.

Measurement of the absolute frequency stability of a reference cavity such as this is a nontrivial matter. One must either construct two independent reference cavities of comparable stability, or use an extremely narrow atomic resonance as a frequency reference. We have been satisified with order of magnitude estimates for our reference stability based on experimental data obtained by others in the field[35]. Similarly constructed and vibration isolated cavities have been found to give approximately 1 kHz short term linewidths. A final determination of the system linewidth will most likely have to wait until a hydrogen $1S-2S$ signal is observed.

There is some discrepancy between the predicted optical properties of the external reference cavity and experimental observations. To characterize the optical losses of the reference cavity we have made measurments of the decay time for optical modes of the cavity. This is often referred to as the cavity lifetime, being the mean lifetime for a resonant photon inside the cavity. The cavity lifetime is given by

$$\tau_c = \frac{l}{L\,c} \tag{4.1}$$

where L is the round trip loss coefficient and l is the roundtrip path length. Measurements of the cavity lifetime for the reference cavity have yielded $\tau_c = 280$ ns, indicating a loss of 0.30% upon reflection from each cavity mirror. The mirrors were specified (and measured) to have a transmission of 0.10%. Cavity lifetime measurements for a cavity temporarily set up with identical mirrors showed no sign of additional loss due to scatter or absorption. We therefore suspect that there has been some contamination of the reference cavity mirrors by something in the vacuum system. We have not made any effort to determine the origin of the contamination because we have not noticed any significant change in the loss level over 18 months and the system performs adequately in spite of the additional losses.

The frequency modulated (FM) sideband technique[34] was used to generate the electrical signal used as the error signal for the servo loop. The FM sideband technique is an effective method for generating an error signal with several advantages over other techniques[32]. We will give a brief overview of the technique and then describe our implementation of it.

The laser beam to be used for error signal generation is phase modulated in an EOM and then mode-matched to the TEM_{00} mode of the reference cavity. The light reflected from the cavity is separated from the incident beam through the use of an optical isolator and detected by a photodiode. If the laser frequency is far from a cavity resonance, the cavity behaves essentially as a high reflectivity mirror, reflecting the carrier and sidebands of the phase modulated light with no phase or amplitude changes. The photodiode signal then contains only a DC component proportional to laser power. If, however, the laser frequency is near a cavity resonance, the balance of phase and amplitude between the carrier and sidebands is disturbed, introducing some amplitude modulation in the reflected light. The photodiode signal then contains a component at the modulation frequency, with the magnitude and phase of the component depending on the relative tuning of the laser and the reference cavity. This RF component is then detected by mixing the photodiode signal in a double balanced mixer with a portion of the EOM drive signal used as the local oscillator. When the local oscillator phase is properly adjusted, one obtains an asymmetric signal with a zero crossing coinciding with the center of the cavity resonance that is well suited for use as an error signal.

The optical system used to generate the error signal is illustrated in Figure 4-2. The dye laser output is focussed into the interaction region of an AOM (Crystal Technology[36] model 3200). A small fraction of the beam (typically 1%) is deflected and frequency shifted in the AOM and used as the "reference light" for error signal generation. In this application the AOM is serving as a beam splitter that can deflect a variable fraction of the laser beam with a variable frequency shift. The deflection fraction and frequency shift are controlled by varying the amplitude and frequency of the RF drive signal applied to the AOM. The variable frequency shift is a means of tuning the locked system. The ability to vary the deflection fraction is exploited to actively maintain the reference light at a fixed level, eliminating any effect of laser power fluctuations on the operation of the frequency stabilization system.

There are some additional factors to consider when using an AOM as a tuning element. As the AOM drive frequency is varied, the deflection angle for the reference light varies proportionally, changing the alignment of the beam with respect to subsequent optics. If not compensated for, this effect would limit the tuning range of this technique to an unacceptably small value. To extend the tuning range we have employed a single mode optical fiber to carry the reference light from the AOM to the rest of the stabilization optics. Now, changes in the AOM deflection angle result in changes in the amount of light coupled into the fiber, but do not change the alignment of the beam with respect to critical elements like the reference cavity. Additionally, the optical system for coupling the light into the fiber was designed to minimize the effect of the varying deflection angle on the fiber input coupling alignment. With these improvements a tuning range of 10 MHz could be achieved before the fiber input coupling was reduced by a factor of 2 from its original value. The RF bandwidth of the AOM is 150-250 MHz, but the range of a continuous scan is limited to 10 MHz. Manual realignment between 10 MHz scan segments is necessary to access the full tuning range of the AOM. A non-polarization-preserving fiber was used in this application even though linear polarization is required for other elements in the stabilization system. This was done because of reports[35] that polarization preserving fiber exhibits a high degree of susceptibility to microphonic inputs. Environmental disturbances were reported to introduce a significant amount of spectral broadening of the light transmitted by the fiber. A polarizing beam splitter was placed at the output of the fiber to insure linear polarization of the reference light.

The light exiting the fiber was collimated by a 20X microscope objective and then passed though a polarizing beam splitter as mentioned above. The reference beam then passed through a Conoptics[37] model M-370 EOM where it was phase modulated as required by the FM sideband technique. The EOM is a single crystal ADP device, with the use of index matching fluid and AR coatings keeping the EOM transmission above 90%. This modulator geometry was chosen to provide a very high degree of pure phase modulation for the transmitted light. The purity of the phase modulation is an important technical issue in the FM sideband technique. If a small amount of amplitude modulation is acquired in a nonideal phase modulator, then the error signal will acquire offsets that will shift the lockpoint of the system away from the center of the cavity resonance. A steady offset is not that detrimental, but typically the mechanisms that introduce "residual amplitude modulation" are sensitive to temperature and laser tuning[38], opening a channel for a time varying offsets that can degrade the system linewidth. The relative merits of the different EOM geometries for producing pure phase modulation is discussed in Ref. [32].

The EOM is driven through a resonant transformer by a 4 W RF power amplifier. The 35 MHz modulation signal originates in a crystal controlled oscillator. The oscillator output is split in a power splitter for driving the EOM amp and serving as the local oscillator in the error signal electronics. A phase shifter based on switchable coax delay lines allows the relative phase of the local oscillator and the EOM drive to be controlled.

The reference light power exiting the EOM is sampled by a beam splitter and detected on the "reference level" photodiode. The reference level photodiode output is fed into a servo control circuit that varies the RF power applied to the AOM to keep the reference light power at a fixed level. This servo circuit compensates for laser power fluctuations up to a bandwidth of approximately 10 kHz.

Before the reference light is directed on the reference cavity it passes through an optical isolator consisting of a polarizing beam splitter and a quarter wave plate. The purpose of the isolator is to prevent undesirable feedback and interference effects between the reference cavity input mirror and other optical surfaces in the system. These effects can shift or distort the error signal, possibly in a time varying way. Additionally, the isolator provides easy separation of the light reflected from the cavity that is used for error signal generation.

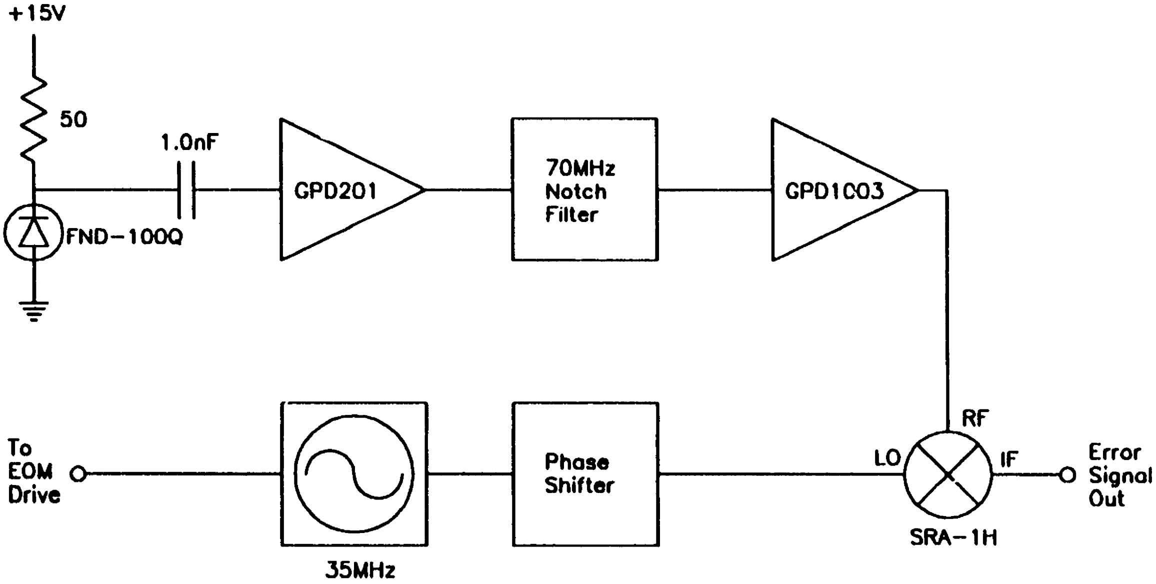

Figure 4-3: RF detection electronics.

As explained earlier, the information on the relative tuning of the laser and reference cavity is carried in the amplitude modulation of the light reflected from the reference cavity. The circuitry built to detect the light and develop a DC error signal suitable for servo locking is shown in Figure 4-3. The light reflected from the cavity is detected by an RF photodiode (EG&G[39] FND100Q). The photodiode output is AC coupled to an Avantek[40] GPD201 RF preamp that provides 30 dB of RF gain. The output of the GPD201 is passed through a 70 MHz notch filter and then into a Avantek GPD1003 that provides another 11 dB of gain. The signal is then connected to the RF port of a Mini-Circuits[41] MCL SRA-1H double balanced mixer. The LO signal is derived from the 35 MHz crystal oscillator with an adjustable phase shift. The DC error signal is then present at the IF port of the mixer.

Servo Loop Design

The nature of the frequency fluctuations in an unstabilized dye laser requires a fairly sophisticated servo loop to substantially reduce the laser linewidth. Qualitatively, the laser possesses noise consisting of both small fluctuations occuring very rapidly, and large deviations that occur slowly. The small, fast fluctuations require a high unity gain frequency for the servo loop, while the large, slow fluctuations require a high loop gain at low frequencies and a wide dynamic range for the loop transducers. In this section we will discuss how these criteria were addressed. Some familiarity with Laplace transform methods of loop analysis (see, for example, Ref. [43]) is assumed on the part of the reader.

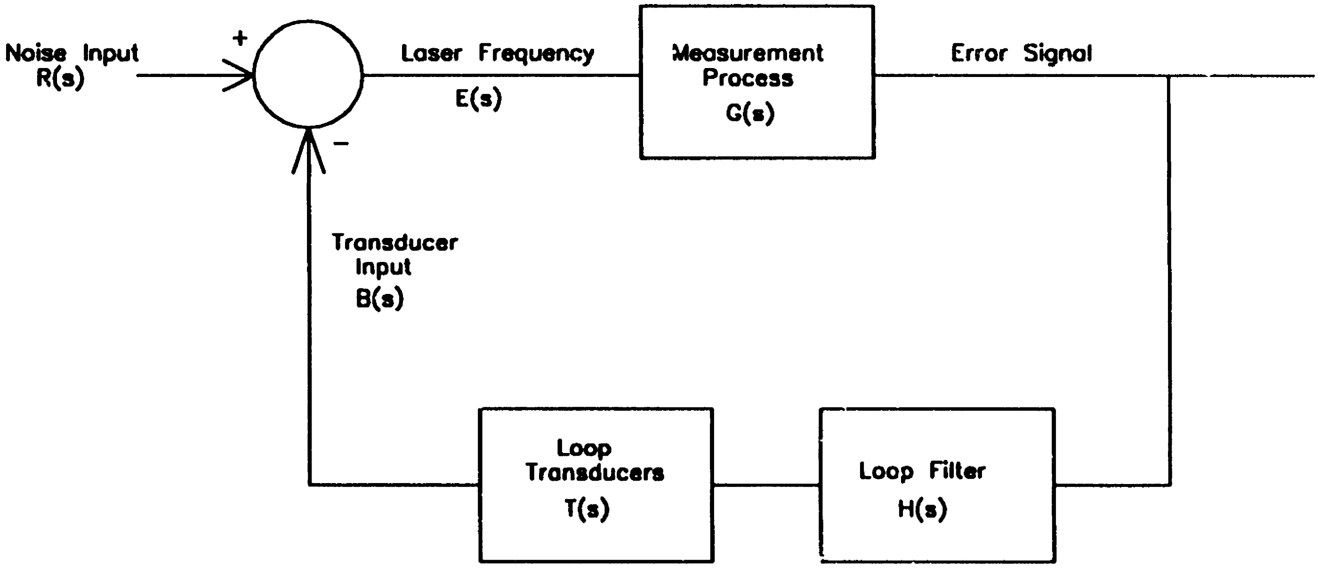

Figure 4-4: Conceptual elements of frequency stabilization loop.

The analysis of servo loop systems is facilitated by diagrams such as Figure 4-4. A physical variable E(s) (s is the Laplace transform variable) is to be controlled via a transducer input B(s). The goal of the experimenter is to design a control system (consisting of G(s), H(s), and T(s)) such that optimum control of E(s) is obtained in the presence of a noise input R(s). In many cases, physical constraints dictate the properties of the measurement process G(s) and the physical transducers T(s). The problem is then reduced to designing the H(s) that will maximize the loop performance within the constraints of G(s) and T(s).

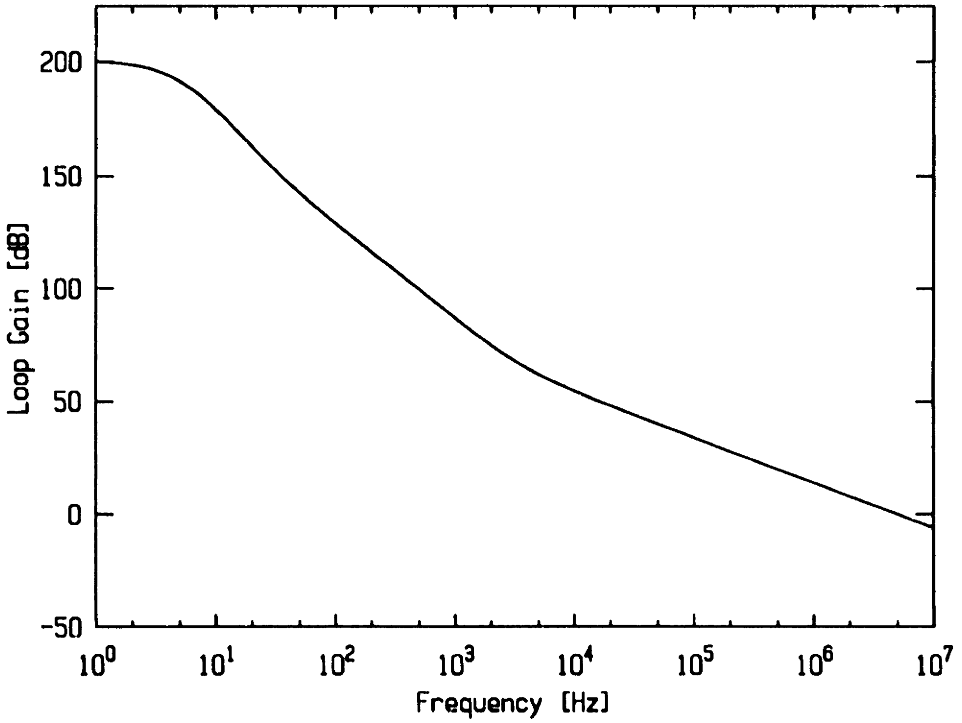

Figure 4-5: Desired overall loop response.

We have previously mentioned the qualitative behavior of the noise inputs R(s): small, fast fluctuations combined with large, slow ones. A reasonable starting point for the overall loop transfer function in this context is shown in Figure 4-5. The unity gain point is at 5 MHz with a 20 dB/decade rolloff near the unity gain point as dictated by loop stability requirements. At lower frequencies the rolloff rate is increased to 40 dB/decade and then to 60 dB/decade to give a high loop gain at low frequencies (below 10 Hz the slope flattens to 0 dB/decade). This form may not be the optimum possible given the exact nature of R(s) and the desired laser performance, but it represents a reasonable approach to obtaining good loop performance given the physical constraints on the system. Our approach to the loop optimization has been to design H(s) such that the convolution (in the time domain) of G(s), H(s), and T(s) is as close as practical to the function in Figure 4-5.

The transfer function G(s) in Figure 4-4 represents the optics and electronics necessary to generate the error signal. This includes the reference cavity and the optics used for the FM sideband technique, along with the circuitry shown in Figure 4-3. An understanding of the behavior of G(s) is necessary to properly design the other parts of the loop. The transfer function for FM sideband error signal generation from a Fabry-Perot interferometer is well represented by a single pole function with the pole at a frequency equal to the inverse of the cavity lifetime $(1/\tau_c)$[34]. In our case this pole occurs at a lower frequency than the loop unity gain point and needs to be taken into account in loop analysis. Another factor that will affect G(s) is the time delay associated with error signal generation. There is a finite time for light propagation through the reference system and for electrical signals to reach the laser. In order that this time delay has a neglible effect on loop operation, the delay should be much less than the inverse of the loop bandwidth. For a unity gain frequency of 5 MHz, this corresponds to a optical path length of 60 m, a condition easily satisfied. This condition may place some constraints on systems that use long lengths of optical fiber or coaxial cable in the feedback loop.

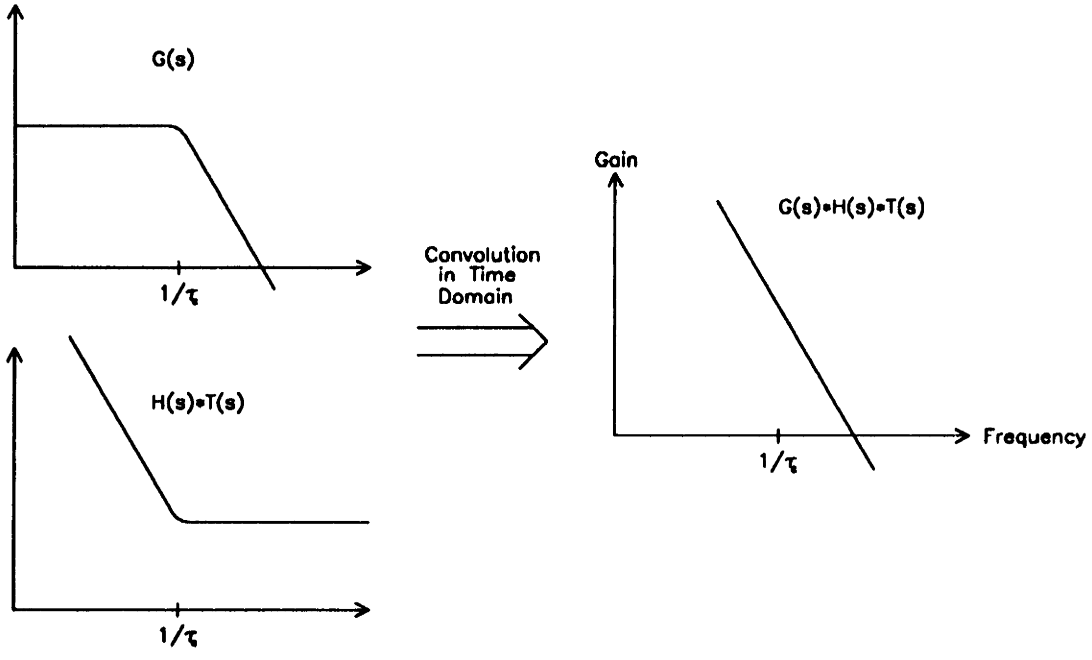

Figure 4-6: Loop design near unity gain frequency.

The approach to loop design for high frequencies is illustrated by Figure 4-6.

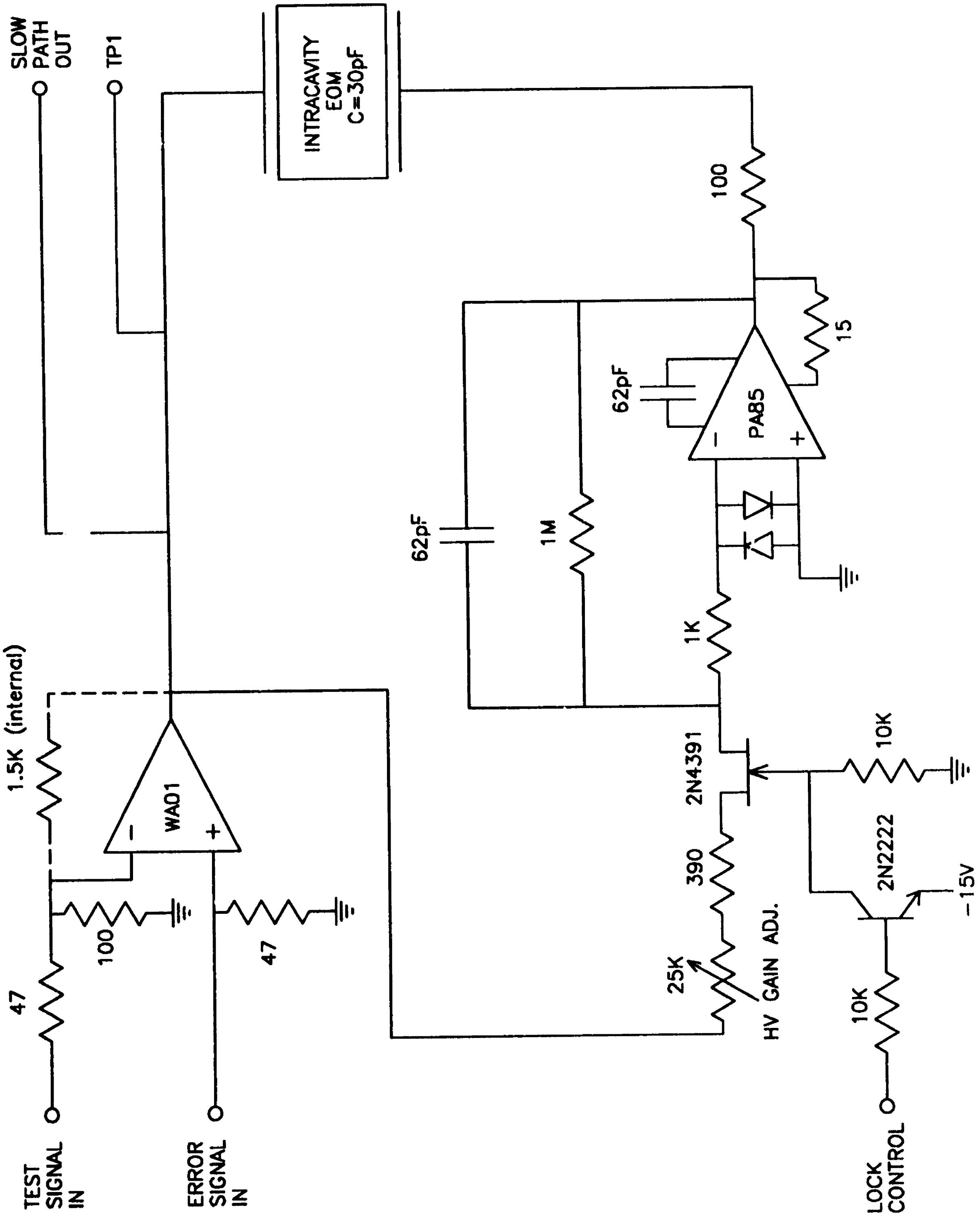

Figure 4-7: EOM drive circuitry.

The goal is to produce a uniform, one pole rolloff for the overall loop response near the unity gain frequency. The pole in G(s) has been compensated for by a zero in H(s)*T(s), giving a uniform rolloff. This has been accomplished through the drive circuitry for the intracavity EOM. The EOM circuitry is shown in Figure 4-7. The error signal is amplified by a factor of 15 by an Apex[45] WA01 operational amplifier and applied to one electrode of the EOM. The other electrode is driven by an inverting integrator which in turn is driven by the WA01 output. The integrator uses an Apex PA85 that has an output voltage swing of ±150 V. This type of connection allows one to gain the high bandwidth attributes of the WA01 and the high voltage swing of the PA85. To understand the transfer function of this circuit we refer again to Figure 4-6. At low frequencies the PA85 branch dominates the gain, but it rolls off with a one pole slope. The WA01 branch has a flat response and at some point the gains of the two branches are equal; at this point the transfer function slope changes from 20 dB/decade to 0 dB/decade. This frequency is adjusted to match the pole frequency of G(s) by varying the gain of the PA85 branch.

At lower frequencies the woofer and tweeter dominate the loop gain. The woofer and tweeter were driven by feeding the amplified version of the error signal available at the WA01 output into the 699 servo electronics. The feedback path for the original 699 servo loop was broken between TP1 and R17 on Coherent schematic 1A9, and both ends of the opened connection were routed to the back panel. By appropriate choice of connections, the 699 transducers could be controlled by their own internal error signal, or one derived from an external source. The approach of using the Coherent electronics comes at the expense of some flexibility in loop design but it saves duplicating existing circuitry and makes it easier to switch between locking to the Coherent cavity and locking to the external reference cavity.

In feeding the error signal into the 699 electronics, care must be taken that the system is well behaved in the crossover region (around 3 kHz) where the tweeter gain and the EOM gain are comparable. To get a smooth crossover we found it necessary to introduce the circuitry shown in Figure 4-8 to adjust the transfer function for the woofer and tweeter. The values in this circuit were determined empirically by

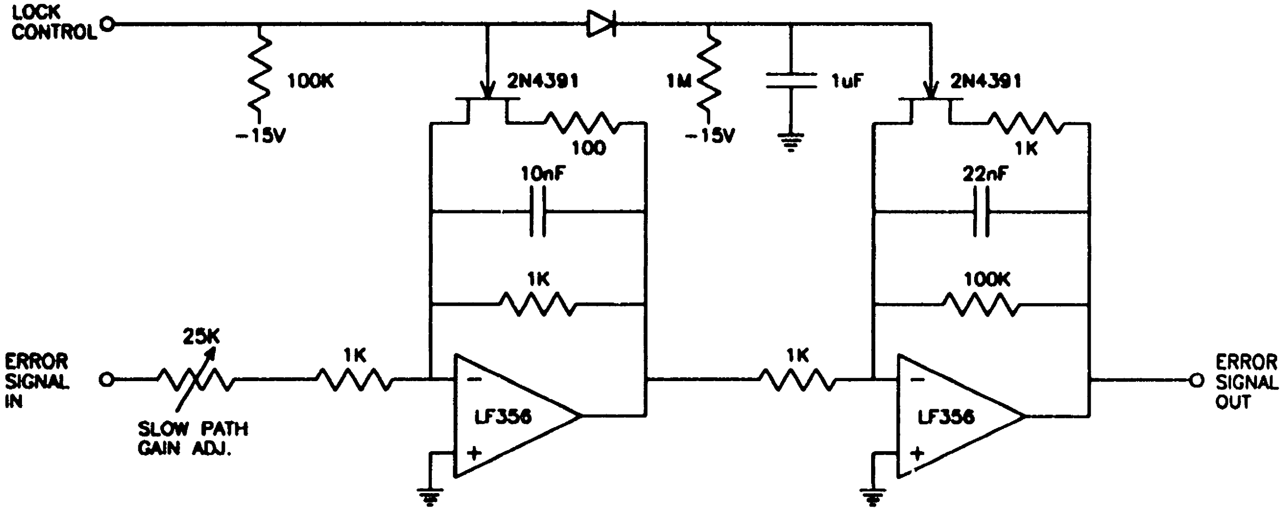

Figure 4-8: Slow path transfer function circuitry.

monitoring the locked loop performance as described in the next section.

Servo Loop Performance

Characterization of the loop performance was greatly facilitated by the availability of a Hewlett-Packard[46] HP4195A vector network analyzer. The closed loop transfer function for the locked loop can be measured by appropriate connection of the HP4195A to the servo electronics. The source output of the 4195 is connected to the TEST SIGNAL IN port of the EOM drive circuit (see Figure 4-7). This connection introduces a test signal into the loop in very close to the same manner as a noise source originating in the laser. The 4195 test port was connected (through a high impedance probe) to TP1 on the EOM drive circuit (see Fig. 4-7). The TP1 signal is an amplified version of the difference between the test signal and the loop response. The degree to which the test signal is suppressed by the loop response is a measurement of the loop gain. We have found this an effective technique for quantifying loop performance as adjustments are made.

An example of the data obtained in this manner is shown in Figure 4-9. This data was obtained during the optimization of the slow path transfer function of Figure 4-8. The dashed line was the starting point for the loop design. The drop in gain in the

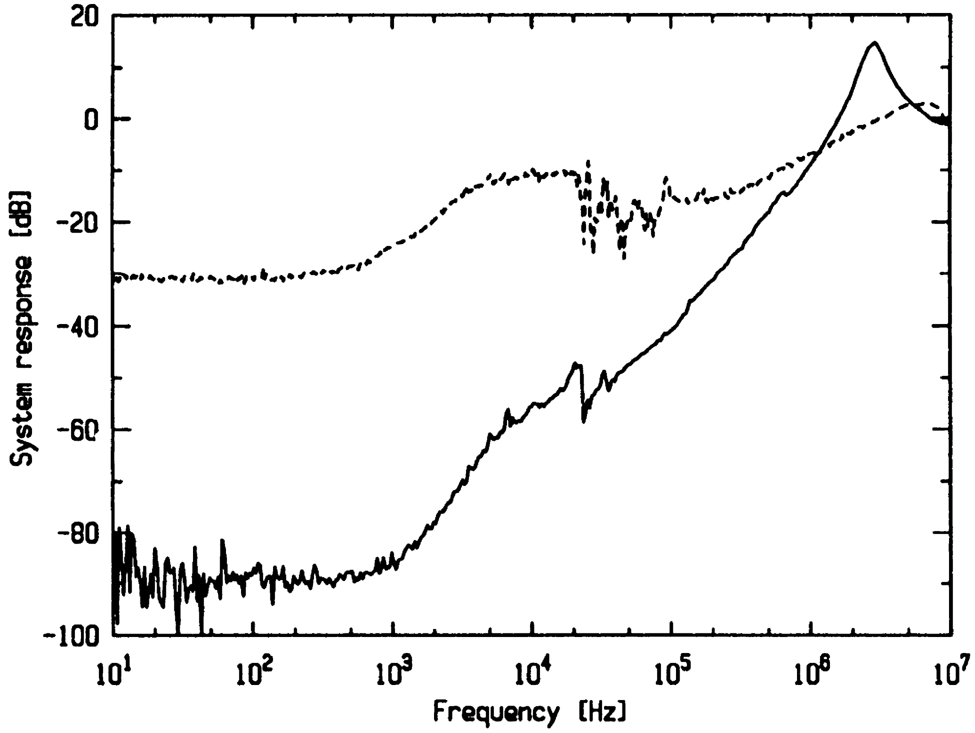

Figure 4-9: Transfer functions of locked loop. The dashed line is an initial trial that shows interference in the tweeter-EOM crossover region. The solid line is representative of the final system adjustment and shows no significant interference. The dynamic range of the network analyzer is exceeded at low frequencies, giving an overestimate of the system response.

tweeter-EOM crossover region indicates an undesirable phase relationship between the two feedback paths resulting in destructive interference between them. After the circuit of Figure 4-8 was introduced in the feedback path and its parameters were optimized, the transfer function indicated by the solid line in Figure 4-9 was observed. The destructive interference in the tweeter-EOM crossover region has been eliminated, improving loop performance in several respects. This type of analysis was also used to optimize the two other main loop adjustments. These adjustments are the overall loop gain and the HV GAIN ADJ. of Figure 4-7. Two methods have been used to vary the overall loop gain. Coarse adjustment was made by varying the RF gain in the error signal circuit of Figure 4-3. Fine adjustment was made by varying the amount of light power sent to the reference system.

The most relevant measure of loop performance is the spectral linewidth of the laser relative to the reference cavity. This can be estimated by observing the loop error signal when the laser is in the locked state. The magnitude of the noise on the error signal is a measure of the laser frequency fluctuations that are not removed by the servo loop. An example of the error signal is shown in Fig. 4-10. The vertical axis is the loop error plotted in Hertz deviation from the reference cavity frequency, and the horizontal axis is time. From the magnitude of the frequency deviation, the residual laser linewidth is estimated to be less than 100 Hz with respect to the reference cavity. Since this value is significantly less than the estimated linewidth of the reference cavity itself (1 kHz), a more rigorous estimate of the laser linewidth by this technique is not interesting.

4.2.3 Redundant Cavity Locking System

A critical practical issue of the performance of a highly stabilized laser system such as this is the robustness of the frequency lock. A system that unlocks with minor contact to the optical table or unavoidable bubbles in the dye jet has serious practical drawbacks. The time necessary to retune and relock the laser after an unlocking event is a considerable hindrance when searching for a hard to find signal.

High stability systems are inherently less stable against large perturbations. The

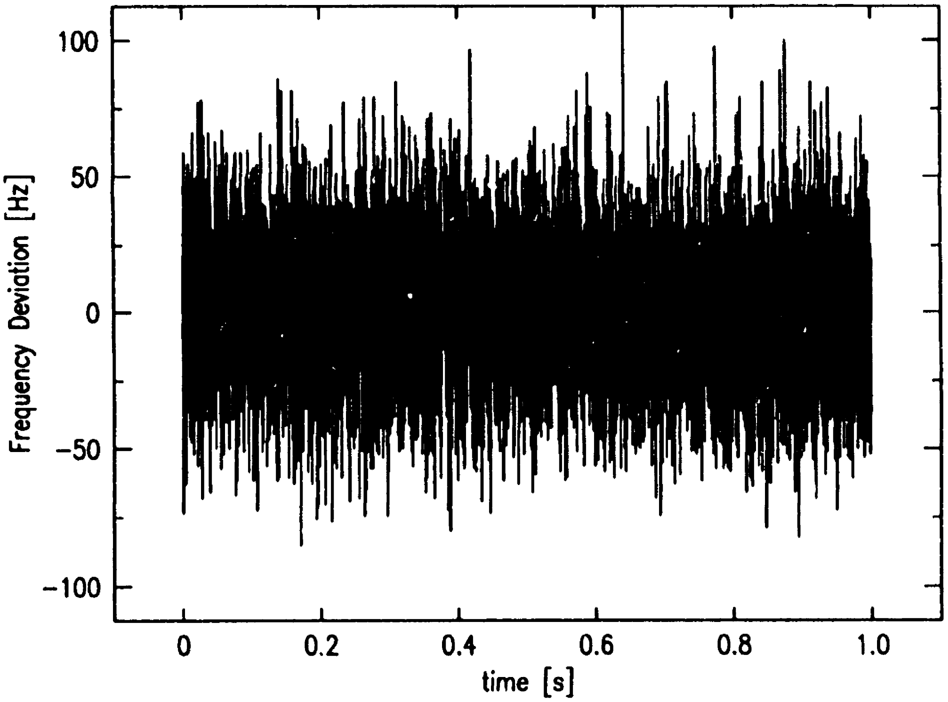

Figure 4-10: Loop error signal for locked laser.

increase in stability is achieved by increasing the gain of the system with respect to frequency fluctuations. An unavoidable consequence of this is that a smaller frequency excursion will drive the system beyond the dynamic range of either the error signal or the loop transducers, making the system unable to compensate for the driving perturbations and possibly making the loop unstable. For example, the error signal from the external reference cavity has a linear range of less than 200 kHz, and excursions larger than 35 MHz change the sign of the error signal, making recovery impossible. This is to be compared to the useful error signal range of 10 GHz for the 699 reference cavity.

We have implemented a design that allows us to gain the advantages of a high stability frequency lock while maintaining the excellent lock recovery characteristics of the original 699. The design has two main functional components. The first is a strategy for detecting the status of the lock to the external reference cavity. The second is a mechanism for switching the source of the error signal according to the lock status. If an external cavity lock is detected, then the system functions in the high stability mode with the external error signal and all three loop transducers active. If the lock to the external cavity is lost, then the system functions in the original 699 configuration with the error signal derived from the 699 reference cavity and the EOM deactivated. The system automatically reacquires the external cavity lock after the perturbation has passed.

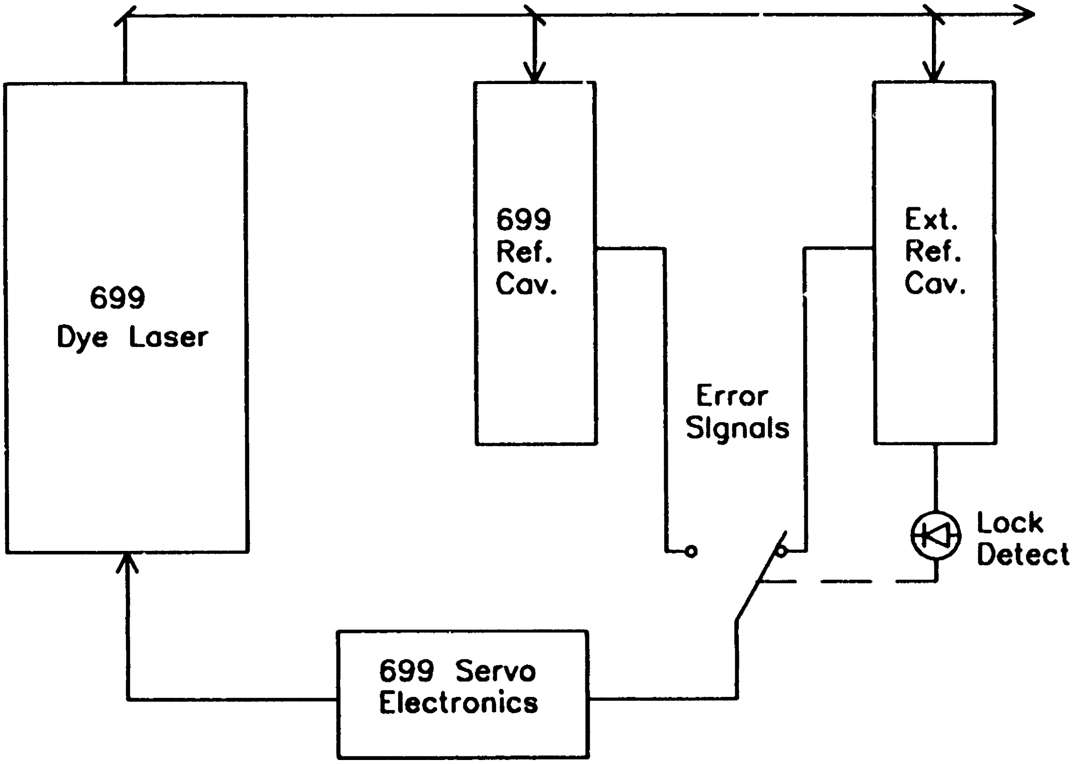

Figure 4-11: Conceptual elements of redundant cavity lock system.

The conceptual elements of the system are shown in Figure 4-11 and the actual circuitry is shown in Figure 4-12. The lock status is determined by monitoring the light level transmitted by the external reference cavity. If there is a measurable transmitted light level, this is taken to indicate that the laser is locked to a cavity resonance, while no light indicates that the lock has been lost. The light level is detected with a 10 μs time constant so that a very short unlock-relock sequence does not cause the system to switch error signals. If the no lock status is detected, then the circuit changes the source of the error signal sent to the 699 electronics via a set of FET switches. At the same time the lock control line is brought to ground, disabling the HV EOM amp. The system is now functioning essentially as an unmodified 699.

If the 699 reference cavity is tuned to the same frequency as the external reference cavity, then the laser will be close to resonance with the external reference cavity after the perturbation has passed. The linewidth of the original 699 is such that a momentary frequency fluctuation may bring the laser into an accidental resonance with the external reference cavity. This resonance would be detected by the cavity transmission and the system would relock in the high stability mode to the original reference cavity fringe. The relocking process is assisted by the fact that the fast EOM amp is active the entire time.

The remaining problem is to ensure that the resonance frequencies of the 699 reference cavity and the external reference cavity always overlap. An active system has been employed to perform this function. When a high stability lock is present, information on the relative tuning of the two cavities can be derived from the internal error signal of the 699. A single pole servo loop maintains the 699 internal error at zero by control of the 699 reference cavity frequency through the external scan function of the 699. If the high stability lock is lost, then the input to this loop is disconnected and the 699 reference cavity tuning is unchanged until the high stability lock is re-established. The external frequency scan controls for the 699 are set so that the 699 reference cavity cannot be tuned more than one free spectral range of the external reference cavity. This guarantees that when the system relocks it will lock only to the same external reference cavity fringe.

This system performs exceptionally well, allowing all but the most careless activity on and around the optical table without losing the lock to the original external cavity fringe. The laser can actually be existinguished by blocking the cavity for more than a second and it will automatically re-establish a high stability lock when the cavity is unblocked. The system has been used many times with no unlocking events over the course of a 6 to 8 hour period.

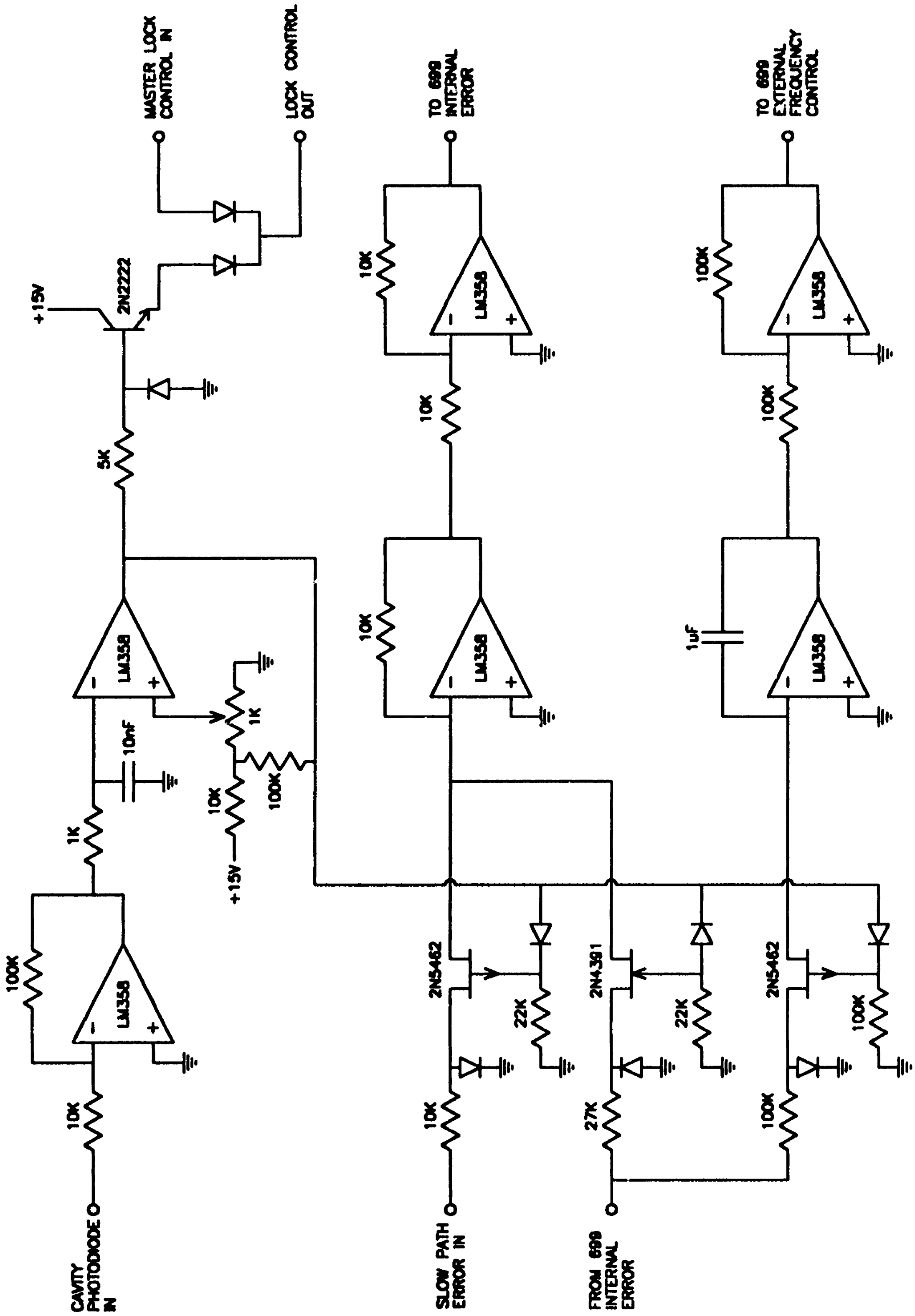

Figure 4-12: Schematic for redundant cavity lock system.

4.3 Frequency Doubling System

4.3.1 Frequency Doubling in BBO

Beta barium borate (BBO) is versatile nonlinear optical material that became commercially available in the late 1980's. It has a relatively large second order nonlinear optical coefficient and wide phase matching and transparency ranges. These properties make it well suited to frequency doubling visible laser sources into the ultraviolet. It is a negative uniaxial crystal with a point group symmetry of 3m. A complete review of its properties is given in Reference [47].

Type I angle tuned phase matching [48] is best suited for second harmonic generation (SHG) of 243 nm. The phase matching angle is

$$\theta_m = 54.6 \text{ degrees.} \tag{4.2}$$

The effective nonlinear optical coefficient for this type of interaction is given by[47]

$$d_{eff} = 1.38 \times 10^{-12} \text{ m/V.} \tag{4.3}$$

The use of angle tuning to achieve phase matching for second harmonic generation in BBO is not without disadvantages. In this scheme, the fundamental light propagates through the crystal as an ordinary wave while the second harmonic propagates as an extraordinary wave. One of the properties of an extraordinary wave in an anisotropic crystal is that the directions of phase propagation($\vec{k}$) and energy propagation($\vec{S}$) are not necessarily the same. The angular difference between $\vec{k}$ and $\vec{S}$ is called the double refraction angle. For a uniaxial crystal with indices n_o and n_e the double refraction angle ρ, is given by[49]

$$\tan\rho = \frac{1}{2} n_o^2 \left(\frac{1}{{n_e}^2} - \frac{1}{{n_o}^2} \right) \sin\theta_m \tag{4.4}$$

where θ_m is the angle between $\vec{k}$ and the optic axis, $\vec{z}$, of the crystal (θ_m is the phase matching angle). The double refraction angle is in a direction such that $\vec{k}$, $\vec{S}$, and $\vec{z}$

all lie in the same plane. For SHG of 243 nm in BBO we find

$$\rho = 4.65 \text{ degrees.} \tag{4.5}$$

The presence of double refraction causes some undesirable complications in the frequency doubling process as will be explained in this section.

We have used Boyd and Kleinman [50] as the primary reference for understanding and optimizing SHG. The optimization of SHG consists of obtaining a nonlinear crystal with the most desirable characteristics (high transparency, long length) and adjusting the properties of the fundamental beam to maximize the amount of second harmonic generated. Boyd and Kleinman treat the problem of finding the optimum focal properties for the fundamental beam given the following quantities: crystal length, index of refraction, double refraction angle, and light wavelength. They find the optimum focussing parameter for crystals with large double refraction angles to be

$$\xi \equiv l/b = 1.39 \tag{4.6}$$

where l is the crystal length and b is the confocal parameter of the fundamental beam inside the crystal. If we apply their treatment to our experimental situation we obtain the following prediction for the amount of second harmonic power generated with optimum focussing

$$P_{sh} = (1.36 \times 10^{-4}) P_f^2 \tag{4.7}$$

where P_f is the fundamental power passing through the crystal and both powers are expressed in Watts. This will be compared with our experimental results later in the section.

4.3.2 External Doubling Cavity

The technical difficulty in generating sufficient levels of UV power can be seen from Equation 4.7. If we simply focus the 0.4 W output of our dye laser into a 10 mm long BBO crystal, only 20 μW of 243 nm light will be generated under optimum conditions. This is substantially less than required in our application. A solution to this problem is to place the crystal inside an optical cavity in which there is a high level of circulating power. The cavity could be the laser cavity itself or an external passive cavity into which the laser power is coupled. These techniques are only practical if the crystal has a sufficiently low level of linear optical losses so that a high level of circulating power can be maintained with the crystal in the cavity. Both approaches (the crystal inside the laser[51] or an external cavity[52]) have been successfully used with BBO to increase the levels of 243 nm produced. We have adopted the external cavity approach because it allows one to separately address the issues of laser operation and frequency doubling at the cost of increased technical complexity.

The frequency doubling cavity system is shown in Figure 4-13. A Brewster cut BBO crystal (9.7 mm path length) is placed in a ring cavity. The laser output is mode matched to the TEM_{00} mode of the cavity. 243 nm light generated in the crystal is coupled out of the cavity by an ultraviolet transmitting cavity mirror. One of the cavity mirrors is mounted on a piezoelectric element that allows the cavity length to be electronically controlled. An active system is employed to maintain the cavity length at the appropriate value to maintain resonance with the incoming laser light. This system will be discussed in detail in this section.

The goal in the design of the SHG cavity is to produce a fundamental light field that will maximize UV generation. The optical losses of the cavity should be minimized and the proper beam focus should be produced at the crystal location. The first issue is primarily a technical one, a matter of obtaining sufficiently high reflectivity mirrors and a low loss crystal. The second issue is addressed by appropriate selection of the radii of curvature for the cavity mirrors and the mirror spacings. We will address the second issue first.

The concepts behind the design of optical cavities have been well treated by Kogelnik and Li[53]. The cavity geometry shown in Figure 4-13 was designed to produce a confocal parameter of 17.1 mm for the fundamental light in the crystal, a value somewhat higher than the optimum of 7.0 mm given by Equation 4.6. This choice was

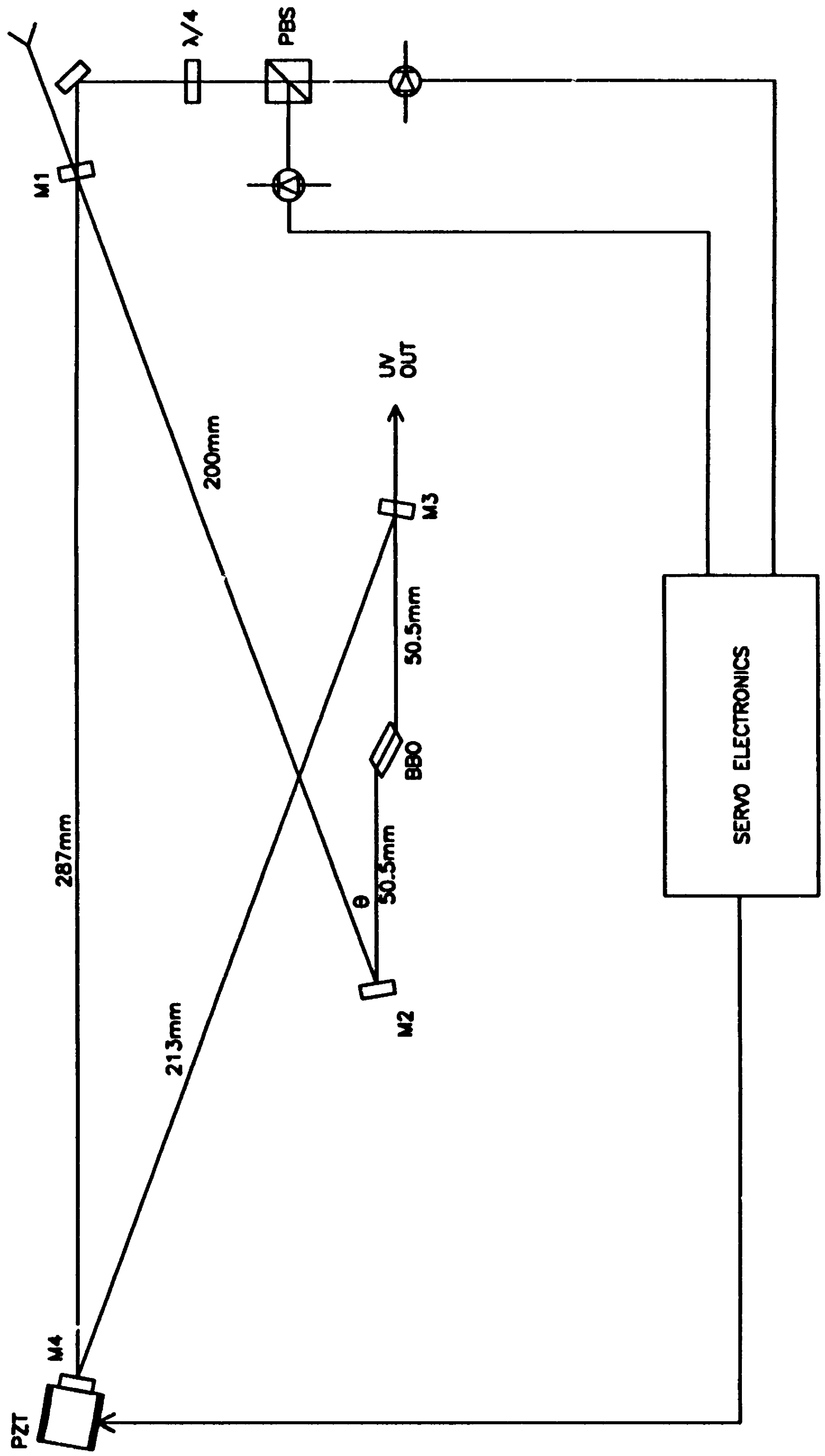

Figure 4-13: Diagram of SHG cavity.

made for technical convenience, and results in only a 20% reduction in UV output. In this design there is another free parameter besides the mirror radii and spacings, the angle θ in Figure 4-13. A value of $\theta = 20$ degrees was chosen so that the two sources of astigmatism in the cavity (the off-axis use of curved mirrors and the Brewster crystal) would cancel each other[54] and yield a nearly circular beam cross section inside the cavity. This strategy for astigmatism compensation requires the normal to the crystal surface and hence the fundamental light polarization to lie in the plane of the cavity.

The most critical parameter in the performance of the frequency doubling system is the optical loss in the doubling cavity. The loss determines the level of intracavity power that can be maintained with a fixed input power. Before discussing the experimental data on this subject we first define some quantities of interest. The ratio between the light power circulating in a resonant cavity and the incident power is known as the enhancement. For perfectly aligned and mode-matched cavity, the enhancement, A, is given by

$$A = \frac{1 - R}{(1 - \sqrt{RV})^2} \tag{4.8}$$

where R is the input coupler reflectivity and V is the fraction of power remaining after one round trip (not including the transmission loss of the input coupler). If R is chosen to maximize the enhancement we find

$$A = 1/(1 - V) \tag{4.9}$$

for $R = V$. Another useful quantity is the cavity finesse, which is given by

$$F = \frac{\pi (RV)^{1/4}}{1 - \sqrt{RV}}. \tag{4.10}$$

Experimental determination of the enhancement is relatively straightforward. The intracavity power is measured by detecting the small amount of light that is transmitted by one of the cavity mirrors (M4). The light level is recorded when the cavity is fully aligned and optimized. Then the input coupler is removed and the light level is recorded when the unenhanced input laser power is incident on the cavity mirror. The ratio of the two values yields the enhancement. Knowledge of the enhancement and the input coupler reflectivity allows one to determine the cavity losses through Equation 4.8.

The cavity losses fall into two categories: mirror losses and crystal losses. In most previous experiments of this kind the crystal losses have been the dominant contribution. In the case of a Brewster cut BBO crystal, transmission losses as low as 0.5% have been reported in the literature[55]. We have seen similar levels for our crystal as well. Losses on this level, however, are not lower than mirror losses observed without careful selection of the cavity mirrors. The cavity mirrors are multilayer dielectric coatings and by proper design their transmission loss can usually be made negligible. Normal dielectric coatings do, however, have a nontrivial level of loss due to scatter and absorption. We have found that the cavity mirrors for the 699 have approximately 0.2% to 0.3% loss due to scatter and absorption. The use of four of these mirrors in the doubling cavity would give approximately 1% loss due to the mirrors alone. Much better mirror performance can be obtained by a combination of "super-polishing" of the substrate and using an ion beam sputtering coating process. The more sophisticated mirrors can be quite expensive to obtain in small quantities so we have used them only where our requirements overlapped with existing mass produced mirrors.

The doubling cavity consists of the following mirrors. M1 is a 1.0% transmission input coupler with a radius of curvature of 1200 mm. It is a low loss, super-polished ion beam sputtered coating[56]. The radius of curvature was the maximum obtainable in a mass produced mirror suitable for use as an input coupler. M2 is a high reflector with a 100 mm radius of curvature, Coherent part number 0158-789-04. M3 is a custom designed mirror to provide a high reflectivity at 486 nm and a high transmission at 243 nm. It was made with a conventional polishing and thermal evaporated coating process and is expected to have a loss level of a few tenths of a percent. M4 is a planar high reflector made with the low loss process.

The enhancement for the doubling cavity was measured to be 100±10. With an input coupler transmission of 1%, this gives a roundtrip cavity loss of 1% (V = 0.990). We attribute half the losses to the BBO crystal and the other half to the two cavity mirrors that were not made with the low loss techniques. If these two mirrors were replaced with custom made low loss mirrors, an enhancement of near 200 may be feasible, yielding a fourfold increase in UV power.

The doubling cavity is only effective at enhancing the laser power if the laser frequency coincides with one of the doubling cavity resonance fringes. Environmental perturbations of the doubling cavity resonances and tuning of the laser require an active system to be employed to maintain resonance between the cavity and the laser. Since the doubling cavity already contains a polarization sensitive element (the BBO crystal), the Hänsch-Couillaud method[57] is an effective way of generating an error signal for servo locking of the cavity to the laser. The piezo mounted cavity mirror (M4) provides a means of tuning the cavity electronically. The piezo is driven by the 3 pole loop filter shown in Figure 4-14. This circuit is loosely based on a circuit developed by Bloomfield[58]. Originally a one pole loop was employed, but it was found to give inadequate performance at low frequencies (500 Hz and below) where the environmental perturbations are most severe. A 3 pole loop gave much better performance while locked, but showed difficulty in making the transition from an unlocked to a locked state. An effective solution to this problem is illustrated in Figure 4-14. The activation of the second two poles has been delayed until approximately 0.5 s after the lock is acquired.

An unexpected technical problem was encountered in the initial setup of the frequency doubling system. The cavity was found to perform well during alignment and when intially locked, but after a short time of being locked with a high circulating power the enhancement would drop dramatically, indicating a significant increase in intracavity losses. The initial enhancement could be regained by a translation of the crystal, indicating that a crystal damage effect was responsible. The damage was not correlated with UV generation as it was found to be independent of adjustment of the phase matching angle. The time necessary for the damage to appear was approximately inversely proportional to the circulating power level. Chopping of the input

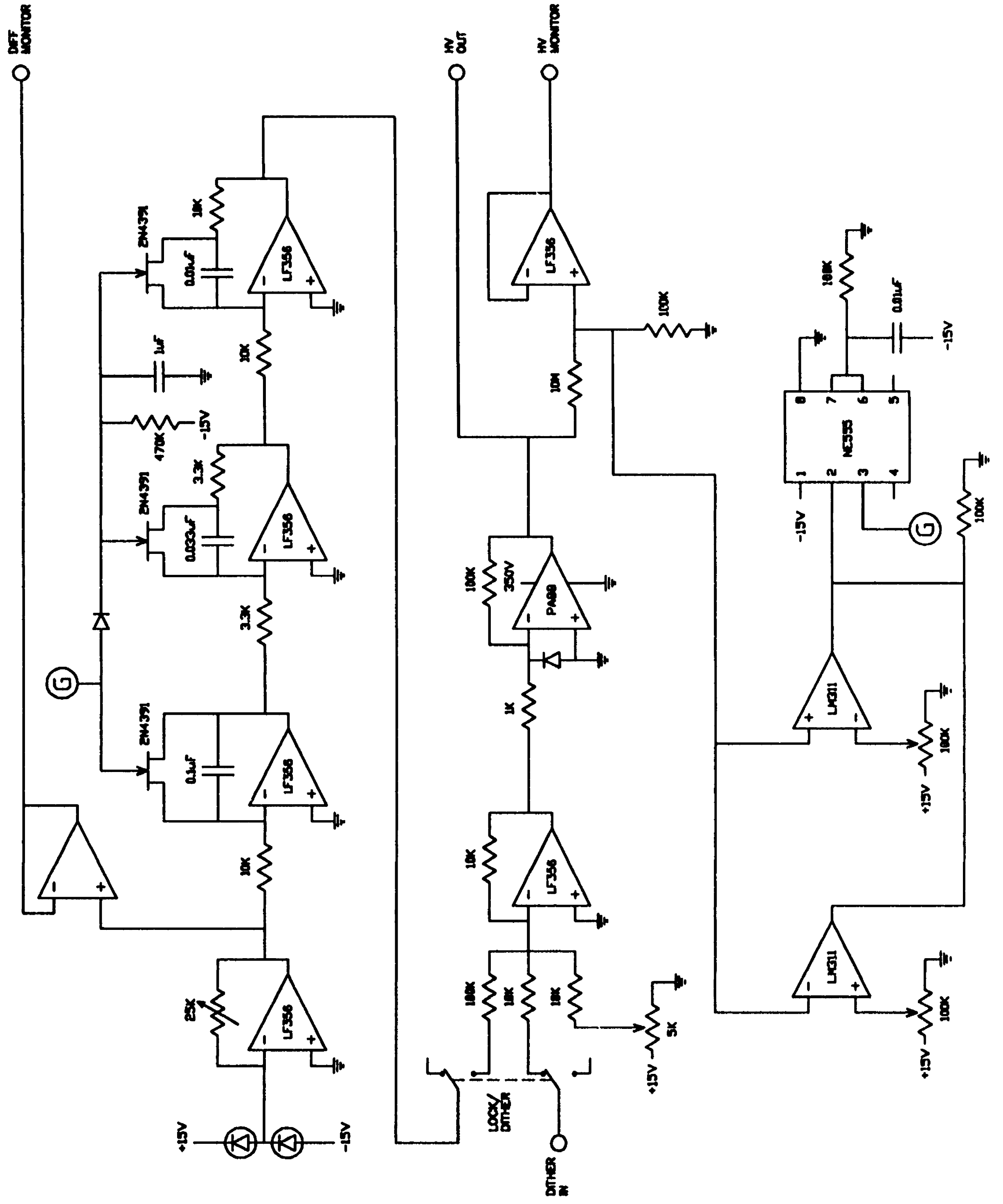

Figure 4-14: SHG cavity servo electronics

beam at frequencies up to 30 kHz reduced the damage time only by the duty cycle of the chopping.

The initial version of the cavity held the crystal in a small box designed to protect the crystal from atmospheric humidity and dust. The box was a 15 mm cube with windowless apertures for the beam and an inlet at the top for flowing of dry nitrogen over the crystal. The crystal was placed in the holder as it was received from the supplier, with no cleaning process being attempted. We became aware of reports[59] that the use of oxygen as a purge gas rather than nitrogen had a beneficial effect on BBO and this was tried without success. One obvious deficiency of the holder was that it was poorly designed to minimize the effects of turbulence in the flowing gas on the optical properties of the cavity. At gas flow rates of 0.5 l/min, the cavity lock was noticeably degraded. A second version of the holder was designed to minimize this effect. The new holder has two separate gas inlets, each with three small holes to blow the gas tangentially across the Brewster surfaces of the crystal. The beams enter through 3 mm ID by 20 mm long tubes instead of simple apertures. The new holder permits gas flow rates of 2 l/min without serious effects. The crystal was cleaned with anhydrous methanol using the "drop and drag" technique prior to its placement in the new holder.

The first experience with the new holder was no more promising. Using nitrogen as the purge gas, the same damage effect was observed. Oxygen was tried again, this time with success. With oxygen flowing over the crystal surfaces, no damage has been observed over months of operation at the highest laser powers available. We do not have a simple explanation for these observations, but we have made some attempts to determine the origin of the damage mechanism. The difference between nitrogen and oxygen with the new holder does not seem to be related to contamination. We have tried using nitrogen from a compressed gas cylinder and from boiloff from liquid nitrogen, both with the same effect. Another interesting point is that very low oxygen flow rates (lower than used with the previous holder) are sufficient for preventing the damage, leaving some open questions about the distinction between the two holders. A final fact is that another group[35] have used BBO in similar applications with the crystal exposed to atmosphere with no reports of optical damage. Since this effect was not of primary interest to this research we did not study it further once a solution was found.

In most conditions, about 400 mW of 486 nm light is available for frequency doubling. The circulating power inside the doubling cavity is a factor of 100 higher, giving 40 W for the fundamental power passing through the crystal. Under these conditions we have measured 20 mW of 243 nm light transmitted out of the cavity. The light power transmitted out of the cavity has been attenuated by reflection losses at the exit face of the crystal (the second harmonic has orthogonal polarization to the fundamental) and by losses in M3, the UV output coupling mirror. Together these losses total 40%, implying 33 mW of UV actually generated in the crystal. There is a large discrepancy between this value and the UV power predicted by Equation 4.7. If we reduce the prediction of Equation 4.7 by 20% to account for the non-optimum focussing of the fundamental beam we predict a value of 170 mW, a factor of 5 higher than the observed value. We have no verified explanation for this discrepancy. A simple explanation is that the BBO crystal was not properly cut to maximize the effective nonlinear coefficient. The linear optical properties of the crystal are invariant with respect to angular orientation of the x and y crystallographic axes around the optic axis (the z axis), but the nonlinear optical properties are not. Improper orientation of the x and y axes with respect to the fundamental light polarization direction (determined by the Brewster surface) would manifest itself as a reduced nonlinear coefficient with no other optically observable consequences. This possibility could be verified by an X-ray diffraction measurement of our crystal, but this has not been done. The current performance of the frequency doubling system is adequate for our initial needs.

4.3.3 Astigmatism Compensation

The largest drawback of using BBO as a nonlinear material is its large double refraction angle. The primary effect of double refraction is seen in the spatial characteristics of the second harmonic beam. A qualitative understanding of this can be gained from

Figure 4-15. UV light generated near the entrance face of the crystal propagates away from the direction of the fundamental light, exiting the crystal at a different transverse location than the fundamental. UV light generated near the exit face exits at the same location as the fundamental. This results in a transverse "smearing" of the UV beam profile in the plane that contains $\vec{k}$, $\vec{S}$, and $\vec{z}$ (hereafter the xz plane). The UV beam profile in the orthogonal plane (the yz plane) is not affected by this and retains a gaussian profile indicative of the fundamental beam. For the overall UV beam profile at the exit face of the crystal we find in the xz plane a broad, non-gausssian profile and in the yz plane a narrow, gaussian profile. We have invested a significant amount of effort to develop a quantitative description of the UV beam profile and understand how to manipulate it to produce a beam profile suitable for our experimental conditions.

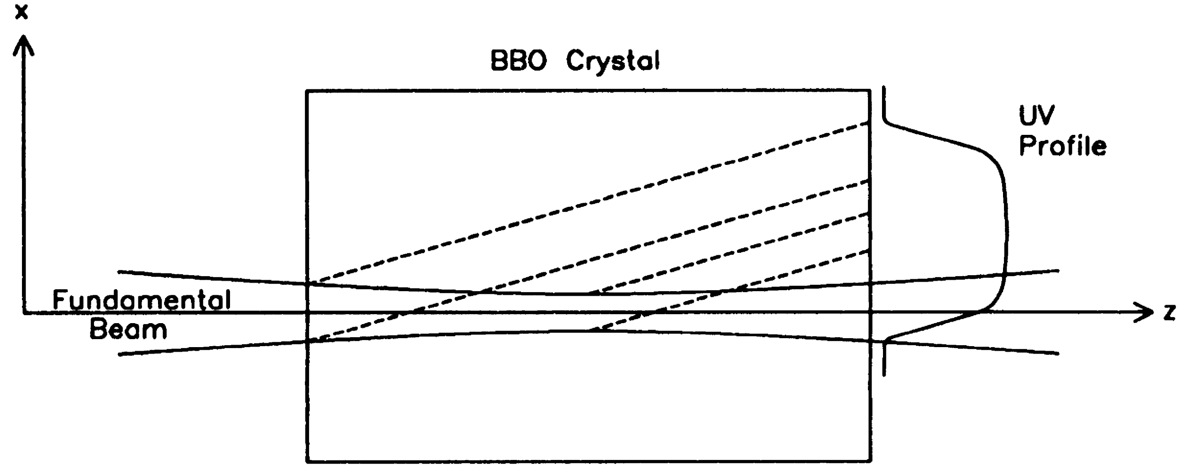

Figure 4-15: Effect of double refraction on UV beam profile. The double refraction angle is exaggerated for clarity.

To motivate a deeper understanding of the UV beam profile, we present a short discussion of our requirements for a useful beam. Doppler-free excitation of the $1S-2S$ transition requires one to produce a high intensity 243 nm standing wave light field for interaction with the hydrogen atoms. This light field must be produced under the constraints of the apparatus neccessary to trap and cool our sample of atomic hydrogen (this is discussed in Chapter 5). The constraints due to the trapping apparatus dictate the use of a beam that can offer near diffraction-limited performance and be retro-reflected with a single spherical optic to produce a high quality standing wave. The most effective way to meet this requirement is to manipulate and filter the UV beam so that it can be introduced into the trap as a nonastigmatic TEM_{00} beam.

Boyd and Kleinman[50] present a thorough treatment of second harmonic generation with gaussian fundamental beams. Their treatment is valid for arbitrary focussing of the fundamental beam and properly takes into account the presence of double refraction. The primary goal in this work was to develop a rigorous expression for the total SHG power generated under specified conditions, and the result is Equation 2.22 of [50]. In the derivation of this result, they present an expression (Equation 2.9) for the complex field amplitude of the second harmonic light field for any point outside the crystal. We have used this expression to numerically calculate the spatial amplitude profile for our second harmonic beam. We do not reproduce their treatment or expression here, but simply present the results of our calculations.

Figure 4-16 shows the calculated UV intensity profile at the exit face of the crystal for our experimental conditions. A confocal parameter of 17.0 mm (inside the crystal) was assumed for the fundamental beam, a value derived from the parameters of the doubling cavity. It was also assumed that the SHG power had been optimized by translating the crystal along the beam axis and by adjusting the phase matching angle, both experimentally realistic assumptions. Furthermore, any crystal absorption at both the fundamental and second harmonic wavelengths was neglected. Although only the intensity profile is shown in Figure 4-16, full amplitude and phase information is determined in our calculations.

It is obvious from Figure 4-16 that the UV beam is not a gaussian, TEM_{00} beam. At this stage the only property that we attribute to it is that it can be described as a paraxial beam. A very thorough discussion of paraxial beams is given by Siegman[60] and it is recommended as a general reference on the subject. In the following discussion we will rely on references to Siegman for clarification of the concepts involved.

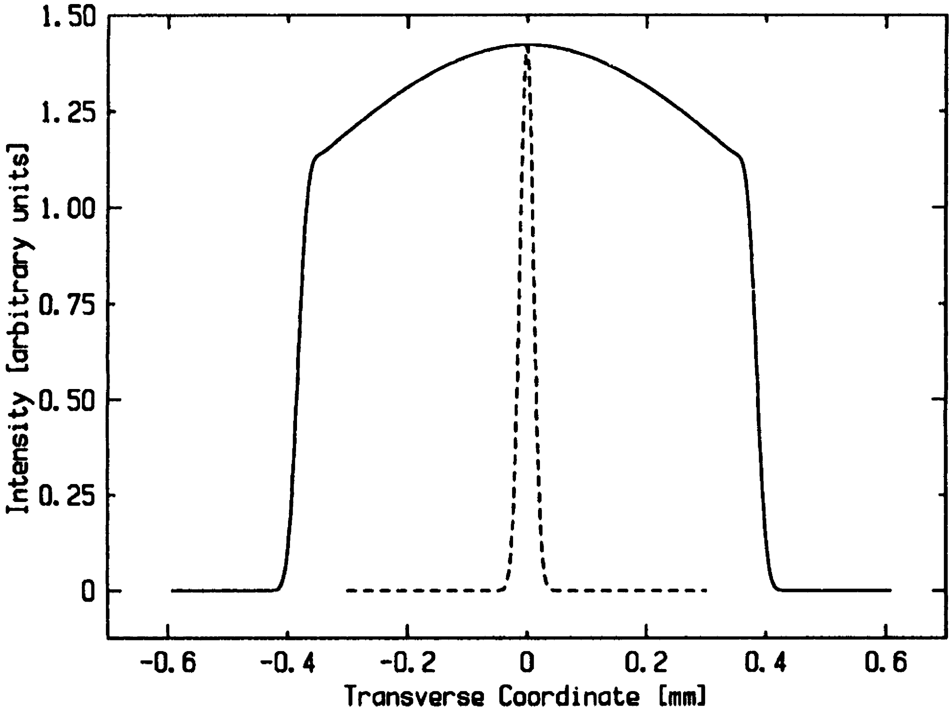

Figure 4-16: UV beam intensity profile. The solid line is the xz plane profile, the dashed line is the yz plane profile.

Siegman writes (Eq. 16.2) an arbitrary paraxial beam as

$$\tilde{E}(x,y,z) \equiv \tilde{u}(x,y,z)e^{-jkz}. \tag{4.11}$$

Here the electric field for the beam is written as a complex quantity that carries the phase and amplitude information for the field that oscillates sinusoidally in time. The spatial behavior of the beam has been separated into two functions, $\tilde{u}(x,y,z)$ and e^{-jkz} (we use the engineering notation of e^{-jkz} instead of e^{ikz} to maintain consistency with Siegman). The motivation for the paraxial approximation is that we need only discuss the properties of $\tilde{u}(x,y,z)$ and specify k to completely determine all properties of the beam. We make two observations about $\tilde{u}(x,y,z)$. First, the specification of $\tilde{u}(x,y,z)$ for a plane of fixed z allows one to determine the value of $\tilde{u}(x,y,z)$ for any point x,y,z from the paraxial wave equation. Thus, by our knowledge of the UV beam amplitude at the exit face of the crystal, we possess a complete description of the UV beam. Secondly, since in our situation the paraxial wave equation is separable in Cartesian coordinates we are free to write

$$\tilde{u}(x,y,z) = \tilde{u}(x,z)\tilde{u}(y,z). \tag{4.12}$$

This allows us to consider to behavior of the beam in the xz and yz planes as two separate problems.

A powerful method for analysis of paraxial beams is to perform a Hermite-gaussian mode expansion of the arbitrary functions $\tilde{u}(x,z)$ and $\tilde{u}(y,z)$ (see Siegman Section 16.4). For example we can write for $\tilde{u}(x,z)$

$$\tilde{u}(x,z) = \sum_n c_n \tilde{u}_n^{b,z_0}(x,z). \tag{4.13}$$

$\tilde{u}_n^{b,z_0}(x,z)$ is the Hermite-gaussian function of order n. Our notation in Equation 4.13 differs from that in Siegman because we have explicitly introduced the variables b and z_0 that parametrize the basis functions used in the expansion. Physically b and z_0 correspond to the confocal parameter and the focal position of the basis function

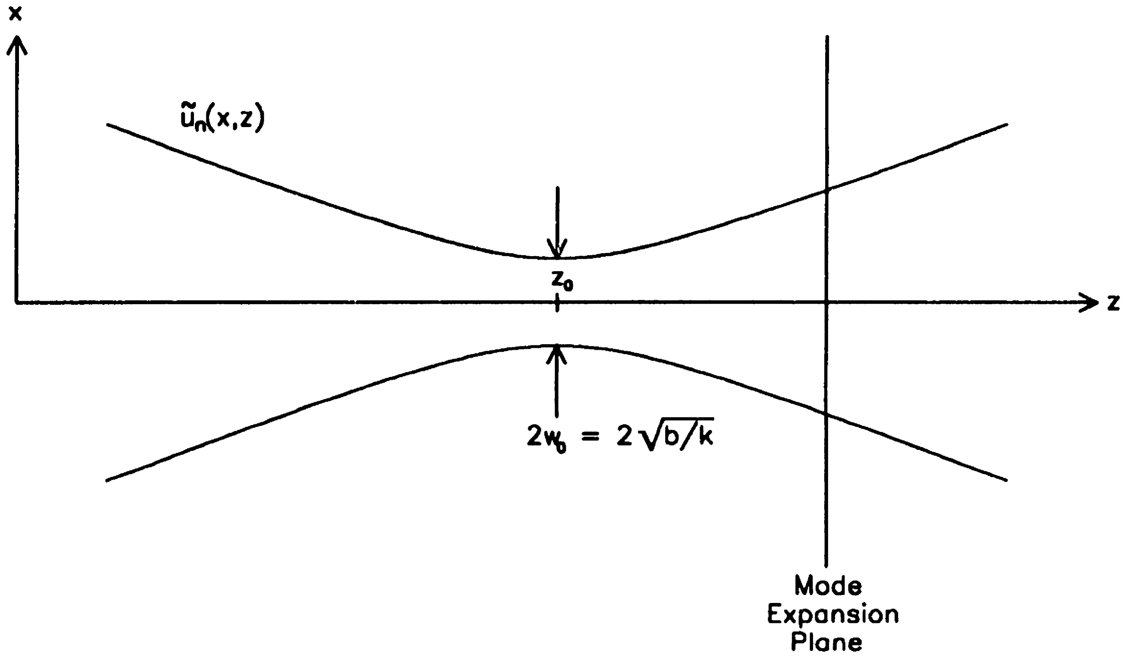

Figure 4-17: Physical significance of Hermite-gaussian parameters b and z_0.

as illustrated in Figure 4-17. There are no constraints on the choice of b and z_0, but an appropriate choice may greatly simplify the expansion and maximize the physical insight gained in the process. The coefficents c_n in Eq. 4.13 can be determined from

$$c_n = \int_{-\infty}^{\infty} \tilde{u}(x,z)\tilde{u}_n^{*b,z_0}(x,z)dx. \tag{4.14}$$

Of particular interest is the coefficient c_0 of the lowest order mode. The magnitude of c_0 indicates the overlap between the arbitrary beam in question and an ideal gaussian beam with parameters b and z_0. The most meaningful expansion in our experimental context results when b and z_0 are chosen to maximize the magnitude of c_0.

This procedure has been employed to characterize our UV beam profile. The case of $\tilde{u}(y,z)$ is completely straightforward. From physical insight into the doubling process (see earlier discussion), we know that $\tilde{u}(y,z)$ corresponds to an ideal gaussian mode with a b and z_0 equal to that of the fundamental (486 nm) beam. The case of $\tilde{u}(x,z)$ is more difficult. There is no a priori choice for b and z_0 in this case. The best values for these parameters were determined by numerically evaluating Eq. 4.14 for $|c_0|^2$ as the parameters were varied. The results of these calculations are shown in Figures 4-18 and 4-19. The values of b = 3825 mm and z_0 = 3 mm were found to maximize $|c_0|^2$. An interesting result of these calculations was that the overlap between $\ddot{u}(x,z)$ and an ideal beam was surprisingly large ($|c_0|^2 \approx 0.92$).

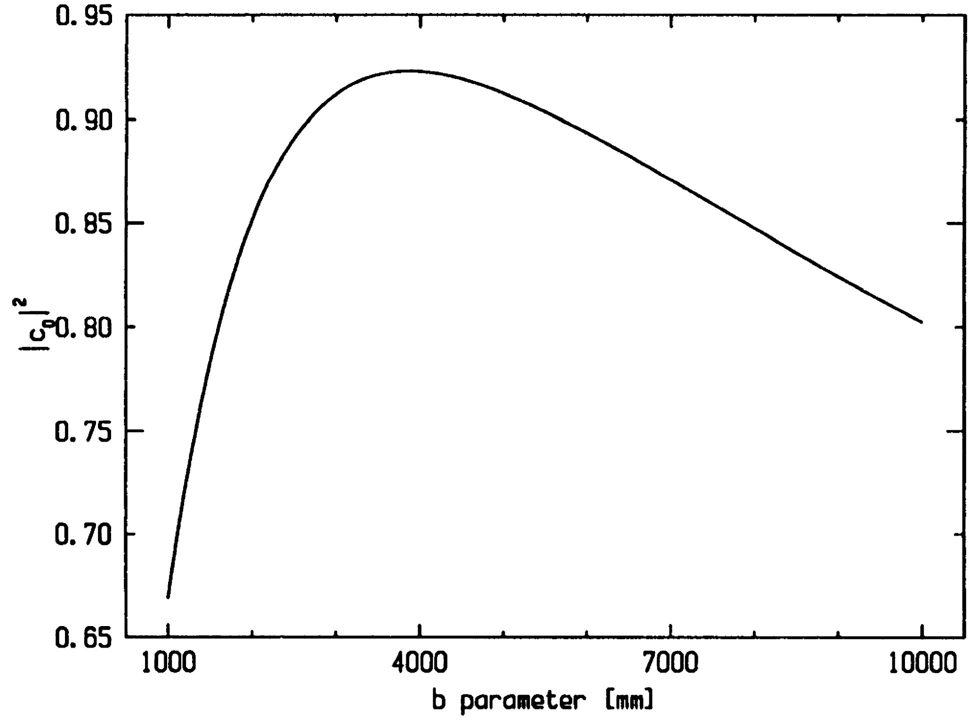

Figure 4-18: Variation in $|c_0|^2$ with b in the Hermite-gaussian expansion. z_0 has been fixed at 3 mm.

At this point we have reached a reasonable characterization of the UV beam. We have determined the lowest order basis functions $\tilde{u}_0^{b,z_0}(x,z)$ and $\tilde{u}_0^{b,z_0}(y,z)$ that maximize the overlap with the real beam profile. The remaining problem is that the parameters b and z_0 for the xz plane are very different than that of the yz plane. This can be treated as a straightforward problem of astigmatism correction for a gaussian beam.

We have adopted a compensation system consisting of one spherical lens and one cylindrical lens (see Figure 4-20). Such a system can compensate an arbitrary degree of astigmatism by appropriate positioning of the lenses along the beam propagation

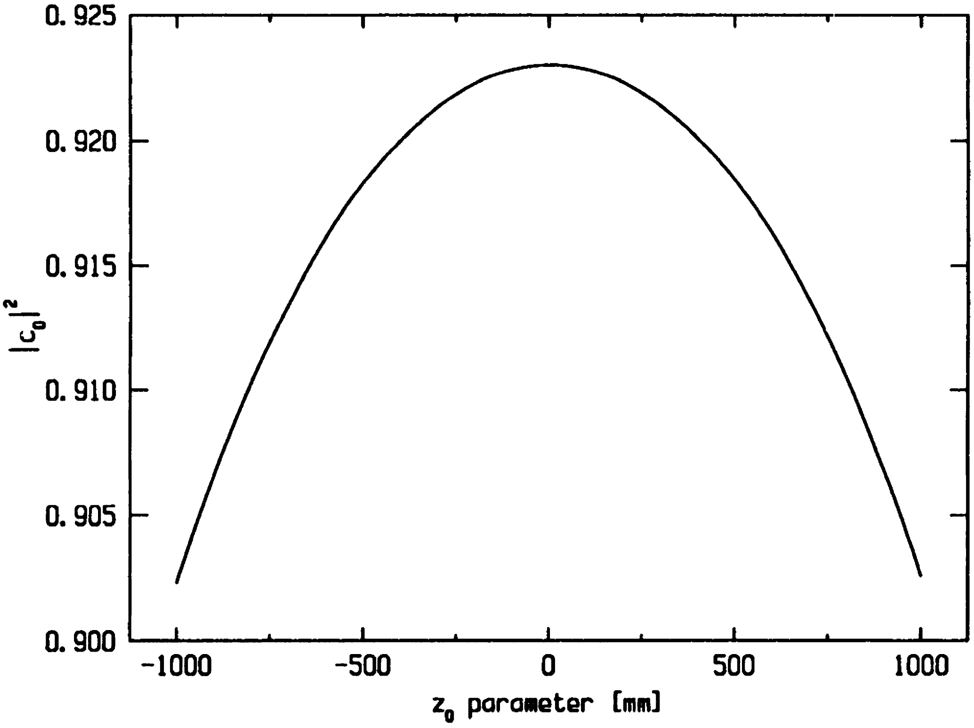

Figure 4-19: Variation in $|c_0|^2$ with z_0 in the Hermite-gaussian expansion. b has been fixed at 3825 mm.

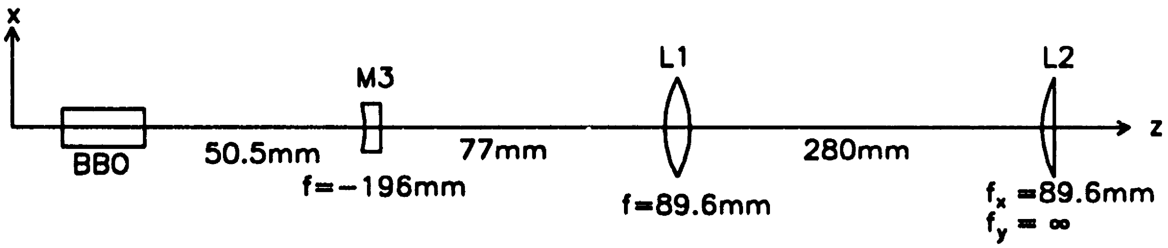

Figure 4-20: Astigmatism compensation system (drawing not to scale).

axis. If the input beam parameters are known and the focal lengths of the lenses have been chosen, then calculation of the lens positions is a straigthforward problem of optical design for gaussian beams. We have found such calculations to give quite good results, needing only minor experimental adjustment to achieve good performance. The algorithm we followed for experimental adjustment went as follows. The system was set up according to the results of design calculations. The degree of compensation was assessed by visual observation of the beam profile in both the near field (< 1 m from the lens) and the far field (approximately 5 m from the lens). A perfectly compensated beam should have a circular cross-section at both points. The position of the cylindrical lens (L2 in Figure 4-20) was continuously varied with a translation stage to obtain optimum compensation. The spherical lens (L1) was then moved a small increment (usually 1 mm) and the process repeated. The positions of L1 and L2 that gave the best results were then set as the final alignment. A series of 3 spherical lenses followed L1 and L2 to expand and collimate the beam for propagation to the hydrogen trap.

4.4 Tellurium Reference Spectrometer

An often troublesome issue in high resolution spectroscopic experiments is the identification of the spectral region to be searched for a (usually) weak signal. Fortunately for us, the hydrogen $1S-2S$ transition has been the subject of several careful experiments in the past and the use of absorption lines in molecular tellurium to find the transition is well documented[61]. We have set up an apparatus to observe saturated absorption lines in $^{130}Te_2$ for use as a calibration of our laser frequency relative to the anticipated frequency of the $1S-2S$ transition. This apparatus is based on the tellurium spectrometer described in Ref. [28]. We will give a very brief description of our spectrometer here.

The saturated absorption spectrum of $^{130}Te_2$ in the neighborhood of one quarter of the $1S-2S$ separation (486 nm light wavelength) is shown in Figure 4-21. The $1S$–$2S$ transition (F = 1) lies 57 MHz below the line denoted by i_2. A diagram of the tellurium spectrometer is shown in Figure 4-22. A cell containing isotopically pure ($\approx 99\%$) $^{130}Te_2$ was heated to 515 ± 10 C in a cylindrical oven. The cell was obtained from Opthos Instruments[62]. The pump and probe beams were both derived from the unshifted dye laser output. The pump beam was then chopped and frequency shifted in an AOM. The pump and probe beams were then aligned to counterpropagate through the tellurium cell, with optical isolators providing easy separation of the beams. The probe beam was detected on a photodiode and amplified in a lockin amplifier. The frequency shift in the pump beam AOM was set at 114 MHz, shifting the observed location of the i_2 line to coincide with the expected location of the hydrogen signal. This system allowed observation of the $^{130}Te_2$ i_2 line with a statistical uncertainty in the line center of 100 kHz. The reader is referred to References [28] and [63] for a discussion of the systematic effects on the line position. We simply note here that cell to cell variations give about a 1 MHz uncertainty in the absolute line position. This uncertainty is larger than the uncertainty due to the temperature of the tellurium cell (a ±10 C uncertainty gives a ±0.3 MHz uncertainty in the line position[28]).

The tellurium reference was used in two contexts. The first use was to calibrate the position of the reference cavity fringes with respect to the hydrogen line. The second was to locate the correct reference cavity fringe on a day to day basis. The reference cavity has a free spectral range of 600 MHz, while the tuning range for our locked system (with manual adjustment) is only 100 MHz, as described in Section 4.2.2. Thus, an arbitrary position for the reference cavity fringes does not guarantee that we can access the hydrogen line with the locked system. Proper positioning of the reference cavity fringes was obtained by varying the temperature of the reference cavity housing, using the tellurium spectrometer as the frequency reference. Identification of which fringe should be used for locking the laser was easily accomplished by referring to the tellurium spectrometer.

The final use for the tellurium spectrometer was the characterization of the long term frequency stability of the reference cavity. The linear drift rate of the reference cavity was determined by measuring the frequency difference between the $^{130}Te_2$ i_2

and the nearest reference cavity fringe at several day intervals. The cavity drift rate was approximately 6 Hz/s after thermal equilibrium had been reached.

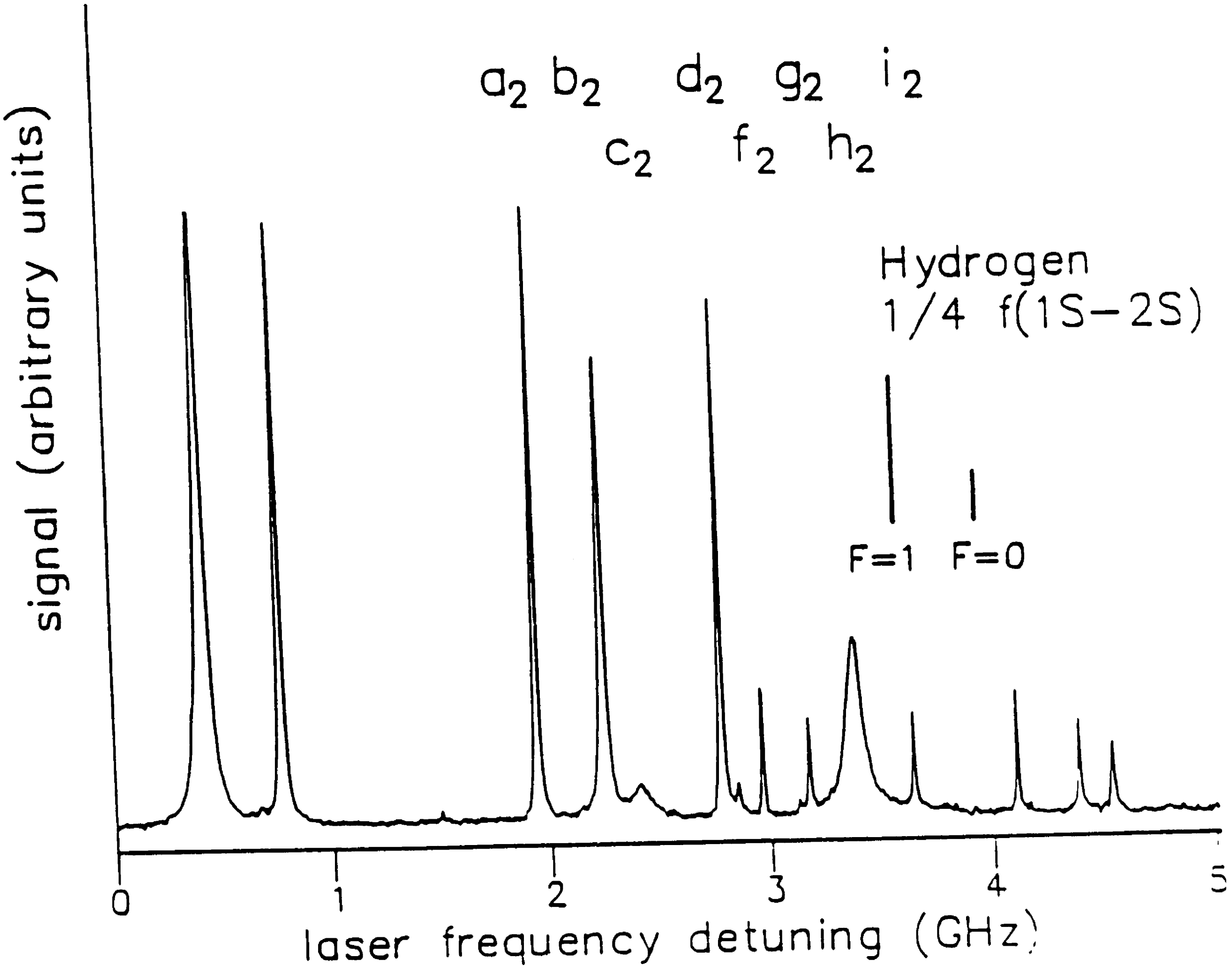

Figure 4-21: Tellurium saturated absorption lines. From Ref. [28].

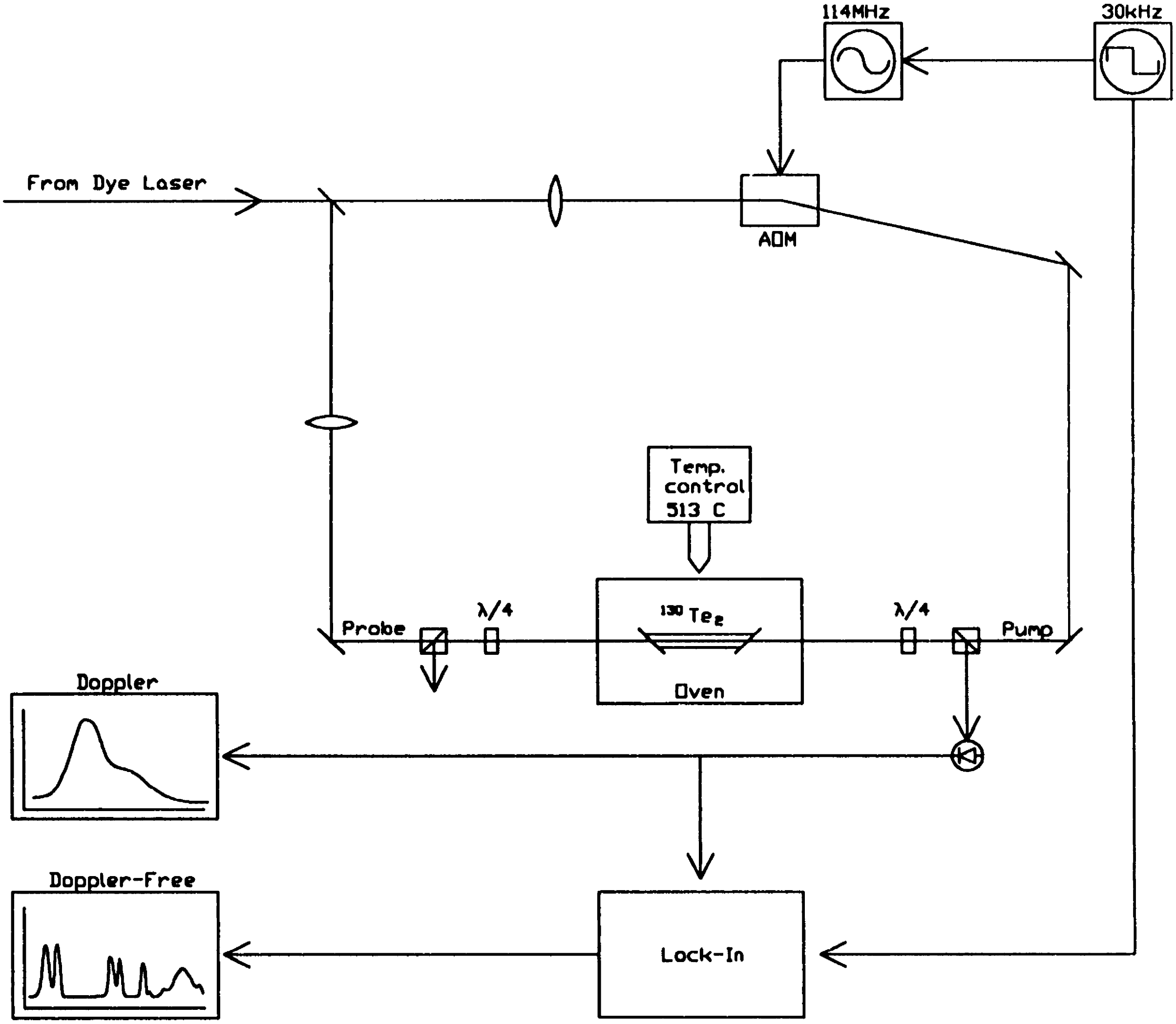

Figure 4-22: Schematic diagram of tellurium reference spectrometer.

Chapter 5

Apparatus Design and Function

This chapter describes the modifications made to the hydrogen trap to observe the $1S-2S$ transition, and the observations made during initial trials.

The principal goal of the modifications was to allow introduction of a 243 nm laser beam along the trap axis and also to detect the L_α fluorescence emitted by the trapped atoms. An additional goal was to control the stray electric fields in the trapping region and to allow the application of a controlled electric field to the sample.

The $1S-2S$ transition has not yet been observed. Initial trials revealed an unexpectedly high level of absorption in the optical windows on the experimental cell. The consequences of this absorption are discussed and strategies for overcoming the problem are described.

5.1 Experimental Apparatus

5.1.1 Experimental Cell

In previous experiments with trapped atomic hydrogen, the electric field in the trapping region was unimportant. The present experiment requires one to control stray electric fields to prevent unnecessary broadening of the $1S-2S$ transition due to Stark shifts and Stark quenching. We also require the ability to apply an electric field of several V/cm to the sample in a controlled manner to induce L_α fluorescence.

A new experimental cell was constructed to fulfill these requirements. The cell and accompanying apparatus are shown in Fig. 5-1.

The basic design of the cell is similar to that described in Ref. [9], except that the construction was modified to provide a metallic inner wall that would reduce the level of stray electric fields present in the trapping region. The inner wall consists of a stainless steel tube (UNS #S32100, 41 mm OD, 0.9 mm wall thickness), rather than an epoxy coated fiberglass tube. Also the top flange was brazed to the tube, and the lower flange was glued with epoxy (Stycast[64] 2850FT). The stainless steel was chosen to have a high electrical resistivity to minimize eddy current heating from ramping of the trap magnets and to have a low residual magnetism.

An electric field can be applied to the sample by two electrodes placed on the inner surface of the cell. They were made by gluing 0.025 mm thick, 6 mm wide brass foil to 6 mm wide by 0.6 mm thick G10 strips. The brass-G10 strips were then glued to the inner surface of the cell, running the length of the cell and diametrically opposed. The inner surface of the cell (including the electrodes) was then gold plated. The electrodes were connected to electrical leads that allowed the application of independent voltages to the two electrodes. Relaxation calculations predict that application of equal and opposite voltages to the electrodes produces an electric field of 11 V/cm per 100 V applied to each electrode.

The new cell contains a bolometer for detecting the recombination energy of atoms released from the trap. The bolometer is nearly identical to the one described in Ref. [9]. It consists of a 0.025 mm thick by 12.7 mm square quartz plate suspended by nylon threads. The temperature of the plate is measured by measuring the resistance of a graphite film[65] deposited on its surface.

Cell Windows

The 243 nm laser beam propagates along the axis of the cell through the trapping region. It enters through an optical window on the top of the atom source and exits through a window at the bottom of the cell. It is then retro-reflected and retraces its path. The performance of these windows is a critical aspect of this experiment.

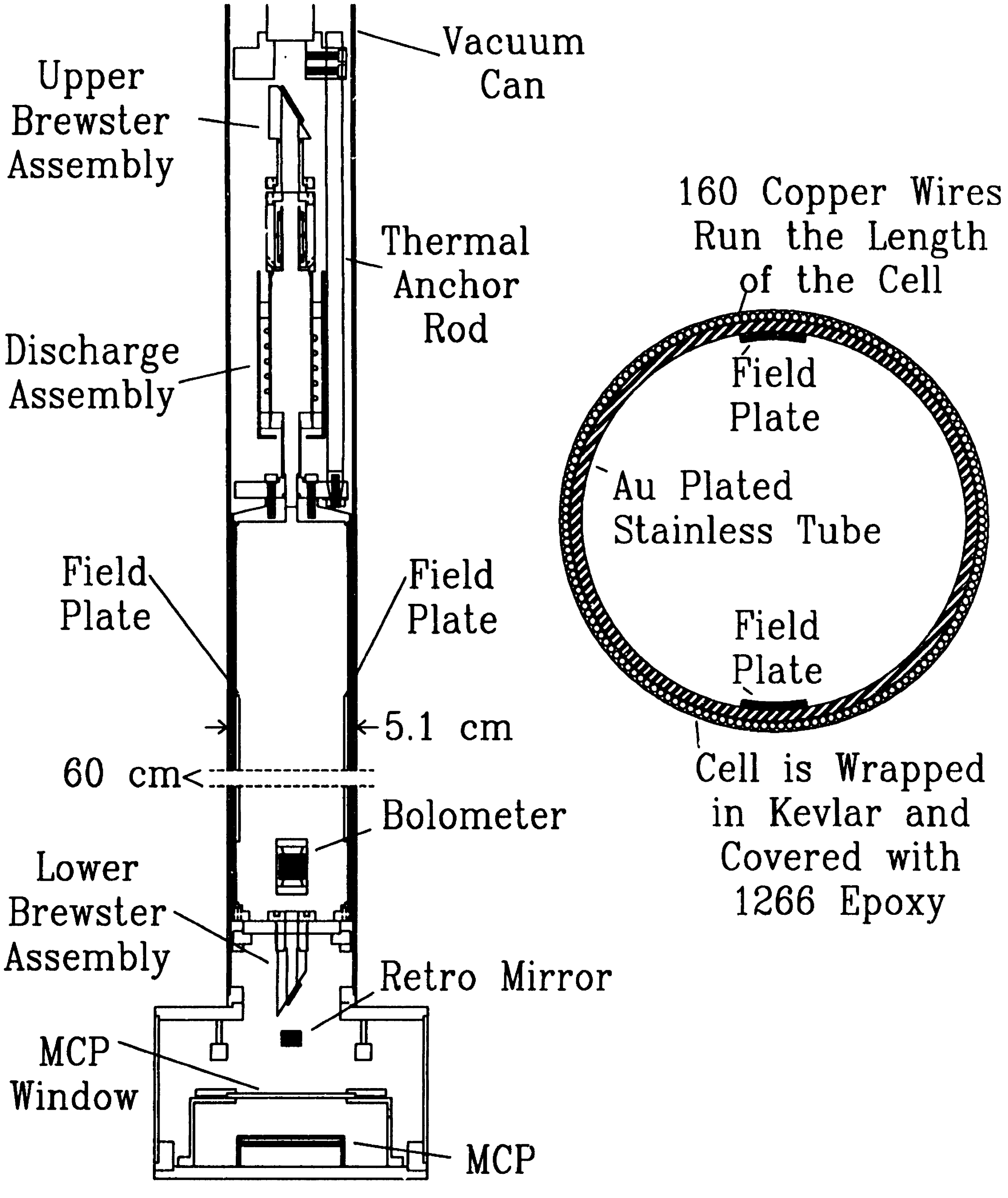

Figure 5-1: Diagram of cell construction. A cross section of the cell is shown at right.

The windows must transmit the 243 nm beam with minimum levels of absorption in the windows themselves, and without partial reflection of the beam to other parts of the cell. A final requirement is that the lower cell window must transmit the L_α fluorescence emitted by the trapped atoms.

We have operated the apparatus with two different configurations for the windows. In the first configuration, the windows were mounted at normal incidence to the beam and antireflection coatings were used to reduce unwanted reflections from the window surfaces. The upper window was coated over its entire clear aperture, while the lower window was only coated over its central 6 mm diameter. The coating pattern for the bottom window eliminated the unwanted surface reflection for the laser beam without requiring the coating to transmit at L_α .

The second window configuration held two uncoated windows at Brewster's angle. Fresnel reflection at the surface was then suppressed without antireflection coatings, eliminating any absorption that may occur if the coatings are nonideal.

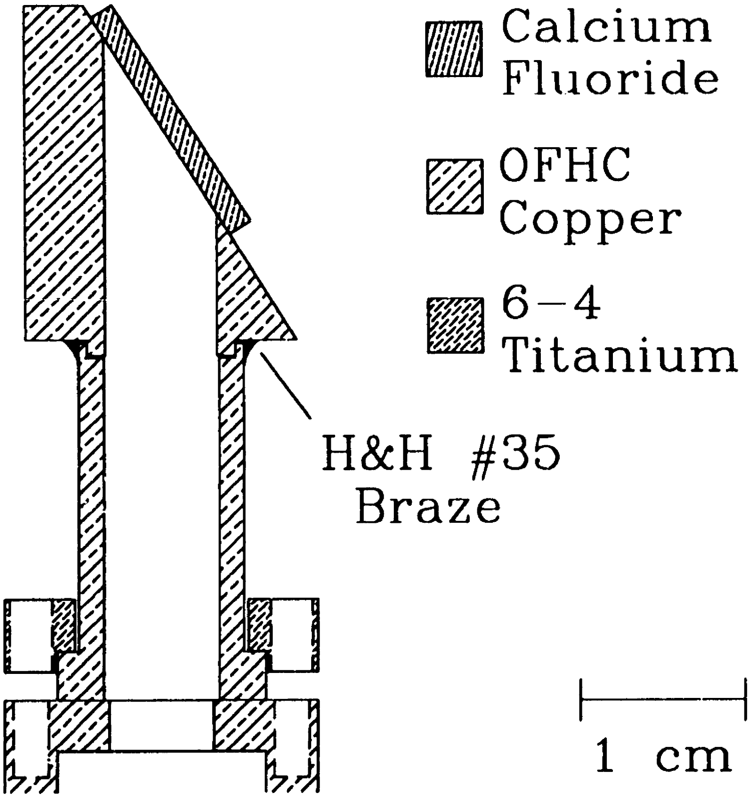

Figure 5-2: Upper Brewster window assembly (Handy & Harmon[66] braze designation is shown).

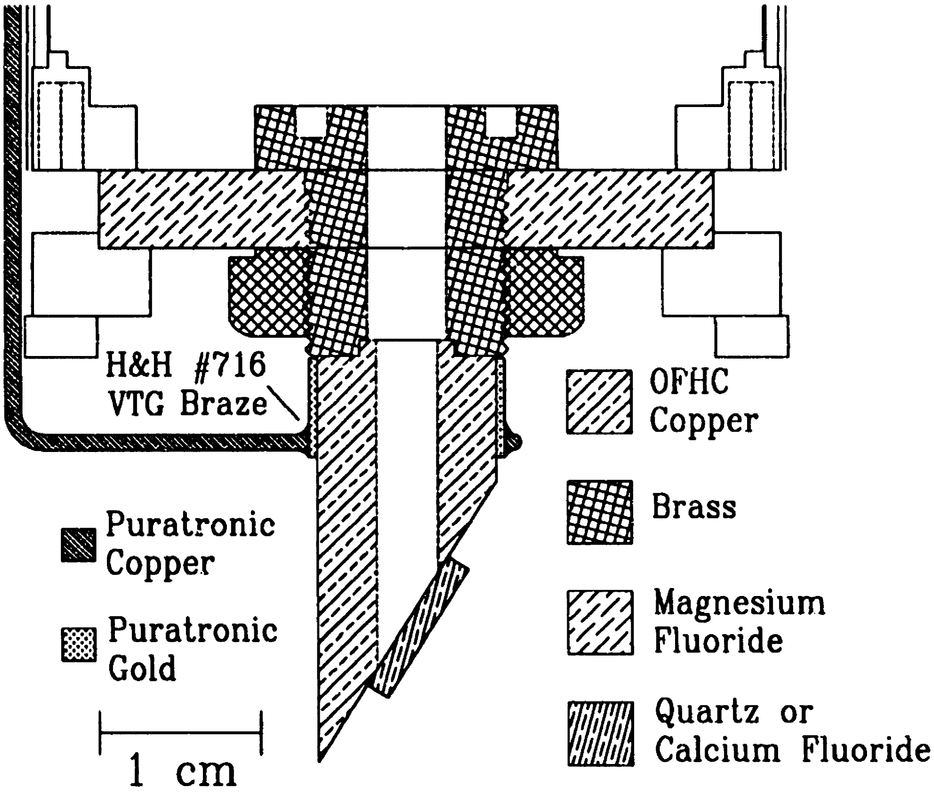

Figure 5-3: Lower Brewster window assembly (Handy & Harmon[66] braze designation is shown).

The upper window subassembly is shown in Figure 5-2. The bulk of the assembly is made out of OFHC copper, with the exception of a titanium clamping ring used to apply the force from the mounting bolts to the soft copper mounting flange (where an indium vacuum seal is made to the atom source). The window is mounted to the upper surface of the subassembly with an epoxy (Stycast 1266) vacuum seal. The particulars of this epoxy vacuum seal will be discussed later.

The lower window subassembly is shown in Figure 5-3. This subassembly mounts using a modified magnesium fluoride lower cell window (hereafter called the outer window) that has a 13 mm hole drilled along its axis. The mounting to the outer window is by an indium vacuum seal. The subassembly consists of two parts, a threaded brass fitting that is used in making the indium seal to the outer window, and an OFHC copper mount that is used in making an epoxy seal to the smaller Brewster window. The two parts are joined using 60/40 tin-lead solder. The entire assembly is thermally anchored to the lower part of the cell by a 1 mm diameter Puratronic[67] copper wire. In this configuration the central 18 mm of the outer window is blocked, but its perimeter is still clear for L_α transmission. The L_α collection solid angle is reduced 30% by this assembly.

We have found seals made with epoxy (Stycast[64] 1266) between OFHC copper and optical materials to be reliable if the thermal expansion of the optical material is close to that of copper between 300 K and 4 K. Values for the thermal expansion of many optical materials may be found in Refs. [68] and [69]. We have found that crystalline quartz and calcium fluoride are usable with this sealing technique, while, for example, magnesium fluoride is not.

The experimental data on the performance of these different window configurations will be discussed in the next section.

5.1.2 243 nm Beam System

Observation of the $1S-2S$ resonance signal requires a well controlled light field to excite the transition. The 243 nm radiation must be directed and focussed to produce a standing wave TEM_{00} mode in the center of the trapping region. In this section we describe the optical system that performs this function.

A schematic diagram of the optical system is shown in Fig. 5-4. A two lens combination focusses the 243 nm beam into the trapping region. The beam is then retro-reflected by a curved mirror at the bottom of the cryostat to form a standing wave. Two types of adjustments are necessary with this system. First, the angle of the retro mirror must be adjusted so that the incident beam strikes it at normal incidence. Second, the effective focal length of the lens combination must be adjusted so that the gaussian beam properties (the focal position and beam radius) of the retro reflected beam match those of the incident beam.

A complicating factor is that the laser source is located a long distance (26 m) from the cryostat. Such a large distance makes it difficult to maintain a high degree of alignment between the incident laser beam and the trap optics. To minimize this problem, we employ an active feedback system to reduce the misalignments that arise from relative motion of the laser source and the cryostat. A quadrant photodiode mounted on the cryostat monitors the position at which the incident laser beam strikes the cryostat. A piezoelectric mounted mirror at the laser source is driven by a feedback circuit to maintain the incident beam position at a fixed value.

Retro Mirror Adjustment

The retro mirror is mounted in a holder suspended by three piezoelectric bimorphs[70]. This allows the retro mirror angle to be adjusted external to the cryostat. Alignment is determined by observing the retro beam external to the cryostat and maximizing its overlap with the incident beam. Initial alignment is facilitated by a quadrant photodiode placed behind the retro mirror (the retro mirror is partially transmitting). This assures that the incident beam strikes the retro mirror near its center. The angle of the retro mirror is then varied with the PZT's to obtain good overlap of the retro beam with the incident beam.

An estimate for the required accuracy of the retro mirror angle adjustment is easily obtained. The retro mirror must reflect the beam so that the axis of the incident beam and the retro beam are within one beam radius at the focus position.

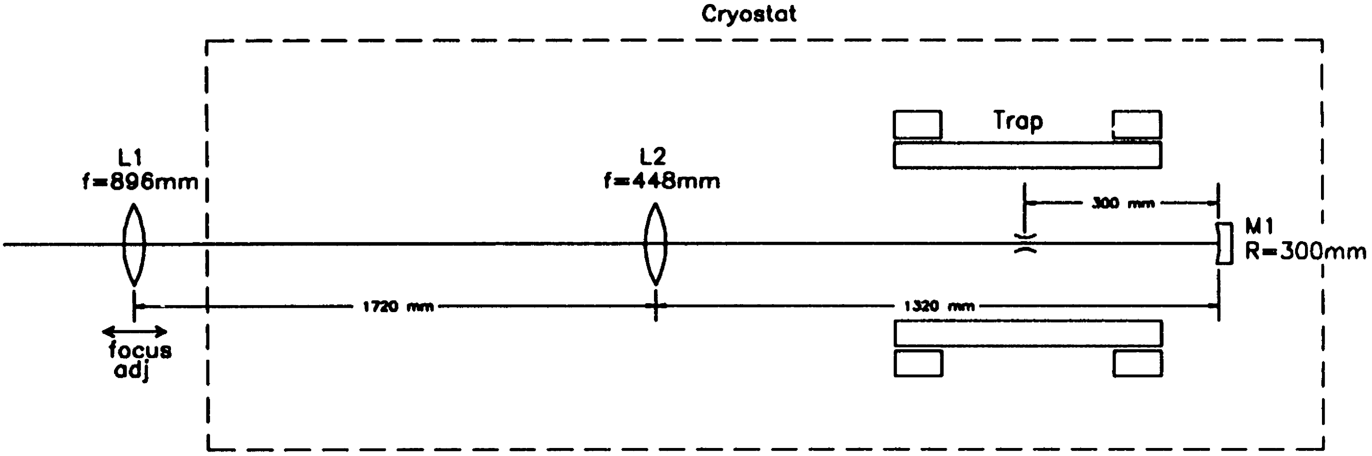

Figure 5-4: Optical system for trap. L1 is Dynasil 1100, L2 is Corning 7940. Both lenses have 2 layer LaF/MgF$_2$ antireflection coatings. M1 has a multilayer LaF/MgF$_2$ reflective coating.

The beam radius is 38 μm and is located a distance of 300 mm away from the retro mirror. This implies that the angle of incidence must be adjusted to within 60 μrad. The signal drops off rapidly for larger deviations due to the gaussian intensity profile of the beams.

The effect of improper alignment can be quantified by evaluating the transition rate as a function of the retro mirror angle. The transition rate is assumed to be proportional to $\int I_1 I_2 dV$, where I_1 and I_2 are the intensities of the incident and retro beams, and the integral is over the volume of the trap. This quantity has been evaluated numerically and expressed as a function of the displacement between the incident beam and the retro beam at the observation point outside the cryostat. The results of this calculation are shown in Figure 5-5. The observation point in this calculation was the location of the laser source (26 m from the cryostat). From Fig. 5-5 we see that a 1 mm displacement gives a factor of 2 reduction in signal size, while a 2.5 mm displacement gives an order of magnitude reduction.

Maintaining the retro mirror alignment is one of the more troublesome aspects of the operation of this apparatus. With a fixed mirror position and the active

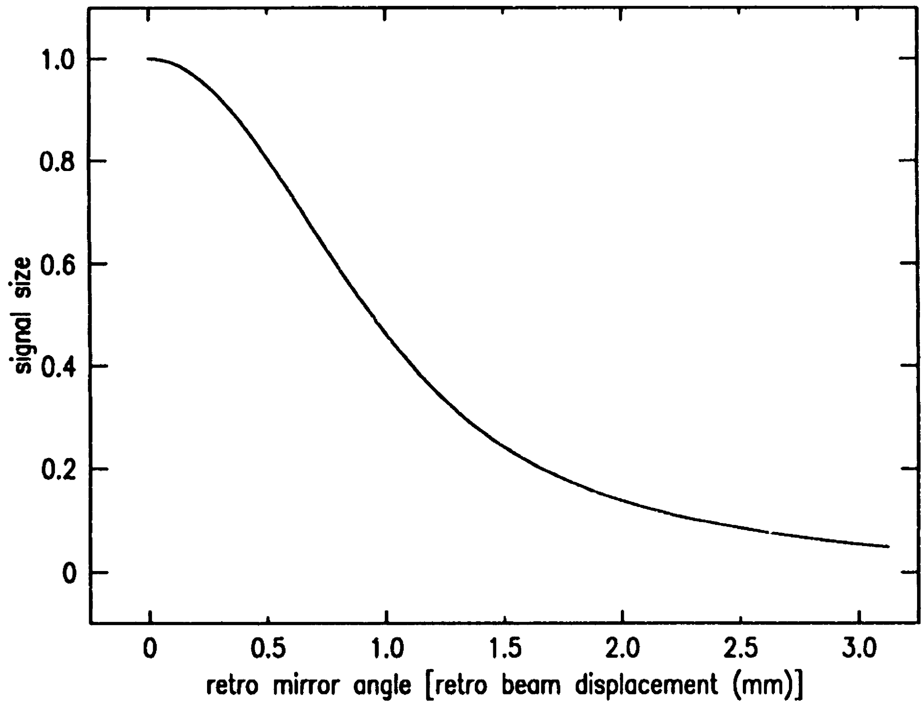

Figure 5-5: Normalized signal size versus retro mirror angle. The retro mirror angle is expressed as the displacement between the incident beam and the retro beam, as observed at the laser source (26 m from the cryostat).

beam pointing system operational, the retro beam position is observed to fluctuate randomly. The amplitude of this fluctuation is approximately 5 mm and its time scale is about 15 s. The mechanism(s) contributing to this fluctuation have not yet been studied. With continuous manual adjustment, the retro beam position can be kept to within an estimated 2 mm of perfect overlap with the incident beam. This introduces a possible reduction in the transition rate by nearly an order of magnitude and requires continuous attention. It would be desirable to improve this situation either by identifying and eliminating the source of the fluctuation, or by developing an additional active feedback system to maintain the retro mirror alignment.

Focus Adjustment

Focus adjustments to the system are made with the lens L1 in Fig. 5-4. L1 is mounted external to the cryostat and its position along the beam axis may be continuously varied by a translation stage. The translation of L1 is used to adjust the gaussian beam parameters of the incident beam in the trapping region. To a first approximation, translation of L1 moves the beam waist of the incident beam along the trap axis with only minor changes in the radius of the beam waist. The distance of the incident beam waist from the retro mirror will strongly effect the beam properties of the retro beam. For one position of L1 the incident and retro beam waist are at the same axial position and have the same radius. This is the desired operating point. Since the confocal parameter of the beams is a small fraction of the radius of the retro mirror, the operating point corresponds to an incident beam waist approximately one radius of curvature away from the retro mirror.

Initial adjustment of L1 is made during apparatus assembly. The position of the incident beam waist is monitored before the cell is attached to the apparatus. The position of L1 is varied until the beam waist is placed one radius of curvature away from the estimated location of the retro mirror. Final adjustment is made after the apparatus is completely assembled. The beam radius of the retro beam is monitored external to the cryostat as L1 is translated. The optimum position of L1 is obtained when the beam radius of the retro beam matches that of the incident beam at the point of observation.

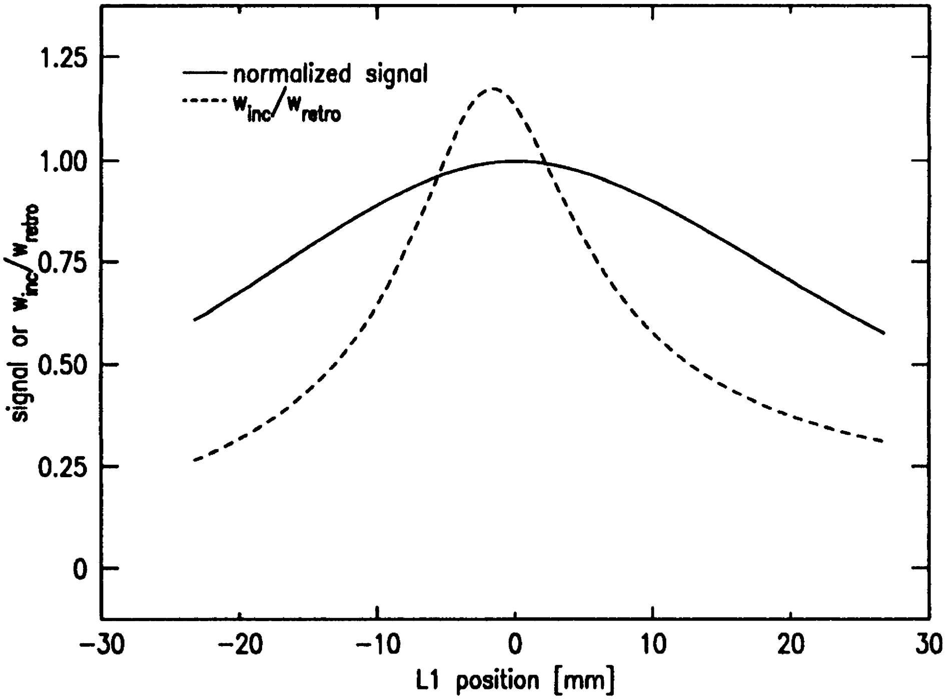

Figure 5-6: Normalized signal size versus focus adjustment. See text for explanation.

The signal dependence on the focus adjustment is not as critical as with the retro mirror adjustment. This dependence is shown in Fig. 5-6. The solid line shows the normalized signal size versus the position of lens L1. The dashed line shows the behavior of the beam radius of the retro beam as a function of the position of L1. The beam radius information is plotted as w_{inc}/w_{retro}, where w_{inc} is the beam radius of the incident beam, and w_{retro} is the retro beam radius. The observation point for the beam radius calculation is taken to be the position of the laser system.

It is a simple matter to adjust the L1 position so that $w_{inc}/w_{retro} > 0.5$. Under these conditions, the signal size is within 20% of its maximum value. Therefore, improper focus adjustment should not interfere with the first observation of a signal.

5.1.3 L_α Fluorescence Detection

The $1S$–$2S$ transition is to be detected by electric field induced L_α fluorescence. The physics of this process is discussed in Chapter 3. Here we discuss the aspects of the apparatus necessary to detect the emitted L_α photons.

The requirements on the cell construction were discussed in Sec. 5.1.1. The lower end of the cell contains a large diameter (38 mm) magnesium fluoride window to transmit the L_α photons out of the cell. The cell also contains field plates to permit the application of an electric field to the atoms to induce the fluorescence.

The L_α photons transmitted from the cell are detected by a microchannel plate detector[71] (MCP). The detector consists of two individual plates operated in the "chevron" configuration for higher overall gain. The plates have a 40 mm diameter active area and the upper surface of the upper plate has a cesium iodide coating as a photocathode. The spectral responsivity of the CsI photocathode provides a 10^6 greater sensitivity of the detector at L_α than at the 243 nm laser wavelength. The overall quantum efficiency for this detector at L_α is estimated to be 20%. The MCP is operated in the pulse counting mode.

An unconventional aspect of this use of the MCP is that it is operated at cryogenic temperatures. The primary effect of the low temperature operation is that the resistance of the MCP increases dramatically. This does not effect the operation of the plate at low counting rates, but the increased resistance limits rate at which charge can be supplied to the channels, reducing the gain of the plate for high counting rates. The MCP is attached to the 4 K vacuum can with a thermal resistance that allows heating of the plate above the 4 K ambient temperature of its surroundings. We have found that operation of the MCP at temperatures between 30 K and 40 K gave a reasonable compromise between maximum counting rate and excessive heating of other parts of the apparatus. Power dissipation in low temperature MCP biasing resistors heat the plate to approximately 30 K when the plate is biased with the 2 kV necessary for pulse counting operation. The blackbody radiation emitted from the MCP at these temperatures produced a noticeable level of heating at the bottom of the cell and a large level of heating on the cell bolometer. This effect was alleviated by enclosing the MCP in a brass chamber with a magnesium fluoride window (see Fig. 5-1). The window allows the L_α to pass, but blocks the very long wavelength blackbody radiation.

The dark count of the MCP was strongly dependent on the vacuum conditions of its environment. If helium exchange gas was used on the cooldown from 77 K to 4 K, then the MCP dark count level was extremely high, with a large number of very large pulses that indicated an ion feedback condition similar to that observed with room temperature MCP's operated with high background gas pressures. This condition could be cured by heating the MCP to 100 K for a period of a few minutes with the rest of the apparatus at 4 K. A further reduction of the dark count was observed after the dilution refrigerator was started and the temperature of the cell was reduced to below 100 mK. It seems probable that this is due to the pumping action of the cold cell surfaces on any remaining helium background gas. The final dark count rates observed were dependent on the operating temperature of the plates. At a MCP temperature of 36 K, the dark count was 20 s^{-1}, while at 63 K it was 60 s^{-1}.

The overall detection efficiency of this system is determined by the solid angle for fluorescence collection, the transmission of the magnesium fluoride windows, and the quantum efficiency of the detector. The limiting aperture for the fluorescence collection is the opening at the bottom of the cell. The solid angle is further reduced by apparatus neccessary for management of the 243 nm laser beam. This apparatus includes the retro mirror assembly and the lower Brewster window assembly. The overall fractional solid angle, $(d\Omega/4\pi)$, for fluorescence collection is 4×10^{-4}. The fluorescence must also pass through two magnesium fluoride windows, one at the bottom of the cell and one that provides blackbody shielding for the MCP. The transmission of these windows has been measured to be approximately 50% each, giving an overall transmission of 25%. The transmission of these windows has been measured before and after the operation of the apparatus and no evidence has been found for L_α absorption due to contamination. The resulting overall detection efficiency including these factors and the 20% quantum efficiency is approximately 2×10^{-5}.

Time Resolved L_α Detection

A technical challenge in this experiment is detecting the small L_α fluorescence emitted by the trapped hydrogen in the presence of scattered light from the 243 nm laser. We propose to use the metastability of the $2S$ state to temporally separate the excitation and fluorescence processes. The laser is turned on and excites the atoms for a time τ. The laser is then turned off and an electric field is applied to the sample, inducing L_α fluorescence. The counter that records the MCP output is gated off during the laser on period and gated on during the laser off period. A diagram of this sequence is shown in Fig. 5-7.

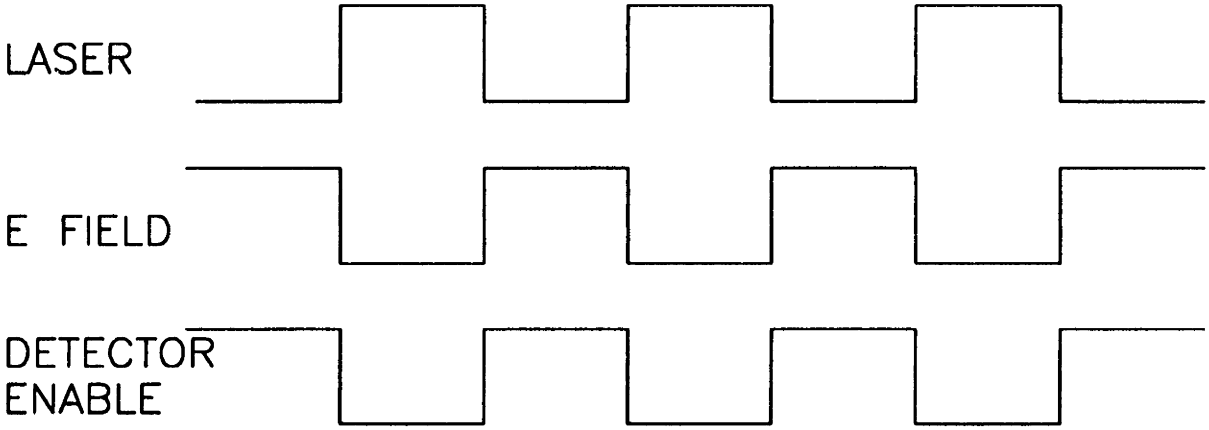

Figure 5-7: Timing for time resolved L_α detection.

The effect of this technique on the transition rate can be understood with the two-level model of the hydrogen atom introduced in Chap. 3. Consider an atom subject to a resonant monochromatic excitation pulse of length τ and Rabi frequency ω_R. The excitation probability for a single pulse is $\frac{1}{4}\omega_R^2\tau^2$. If these pulses are repeated at a rate F/τ (F is the duty cycle of the chopping), then the excitation probability per unit time is $R_{ex} = \frac{1}{4}F\omega_R^2\tau$. Coherence between the pulses is neglected because the application of the electric field induces a radiative decay and destroys any coherence between the ground and excited states. This rate can be compared to the excitation rate in the case of homogeneous broadening as discussed in Chap. 3, where $R_{ex} = \omega_R^2/\Delta\omega$. Thus, the effect of the chopping on the excitation rate can be modeled as a source of homogeneous linewidth $\Delta\omega_{chop} = 4/\tau$ (the reduction in excitation rate due to the duty cycle is considered separately).

The optimum choice for the chopping rate will occur for $\tau \approx 4/\Delta\omega_{eff}$, where $\Delta\omega_{eff}$ is the effective linewidth from all other sources. A shorter value for τ reduces the signal due to additional broadening. A longer value may be detrimental if $\Delta\omega_{eff}$ is due to a decay of the $2S$ state, since the atoms may decay before the laser pulse ends and the detector is enabled. For a time-of-flight broadened sample at $T = 100\ \mu$K, the optimum choice would correspond to $\tau \approx 80\ \mu$s.

Chopping of the laser was accomplished by chopping of the 486 nm light in an acousto-optic modulator before it was frequency doubled to produce 243 nm light (see Chap. 4 for a description of the laser system). This was done because we had no suitable modulator for direct modulation of the UV light. This approach limited the chopping rate and duty cycle. Chopping rates that were near the loop bandwidth (10 kHz) for the frequency doubling cavity servo system interfered with the servo operation. A chopping rate of 100 kHz with a 50% duty cycle ($\tau = 5\ \mu$s) was the best compromise between servo stability and optimum chopping rate.

5.1.4 Magnet Modifications

The effects of radiation trapping were discussed in Chapter 3. There we found that in high density ($n \geq 10^{13}$ cm^{-3}) samples there would be strong radiation trapping effects that could seriously attenuate the L_α fluorescence in the direction of the trap axis. This problem has been addressed with a modification to the trap magnet system which is described here.

The effect of the modifications to the trap magnet system are illustrated in Fig. 5-8. The axial field profile of the original magnet system of Ref. [9] has a fixed trap length of approximately 260 mm, which is longer than optimum from the point of view of radiation trapping (see the discussion in Chap. 3). A simple modification was made to the trap magnet system that provides a shorter axial field profile with a

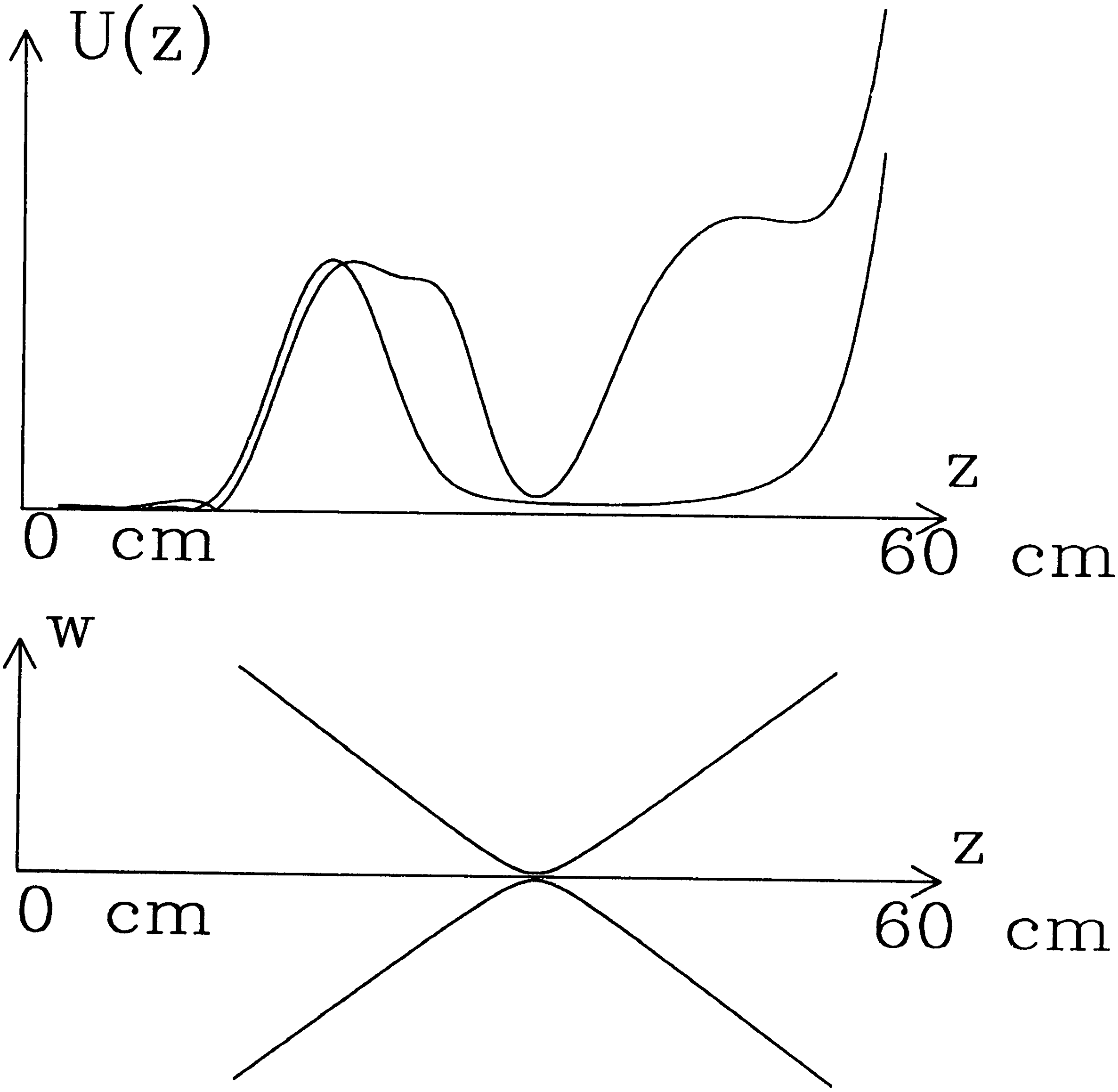

Figure 5-8: Magnet system modifications. The original magnet profile is shown with the new, shorter configuration in the upper figure. The lower figure illustrates the location of the beam focus.

trap length of 40 mm. Also illustrated in the diagram is the profile of the laser beam in the trapping region. In the new configuration, the sample length is approximately equal to twice the divergence length of the beam.

The reduced sample length is only important when one is attempting to observe the $1S-2S$ transition. The atoms can be loaded into the trap and evaporatively cooled to submillikelvin temperatures with the original trap configuration. Once the atoms are cooled, they may be compressed in the axial direction with relatively weak fields (approximately 10 mT for 700 μK atoms). This capability was added with additional coils on the bias solenoid of Ref. [9]. When fully energized, these coils provide an axially confining well 0.7 mK deep and 40 mm long. The center of the trap is chosen to coincide with the focus of the beam.

5.2 Experimental Observations

Initial attempts at observation of the $1S-2S$ transition with this apparatus have revealed the presence of an unexpectedly high level of absorption in the windows on the experimental cell. The absorption causes a heating of the windows, which leads to an evaporation of the superfluid helium film that coats the inner surface of the windows. Evaporating helium atoms enter the trapping region and collide with the trapped hydrogen atoms, removing them from the trap. This effect is discussed in more detail in Sec. 5.2.2. This absorption has thus far prevented the observation of the $1S-2S$ transition.

In Section 5.2.1 we describe our experimental efforts and observations. In Section 5.2.2 we discuss the consequences of the window absorption and our current knowledge about the mechanism responsible for it. Finally, in Section 5.2.3, we discuss improvements to the apparatus that should permit observation of the $1S-2S$ transition with the current levels of window absorption.

5.2.1 Experimental Efforts

There have been three experimental trials with the apparatus described in this thesis. The window absorption was observed in the first trial. Observation of the $1S-2S$ transition was attempted unsuccessfully in spite of the window absorption. Subsequent trials have centered on improving the absorption problem by using different configurations and materials for the cell windows. Unfortunately, the subsequent trials did not yield significant progress.

The observations presented here relate primarily to window absorption. We have two methods for characterizing optical losses in the trap apparatus. The first method is the measurement of the optical transmission of the system by determining the ratio of the powers in the incident and retro reflected beams. The accuracy of the transmission measurement with our apparatus is estimated to be 10% of the incident power level. The second method is a calorimetric measurement of the heating of the cell windows due to the laser beam. The accuracy of the calorimetric measurement is estimated to be 3% of the incident power level. The calorimetric method is a more direct measurement of the actual quantity of interest, but it can only be employed at the lowest operating temperatures of the apparatus where the thermal conductivities and heat capacities of the materials are small enough that small amounts of power deposition cause a measurable degree of heating. The transmission measurement is less direct, but it has the advantage that it may be employed at any temperature.

Trial 1

Antireflection coated optics were used in this run. The lower window was a VUV grade[72] magnesium fluoride, and the upper window was Z-cut crystalline quartz[73]. Both windows were coated with a two layer LaF/MgF_2 antireflection coating[56]. The "pump and flush" procedure described in Sec. 5.2.2 was used to minimize the potential for contamination of the windows.

Calorimetric measurements indicated an absorption level of 8% in the lower window. The upper window also displayed similar levels of absorption. The optical transmission of the system was not recorded due to an apparatus malfunction and loss of the transmission calibration. An attempt was made to observe the $1S-2S$ transition in spite of the window absorption. The details of this attempt are described later in this section.

Trial 2

The absorption in Trial 1 was originally suspected to be due to antireflection coatings on the window surfaces. Large absorption levels in ultraviolet dielectric coatings used in vacuum chambers had been reported previously[52] and it seemed probable that a similar mechanism was occuring here. The approach adopted on this hypothesis was the modification of the apparatus to accept windows mounted in the Brewster configuration. These modifications are described in Sec. 5.1.1. The window material used in the Brewster configuration was z-cut crystalline quartz[73]. The "pump and flush" technique was used to remove the air from the system.

The optical transmission of the system was measured as the system was cooled down. Transmission measurements were made at 300 K, 77 K, and 0.3 K. The transmission did not vary between 300 K and 77 K, but at 0.3 K it had dropped to 20% of its original value. Calorimetric measurements indicated that 60% of the laser power was deposited in the lower window, while 20% was deposited in the upper window. This absorption level was far too high for a reasonable attempt at observation of the $1S-2S$ transition. A leak was found in the apparatus as it was warmed up. However, it is not considered probable that air would have reached the surfaces of the cell windows.

Trial 3

Calcium fluoride windows were used in the Brewster configuration in this run. The material was Optopur[74] grade calcium fluoride, and the window surfaces were "super-polished"[56]. The "purging" technique described in Sec. 5.2.2 was used to remove the air from the system.

Roundtrip optical transmission measurements were made for this system at 300 K, 77 K, 4 K, and 0.3 K. The transmission did not vary between 300 K and 4 K, but a

$15 \pm 10\%$ decrease was observed between 4 K and 0.3 K. Calorimetric measurements indicated a single pass absorption level of 8% in the lower window, with similar levels of heating observed in the upper window. The transmission data suggests that this absorption occurred as the windows were cooled below 4 K, but sufficient accuracy was not available to make this a firm conclusion. The absorption levels observed in this run were similar to those observed in Trial 1.

Analysis of Trial 1

In this section we describe the attempt to observe the $1S-2S$ transition during Trial 1. We first describe the operating conditions and then estimate the signal size.

The laser power was limited to 0.5 mW average power due to the window absorption. This limitation is discussed in more detail in Sec. 5.2.2. The chopping rate for the time-resolved L_α detection scheme (see Sec. 5.1.3) was 100 kHz with a 50% duty cycle. These values were imposed by the apparatus used to chop the beam.

A hydrogen sample was prepared with a density of 7×10^{12} cm^{-3} and a temperature of 2 mK. This experiment was carried out before the detailed analysis of the radiation trapping effects in Chapter 3, and the modifications to the magnet system described earlier in this chapter had not yet been implemented. The full trap length of 260 mm was used with the focus of the laser placed 50 mm from the lower end of the sample. The effect of radiation trapping in this geometry will be calculated later. The temperature was significantly higher than the lowest temperatures achievable with the trap, but the higher than optimum chopping rate for the laser negated any advantage from working with colder atoms.

We can use the results of Chap. 3 to estimate the transition rate under these conditions. Following the discussion in Sec. 5.1.3, we model the effect of the chopping of the laser as an instrumental linewidth contribution, $\Delta\omega_{inst} = 4/\tau$. This allows us to use the results obtained in Chap. 3 to estimate the transition rate. Using Eq. 3.55 and inserting the numerical values from the above discussion, we find a total transition rate of

$$R_{TOTAL} = 3.6 \times 10^{7} \text{ s}^{-1}. \tag{5.1}$$

We now estimate the effect of radiation trapping on the detection of the emitted L_α photons. We extend the discussion of radiation trapping in Chap. 3 to account for the variation in excitation rate due to divergence of the beam. The L_α photons are emitted along the length of the beam according to the local $1S-2S$ excitation rate, which varies as $I^2(\vec{r})$. $I^2(\vec{r})$ varies as $1/w^2(z)$, where $w(z)$ is the radius of the beam at position z. We assume L_α photons emitted at position z experience an attenuation of $e^{-n\sigma(z-z_{min})}$, where z_{min} is the location of the lower edge of the sample. We define a transmission factor

$$S = \frac{\int_{z_{min}}^{z_{max}} dz \frac{1}{z^2+z_o^2} \exp(-n\sigma(z - z_{min}))}{\int_{z_{min}}^{z_{max}} dz \frac{1}{z^2+z_o^2}} \tag{5.2}$$

where the variation of $w^2(z)$ has been written as $z^2 + z_o^2$, where z_o is the divergence length of the beam. For our situation we find $S = 0.08$.

The total detection efficiency of L_α was estimated in Chap. 5 to be 2×10^{-5}. Including the effects of radiation trapping and collection efficiency, we find a predicted count rate, R, of

$$R = 55 \ \mathrm{s}^{-1}. \tag{5.3}$$

The laser was scanned over a range of 10 MHz (at the 486 nm laser frequency), centered around the expected location of the $1S-2S$ transition. This scan range was covered multiple times in a series of 1 MHz scans taken sequentially. The effective integration time for photon counting during these scans was 1 s. The detector dark count was approximately 100 s^{-1}, giving a 10 s^{-1} noise level in a 1 s integration time. This yields a predicted signal to noise ratio of 5 for these conditions.

The count rate estimated in Eq. 5.3 represents the ideal case. There are several factors that may reduce the count rate below this value. The uncertainty in the detection efficiency is estimated to be a factor of 2. Uncertainty in the absolute value for the laser power contributes an estimated factor of 2 uncertainty in the count rate. The most significant uncertainty is the adjustment of the retro mirror angle. As discussed in Sec. 5.1.2, this adjustment can only be maintained within a factor of 10 of its optimum value. Together, these factors contribute an uncertainty to the count rate that is larger than the expected signal to noise ratio.

The improvements in signal to noise ratio obtainable with longer integration times were not considered worthwhile in view of the large increases necessary to provide a favorable expected signal to noise ratio. Instead, effort was directed toward solving the window absorption problem that limited the laser power. These efforts are described in Sec. 5.2.2. Strategies for increasing the signal to noise ratio that are unrelated to the window absorption problem are discussed in Sec. 5.2.3.

5.2.2 Window Absorption

Our apparatus is very sensitive to absorption of laser power by the cell windows. At the low operating temperatures ($T < 0.3$ K) of the cell windows, the thermal conductivity and heat capacity of the window materials are several orders of magnitude lower than their room temperature values, and the deposition of even small amounts of heat leads to a significant temperature rise. We recall from Chap. 2 that the inner surface of the experimental cell is covered with a superfluid helium film that is necessary when loading the trap. If the surface temperature of the window rises to a point where helium has a significant vapor pressure, then the superfluid film will begin to evaporate. This evaporating helium will give rise to a flux of relatively high energy (on the order of 1 K) helium atoms through the trapping region. Collisions between the evaporated helium atoms and trapped hydrogen atoms will remove the hydrogen atoms from the trap. Excessive levels of window heating shorten the trap lifetime through this effect.

The primary consequence of window absorption is an upper limit to the laser power that can be used without an unacceptable reduction in the trap lifetime. A short trap lifetime is a serious obstacle to a careful search for a signal, since a significant time investment is needed to prepare a sample. This effect was characterized using the cell bolometer to measure the number of atoms remaining in the trap after the laser beam was admitted to the cell at a known power. In Trial 1 of Sec. 5.2.1, an average laser power of 0.5 mW reduced the trap lifetime to 30 s. This power was chosen as the best compromise between short trap lifetime at high laser powers and low excitation rates at low laser powers.

From the measured value for the trap lifetime we can estimate the mean flux of helium atoms passing through the trap region. The flux is given by

$$\Phi = \frac{1}{\sigma\tau} = 2 \times 10^{13} \quad \mathrm{cm^{-2}s^{-1}} \tag{5.4}$$

where a value of $\sigma = 20$ Å^2 [75] has been used for the hydrogen-helium scattering cross section. For a mean sample distance from the window of 30 cm, this gives a total evaporation rate of $R_{ev} \approx 1 \times 10^{17}$ s^{-1}. The value for the heat of vaporization for helium can be used to estimate an energy of evaporation per helium atom of 10 K. This value, multiplied by the evaporation rate, corresponds to 15 μW of power carried away by the evaporating helium atoms. This is to be compared with 75 μW of total power dissipated in the window by the laser.

A detailed thermal model of the window heating would require knowledge of where the laser power was being deposited (surface or bulk), the behavior of the thermal conductivity of the window material in the temperature range of 0.1 to several K, and an accurate model for the thermal anchoring of the window to its environment. Reliable data on these quantities is not easily obtained. However, crude models for the thermal gradients within the window easily account for a several Kelvin temperature rise in the case of a surface absorption mechanism. This is enough to account for the observed helium evaporation rate. A bulk absorption mechanism would yield a lower temperature rise, but can still account for these observations.

Absorption Mechanism

The mechanism for the absorption of the 243 nm radiation by the windows has not been positively identified. The observed loss levels are much higher than those observed with the same optics in more conventional applications. This application for the cell windows is unconventional in two respects: they are exposed to vacuum, and they are used at cryogenic temperatures. This opens two classes of potential absorption mechanisms. The first class is absorption due to migration of contaminants to the optical surfaces when the system is evacuated. The second class is an intrinsic material effect that occurs due to the low temperature.

There is conflicting evidence as to which class is responsible for the absorption. It is highly unlikely that losses due to contamination would display any temperature dependence below 77 K. This was unquestionably observed in Trial 2, and suggested by observations in Trial 3. The conclusion that an intrinsic effect is responsible is weakened by the presence of the leak noted in Sec. 5.2.1. Also, the possibility exists that an intrinsic effect exists for the crystalline quartz optics used in Trial 2, but not for the other optics.

The contamination hypothesis is favored by observations made with a separate apparatus constructed to perform calorimetric measurements of window absorption at 4 K. These measurements have yielded rather consistent absorption levels of 2-3%, independent of window material or window thickness. The vacuum environment of this apparatus contains considerably fewer potential sources of contamination than the trap apparatus, so the lower absorption level than observed in Trial 1 and 3 is reasonable. For an intrinsic effect to be consistent with these observations, it must occur at a temperature between 4 K and the operating temperature of the cell windows (≈ 0.3 K).

The possibility of window absorption due to contamination was anticipated because this effect had been reported previously[16]. We have taken reasonable precautions to minimize the possibility of losses due to this effect. The vacuum environment in our apparatus contains many potential sources of hydrocarbon contaminants, and would therefore seem prone to development of losses. However, during operation the apparatus is at cryogenic temperatures where all hydrocarbon species are immobile. One would not expect contamination in these conditions. Before the apparatus can be cooled down the vacuum spaces must be cleared of air that may otherwise freeze on the optical surfaces. To minimize the possibility of contamination during this procedure we have avoided evacuating the apparatus for extended periods of time while it is at room temperature. We have employed two different procedures to remove the air from the vacuum spaces. The first is a "pump and flush" technique where the system is partially evacuated (to ≈ 1 torr) and then immediately backfilled with dry nitrogen. This process is repeated several times and the air is cleared by successive dilutions. Care is taken not to expose the system to the laser beam during the procedure. The second technique is a "purging" technique where the air is diluted by a continuous flow of dry nitrogen. After employing one of these techniques the system is then cooled to 77 K. Once the system is at 77 K it is assumed that it may be evacuated and exposed to the laser beam without risk of contamination. If contamination is responsible for the absorption observed in Trials 1 and 3, then it would seem that these two techniques are comparable in their effectiveness.

5.2.3 Apparatus Improvements

Two strategies have been identified for progress if the window absorption cannot be reduced below its current level. The first strategy consists of modifying the laser system so that the 243 nm beam may chopped at the optimum rate and duty cycle. The second strategy is to remove the superfluid helium film from the experimental cell after the trap has been loaded. We discuss these strategies separately.

Chopping Rate and Duty Cycle

The limitations imposed on the rate and the duty cycle for the laser chopping could be removed by obtaining an acousto-optic modulator that would permit direct modulation of the 243 nm beam. This would allow optimum selection of the laser pulse length (80 μs instead of the current 5 μs), yielding an approximate factor of 16 increase in the transition rate. It would also allow operation at duty cycles much different than 50%. The quadratic dependence of $1S$–$2S$ transition on laser power (versus the linear dependence for the window heating) gives an incentive to work at high peak powers and low duty cycles.

The potential improvement from working at low duty cycles can be estimated as follows. We assume the transition rate is proportional to time average of the square of the laser power, $< P^2 >$. The window heating problem is assumed to limit the average laser power, independent of the duty cycle. If we consider a laser sequence of pulses of fixed length τ repeated with duty cycle F and a fixed average power, one can easily show that $< P^2 >$ is proportional to $1/F$. This proportionality holds until F is reduced to the point where the maximum available laser power is used in the pulse. In our case this should allow an order of magnitude increase in the transition rate.

An additional improvement in the signal to noise ratio may be realized if the noise is due to a dark count with a Poisson time distribution. If we assume that the signal fluorescence is collected in a time comparable to τ immediately after the laser pulse, then the signal counter can be gated off during the interval between the laser pulses if this interval is longer than τ. For low duty cycles, the total time that the signal counter is gated on varies as $1/F$. For a Poisson dark count distribution, this corresponds to a noise level that varies as $1/\sqrt{F}$. Thus, the combination of the increase in transition rate and the decrease in noise level give an overall dependence of $1/F^{3/2}$ for the signal to noise ratio.

Helium Film Removal

The superfluid helium film that covers the inner surface of the experimental cell is only necessary during the loading phase of trap operation. In the loading phase, the atoms experience collisions with the walls of the cell, and the helium film is necessary to provide a surface with a low binding energy. Otherwise, excessive surface adsorption on the cell walls would prevent trap loading. Once the atoms have been loaded into the trap, the helium film could, in principle, be removed. If the film were removed from the cell, the apparatus should not be as sensitive to heating of the cell windows. The negative effect of the window heating is that helium evaporates from the surface, not the temperature rise itself.

A relatively simple modification of the apparatus should permit removal of the helium film from the cell region on the time scale of minutes. A “film pump” device could be constructed and connected to the cell. A schematic illustration of such a device is illstrated in Fig. 5-9. The film would be removed by superfluid flow to a heated region where it evaporates and subsequently condenses on a cold surface that surrounds the heated region. The time constant for film depletion from the cell can be estimated from knowledge of the flow rate of superfluid films and the surface area of the cell region. These estimates are in the range of 15 s for our apparatus geometry, which is much shorter than a typical trap lifetime.

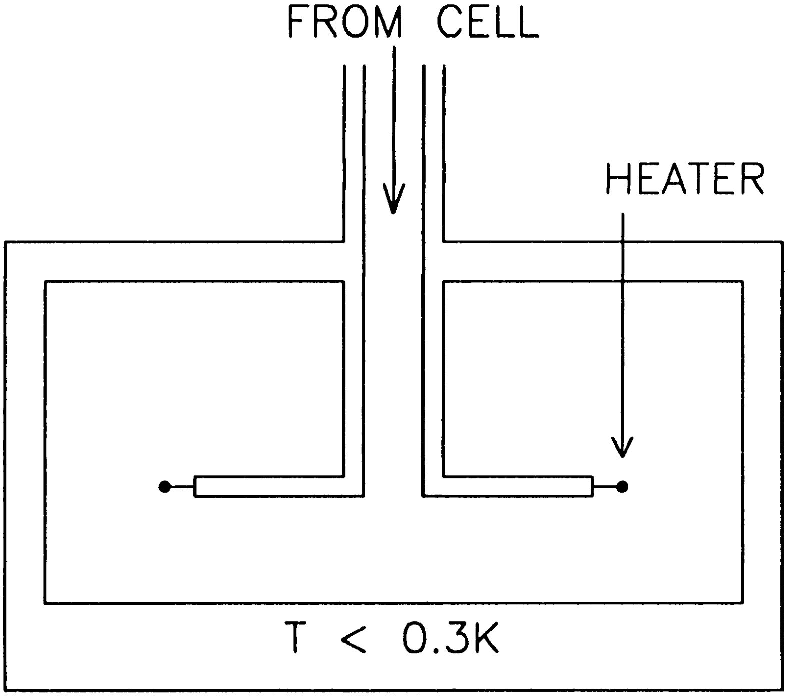

Figure 5-9: Schematic illustration of "film pump" device.

Chapter 6

Future Studies with Cold Hydrogen

In this chapter we discuss the possibilities for research made possible by laser spectroscopy of magnetically trapped hydrogen. Of primary interest is the use of a $1S$–$2S$ resonance signal as a probe for the temperature and density of a trapped hydrogen gas, and as a probe for detecting Bose condensation. Ultra-high resolution spectroscopy of atomic hydrogen is also of interest.

In Section 6.1 we calculate the anticipated properties of a $1S$–$2S$ resonance signal under our experimental conditions. In Section 6.2 we discuss the use of the $1S-2S$ signal as a probe for the temperature and density of a trapped hydrogen gas. In Section 6.3 we discuss the possibility of using trapped hydrogen as a medium for ultra-high resolution spectroscopy of the $1S-2S$ transition. We conclude in Section 6.4 with the introduction of a new approach to detecting Bose condensation with laser spectroscopy of the $1S-2S$ transition.

6.1 $1S-2S$ Transition Lineshape

The general properties of two-photon lineshapes in counterpropagating optical beams have been thoroughly discussed (see, for example, Ref. [76]). However, in the case of very cold hydrogen we expect to see some unique features in the lineshape. These features are introduced here for the first time.

The $1S-2S$ transition lineshape consists of two distinct components: a "Doppler-free" (DF) component, and a "Doppler-sensitive" (DS) component. The DF component is due to the absorption of one photon from each of the counterpropagating beams, while the DS component is due to the absorption of two photons from a single beam. A quantitative understanding of these features may be gained upon examination of the two-photon interaction Hamiltonian of Eq. 3.5:

$$\frac{V_{ab}(t)}{\hbar} = \left[\frac{ea_0}{2\hbar}\right]^2 e^{-2i\omega t} \sum_n \frac{\vec{d}_{an} \cdot [\vec{E}_1 + \vec{E}_2] \quad \vec{d}_{nb} \cdot [\vec{E}_1 + \vec{E}_2]}{\omega_{bn} + \omega} \tag{6.1}$$

where $\vec{E}_1(\vec{r}, t)$ and $\vec{E}_2(\vec{r}, t)$ are the driving fields for the two-photon interaction. They are assumed to be paraxial optical beams as defined in Eq. 3.2. Equation 6.1 can be written as

$$\frac{V_{ab}(t)}{\hbar} = V_{ab}^{11} + V_{ab}^{22} + (V_{ab}^{12} + V_{ab}^{21}) \tag{6.2}$$

where

$$V_{ab}^{ij}(t) = \left[\frac{ea_0}{2\hbar}\right]^2 e^{-2i\omega t} \sum_n \frac{\vec{d}_{an} \cdot \vec{E}_i \, \vec{d}_{an} \cdot \vec{E}_j}{\omega_{bn} + \omega}. \tag{6.3}$$

If we now consider the spatial variation of $\vec{E}_i$ and $\vec{E}_j$, we obtain

$$V_{ab}^{ij}(\vec{r}, t) = \left[\frac{ea_0}{2\hbar}\right]^2 e^{-2i\omega t} \sum_n \frac{\vec{d}_{an} \cdot \vec{\epsilon}_i \, \vec{d}_{an} \cdot \vec{\epsilon}_j}{\omega_{bn} + \omega} E_i E_j U_i(\vec{r}) U_j(\vec{r}) e^{i(\vec{k}_i + \vec{k}_j)\cdot\vec{r}}. \tag{6.4}$$

If $\vec{\epsilon}_1$ and $\vec{\epsilon}_2$ are collinear, then this can be simplified using the quantity D_{ab} defined in Eq. 3.9. We find

$$V_{ab}^{ij}(\vec{r}, t) = \tfrac{1}{2} D_{ab} \sqrt{I_i(\vec{r}) I_j(\vec{r})} e^{i(\vec{k}_i + \vec{k}_j)\cdot\vec{r}} e^{-2i\omega t} \tag{6.5}$$

where $I_i(\vec{r}) = \frac{1}{2}\epsilon_o E_i^2(t) |U_i(\vec{r})|^2$ is the intensity of the beam i. In writing this we have neglected the phase of the complex quantity $U_i(\vec{r})$. This will be justified later. If $\vec{E}_1$ and $\vec{E}_2$ are counterpropagating beams, then $\vec{k}_1 = -\vec{k}_2$. Equation 6.2 can then be written

$$\frac{V_{ab}(\vec{r},t)}{\hbar} = e^{-2i\omega t} D_{ab} \left[\tfrac{1}{2} I_1(\vec{r}) e^{2i\vec{k}_1\cdot\vec{r}} + \tfrac{1}{2} I_2(\vec{r}) e^{2i\vec{k}_2\cdot\vec{r}} + \sqrt{I_1(\vec{r}) I_2(\vec{r})}\, \right]. \tag{6.6}$$

The first two terms possess a $e^{2i\vec{k}\cdot\vec{r}}$ spatial dependence and are responsible for the Doppler-sensitive absorption. The final term has no spatial phase dependence and is free of the Doppler effect (to first order). The neglect of the phase of $U_i(\vec{r})$ can now be justified. For the DS terms, the phase variation of $U_i(\vec{r})$ is much weaker than $e^{2i\vec{k}\cdot\vec{r}}$ and can therefore be neglected. For the DF , term the overall envelope function is $U_1(\vec{r})U_2(\vec{r})$. In the case of ideal counterpropagating gaussian beams (which we consider here), $U_1(\vec{r}) = U_2^*(\vec{r})$, and the phase variation due to the envelope vanishes.

In considering transition rates due to the Hamiltonian of Eq. 6.6, it is possible to calculate the transition rates due to each of the three terms separately, then add them to find the overall transition rate. This is justified by the fact that the terms have such different behavior with respect to atomic motion. For a given frequency of the perturbation, the different terms in Eq. 6.6 will be resonant with separate velocity classes within the velocity distribution. In a normal gas only a negligible fraction of atoms near $v = 0$ would be resonant with all three terms.

Another manner in which the DS terms differ from the DF term is that of photon recoil. Net momentum is transferred to the atom in a DS absorption, while no net momentum is transferred in a DF absorption. Simple energy and momentum conservation considerations show that the apparent resonance frequency of an atom in DS absorption is shifted upward by an amount $\omega_{recoil} = 2\hbar k^2/M$ by this effect. DF absorption is not shifted by recoil effects. As will be seen later, the recoil shift has important consequences on the form of the lineshape. It also plays a key role in our technique for detecting Bose condensation.

6.1.1 Doppler-Free Transition Lineshape: Time-of-flight Broadened Case

In Chapter 3 we discussed the anticipated contributions to the Doppler-free $1S-2S$ linewidth. We found that, when the beams are tightly focussed to produce high transition rates, time-of-flight broadening is expected to dominate the linewidth, except under conditions where a trapped atom may maintain coherence through multiple passes through the beam. This case is of particular interest for using the $1S-2S$ signal as a probe of the sample. The high transition rates obtained with focussed beams give a high bandwidth probe of the sample. In this section we treat the lineshape for the Doppler-free $1S-2S$ transition in the time-of-flight broadened case. We shall assume the other sources of instrumental broadening (Stark shifts and laser linewidth) can be neglected.

The problem of time-of-flight broadening for Doppler-free two-photon transitions has been considered previously by Beausoleil[16] and Biraben, et al.[77]. Both treatments neglect the axial variation of the gaussian beam used to excite the transition. Our treatment will include the axial variation of the beam within the paraxial approximation.

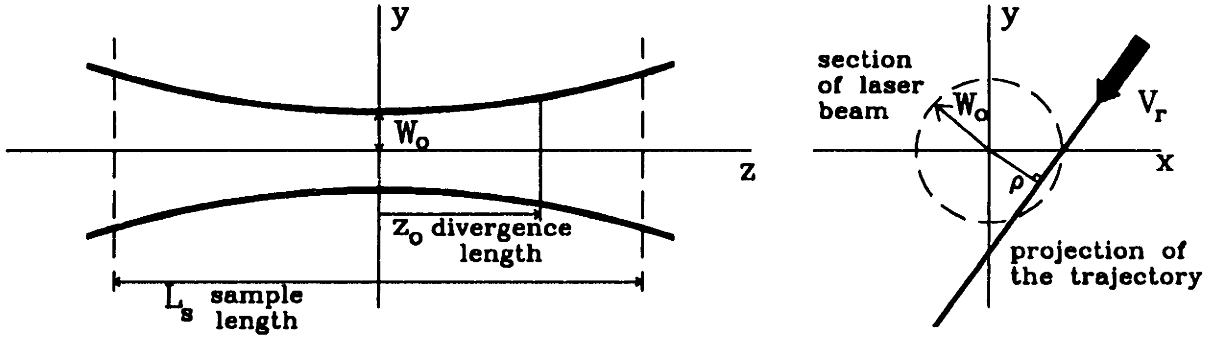

Figure 6-1: Interaction region and trajectories for time-of-flight broadening. After Ref. [77].

Consider the excitation region illustrated in Fig. 6-1. Counterpropagating TEM_{00}

beams are focussed into the trapping region. The two beams are derived from the same laser and are assumed to have the same intensity profile. The intensity profile is

$$I(x,y,z) = \frac{2P_l}{\pi w^2(z)}\exp\Big(\frac{-2(x^2+y^2)}{w^2(z)}\Big) \tag{6.7}$$

where $w(z)$ is the beam radius at axial position z, and P_l is the laser power. $w(z)$ is given by

$$w(z) = \sqrt{\frac{2}{kz_o}}\sqrt{z^2+z_o^2} \tag{6.8}$$

where z_o is the divergence length for the beam. We assume that the variation in the trapping potential can be neglected over the radial extent of the beam. This is justified in our situation due to the tight focussing of the beams. Under these conditions, the trajectories through the excitation region are the same as in a free gas.

We follow the treatment of Biraben et al.[77] and classify the atom trajectories by the magnitude of their velocities in the transverse plane, v_r, and their closest approach to the beam axis, ρ. The axial velocity does not enter into the problem as long as the axial variation of the beam can be neglected over one atom's trajectory. This will be true for nearly all trajectories as long as the beam satisfies the paraxial approximation. An atom passing though the intensity profile of Eq. 6.7 with ρ and v_r at axial position z will experience a time varying intensity given by

$$I(\rho,v_r,z,t) = \frac{2P_l}{\pi w^2(z)}\exp\Big(-\frac{2\rho^2}{w^2(z)} - \frac{2(v_r t)^2}{w^2(z)}\Big). \tag{6.9}$$

We note that the time variation of this intensity impulse is gaussian for all trajectories. ρ defines the amplitude of the impulse and v_r defines its width.

We now use our two-level model for the hydrogen atom introduced in Chap. 3 to calculate the transition probability due to the intensity impulse of Eq. 6.9 From Eq. 6.6, the interaction Hamiltonian for the Doppler-free component is

$$\frac{V_{ab}(\vec{r},t)}{\hbar} = D_{ab}I(\vec{r},t)e^{-2i\omega t}. \tag{6.10}$$

Substituting Eq. 6.9 into Eq. 6.10, we find

$$\frac{V_{ab}(\rho, v_r, t, z)}{\hbar} = D_{ab}\frac{2P_l}{\pi w^2(z)}\exp\Big(-\frac{2\rho^2}{w^2(z)} - \frac{2(v_r t)^2}{w^2(z)}\Big)e^{-2i\omega t}. \tag{6.11}$$

A ground state atom subject to the time varying perturbation of Eq. 6.11 will be excited with probability

$$P_{ba}(\Omega, \rho, v_r, z) = \frac{1}{\hbar^2}\Big|\int_{-\infty}^{\infty} e^{i\omega_{ab}t}V_{ab}(\rho, v_r, z, t)dt\Big|^2 \tag{6.12}$$

where ω_{ab} is the resonance frequency of the atom, and $\Omega = 2\omega - \omega_{ab}$ is the angular frequency detuning of the laser. Eq. 6.12 is a perturbation expression valid only for $P_{ab} \ll 1$. This condition will be addressed later. Inserting Eq. 6.11 into Eq. 6.12, we can find the transition probability for a trajectory with ρ, v_r, and z. This yields

$$P_{ba}(\Omega, \rho, v_r, z) = \frac{2}{\pi}|D_{ab}|^2 P_l^2 \frac{1}{v_r^2 w^2(z)}\exp\Big(-\frac{4\rho^2}{w^2(z)} - \frac{w^2(z)\Omega^2}{4v_r^2}\Big). \tag{6.13}$$

The condition that $P_{ba} \ll 1$ for the validity of Eq. 6.12 can be expressed

$$v_r^2 \gg \frac{2}{\pi}|D_{ab}|^2\frac{P_l^2}{w^2(z)}. \tag{6.14}$$

Under typical experimental conditions, ($T = 100\ \mu$K, $P_l = 10$ mW, $w_o \geq 30\ \mu$m) this condition is satisified for greater than 99% of the atoms. We shall neglect the effect of atoms that do not satisfy Eq. 6.14.

The total number of excitations occurring per unit time, $R_{TOTAL}(\Omega)$, is found by integrating Eq. 6.13 over all trajectories, including a factor of v_r to give the rate at which the atoms enter the excitation region. Assuming the velocity distribution is isotropic, we can write[77]

$$R_{TOTAL}(\Omega) = 2\int_{z_{min}}^{z_{max}} dz\ n(z)\int_0^{\infty} d\rho \int_0^{\infty} v_r dv_r P_{ba}(\Omega, \rho, v_r, z) f(v_r) \tag{6.15}$$

where $f(v_r)$ is the transverse velocity distribution. The limits of the integral in the axial direction are defined by the extent of the atoms. We have also allowed for a possible variation in sample density in the axial direction through $n(z)$. The leading factor of 2 in Eq. 6.15 accounts for the two possible directions of v_r for each value of ρ. We now substitute Eq. 6.13 into Eq. 6.15 and perform the integration over ρ to obtain

$$R_{TOTAL}(\Omega) = \frac{1}{\sqrt{\pi}}|D_{ab}|^2 P_l^2 \int_{z_{min}}^{z_{max}} dz \frac{n(z)}{w(z)} \int_0^\infty v_r dv_r f(v_r) \exp\Big(-\frac{w^2(z)\Omega^2}{4v_r^2}\Big). \tag{6.16}$$

This expression is valid for any transverse velocity distribution $f(v_r)$ for which most atoms satisfy Eq. 6.14. Next we assume $f(v_r)$ to be a Maxwellian velocity distribution at temperature T, which is given by

$$f(v_r) = \frac{2v_r}{v_{ro}^2} \exp\Big(-\frac{v_r^2}{v_{ro}^2}\Big) \tag{6.17}$$

where $v_{ro} = \sqrt{2k_B T/M}$ is the rms transverse velocity. Then we can perform the integration over v_r in Eq. 6.16 to obtain our final result

$$R_{TOTAL}(\Omega) = |D_{ab}|^2 P_l^2 \frac{1}{v_{ro}} \int_{z_{min}}^{z_{max}} dz \frac{n(z)}{w(z)} \exp\Big(-\frac{w(z)|\Omega|}{v_{ro}}\Big). \tag{6.18}$$

We see that the overall lineshape is a composite of exponential lineshapes. This expression can be numerically integrated over the axial extent of the sample to obtain the overall lineshape.

If the extent of the sample is less than the divergence length of the beam, and has a uniform density, then we can write $w(z) \approx w_0$ and perform the final integration in Eq. 6.18 to obtain

$$R_{TOTAL}(\Omega) = n_o l_s |D_{ab}|^2 P_l^2 \frac{1}{w_0 v_{ro}} \exp\Big(-\frac{w_0|\Omega|}{v_{ro}}\Big). \tag{6.19}$$

This agrees with the result of Beausoleil[16]. The FWHM of this lineshape (expressed in Hertz) is given by

$$\Delta\nu = \frac{1}{\pi} \ln 2 \, \frac{v_{ro}}{w_0}. \tag{6.20}$$

6.1.2 Doppler-sensitive Transition Lineshape

The lineshape for Doppler-sensitive absorption is dominated by the first order Doppler broadening. Since the linewidth due to the Doppler broadening will be much larger than any other contribution, we can provide a more general treatment that makes no detailed assumptions about other sources of linewidth.

We first consider Doppler-sensitive absorption from a single beam with propagation vector $\vec{k}$. An atom moving with velocity v_z with respect to $\vec{k}$ will have a resonance frequency (in the laboratory frame)

$$\omega_a = \omega_{ab} + 2kv_z + \omega_{recoil} \tag{6.21}$$

where ω_{ab} is the $1S-2S$ frequency interval and $\omega_{recoil} = 2\hbar k^2/M$ is the recoil shift. We write the excitation rate for this atom (using Eq. 6.6) as

$$R_a(\Omega) = |D_{ab}|^2 \, \frac{\pi}{2} g(\Omega - 2kv_z - \omega_{recoil}) \, I^2 \tag{6.22}$$

where $g(\delta)$ is a normalized lineshape function ($\int g(\delta)d\delta = 1$). $g(\delta)$ describes the single atom lineshape due to an unspecified broadening mechanism. The total sample transition rate is found by integrating the single atom transition rate over the sample velocity and spatial distribution

$$R_{TOTAL}(\Omega) = \int dv_z \int d\vec{r}\, n(\vec{r}, v_z).\ R_a(\Omega - 2kv_z - \omega_{recoil}) \tag{6.23}$$

Next, we assume that the velocity distribution is spatially independent so that we can write $n(\vec{r}, v_z) = n(\vec{r})f(v_z)$. Then we can write

$$R_{TOTAL}(\Omega) = \frac{\pi}{2}|D_{ab}|^2 \int d\vec{r} n(\vec{r}) I^2(\vec{r}) \int dv_z f(v_z) g(\Omega - 2kv_z - \omega_{recoil}). \tag{6.24}$$

Strictly speaking, $g(\Omega - kv_z - \omega_{recoil})$ may also be a function of position as in the case of time-of-flight broadening in a strongly focussed beam. However, we will see later that this can be neglected. Assuming the radial extent of the sample is much greater than the beam, we can substitute Eq. 6.7 for $I(\vec{r})$ into Eq. 6.24 and perform the integral over r to obtain

$$R_{TOTAL}(\Omega) = \tfrac{1}{2}|D_{ab}|^2 P_l^2 \int dz \frac{n(z)}{w^2(z)} G(\Omega) \tag{6.25}$$

where

$$G(\Omega) = \int dv_z f(v_z) g(\Omega - 2kv_z - \omega_{recoil}). \tag{6.26}$$

$G(\Omega)$ is a convolution of the Maxwellian velocity distribution, $f(v_z)$, and the single atom lineshape, $g(\delta)$. For any experimentally realistic velocity distribution the width of the Doppler profile will be much larger than the width of $g(\delta)$. Then $g(\delta)$ can be replaced in the integral over v_z by a delta function with negligible error. Then we have

$$G(\Omega) = \frac{1}{2k} f\Big(\frac{\Omega - \omega_{recoil}}{2k}\Big). \tag{6.27}$$

If $f(v_z)$ is due to a Maxwellian velocity distribution at temperature T, then $G(\Omega)$ is given by the familiar Doppler profile

$$G(\Omega) = \sqrt{\frac{M}{8\pi k^2 k_B T}} \exp\Big(\frac{-M(\Omega - \omega_{recoil})^2}{8k_B T k^2}\Big). \tag{6.28}$$

We obtain a particularly simple expression for $R_{TOTAL}(\Omega)$ if we can assume the sample is unform in the axial direction. The integral over z in Eq. 6.25 can be performed to obtain

$$R_{TOTAL}(\Omega) = n_0 \frac{k}{4} |D_{ab}|^2 P_{laser}^2 \Big(\arctan(z_{max}/2z_o) - \arctan(z_{min}/2z_o)\Big) G(\Omega) \tag{6.29}$$

where n_0 is the sample density, and z_o is the divergence length of the beam. In a counterpropagating beam geometry the total Doppler-sensitive transition rate is a factor of 2 higher due to absorption from each of the two beams. Thus, the overall Doppler-sensitive transition rate is

$$R_{TOTAL}(\Omega) = n_0 \frac{k}{2} |D_{ab}|^2 P_{laser}^2 \Big(\arctan(z_{max}/2z_o) - \arctan(z_{min}/2z_o)\Big) G(\Omega). \tag{6.30}$$

6.1.3 Overall Lineshape

We can obtain the overall lineshape by summing the contributions from the Doppler-free component of Eq. 6.18 and the Doppler-sensitive component of Eq. 6.30. An example of this lineshape in our experimental conditions is shown in Fig. 6-2.

The Doppler-free and the Doppler-sensitive components give two distinct features. The DF component is centered on the unshifted $1S-2S$ transition frequency, with a linewidth determined by the time-of-flight broadening. The DS component has a linewidth determined by the first-order Doppler broadening, and its center is shifted by the recoil shift. We note that the recoil shift is comparable in magnitude to the Doppler width. This unusual experimental situation, as compared to more common two-photon lineshapes (see, for example, Demtröder[76]), is due to the combination of a light atom, an energetic transition, and the low temperature sample.

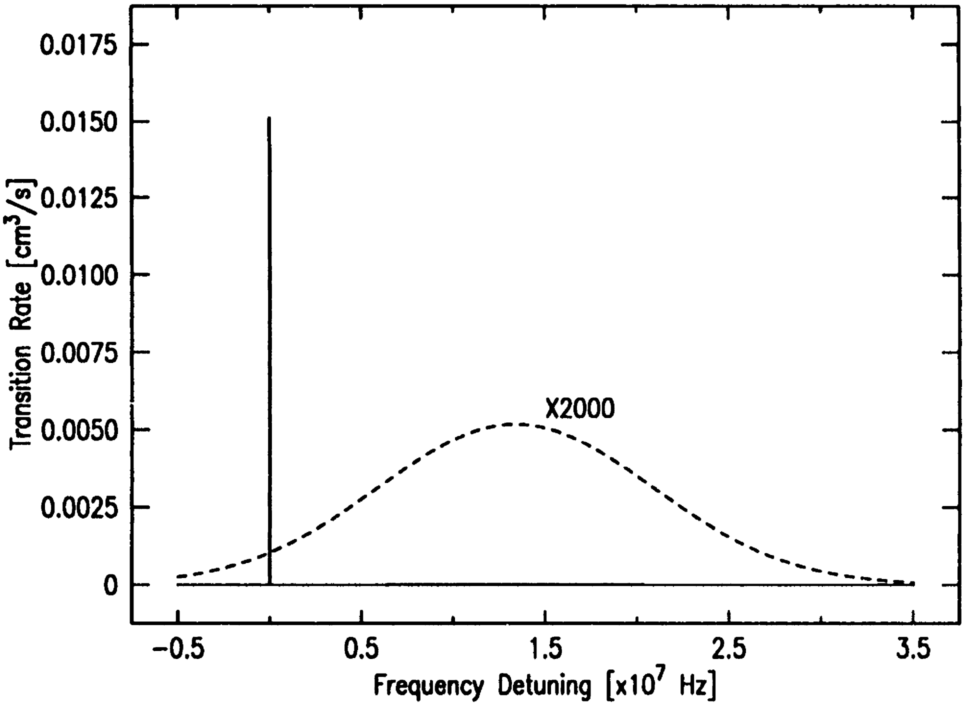

Figure 6-2: Example of predicted lineshape for $T = 100\ \mu$K, $w_0 = 38\ \mu$m, $l_s = 40\ mm$, and $P_{laser} = 10$ mW. The transition rate is is plotted in units of excitations per second at unit density (in cm^{-3}). The dashed line shows the Doppler-sensitive component magnified by a factor of 2000.

Examples of the Doppler-free lineshapes are shown in Figures 6-3 and 6-4. Figure 6-3 shows the lineshape in our experimental conditions (l_s = 40 mm, w_0 = 38 μm, T = 100 μK). To illustrate the effect of the beam divergence on the time-of-flight lineshape, the dashed line shows a normalized lineshape for a hypothetical sample length of 2 mm. In Figure 6-4 we show analogous lineshapes for w_0 = 114 μm. Here the divergence of the beam is small enough that the sample length does not significantly affect the lineshape over the range of experimental interest.

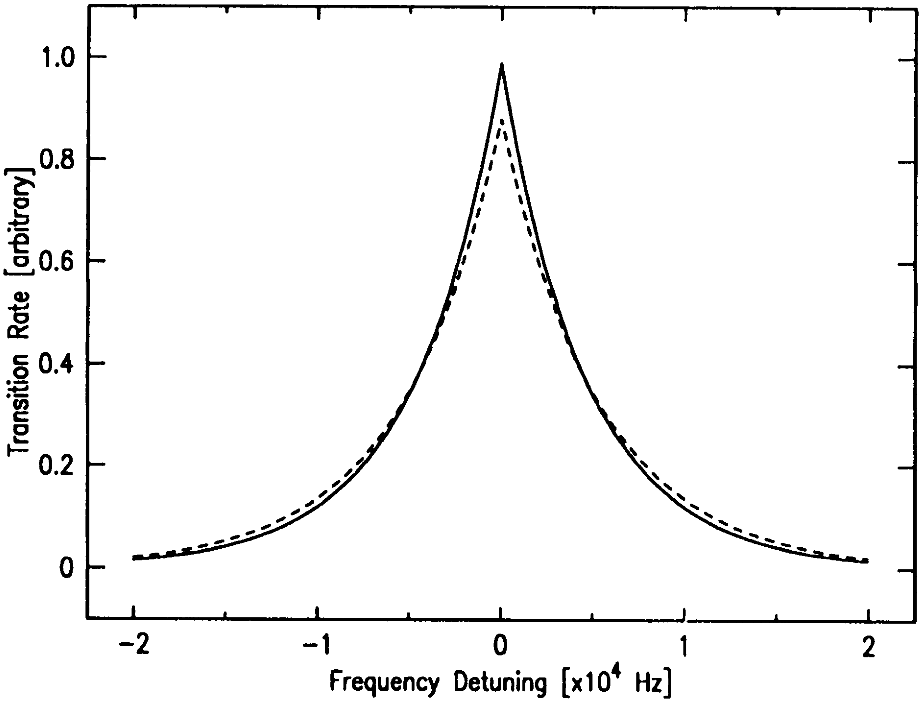

Figure 6-3: Examples of predicted time-of-flight broadened Doppler-free lineshapes for T = 100 μK, w_0 = 38 μm (divergence length z_o = 19 mm). The solid line is for an axially extended sample (l_s = 40 mm), the dashed line is for a sample restricted to the focus of the beam (l_s = 2 mm). The two lineshapes are normalized to have the same area for ease of comparison.

6.2 Temperature and Density Measurement

A major goal in the development of the laser based detection system is the ability to obtain information about the behavior of the sample. In particular, rapid mea-

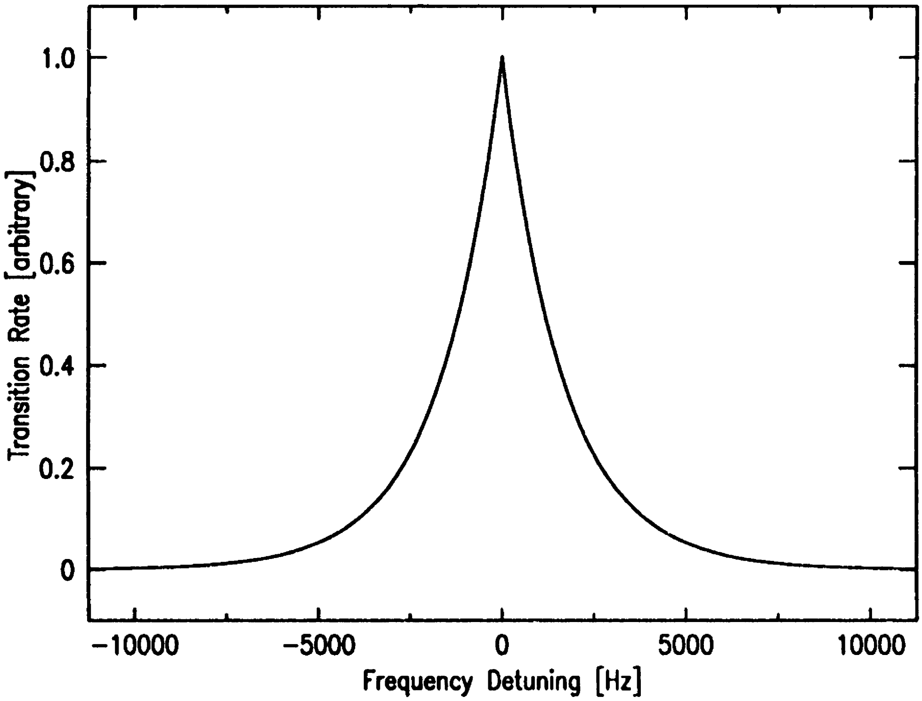

Figure 6-4: Examples of predicted time-of-flight broadened Doppler-free lineshapes for T = 100 μK, w_0 = 114 μm (divergence length z_o = 190 mm). Here there is no discernable difference between an extended sample (l_s = 40 mm) and a sample restricted to the focus of the beam ($l_s = 2$ mm).

surements of the sample density and the sample temperature are important. In this section we discuss possible strategies for extracting this information from the $1S-2S$ resonance signal. The discussion is qualitative since developing a comprehensive strategy before the first observation of the $1S-2S$ transition would be premature.

6.2.1 Spectral Measurements

Temperature Measurement

The finite temperature of the sample manifests itself in two direct ways in the $1S-2S$ transition lineshape. The Doppler-free (DF) lineshape is time-of-flight broadened and the Doppler-sensitive (DS) lineshape is first order Doppler broadened.

Measurement of the DS lineshape is perhaps the most direct way to find the sample temperature. It would also allow straightforward interpretation of non-Maxwellian distributions. It has one serious drawback, however. The Doppler broadening reduces the resonant transition rate by a factor of approximately 6000 compared to the DF lineshape in our experimental conditions, as shown in the previous section. This reduces the potential signal rate of this technique compared to a DF based technique by the same factor.

Measurement of the sample temperature through the DF lineshape appears more promising. If the instrumental sources of linewidth can be made negligible compared to the time-of-flight broadening, then the time-of-flight lineshape contains a complete description of the transverse velocity distribution. If the transverse velocity distribution is known to be Maxwellian, then a temperature can extracted by fitting the measured lineshapes to the lineshape of Eq. 6.18. If the functional form for the velocity distribution is unknown, then it may be obtained through deconvolution of Eq. 6.16.

In general, the use of the DF lineshape as a temperature measurement technique requires knowledge of the axial density profile of the sample. This is due to the fact that the divergence of the beam introduces an axially varying time-of-flight broadening. This can be accounted for in the analysis of the lineshape if the axial density profile is known. However, uncertainties in the trapping potential may be a serious practical limitation in carrying this out. This can be overcome by loosening the focus of the beam so that its divergence over the length of the trap is minimal. This reduces the intensity of the beam (which reduces the transtion rate), and reduces the linewidth (which places increased constraints on instrumental linewidth). However, the divergence length of the beam varies quadratically with the beam radius, so only a modest (estimated factor of 3) reduction in the transition rate is necessary to eliminate the sensitivity to the axial density profile.

If the instrumental linewidth due to Stark shifts or laser linewidth are unexpectedly large, then the experimental resolution may not be sufficient to resolve the time-of-flight lineshape. If this is the case, an alternative technique can be employed. If the beams that excite the transition are crossed at an angle in the trapping region, a "partial" Doppler effect is added to the DF lineshape. By varying the angle at which the beams cross, the amount of Doppler broadening may be controlled. This allows the experimenter to adjust the optimum amount of Doppler broadening to overcome the instrumental linewidth without the excessive amount of broadening (and transtion rate reduction) present in the DS lineshape. This approach has the disadvantage that it requires a significantly more complex optical system, and it is not clear how initial alignment of the crossed beam geometry could be accomplished given the limited experimental access to the cryostat. A final drawback is that crossing the beams reduces the volume over which they overlap, giving a reduction in signal.

Density Measurement

The transition rate observed on resonance is proportional to the integrated atom density along the beam. In the time-of-flight broadened case, the resonant transition rate is also temperature dependent, so a lineshape measurement is necessary if the sample temperature is unknown. In this case, the area under the resonance curve is proportional to the integrated sample density. The constant of proportionality could be determined by calibrating the detected count rate with the bolometric detection technique currently in use.

6.2.2 Spatial Measurements

Previous discussions have been based on the assumption that the laser beam is fixed with respect to the trapping potential. If the laser beam and trap are translated with respect to one another, measurements of the spatial distribution of the atom density within the trapping potential can be obtained. If the shape of the trapping potential is known, the temperature of the sample can be determined. Such measurements could be useful if none of the spectral measurements discussed above prove practical.

6.3 High Resolution Spectroscopy of Trapped Hydrogen

The interest in high resolution laser spectroscopy of the $1S-2S$ transition in atomic hydrogen was discussed in Chap. 1. The extremely narrow natural linewidth (1.3 Hz) of this transition makes it of interest for precision measurements and potential applications for future optical frequency standards. In this section we discuss the opportunities for high resolution laser spectroscopy with cold trapped hydrogen.

An important advantage of magnetically trapped hydrogen for high resolution spectroscopy is that the confinement of the atoms makes it possible to consider extremely long interaction times between the atoms and the radiation source. Submillikelvin atoms may be confined with modest magnetic field gradients to a region of space small enough that the natural linewidth of the $1S-2S$ transition may be saturated with currently available laser powers. The high densities achievable with a magnetic trap offer important signal to noise advantages over cooled beam or fountain[12] experiments.

In Chap. 3 we discussed the anticipated line broadening mechanisms with the $1S-2S$ transition in magnetically trapped hydrogen. It is interesting to consider what limitations these mechanisms place on the ultimate resolution achievable with this system.

The instrumental sources of linewidth identified in Chap. 3 can presumably be reduced to negligible levels with enough effort on the part of the experimentalist. The time-of-flight broadening can be eliminated by confining the atoms to within the laser beam. Laser linewidths on the Hertz level have been observed in the laboratory and should be achievable at the $1S-2S$ wavelength. Stark broadening can be reduced below the natural linewidth if stray electric fields can be kept below 20 mV/cm, an experimentally realistic goal.

We now discuss intrinsic sources of linewidth identified in Chap. 3. The AC Stark effect and the photoionization rate are intensity dependent and are comparable to the natural linewidth for the $1S-2S$ saturation intensity. They therefore pose no serious problem. The first order Doppler effect can be eliminated with careful control of the light field, and the second order Doppler effect is negligible at these temperatures. Collisional quenching of the $2S$ state is not well enough understood to make a reliable estimate of its contribution to the $1S-2S$ linewidth. We note, however, that it is not a truly intrinsic effect in that it can be made arbitrarily small by a reduction in density.

Zeeman broadening appears to be the ultimate limit to the resolution of the $1S$–$2S$ transition with magnetically trapped hydrogen. As discussed in Chap. 3, a relativistic correction to the electron magnetic moment introduces a small first order frequency shift of the $1S-2S$ transition frequency with magnetic field. Expressing this shift as an angular frequency, we find

$$\omega_B = \frac{\alpha^2 \mu_B}{4\hbar} B = 1.1 \times 10^6 \; B \;\; 1/\mathrm{Ts}. \tag{6.31}$$

We consider the effect of this perturbation on a gas of cold hydrogen confined in a three dimensional harmonic well. We write the potential as

$$U(\vec{r}) = \mu_B |\vec{B}(\vec{r})| = \tfrac{1}{2} m \omega_T^2 \, r^2. \tag{6.32}$$

Consider an atom in an orbit with energy kT and ellipticity ϵ. Its distance from the trap center will vary in time as

$$r(t) = \sqrt{\frac{kT}{m\omega_T^2}}(1 - \frac{2\epsilon}{(1+\epsilon^2)}\cos 2\omega_T t)^{-1/2}. \tag{6.33}$$

As the atom moves in the trap, its resonance frequency is shifted by the Zeeman shift of Eq. 6.31. The shift can be written as a function of the atom's position

$$\omega_B(\vec{r}) = \frac{\alpha^2\mu_B}{4\hbar}|\vec{B}(\vec{r})| = \frac{\alpha^2 m\omega_T^2}{8\hbar}r^2. \tag{6.34}$$

Using Eq. 6.33, we can write the Zeeman frequency shift as a function of time

$$\omega_B(t) = \omega_{B0}(1 - \frac{2\epsilon}{(1+\epsilon^2)}\cos 2\omega_T t) \tag{6.35}$$

where ω_{B0} is given by

$$\omega_{B0} = \frac{\alpha^2 kT}{8\hbar} = 9.0 \times 10^5\, T \;\; 1/\mathrm{Ks}. \tag{6.36}$$

The Zeeman shift is a periodic modulation of the atom's resonance frequency. The effect of this modulation on the absorption spectrum of the atom depends on the relative sizes of ω_T, ω_{B0}, and γ_s, the natural linewidth. The relationship between these is completely specified by an atom energy, kT, a confinement radius, r_o, and the natural linewidth. Consider the two ratios:

$$\frac{\omega_T}{\omega_{B0}} = \frac{8\sqrt{2}\hbar}{\alpha^2 r_o\sqrt{mkT}} = 3.7 \times 10^{-5}\,\frac{1}{r_o\sqrt{T}} \;\; \mathrm{mK}^{1/2} \tag{6.37}$$

$$\frac{\omega_{B0}}{\gamma_s} = \frac{\alpha^2 kT}{8\hbar\gamma_s} = 1.0 \times 10^5\, T \;\; \mathrm{K}. \tag{6.38}$$

For experimentally realistic values of $T = 100\ \mu$K and $r_o = 100\ \mu$m, these give

$$\frac{\omega_T}{\omega_{B0}} = 146 \tag{6.39}$$

$$\frac{\omega_{B0}}{\gamma_s} = 10 \tag{6.40}$$

We see that, under these conditions, $\omega_T \gg \omega_{B0} \gg \gamma_s$. Physically, this regime corresponds to an atom being coherently driven over many trap oscillation periods. As it oscillates, its resonance frequency is modulated at frequency $2\omega_T$ with a (small) modulation index given by

$$n = \frac{\epsilon}{(1+\epsilon^2)} \frac{\omega_{B0}}{\omega_T} \ll 1. \tag{6.41}$$

The time average of the resonance frequency over many trap oscillations is shifted by an amount ω_{B0}. Since the modulation index is small for all ϵ, the absorption spectrum will be dominated by the "carrier" at frequency $\omega_o + \omega_{B0}$. Thus, an atom's absorption spectrum is determined only by the energy of its orbit, independent of its ellipticity.

From the above discussion we can easily infer the absorption spectrum for a thermal ensemble of atoms. If the collision time between atoms is long compared to the natural lifetime, then collisions may be negelected and atoms can be assumed to follow individual stable orbits as in the above discussion. The direct correspondence between the frequency shift and the energy for an individual atom allows us to express the absorption spectrum for the ensemble as a function of its energy distribution. The absorption of the ensemble at a detuning Ω from the zero field resonance frequency is given by

$$A(\Omega) \propto N_\Omega(\Omega) \tag{6.42}$$

where $N_\Omega(\Omega)$ is the number of atoms with average Zeeman resonance frequency shift, Ω. Expressing this in terms of the energy distribution, we have

$$A(\Omega) \propto N_E(8\hbar\Omega/\alpha^2) \tag{6.43}$$

where $N_E(E)$ is the energy distribution of the ensemble.

6.4 Detecting Bose Condensation: The Recoil Shift Technique

The dramatic progress achieved with magnetic trapping and evaporative cooling of hydrogen makes one optimistic that the conditions necessary for Bose-Einstein condensation will be reached soon. We describe here a promising new technique that should offer a sensitive and unambiguous method for the first observation of a Bose condensate.

In considering the first observation of BEC there is a need for considering detection techniques that are both sensitive and unambiguous. Sensitivity is a primary concern. In an inhomogeneous potential, condensate densities are typically much higher than the normal component densities. The high condensate densities will lead to increased decay rates through dipolar relaxation. It is quite possible that only very small condensate fractions may be achievable under these conditions.

It is also highly desirable that the technique be unambiguous. The best evidence for Bose condensation would be a direct observation of condensation in momentum or position space. Inference of condensation through the measurement of another physical variable would be less compelling.

Most previously suggested techniques for detecting BEC fail at one or both of these criteria. An example of this is the early suggestion[3] that BEC could be detected by a spatial condensation in an inhomogeneous potential. This technique should be unambiguous, but its sensitivity is limited. A very small condensate fraction would be obscured by the density profile due to the normal component. More recent suggestions[78] that BEC could be detected by an increase in the decay rate of a sample suffer from the same sensitivity problem and offer less convincing proof that BEC has been observed.

The Recoil Shift Technique

We propose here a new technique for detecting BEC using the $1S-2S$ transition in atomic hydrogen, which we call the recoil shift technique. The technique is based on the observation of the zero momentum condensate in the Doppler-sensitive component of the $1S-2S$ transition.

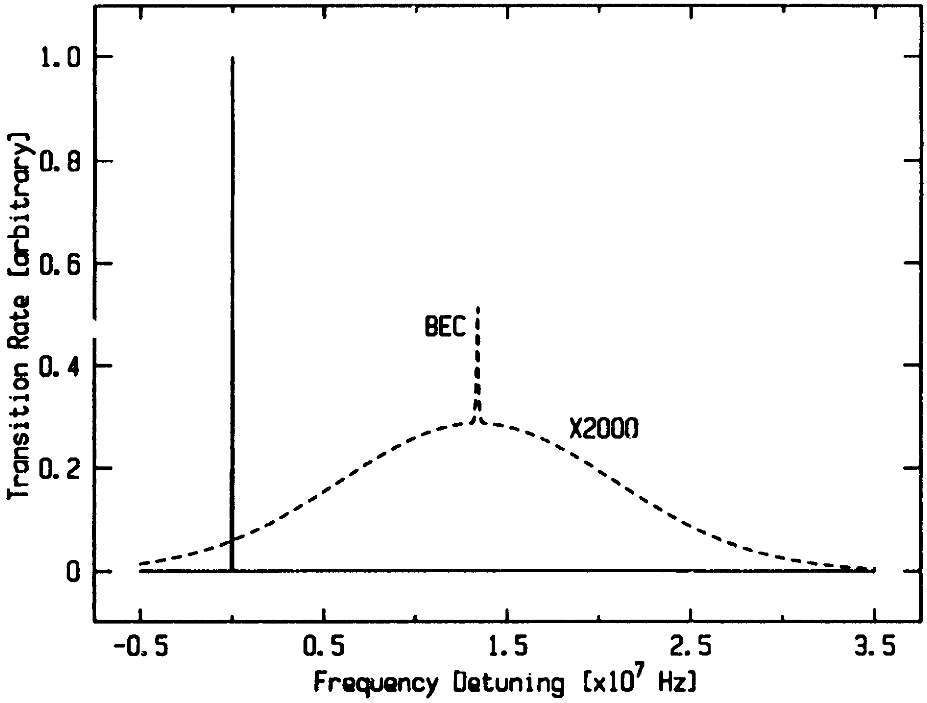

Figure 6-5: Hypothetical $1S-2S$ transition lineshape with a Bose condensate.

An example of how a Bose condensate should effect the $1S$–$2S$ transition lineshape is illustrated in Figure 6-5. Since the condensate occupies a zero momentum state, its transition lineshape due to the Doppler-sensitive terms of the two-photon Hamiltonian is not broadened by the Doppler effect. However, the energy and momentum conservation conditions that give rise to the recoil shift still apply to excitation of atoms out of the condensate. One would therefore expect the condensate to give rise to a narrow spectral feature at the center of the Doppler-sensitive lineshape. The condensate feature is easily distinguished from the Doppler-free absorption of the normal component since it is displaced by the recoil shift.

The potential sensitivity of this technique is exceptionally high. The momentum space condensation of the condensate results in a spectral concentration of its Doppler-sensitive lineshape. This spectral concentration provides a strong enhancement of the resonant transition rate for the condensate over the Doppler-broadened normal component. Because of the extremely high resolution of the $1S-2S$ transition, the enhancement factor can be huge.

The minimum detectable mean condensate density (over the laser beam) in the presence of a normal component density, n, should be roughly

$$n_{BEC} \approx \frac{\Delta\nu_{DOPPLER}}{\Delta\nu_{BEC}}\, n \tag{6.44}$$

where $\Delta\nu_{BEC}$ is the linewidth for the condensate and $\Delta\nu_{DOPPLER}$ is the Doppler linewidth for the normal component. It is unclear what to expect for the linewidth of the condensate. It is possible that interactions between the condensate atoms could broaden the line significantly. Neglecting this possibility, in the near term the linewidth would be limited by instrumental sources, most likely on the kHz level. This gives a preferential sensitivity for the condensate on the order of 1000. If the natural linewidth of the $1S-2S$ transition is resolvable with a Bose condensate, this factor will approach 10^6.

The basic concept of this technique is the measurement of the momentum distribution through the Doppler broadening of a narrow transition. In this sense, it is not that novel. However, the use of a two-photon transition offers a significant advantage. The Doppler-free absorption from the normal component provides a frequency marker that can be used to identify the spectral region to be carefully searched for indications of BEC. Without this marker, the appropriate spectral region can only be identified by finely splitting the Doppler-broadened line of the normal component.

Appendix A

Publications by the Author

VOLUME 61, NUMBER 8 PHYSICAL REVIEW LETTERS 22 AUGUST 1988

Evaporative Cooling of Spin-Polarized Atomic Hydrogen

Naoto Masuhara, John M. Doyle, Jon C. Sandberg, Daniel Kleppner, and Thomas J. Greytak
Department of Physics and Center for Materials Science and Engineering, Massachusetts Institute of Technology, Cambridge, Massachusetts 02139

and

Harald F. Hess and Greg P. Kochanski
AT&T Bell Laboratories, Murray Hill, New Jersey 07974

(Received 1 June 1988)

A gas of hydrogen atoms, confined in a static magnetic trap, has been evaporatively cooled to temperatures of a few millikelvin. The initial trap configuration held the gas at 38 mK for as long as 5 h. Evaporative cooling reduced the temperature to 3.0 mK while maintaining the central density at 7.6×10^{12} cm^{-3}. These values were determined by measurement of the rate of electronic spin relaxation and are in agreement with model calculations. Further cooling to 1 mK (inferred from the model) has been achieved. Measurements were made of the efficiency of the evaporative cooling process.

PACS numbers: 32.80.Pj, 67.65.+z, 76.90.+d

In a recent experiment[1] we demonstrated that hydrogen atoms in the low-field-seeking hyperfine states, precooled by a dilution refrigerator, can be confined in a magnetic trap[2] and thermally decoupled from the walls. We report here experiments demonstrating that the trapped atoms can be evaporatively cooled[3,4] by lowering the trapping fields. The temperature of the trapped atoms has been reduced to 3.0 mK, and possibly as low as 1 mK. In our previous work we had to infer the temperature of the gas by comparing the behavior of the atoms in the trap with the results of a theoretical model. We have verified the predictions of this model by independently determining the temperature from the measured dipole-dipole electronic spin-relaxation rate. The demonstration of evaporative cooling marks a significant step toward the study of atomic hydrogen in the low-temperature quantum regime and has potential applications to ultra-high-resolution spectroscopy of hydrogen and to the study of low-temperature atom-surface collisions.

We will first describe the results for a trap with fixed magnetic fields in order to demonstrate our method for determining the temperature. We will then describe the evaporative cooling caused by lowering the trapping fields and conclude with a discussion of the cooling efficiency.

A detailed description of the apparatus is given in Ref. 1. Hydrogen atoms produced by a low-temperature rf discharge flow vertically down a magnetic field gradient into a magnetic trap. The trap employs a cylindrical quadrupole field to confine the atoms radially and two solenoid fields to confine them along the axis. The lower solenoid determines the trap depth, E_t. Below the trap, at the bottom of a 30-cm tube, is an atom detector that operates on the zero-field hyperfine resonance (1.4 GHz).

During the filling of the trap the atoms become electron polarized due to the field gradient between the source and trap; nuclear polarization develops in the trap due to spin-exchange collisions. The number of atoms loaded into the trap under fixed conditions is reproducible to within 5%. The confining fields may either be held constant at their original high values, or reduced to obtain evaporative cooling. After being held for a specified time, the atoms are dumped from the trap into the detector by turning off the lower solenoid.

In our experiments to date the only property of the gas that can be measured directly is the total number of atoms N in the trap at the time of the dump. For example, Fig. 1(a) shows N versus the holding time for each fill (similar to those reported earlier) in which the trapping fields are held constant. N decreases rapidly at first as hot atoms escape over the fixed barrier. Because each escaping atom removes an energy much greater than that of an average trapped atom, the gas cools rapidly. After about 200 s, atom loss due to evaporation slows considerably and loss due to electronic relaxation begins to dominate. Here dipole-dipole collisions[5] cause relaxation into hyperfine states which are expelled from the trap.

In order to understand the observed behavior quantitatively, we have developed a model of the gas in the trap. It allows us to predict the number, density, and temperature of the atoms in the trap at any time. Our model computes the energy and particle flow out of the trap resulting from evaporation, electronic relaxation, and field reduction. It continuously readjusts the temperature. An exact kinetic-theory calculation[3,6] is used to obtain the rate at which atoms in the trap are promoted, by collisions, into states above the threshold energy for escape, E_t. The distribution function for the trapped atoms is represented by a truncated Boltzmann distribution of

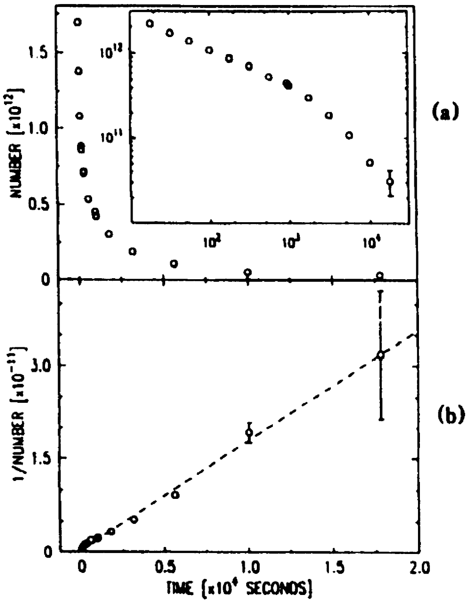

FIG. 1. Total number of atoms N in a 475-mK-deep trap. (a) N vs time (inset: same data, log-log plot). (b) N^{-1} vs time; the dashed line corresponds to a temperature of 38 mK.

temperature T and maximum energy E_t. A separate, more extensive calculation[6] that does not fix the functional form of the distribution function indicates that the truncated Boltzmann approximation is valid when the mean energy of an atom in the trap is much less than E_t.

An important prediction of our model is that after an initial period of rapid decay the ratio of trap depth to temperature, $\eta \equiv E_t/kT$, quickly approaches a limiting value. This value depends only weakly on the relaxation rate or the parameters of the trap. In this regime the atom loss is due primarily to relaxation. The relaxation takes place preferentially in the high-density region of the cell where the potential energy is small. Consequently, an escaping atom carries away slightly less energy than the average energy of a trapped atom. This process, by itself, would cause the gas to warm.[7] The limiting value of η occurs when the heating due to relaxation balances the cooling due to evaporation. Only a small fraction of the atoms lost [about $1/(\eta-2)$] must evaporate over the barrier in order to maintain this balance. Our model predicts a limiting value $\eta = 12.9$ for the conditions during the decay shown in Fig. 1, where the trap is maintained at high field (as in our original experiments). Because $E_t/k = 475$ mK for this configuration, we expect the temperature to stabilize at 37 mK.

To confirm the validity of our model, we use the following independent method for determining the temperature. The loss of atoms due to relaxation alone can be treated analytically. The temperature, the total number of atoms in the trap N, and the number density on the axis n_0 are related by $N = n_0 V_{\rm eff}(T)$, where the effective volume is given by[8]

$$V_{\rm eff}(T) = V_0 \frac{(kT)^\delta}{E_w^2 E_t^{\delta-2}}. \tag{1}$$

V_0, δ, E_w, and E_t are parameters which describe geometrical properties of the trap. $V_0 = 77\ \mathrm{cm}^3$ is a characteristic volume. $\delta = 2.27$ is an exponent that describes which portion of the volume corresponds to a given value of the magnetic potential energy U: $dV \propto U^{\delta-1} dU$. ($\delta$ would be 2 for an infinite cylindrical quadrupole trap and 3 for a spherical quadrupole.) E_w is the difference in magnetic potential energy between the center of the trap and the wall. For the data shown in Fig. 1, the magnetic field at the wall is 0.752 T corresponding to $E_w/k = 505$ mK. It can be shown that the loss of atoms from the trap due to the dipole-dipole relaxation is described by

$$\dot{n}_0 = -\left(\tfrac{1}{2}\right)^\delta g_{\rm eff} n_0^2, \tag{2}$$

where $g_{\rm eff}$ is the dipole relaxation rate constant for a uniform density sample evaluated at the trap temperature and averaged over the magnetic fields involved.

Even in the regime where the chief atom-loss mechanism is dipole relaxation, a small amount of evaporation continues to occur. It can be shown[8] that the total loss rate exceeds that due to relaxation alone by a factor of about $(\eta-1)/(\eta-2)$. Thus the time derivative of N^{-1} takes on the following value which depends only on the temperature:

$$\frac{d}{dt} N^{-1} = \left(\frac{\eta-1}{\eta-2}\right)\left(\frac{1}{2}\right)^\delta \frac{g_{\rm eff}}{V_{\rm eff}(T)}. \tag{3}$$

This expression can be used to determine the temperature of the gas from the slope of a plot of N^{-1} vs t:

$$T = \frac{E_t}{2k}\left[\left(\frac{\eta-1}{\eta-2}\right)\left(\frac{E_w}{E_t}\right)^2 \frac{g_{\rm eff}}{V_0\, dN^{-1}/dt}\right]^{1/\delta}. \tag{4}$$

In particular, if the temperature is constant, the slope of N^{-1} vs t will also be constant. In principle, our theoretical model for the detailed behavior of atoms in the trap enters Eq. (4) through the temperature dependence of $g_{\rm eff}$ and through the η-dependent correction factor. These effects are minor, however, typically 4% of the temperature.

Figure 1(b) shows the data from Fig. 1(a) replotted in this manner. After about 200 s, the slope achieves a constant value, $1.8\times10^{-15}\ \mathrm{s}^{-1}$. This verifies our assertion that η approaches a limiting value. Using the value $g_{\rm eff} = 1.8\times10^{-15}\ \mathrm{s}^{-1}\ \mathrm{cm}^3$ obtained from the calculations of Lagendijk, Silvera, and Verhaar,[5] together with the measured slope, gives an asymptotic temperature of 38 mK. This is in good agreement with the prediction, 37 mK, given by the detailed model of the trap behavior de-

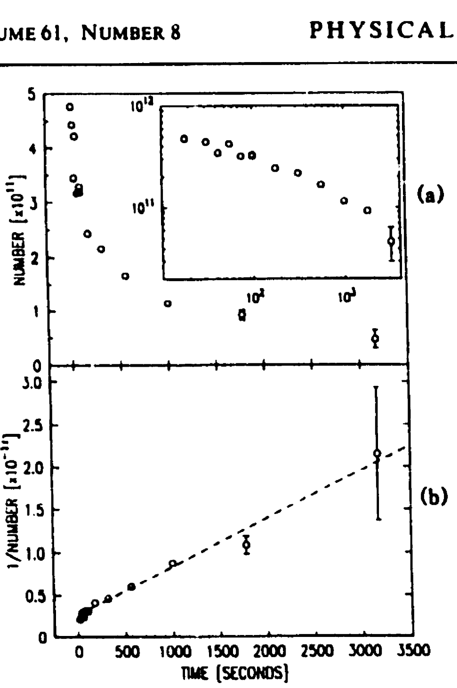

FIG. 2. Total number of atoms N in a 50-mK-deep trap. (a) N vs time (inset: same data, log-log plot). (b) N^{-1} vs time; the dashed line corresponds to a temperature of 3.0 mK.

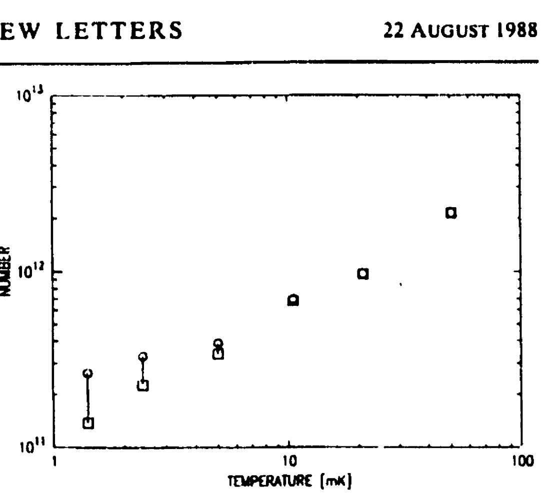

FIG. 3. Number of atoms remaining in the trap after evaporative cooling as a function of temperature. The points represent conditions in the trap just after the fields stop changing. The dotted line corresponds to $N \propto T^{1/1.75}$.

scribed above. The on-axis density follows from Eq. (1) and the measured value of N; it is time dependent and decreases from $n_0 = 4.9 \times 10^{12}$ cm^{-3} at 100 s to $n_0 = 1.4 \times 10^{11}$ cm^{-3} after a hold time of 5 h.

Fills designed to demonstrate evaporative cooling begin under the same conditions as those in Fig. 1. However, 20 s after the source discharge has ended, the threshold field for escape E_t is reduced exponentially by a factor of 9.5 to $E_t/k = 50$ mK, with a time constant of 40 s. In the field configuration we used, the threshold field—the saddle point in the potential barrier over which the atoms escape—is located at the lower end of the trap. The escaping atoms spill into the large-volume, zero-field region of the apparatus.[1] The cooling of the gas accompanying the evaporation would normally increase the density of the trapped atoms due to the decrease in $V_{\rm eff}$ described by Eq. (1), thereby increasing the dipole-dipole decay rate. In order to keep the density roughly constant, we reduced the quadrupole field that provides the radial confinement simultaneously with the reduction of the threshold field. We lowered E_w/k exponentially with a time constant of 55 s to a final value of 88 mK.

After the fields have achieved their final constant values, the decay of the density is measured as before: see Fig. 2. Again the initial period of rapid decay due to continuing evaporation is followed by a region of slower decay dominated by dipole-dipole relaxation. At these low magnetic fields and temperatures $g_{\rm eff}$ is assumed to take its value[5] at $B = 0$, $T = 0$: $g_{\rm eff} = 1.0 \times 10^{-15}$. Using this value and the trap parameters appropriate to Fig. 2, our model predicts $\eta = 12.1$, corresponding to a temperature of 4.0 mK. Figure 2(b) shows the plot of N^{-1} used to determine the final temperature in the trap. The solid line has a slope of 5.6×10^{-15} s^{-1}, corresponding to a temperature of 3.0 mK. At 100 s after the fields have stopped decreasing, $n_0 = 7.6 \times 10^{12}$ cm^{-3}.

The limiting factors in measuring the absolute value of the temperature through Eq. (4) are uncertainties associated with the determination of N and the accuracy of the theoretical value of g. The uncertainty in the filling factor of the hyperfine resonance detector scales all values of N by the same factor, known only to ±50%. Further temperature-dependent uncertainties in N (discussed below), and our ability to measure the slope of N^{-1}, limit the accuracy of our experimentally derived temperatures to ±30%.

A series of evaporations was done with identical time constants but different final trapping fields. The lowest final trap depth was 14 mK. Assuming that our model of cooling holds and the values of the trap parameters are still constant at these low fields, the gas temperature was about 1 mK. However, in this case the number of atoms remaining in the trap was insufficient to allow a direct experimental determination of the temperature.

Figure 3 shows the number of atoms remaining in the trap after evaporation as a function of temperature. The increasing uncertainty in the values of N at lower temperatures reflects ambiguities associated with the transport of atoms down the ^{3}He-coated tube between the trap and detector. If the time for atoms to bounce to the detector becomes long compared to the spin-relaxation time of the atoms on the cell wall,[1] the hyperfine resonance signal is reduced. The squares in Fig. 3 represent values of N based on the assumption that the transit time is negligible. The circles represent values assuming molecular flow with diffusive scattering at the walls and a sticking coefficient[9] of $0.33T$. The sticking coefficient determines how quickly the slow cold atoms speed up by being heated to the wall temperature.

The dotted curve in Fig. 3 represents a power-law behavior, $N \propto T^{1/\gamma}$, with $\gamma = 1.75$. With use of the formalism outlined in Ref. 3, $\gamma(T)$ can be calculated for the temperature range and experimental conditions pertaining to our trap. For the temperature range 3 to 30 mK we would predict $1.5 < \gamma < 1.8$, which is in good agreement with the measured value.

The evaporative cooling which we have demonstrated here should allow the production of hydrogen atoms with temperatures as low as 30 μK.[3] At present our limitations are not in the achievement of these conditions, but rather in the detection of the remaining atoms and the measurement of their temperature. We are currently developing optical methods for studying the atoms while they are still in the trap.

We have received a copy of unpublished work[10] by van Roijen *et al.* describing magnetic confinement of atomic hydrogen in thermal contact with the walls at temperatures down to 80 mK.

We thank Michael Balister of the National Radio Astronomy Observatory for the loan of a low-temperature microwave amplifier that allowed a substantial increase in the sensitivity of our detector. This research is supported by the National Science Foundation under Grant No. DMR-85-13769. One of us (J.C.S.) is supported by a National Science Foundation Graduate Fellowship.

---

[1] H. F. Hess, G. P. Kochanski, J. M. Doyle, N. Masuhara, D. Kleppner, and T. J. Greytak, Phys. Rev. Lett. 59, 672 (1987).

[2] D. E. Pritchard, Phys. Rev. Lett. 51, 1366 (1983).

[3] H. F. Hess, Phys. Rev. B 34, 3476 (1986). The equation for $\dot{Q}_{\rm rel}$ in this reference should read $\dot{Q}_{\rm rel} = \frac{1}{3}(3+C) \times k_B T(1-f)N$.

[4] T. J. Tommila, Europhys. Lett. 2, 789 (1986).

[5] A. Lagendijk, I. F. Silvera, and B. J. Verhaar, Phys. Rev. B 33, 626 (1986); H. T. C. Stoof, J. M. V. A. Koelman, and B. J. Verhaar, to be published. In computing g from these references, we have used the three processes $dd \rightarrow aa$, $dd \rightarrow ac$, and $dd \rightarrow ad$.

[6] G. P. Kochanski, Ph.D. thesis, Massachusetts Institute of Technology, 1987 (unpublished).

[7] We have also taken into account the small additional energy (about half the hyperfine energy) that may be deposited in the gas if a low-field-seeking product of the relaxation remains trapped.

[8] Details of the calculations will be presented in a subsequent, more extensive paper on these experiments.

[9] J. J. Berkhout, E. J. Wolters, R. van Roijen, and J. T. M. Walraven, Phys. Rev. Lett. 57, 2387 (1986).

[10] R. van Roijen, J. J. Berkhout, S. Jaakkola, and J. T. M. Walraven, preceding Letter [Phys. Rev. Lett. 61, 931 (1988)].

Reprinted from Journal of the Optical Society of America B

Energy distributions of trapped atomic hydrogen

J. M. Doyle, J. C. Sandberg, N. Masuhara, I. A. Yu, D. Kleppner, and T. J. Greytak

Department of Physics, Massachusetts Institute of Technology, Cambridge, Massachusetts 02139

Received April 7, 1989; accepted May 30, 1989

Progress on magnetic confinement and evaporative cooling of spin-polarized atomic hydrogen is described, and the first results are presented for the energy distribution of the trapped gas. Data are displayed for energy distributions during various stages of cooling. For the lowest temperature studied the results are in good agreement with the calculated distribution for a temperature of 800 μK.

INTRODUCTION

Because of its simplicity, atomic hydrogen is often the system of choice for research on physical phenomena in condensed-matter and atomic physics. Through the use of a magnetic trap, atomic hydrogen can now be cooled into new regimes for studying collisional phenomena and surface interactions and for high-resolution spectroscopy. Our method does not employ laser cooling but uses a dilution refrigerator to load an atomic-hydrogen sample into a magnetic trap. The temperature is then reduced by evaporative cooling. We review here some of the techniques and opportunities for spin-polarized atomic hydrogen. We also report results obtained with a new bolometric detection technique that make it possible to measure the energy distribution of the trapped atoms. The gas temperature can be determined directly from this energy distribution. The results reveal that a temperature has been achieved that is comparable with the recoil limit for Lyman-α laser cooling of hydrogen, $T = (h\nu)^2/2mc^2k \approx 650\ \mu\text{K}$.

Spin-polarized atomic hydrogen and deuterium occupy a unique position in the spectrum of atomic behavior at low temperature. They are the only atomic systems whose zero-point motion is extensive enough to overcome the attractive interatomic interactions, permitting them to remain gases at $T = 0$.[1,2] Early experiments demonstrated that under suitable conditions atomic hydrogen could be stabilized against recombination and maintained at densities of $10^{16}\ \text{cm}^{-3}$ or higher.[3-5] This was accomplished by introducing atomic hydrogen into a liquid-helium-coated vessel at a temperature of approximately 0.4 K in a magnetic field of 10 T. At such a low temperature and high magnetic field the gas is nearly 100% electron polarized. The electron polarization substantially inhibits recombination. Subsequent studies showed that the hydrogen confined in this manner can also develop a high nuclear polarization, further enhancing the stability of the gas.[6,7] Surface adsorption can catalyze the recombination of atoms into molecules, but the small binding energy of atomic hydrogen on liquid helium substantially reduces this effect at temperatures above 0.2 K.

The quantum nature of a cold gas is exhibited most dramatically when the thermal de Broglie wavelength $[\lambda = h/(2\pi mkT)^{1/2}]$ becomes comparable with the interparticle spacing $(n^{-1/3})$. Under these conditions Bose–Einstein condensation (BEC) should occur. Initial attempts to achieve BEC in hydrogen used compression of a cold gas to reduce the interparticle spacing.[8-10] Unfortunately, before the necessary density was achieved the gas became unstable owing to a three-body dipolar recombination mechanism. The highest density attained in this manner was $4.5 \times 10^{18}\ \text{cm}^{-3}$ at a temperature of 570 mK.[8] This is a factor of 50 too low to permit observation of BEC at this temperature. If one instead tries to maintain a constant density and increase λ by cooling the sample, the atoms adsorb on the surface. The surface density increases to the point where the sample becomes unstable owing to a high surface three-body recombination rate. Although there are some proposals[11,12] to get around these instability problems while still using helium-coated walls to contain the sample, attention has turned to wall-free trapping of the gas. We describe here the operation of the trap and a new type of atom detector. Initial results obtained with the detector are presented.

HYDROGEN TRAP

We use a wall-free confinement scheme for atomic hydrogen that was proposed by Hess.[13] The hydrogen atoms are confined in a static magnetic-field minimum by the interaction of the atom's magnetic moment with the field. Loading the trap requires a dilution refrigerator to cool the atoms to a temperature well below the typical trap depth of 1 K. This field configuration traps only the low-field-seeking states of hydrogen. These states are unstable and will ultimately decay by means of electron spin-flip transitions induced by dipolar interactions between the magnetic moments of the trapped atoms.[14] The spin-flipped atoms are quickly expelled from the trap. This two-body decay mechanism limits the lifetime of the sample to 1 sec at densities of $10^{15}\ \text{cm}^{-3}$. The lifetime is inversely proportional to the density; for lower densities the lifetime is sufficient to permit careful investigation of the sample.

For a wide range of initial conditions the temperature of the trapped gas quickly approaches a value determined solely by the geometry of the trapping fields. Dipolar relaxation takes place preferentially in the high-density region of the trap where the potential energy is small. Consequently, an escaping atom carries away slightly less energy than the average energy of a trapped atom. This process, by itself, would cause the gas to warm. However, there is a competing cooling mechanism. Elastic collisions between trapped at-

0740-3224/89/112244-05$02.00

oms continually generate atoms whose total energy is greater than the trap depth. These atoms escape, carrying more energy than the average energy of a trapped atom. The limiting value of temperature is determined almost completely by the trap depth and occurs when heating due to relaxation balances cooling due to evaporation. For typical experimental parameters this temperature corresponds to approximately one tenth of the trap depth.

The trapped atoms can be further cooled by forced evaporation.[13] This method consists of slowly lowering the trap depth, forcing the hottest atoms in the sample to leave. If the trap depth is much higher than the temperature of the sample, then the escaping atoms carry away many times the average energy per atom. Under these conditions a large amount of energy may be removed with the loss of relatively few atoms. Elastic collisions in the sample redistribute the remaining energy, lowering the temperature of the gas. This technique is efficient until the elastic collision rate becomes comparable with the decay rate, which for hydrogen corresponds to a limiting temperature of ~30 μK. The eventual goal of BEC may be attainable by this method.[13]

In our earlier research[15,16] the techniques described above allowed us to trap 5×10^{12} atoms at a density of 8×10^{12} cm^{-3} and a temperature of 38 mK. Samples were held in the trap for as long as 5 h. Evaporative cooling enabled us to achieve a temperature of 3 mK while maintaining the same density. This temperature was determined indirectly, using the measured dipolar decay rate of atoms from the trap in combination with the known decay constant.[17] The limitation to achieving lower temperatures in these experiments was inadequate sensitivity for detecting the remaining atoms. Other experiments with hydrogen in minimum B-field configurations have been reported by van Roijen *et al.*[18] They used a different geometry that made it possible to obtain initial densities as high as 3×10^{14} cm^{-3}. The dipolar decay mechanism becomes a serious problem at densities much higher than this. However, because of geometrical constraints, forced evaporative cooling was not possible in their apparatus. We believe that it should be possible to design an apparatus that can achieve these high densities while also allowing forced evaporative cooling.

APPARATUS

The apparatus is described in detail in Ref. 15, except for the bolometer, which is described below. The apparatus is illustrated in Figs. 1 and 2. Hydrogen atoms produced by a low-temperature rf discharge flow vertically down a magnetic-field gradient into a magnetic trap. The trap employs a cylindrical quadrupole field to confine the atoms radially and two solenoid fields to confine them along the axis.[13,19] The lower solenoid determines the trap depth. The atoms are detected by a zero-field hyperfine resonance (1.4-GHz) detector located below the trap. Just above the resonator is a bolometer that also serves as an atom detector. The walls of the cell are covered with a superfluid ^{4}He film.

During the filling stage of operation the atoms become electron polarized because of the field gradient between the source and the trap; nuclear polarization develops in the trap by spin-exchange collisions. The number of atoms loaded into the trap under fixed conditions is reproducible to within 5%. The confining fields may either be kept constant at their original high values or reduced to obtain evaporative cooling. After the atoms are held for a specified time they are dumped from the trap into the detector region by turning off the lower solenoid.

During the evaporative cooling process the currents of the cylindrical quadrupole and the axial solenoids are varied independently. To a large extent this permits independent control over the sample density and temperature. The trap depth, and hence the sample temperature, is determined by the solenoidal field, while the effective sample volume is determined principally by the strength of the cylindrical quadrupole field.

NEW DETECTOR

We recently developed a method of measuring the energy distribution of atoms in the trap through the use of a sensitive bolometer that measures the recombination energy of atoms as they emerge from the trap. Because of its fast response time and high sensitivity, the detector makes it possible to determine the temperature of the trapped hydrogen and to obtain a wealth of information about the nonequilibrium thermal processes taking place in the trap.

The bolometer is a 0.02 mm × 10 mm × 50 mm quartz plate suspended by nylon threads. The resistive element is a thin graphite film.[20] The bolometer temperature is maintained at a constant value through the use of a constant-temperature detector circuit.[21] Typically, the bolometer is maintained at a temperature of 280 mK through the application of 10 nW of resistive heating. This temperature is low

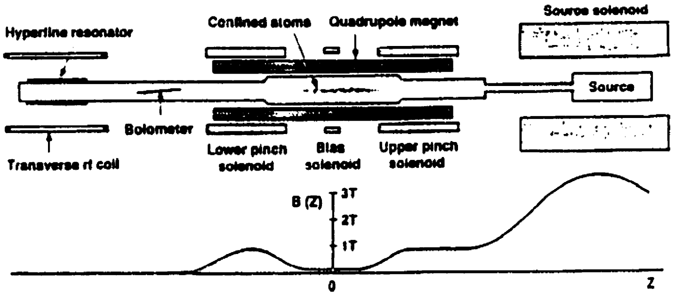

Fig. 1. Schematic of the apparatus. The magnitude of the on-axis magnetic field is indicated. The actual field profile is produced by the illustrated coils and 11 other coils that have been omitted from this diagram for clarity. The total length of the apparatus is 71 cm. The diameter of the trap region is 2.4 cm.

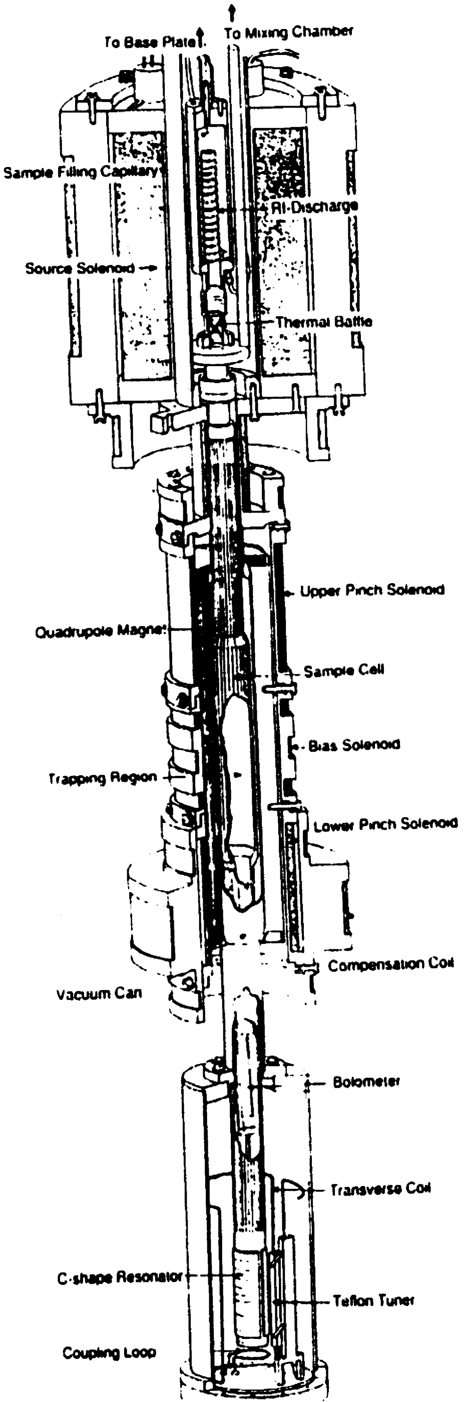

Fig. 2. Cutaway view of the apparatus. The detection region contains both a bolometer and a zero-field hyperfine resonator. The complexity of the magnet configuration is required for use of the hyperfine resonance detector.

enough to maintain a helium coating on the bolometer surface. The power deposited upon the bolometer from external sources can be determined from the current required to maintain a constant temperature. When the lower solenoid is turned off, the atoms flow out of the trap into the detection region. When the cell wall temperature is below 50 mK, the atoms quickly stick to the ^{4}He-coated walls and recombine. We determined that 4% ± 2% of the total recombination heat is deposited onto the bolometer by calibrating the bolometer signal against the hyperfine resonance signal. Thus the uncertainty in the absolute value of the total number of trapped atoms is ±50%. The bolometer signal is linear and reproducible to within 10%. The response time of the bolometer is less than 20 msec. The bolometer system has a noise power of 1 pW; with our shortest dump time of 0.5 sec, the minimum detectable signal is less than 10^8 trapped atoms.

ENERGY DISTRIBUTION OF THE TRAPPED ATOMS

We have been able to measure the energy distribution in the trap, $N(E)$, where $N(E)\mathrm{d}E$ is the number of atoms with energies between E and $E + \mathrm{d}E$. The field of the lower solenoid is reduced linearly to zero in 4 sec; atoms above the energy of the lower field barrier escape and recombine in less than 0.2 sec, a time much shorter than that of the trap dump. By simultaneously measuring the escaping atom flux and the corresponding barrier height as the trap is dumped, $N(E)$ is obtained. It was experimentally verified that the dump time is much shorter than the time scale associated with changes in $N(E)$. Comparisons with calculated distributions based on the field profile and an assumed temperature yield the measured temperature of the gas. The magnetic-field profile used in these calculations was numerically evaluated for all the current elements that influence the magnetic field in the trapping region. The calculated profile was then used in a numerical integration over the trap volume with a thermal density distribution to yield the cal-

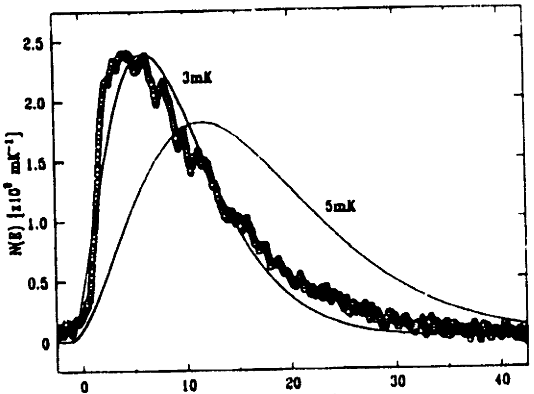

Fig. 3. Energy distribution of atoms in a 44-mK-deep trap. Solid curves are calculated distributions for gas temperatures of 3 and 5 mK. The wiggles in the data are believed to be caused by small irregularities in the trapping field. The total atom number and maximum density are, respectively, 3×10^{10} and 7×10^{11} cm^{-3}.

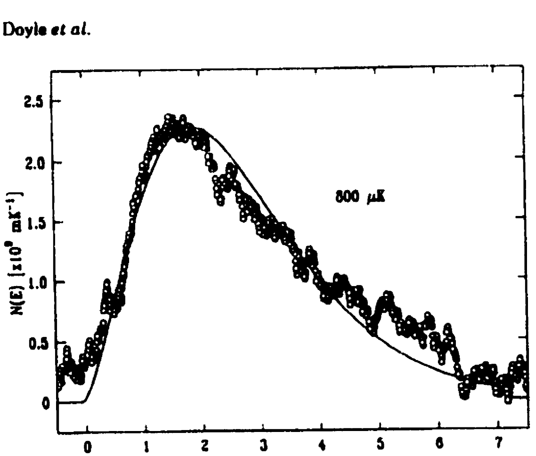

Fig. 4. Energy distribution of atoms in an 8-mK-deep trap. The solid curve is the calculated distribution for a gas temperature of 800 μK. The total atom number and maximum density are, respectively, 8×10^9 and 9×10^{10} cm^{-3}.

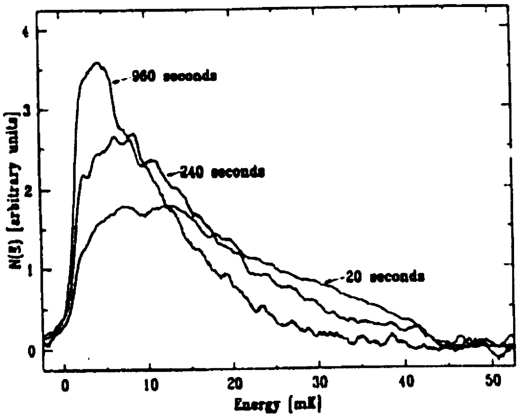

Fig 5. Energy distributions at various times after a rapid evaporation sequence. Data are normalized to a fixed atom number. There are three times as many atoms at 20 sec as at 960 sec.

culated $N(E)$. Figure 3 shows the distribution of atoms in a 44-mK deep trap. The calculated curve (solid curve) represents a gas temperature of 3.0 mK. This confirms earlier measurements[16] based on the decay dynamics, which gave 3 mK for similar trap parameters. Shown in Fig. 4 are the measured distribution of atoms in an 8-mK-deep trap and the calculated curve for a gas temperature of 800 μK.

The accuracy of the comparison between the calculated and measured distributions is limited mainly by the uncertainties in our magnetic-field profiles caused by persistent currents in the superconducting trap magnets. Estimates of the size of the effect limit the accuracy of the comparison to ~100 μK. If the sample number and temperature are known, one is able to obtain the spatial density distribution in the trap. The maximum of the density distribution is strongly dependent on the details of the trap field profile; uncertainties in our field profiles limit the accuracy of our values for the maximum density (given in the figure captions) to approximately a factor of 2.

Our method makes it possible to observe how atoms thermalize toward a steady-state temperature. A sample is loaded into a trap with depth 410 mK. The trap fields are then lowered to a trap depth of 44 mK at a rate too fast for the atoms to maintain a quasi-equilibrium state. In Fig. 5 the distributions of the atoms in the trap are shown for various holding times after the finish of the trap-lowering sequence. One can see that initially the atoms have not quite settled into the trap. As time progresses the atoms undergo elastic *s*-wave collisions, which thermalize the gas toward its final distribution. The *s*-wave collision time at the center of the trap is ~3 sec.

Our bolometric technique should also be sensitive to deuterium recombination. We attempted to trap deuterium in our present apparatus but were unable to demonstrate trapping. We believe that the high surface recombination rate[22] and high binding energy to the helium film inhibited transport of deuterium from the source region to the trap region. We are optimistic that these loading difficulties can be overcome with improvements to the source.

NEW OPPORTUNITIES

Among the research that can be pursued with cold hyodrgen is the study of the sticking probability of ultracold atoms on a well-defined surface such as liquid helium. This system is well suited for testing the prediction that the sticking probability will vanish as the incident atom energy goes to zero.[23,24] The sticking probability has been studied for temperatures to 80 mK.[25] Predictions are that the temperature dependence of the sticking probability at low temperatures is extremely sensitive to the form of the atom–surface interaction potential.[24]

We are currently developing a new technique for studying trapped hydrogen based on laser excitation of the 1*S*–2*S* two-photon transition. As a diagnostic method, this approach offers the possibility of studying the trapped gas with extremely high resolution both in real space and in momentum space. The transition will be excited by 243-nm light from a cw laser source. Normally such a transition is studied by Doppler-free spectroscopy, using counterpropagating beams. The spatial distribution of the atoms can be mapped by translating the beam; by using copropagating beams the momentum profile of the gas can be studied in great detail. To detect the excited atoms, a small electric field will be applied to mix the 2*S* and the 2*P* states, causing them to emit Lyman-α photons spontaneously that may be easily detected. We believe that this method is well suited to the search for BEC and for investigating ultracold atom–surface interactions. In addition, trapped hydrogen or deuterium is an ideal target for ultrahigh-resolution spectroscopy. It may be possible to achieve resolution of the 1*S*–2*S* transition of the order of the natural linewidth (≈2 Hz). Exploiting such a narrow linewidth will require a new generation of stabilized lasers, a challenge being investigated by other groups.[26]

CONCLUSION

We have cooled atomic hydrogen to temperatures comparable with the Lyman-α photon-recoil limit. The thermal distribution of atoms in the trap has been measured to temperatures of 800 ± 100 μK. Thermalization due to elastic *s*-

wave collisions has been observed. These measurements have been made possible by the development of a sensitive bolometric technique, which should be useful for deuterium as well. Atomic hydrogen can now be produced at temperatures and densities of interest for spectroscopy and atom-surface physics.

ACKNOWLEDGMENT

This research was supported by National Science Foundation grant DMR-8815555. That of J. C. Sandberg is supported by a National Science Foundation Graduate Fellowship.

The authors are also with the Center for Materials Science and Engineering, Massachusetts Institute of Technology.

REFERENCES AND NOTES

1. W. C. Stwalley and L. H. Nosanow, Phys. Rev. Lett. 36, 910 (1976).
2. R. M. Panoff and J. W. Clark, Phys. Rev. B 36, 5527 (1987).
3. I. F. Silvera and J. T. M. Walraven, Phys. Rev. Lett. 44, 164 (1980).
4. R. W. Cline, D. A. Smith, T. J. Greytak, and D. Kleppner, Phys. Rev. Lett. 45, 2117 (1980).
5. Reviews are given by T. J. Greytak and D. Kleppner, in *New Trends in Atomic Physics, Proceedings of the Les Houches Summer School, Session XXXVIII*, G. Greenberg and R. Stora, eds. (North-Holland, Amsterdam, 1984); I. F. Silvera and J. T. M. Walraven, in *Progress in Low Temperature Physics*, D. Brewer, Ed. (North-Holland, Amsterdam, 1986), Vol. 10, Chap. D.
6. R. W. Cline, T. J. Greytak, and D. Kleppner, Phys. Rev. Lett. 47, 1195 (1981).
7. B. W. Statt and A. J. Berlinsky, Phys. Rev. Lett. 45, 2105 (1980).
8. D. A. Bell, H. F. Hess, G. P. Kochanski, S. Buchman, L. Pollack, Y. M. Xiao, D. Kleppner, and T. J. Greytak, Phys. Rev. B 34, 7670 (1986).
9. R. Sprik, J. T. M. Walraven, and I. F. Silvera, Phys. Rev. B 32, 5668 (1985).
10. T. Tomila, S. Jaakkola, M. Krusius, I. Krylov, and E. Tjukanov, Phys. Rev. Lett. 56, 941 (1986).
11. Yu. Kagan and G. V. Shlyapnikov, Phys. Lett. A 130, 483 (1988).
12. I. F. Silvera, J. D. Gillaspy, and J. G. Brisson, in *Proceedings of Spin-Polarized Quantum Systems Conference, Torino, Italy, June 1988*, preprint (World Scientific, Singapore, to be published).
13. H. F. Hess, Phys. Rev. B 34, 3476 (1986). The equation for Q_{rel} in this reference should read as $Q_{rel} = \frac{1}{2}(3' + C)k_BT(1 - f)N$. Correspondingly, Eq. (4) should be

$$\gamma = \frac{2}{3}\left(\eta_{ev} + 2 - \frac{3}{2} - \frac{C}{2}\right)\gamma - \frac{1}{3}C \cdot$$

14. A. Lagendijk, I. F. Silvera, and B. J. Verhaar, Phys. Rev. B 33, 626 (1986).
15. H. F. Hess, G. P. Kochanski, J. M. Doyle, N. Masuhara, D. Kleppner, and T. J. Greytak, Phys. Rev. Lett. 59, 672 (1987).
16. N. Masuhara, J. M. Doyle, J. C. Sandberg, D. Kleppner, T. J. Greytak, H. F. Hess, and G. P. Kochanski, Phys. Rev. Lett. 61, 935 (1988).
17. H. T. C. Stoof, J. M. V. A. Koelman, and B. J. Verhar, Phys. Rev. B 38, 4688 (1988).
18. R. van Roijen, J. J. Berkhout, S. Jaakkola, and J. T. M. Walraven, Phys. Rev. Lett. 61, 931 (1988).
19. D. E. Pritchard, Phys. Rev. Lett. 51, 1366 (1983).
20. B. Dodson, T. Low, and J. Mochel, Rev. Sci. Instrum. 48, 290, (1977).
21. R. A. Sherlock, J. Phys. E 17, 386 (1984).
22. I. Shinkoda, M. W. Reynolds, R. W. Cline, and W. N. Hardy, Phys. Rev. Lett. 57, 1243 (1986).
23. D. S. Zimmerman and A. J. Berlinsky, Can. J. Phys. 61, 508 (1983).
24. V. V. Goldman, Phys. Rev. Lett. 56, 612 (1986).
25. J. J. Berkhout, E. J. Wolters, R. van Roijen, and J. T. M. Walraven, Phys. Rev. Lett. 57, 2387 (1986).
26. R. Kallenbach, C. Zimmerman, D. H. McIntyre, and T. W. Hänsch, Opt. Commun. 70, 56 (1989).

Hydrogen in the Submillikelvin Regime: Sticking Probability on Superfluid ^{4}He

John M. Doyle, Jon C. Sandberg, Ite A. Yu, Claudio L. Cesar, Daniel Kleppner, and Thomas J. Greytak
Department of Physics and Center for Materials Science and Engineering,
Massachusetts Institute of Technology, Cambridge, Massachusetts 02139
(Received 20 May 1991)

We have measured the sticking probability of atomic hydrogen on a superfluid ^{4}He surface for atom energies between 100 μK and 1 mK. The sticking probability shows little variation with energy over this interval, and is close to the value 0.2. The studies were carried out using a magnetic trap that produced a density of 8×10^{13} cm^{-3} at a temperature of 100 μK.

PACS numbers: 67.65.+z, 32.80.Pj, 68.10.Jy

Advances in laser [1] and evaporative [2] cooling have made it possible to experiment with matter in the gaseous state at temperatures in the μK regime. One of the new opportunities presented by these gases is the chance to study their interaction with cold surfaces. The probability that an atom is adsorbed in a surface collision—the sticking probability $s(E)$—depends on the atom-surface potential, the coupling between the atom and the surface excitations, the temperature of the surface, and the energy E of the atom. The regime of weak interactions and low energy is of particular interest. When the coupling is weak and the energy is sufficiently low [3,4], the sticking probability for a finite-range potential must vary as $E^{1/2}$. At higher energies, however, the sticking probability can be extremely sensitive to the atom-surface potential.

Atomic hydrogen incident on a superfluid ^{4}He surface is a particularly attractive system to study: The excitations of the surface—ripplons—are well understood and the atom-surface potential is so shallow that there is only one bound state for motion perpendicular to the surface. We have measured the sticking probability for atom energies between 100 μK and 1 mK, and have observed its qualitative behavior between 1 and 20 mK. An unexpected feature of the results is that we find that the values for $s(E)$ are contrary to the well established trend [5,6] at higher energies. Our data vary only slightly as E is changed over 2 order of magnitude, and we see no evidence of the expected $E^{1/2}$ low-energy behavior.

In these experiments hydrogen atoms are trapped and evaporatively cooled in an apparatus similar to one we have used previously [7], but which has been redesigned to achieve lower temperatures and higher densities [8]. The experimental cell is a vertical cylindrical tube 4.4 cm in diameter and 65 cm long. The inner surface is covered with a saturated film of superfluid ^{4}He. The temperature of the film can be varied from 20 to 600 mK. Initially the atoms are confined in the upper part of the cell by static magnetic fields. A quadrupole trapping field confines the atoms radially. Two solenoids confine the atoms longitudinally, forming a pencil-shaped trapping region 20 cm long. The upper solenoid prevents atoms from returning to the rf-discharge atom source. The lower solenoid produces a potential-energy barrier of height E_t separating the trapped atoms from the lower section of the cell. Atoms that manage to pass over this barrier and flow into the lower section of the cell are free to collide with the walls. They are adsorbed and then rapidly recombine into H_2. A sensitive bolometer [9] is located at the bottom of the cell. The recombining atoms give up a fraction of their energy to it. The bolometer signal provides an accurate measure of the flux of atoms from the trap.

By suitably varying E_t it is possible either to cool the trapped atoms or to measure their temperature. The equilibrium temperature of the trapped gas is governed by a balance between cooling due to high-energy atoms escaping over the field barrier E_t (evaporation) and heating due to two-body dipolar decay [10] of atoms in the trap. Experimentally one finds that the equilibrium temperature is a well-defined fraction of E_t. This fraction, which varies smoothly with changes in the operating conditions of the trap, is typically between 0.05 and 0.15. If E_t is lowered at a rate that is slow compared to the equilibration rate in the trap, the gas is cooled to a new equilibrium temperature at the expense of the loss of some atoms. If E_t is lowered much faster than the equilibration rate, the trapped atoms are unable to readjust their energies. In this case the energy distribution $N(E)$ can be determined by simultaneously measuring the flux of escaping atoms and the corresponding value of E_t as the entire contents of the trap are dumped. The temperature of the gas can be found by comparing $N(E)$ with calculated distributions based on the known field profile in the trap.

Figure 1(a) displays the energy distribution of 7.4×10^{12} atoms evaporatively cooled to a temperature of 1.1 mK and central density of 1.6×10^{13} cm^{-3}. Using these conditions as a starting point, an identical sample was further cooled to a temperature of 190 μK as displayed in Fig. 1(b). During that cooling the central density increased by a factor of 2.5 to 4.0×10^{13} cm^{-3}. Figure 1(c) shows the results of another evaporation in which 3×10^{11} atoms were cooled to 100 μK at a density of 8×10^{13} cm^{-3}. At this density, the critical temperature for Bose-Einstein condensation is 30 μK, only a factor of 3.5 lower.

We used our cold, trapped atoms to measure $s(E)$ at

Corrected reprint [see PRL 67, 1476(E) (1990)]

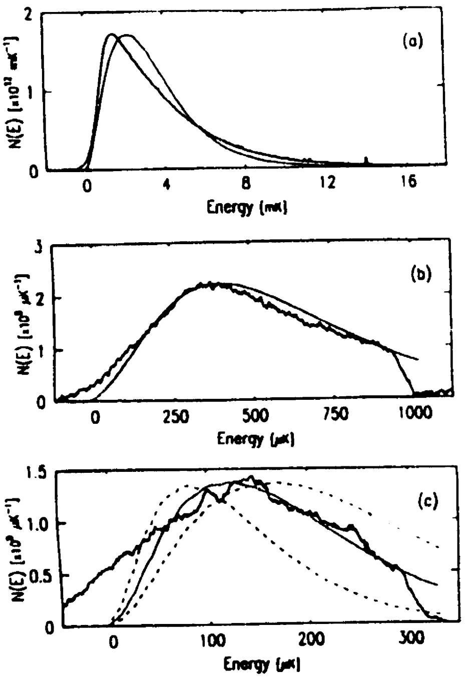

FIG. 1. Energy distributions for evaporatively cooled atomic hydrogen. The solid curves give the calculated distributions for atoms at (a) 1.1 mK, (b) 190 μK, and (c) 100 μK. The dashed curves in (c) are for temperatures 30% higher and lower than the best-fit value. We believe the finite atom signals at $E<0$ are due to a small axial field inhomogeneity (<1 G) that slightly deforms the bottom of the trap. Although such a deformation could influence the determination of the density, measured densities were verified with sample decay measurements.

temperatures below 1 mK. The method starts with atoms at equilibrium in the trap with a known distribution $N(E)$. The radial confining field is rapidly lowered to zero, allowing the trapped atoms to interact with the wall. Axial confinement is maintained by the upper and lower solenoids. After a specified interval, typically 0.1 to 5 s, the radial confining field is returned to its initial value and the energy distribution is measured (see Fig. 2). While the fields are down atoms may stick to the walls where they quickly recombine [8] and are lost. By measuring the distribution after different times, we confirmed that atoms in each energy interval decayed exponentially and we determined their corresponding decay time.

In analyzing the results we assume that surface sticking is the only source of atom loss. Theoretical calculations [11,12] indicate that at these low energies the probability of inelastic nonsticking collisions is negligible. We have verified this assertion experimentally. The energy distribution of the recovered atoms does not show a contribution from atoms whose energy has been raised by their encounter with the wall. Another conceivable source of atom loss is electronic spin relaxation. If the spin flip occurs during a nonsticking wall collision, the resulting high-field-seeking atom will be lost from the trap without having been adsorbed on the wall. Analysis [8] of data taken in earlier experiments [7] indicates that the spin relaxation takes place only after the atoms have been adsorbed. Thus, the process does not influence our results.

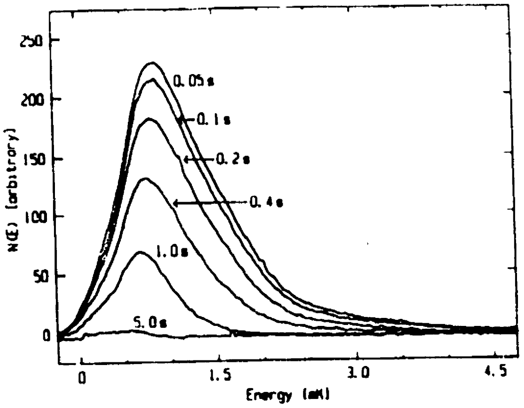

FIG. 2. Evolution of the energy distribution resulting from lowering the radial confining fields to zero for an interval of time and then raising them again. The down times for the different curves are indicated. These data are for an initial starting temperature of 500 μK. Data were taken for initial starting temperatures between 500 μK and 3 mK. The agreement between sets was good.

The decay rate of the atoms depends on both the collision rate with the surface and $s(E)$. The number of atoms should decay exponentially with a rate

$$\tau(E)^{-1}=\eta(2E/MD^2)^{1/2}s(E). \tag{1}$$

D is the cell diameter, M is the atomic mass, and η is a dimensionless factor relating the atom's mean free path to D. For monoenergetic atoms scattering diffusely in an infinite cylinder, η would be exactly equal to 1.0. In practice, adjustments must be made for the finite length of the trapping region and the fact that some of the atoms may stick to the wall in a location where their magnetic potential energy is still finite. We have used a Monte Carlo simulation which calculates atomic trajectories to determine that $\eta=0.95$ for our situation.

To determine $s(E)$ from the decay times involves one additional step. Because adiabatic cooling occurs as the field is lowered, the mapping of initial energies in $N(E)$ into the final atom energies at the wall must be determined. The potential energy at the wall, E_w, is proportional to the strength of the quadrupole fields responsible for the radial confinement of the atoms. As E_w is lowered, the energy E of a given trapped atom is lowered by an amount that depends on E_w. The mapping for an ideal cylindrical quadrupole potential is $E \propto E_w^{4/7}$. This is expected to be a good approximation to our situation provided that the atoms cannot reach the wall, that is, when $E < E_w$. If $E > E_w$, the wall itself helps to confine the atoms and the energy mapping is more complex, although calculable. For the conditions under which data were taken, from 50% to 80% of the adiabatic cooling occurred before E_w passed through the atom energy as E_w was reduced to zero. The time for raising or lowering the fields was > 30 times longer than the time for the atom to make one radial oscillation in the trap.

We verified that the changes associated with cycling the quadrupole fields were reversible by comparing $N(E)$ before and after cycles that were too shallow to permit any atoms to touch the walls. We found no measurable difference between the distributions before and after such cycles. We measured the energy mapping under the specific conditions used in these sticking-probability measurements and found that for $E < E_w$ it was close to the pure-quadrupole result [8]. Because the atoms begin to stick and recombine when $E > E_w$, we could not extend these tests to the fully expanded gas. Thus, when determining $s(E)$ by this method we have had to assume that our calculations for the energy mapping remain valid down to $E_w = 0$. The resulting data are plotted as circles in Fig. 3. If the energy reduction in the final stage of expansion were not as large as predicted, typically a factor of 2.5, the value of the atom energy assumed in the calculation of the sticking probability would be in error. We have computed this possible systematic error and find that it is unimportant. This method is useful in the range 100 μK to 1 mK. Below 100 μK it is limited by uncertainities in the residual magnetic fields. Above 1 mK it is limited by the rapid decay rate of the atoms.

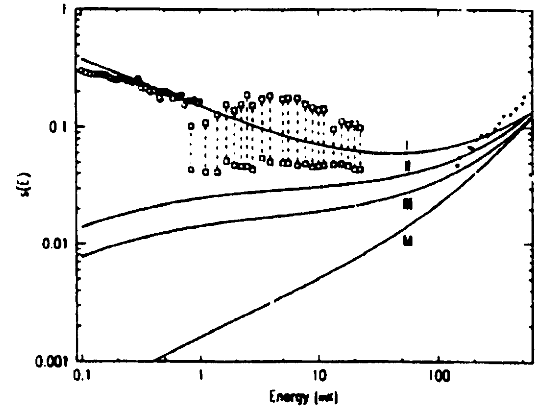

FIG. 3. Sticking probability vs atom energy. The open symbols represent our measurements. Our higher-temperature results (open squares) depend on the nature of the elastic atom-surface scattering and are plotted for the extremes of diffuse scattering, lower symbols, and specular reflection, upper symbols. The results at low temperature (open circles) do not depend on this distinction. The typical total error (including random and systematic errors) is ±35%. The solid triangles are the earlier results of Berkhout *et al.* [5]. The solid lines represent various theoretical models discussed in the text.

Another method for determining $s(E)$ is to measure the recombination time of atoms released into the detection region at the bottom of the cell. This method is applicable for energies above 1 mK. A pulse of atoms is released from the trap by lowering E_t by a small amount, typically a 10% reduction, and then quickly raising it again. The released atoms "slide" down the magnetic-field gradient and bounce about in the detection region. They are confined in one direction by the field of the lower solenoid, and in all others by ^{4}He-covered walls. The energy distribution of the released atom remains narrow and nonthermal, although the distribution of incident angles becomes random.

The response time of the bolometer to a pulse of atoms released into the lower cell was measured to be 60 ms. An exponential decay curve for the atoms, convolved with the system response function, was fitted to the bolometer signal. The resulting values of the lifetime $\tau(E)$ ranged from 60 ms at 20 mK to 300 ms at 1 mK. As in the previous method, Eq. (1) is used to determine $s(E)$ from the observed values of $\tau(E)^{-1}$. In this case, however, the value of the factor η depends on the macroscopic surface roughness of the helium film. The atoms released from the trap gain a significant amount of momentum along the axis as they slide down the potential hill; essentially, a beam is formed. If the atoms reflect specularly from the film on the bottom surface of the cell, they may oscillate up and down for some time before beginning to collide with the cylindrical walls as well. For this case our Monte Carlo calculation gives $\eta = 0.36$. If the reflection is diffuse, perhaps caused by an accumulation of solid molecular hydrogen between the helium film and the wall, the distribution of atomic velocities will randomize more quickly. In this case we calculate that $\eta = 0.93$. We cannot independently determine the reflection conditions that apply in this experiment. For this reason we have plotted in Fig. 3 the values of $s(E)$ that would result in each of the two limiting cases. In the method used below 1 mK the distribution of initial incident angles is essentially random to begin with and the question of surface roughness is unimportant. Comparison of the results of the two methods for energies where they overlap seems to indicate that the reflections are closer to specular than diffuse.

The data plotted in Fig. 3 were taken at a wall temperature of 50 mK. It has been predicted that $s(E)$ should be independent of the wall temperature as long as that temperature is well below the energy of the ripplon created when the atom is adsorbed [13]. Conservation of energy and momentum in the adsorption process set the ripplon energy to be 0.6 K. We have measured the sticking probability at several energies for wall temperatures between 40 and 80 mK. No change in $s(E)$ with wall temperature was observed within this range.

Earlier measurements of sticking probabilities at higher temperatures [5,6] yielded $s(T)$ rather than $s(E)$. Those results are plotted in Fig. 3. They are consistent with the expression [5] $s(T)=0.33T$. The lowest value of $s(T)$ obtained for pure ^{4}He in those experiments was 0.05 at 145 mK.

The solid curves in Fig. 3 are calculations of $s(T)$ by Goldman [12] for several models of atom-surface potential. Parameters in each model were adjusted to give a minimum energy of 4.5 K at a distance 0.42 nm from the surface. By way of comparison, the de Broglie wavelength of the atoms, which is proportional to $E^{-1/2}$, increases from 22 nm at 20 mK to 310 nm at 100 μK. These theoretical results, and the earlier high-temperature measurements, assume a thermal distribution of incident atoms. In Fig. 3 they are plotted at the energies of the equivalent temperatures.

The curve M results from a Morse potential, originally investigated because some of the required calculations can be done analytically. Curves I, II, and III represent more realistic approximations. The major difference between the potentials used in I and II is the energy μ_0 necessary for the hydrogen atom to penetrate into the bulk liquid: I uses $\mu_0=37$ K and II uses $\mu_0=75$ K. Recent measurements of μ_0 for deuterium [14] can be used to infer that μ_0 in hydrogen should be less than 75 K. However, considering the extreme sensitivity of the theory to the form of the potential in this energy range, we feel that it is premature to speculate on the merits of one model over another.

We thank William Sampson of Brookhaven National Laboratory for help in the design and construction of our superconducting quadrupole magnets. One of us (J.C.S.) gratefully acknowledges support of the AT&T Bell Laboratories Ph.D. Scholarship Program. Another (C.L.C.) wishes to thank CNPq and ETFCE (Brazil) for financial support. This research is supported by the National Science Foundation under Grant No. DMR-88-15555 and the Air Force Office of Scientific Research under Grant No. AFOSR-90-0127.

---

[1] See, for example, C. N. Cohen-Tannoudji and W. D. Phillips, Phys. Today 43 (10), 33 (1991).

[2] H. F. Hess, Phys. Rev. B 34, 3476 (1986).

[3] Yu. Kagan and G. Y. Shlyapnikov, Phys. Lett. 95A, 309 (1983).

[4] Th. Martin, R. Bruinsma, and P. M. Platzman, Phys. Rev. B 38, 2257 (1988).

[5] J. J. Berkhout, E. J. Wolters, R. van Roijen, and J. T. M. Walraven, Phys. Rev. Lett. 57, 2387 (1986).

[6] J. A. Helffrich, M. P. Maley, and M. Krusius, Phys. Rev. B 42, 2003 (1990). (This work determined the accommodation coefficient $a(T)$. At low temperatures, $a(T)=1.5s(T)$ [see D. S. Zimmerman and A. J. Berlinsky, Can. J. Phys. 61, 508 (1983)].)

[7] N. Masuhara, J. M. Doyle, J. C. Sandberg, D. Kleppner, T. J. Greytak, H. F. Hess, and G. P. Kochanski, Phys. Rev. Lett. 61, 935 (1988).

[8] J. Doyle, Ph.D. thesis, MIT, 1991 (unpublished).

[9] J. M. Doyle, J. C. Sandberg, N. Masuhara, I. A. Yu, D. Kleppner, and T. J. Greytak, J. Opt. Soc. Am. B 6, 2244 (1989).

[10] A. Lagendijk, I. F. Silvera, and B. J. Verhaar, Phys. Rev. B 33, 626 (1986).

[11] Yu. Kagan, G. V. Shlyapnikov, and N. A. Glukhov, Pis'ma Zh. Eksp. Teor. Fiz. 40, 287 (1984) [JETP Lett. 40, 1072 (1984)].

[12] V. V. Goldman, Phys. Rev. Lett. 56, 612 (1986).

[13] Zimmerman and Berlinsky, Ref. [6].

[14] M. W. Reynolds, M. E. Hayden, and W. N. Hardy, J. Low Temp. Phys. (to be published).

Bibliography

[1] T. J. Greytak and D. Kleppner, "Lectures on spin-polarized hydrogen," in *New Trends in Atomic Physics* (G. Grynberg and R. Stora, eds.), (Amsterdam), p. 1127, Les Houches Summer School, North-Holland, 1982.

[2] I. F. Silvera and J. T. M. Walraven, "Spin-polarized atomic hydrogen," in *Progress in Low Temperature Physics Volume X* (D. F. Brewer, ed.), ch. 3, p. 139, Elsevier, 1986.

[3] I. F. Silvera and J. T. M. Walraven, "Stabilization of Atomic Hydrogen at Low Temperature," *Physical Review Letters*, vol. 44, p. 164, 1980.

[4] D. A. Bell, H. F. Hess, G. P. Kochanski, S. Buchman, L. Pollack, Y. M. Xiao, D. Kleppner, and T. J. Greytak, "Relaxation and recombination in spin-polarized atomic hydrogen," *Physical Review B*, vol. 34, p. 7670, 1986.

[5] H. Hess, "Evaporative cooling of magnetically trapped and compressed spin-polarized hydrogen," *Physical Review B*, vol. 34, p. 3476, 1986.

[6] H. F. Hess, G. P. Kochanski, J. M. Doyle, N. Masuhara, D. Kleppner, and T. J. Greytak, "Magnetic Trapping of Spin-Polarized Atomic Hydrogen," *Physical Review Letters*, vol. 59, p. 672, 1987.

[7] N. Masuhara, J. M. Doyle, J. C. Sandberg, D. Kleppner, T. J. Greytak, H. F. Hess, and G. P. Kochanski, "Evaporative Cooling of Spin-Polarized Atomic Hydrogen," *Physical Review Letters*, vol. 61, p. 935, 1988.

[8] J. M. Doyle, J. C. Sandberg, A. I. Yu, C. L. Cesar, D. Kleppner, and T. J. Greytak, "Hydrogen in the Submillikelvin Regime: Sticking Probability on Superfluid ^{4}He," *Physical Review Letters*, vol. 67, p. 603, 1991.

[9] J. M. Doyle, *Energy Distribution Measurements of Magnetically Trapped Spin Polarized Atomic Hydrogen: Evaporative Cooling and Surface Sticking.* PhD thesis, Massachusetts Institute of Technology, 1991.

[10] T. Andreae, W. Konig, R. Wynands, D. Leibfried, F. Schmidt-Kaler, C. Zimmermann, D. Meschede, and T. W. Hänsch, "Absolute Frequency Measurement of the Hydrogen 1S-2S Transition and a New Value of the Rydberg Constant," *Physical Review Letters*, vol. 69, p. 1923, 1992.

[11] F. Schmidt-Kaler, D. Leibfried, M. Weitz, and T. W. Hänsch, "Precision Measurement of the Isotope Shift of the 1S-2S Transition of Atomic Hydrogen and Deuterium," *Physical Review Letters*, vol. 70, p. 2261, 1993.

[12] R. G. Beausoleil and T. W. Hansch, "Ultrahigh-resolution two-photon optical Ramsey spectroscopy of an atomic fountain," *Physical Review A*, vol. 33, p. 1661, 1986.

[13] D. G. Friend and R. D. Etters, "A dilute hard-sphere Bose-gas model calculation of low-density atomic-hydrogen gas properties," *Journal of Low Temperature Physics*, vol. 39, p. 409, 1980.

[14] H. T. C. Stoof, J. M. V. A. Koelman, and B. J. Verhaar, "Spin-exchange and dipole relaxation rates in atomic hydrogen: Rigorous and simplified calculations," *Physical Review B*, vol. 38, p. 4688, 1988.

[15] I. D. Setija, H. G. C. Werij, O. J. Luiten, M. W. Reynolds, T. W. Hijmans, and J. T. M. Walraven, "Optical cooling of atomic hydrogen in a magnetic trap," *Physical Review Letters*, vol. 70, p. 2257, 1993.

[16] R. G. Beausoleil, *Continuous-Wave Measurement of the 1S-2S Transition Frequency in Atomic Hydrogen: The 1S Lamb Shift.* PhD thesis, Stanford University, 1986.

[17] G. Grynberg, B. Cagnac, and F. Biraben, "Multiphoton Resonant Processes in Atoms," in *Coherent Nonlinear Optics: Recent Advances* (M. S. Feld and V. S. Letokhov, eds.), Springer-Verlag, 1980.

[18] F. Bassani, J. J. Forney, and A. Quattropani, "Choice of Gauge in Two-Photon Transitions: 1S-2S Transition in Atomic Hydrogen," *Physical Review Letters*, vol. 39, p. 1070, 1977.

[19] J. H. Tung, X. M. Ye, G. J. Salamo, and F. T. Chan, "Two-photon decay of hydrogenic atoms," *Physical Review A*, vol. 30, p. 1175, 1984.

[20] H. A. Bethe and E. E. Salpeter, *Quantum Mechanics of One- and Two-Electron Atoms*, p. 214. Plenum Publishing Corp., 1977.

[21] C. A. Slocomb, W. H. Miller, and H. F. Schaefer, "Collisional Quenching of Metastable Hydrogen Atoms," *Journal of Chemical Physics*, vol. 55, p. 926, 1971.

[22] S. R. Ryan, S. J. Czuchlewski, and M. V. McCusker, "Collisional quenching of metastable hydrogen atoms by atoms and molecules," *Physical Review A*, vol. 16, p. 1892, 1977.

[23] H. A. Bethe and E. E. Salpeter, *Quantum Mechanics of One- and Two-Electron Atoms*, p. 287. Plenum Publishing Corp., 1977.

[24] D. S. Elliott, M. W. Hamilton, K. Arnett, and S. J. Smith, "Two-Photon Absorption from a Phase-Diffusing Laser Field," *Physical Review Letters*, vol. 53, p. 439, 1984.

[25] H. A. Bethe and E. E. Salpeter, *Quantum Mechanics of One- and Two-Electron Atoms*, p. 287. Plenum Publishing Corp., 1977.

[26] H. A. Bethe and E. E. Salpeter, *Quantum Mechanics of One- and Two-Electron Atoms*, p. 253. Plenum Publishing Corp., 1977.

[27] B. H. Bransden and C. J. Joachain, *Physics of atoms and molecules*, p. 212. Longman, 1983.

[28] D. H. M^{c}Intyre, *High Resolution Laser Spectroscopy of Tellerium and Hydrogen: A Measurement of the Rydberg Constant.* PhD thesis, Stanford University, 1987.

[29] Radiant Dyes Laser Accessories GmbH; Wermelskirchen, Germany.

[30] Filterite Incorporated; Timonium, Maryland.

[31] Gsänger Optoelktronik GmbH; Planegg, Germany.

[32] C. Salomon, D. Hils, and J. L. Hall, "Laser stabilization at the millihertz level," *Journal of the Optical Society of America B*, vol. 5, p. 1576, 1988.

[33] R. Kallenbach, C. Zimmermann, D. H. McIntyre, and T. Hänsch, "A Blue Dye Laser with Sub-Kilohertz Stability," *Optics Communications*, vol. 70, p. 56, 1989.

[34] R. W. P. Drever, J. L. Hall, F. V. Kowalski, J. Hough, G. M. Ford, A. J. Munley, and H. Ward, "Laser Phase and Frequency Stabilization Using an Optical Resonator," *Applied Physics B*, vol. 31, p. 97, 1983.

[35] J. C. Bergquist, 1991. private communication.

[36] Crystal Technology Incorporated; Palo Alto, California.

[37] Conoptics Incorporated; Danbury, Connecticut.

[38] E. A. Whittaker, M. Gehrtz, and G. C. Bjorklund, "Residual amplitude modulation in laser electro-optic phase modulation," *Journal of the Optical Society of America B*, vol. 2, p. 1320, 1985.

[39] EG&G Photon Devices; Salem, Masssachusetts.

[40] Avantek Incorporated; Santa Clara, California.

[41] Mini-Circuits Incorporated; Brooklyn, New York.

[42] M. Zhu and J. L. Hall, "Sub-Hertz Locking of a Commercial Dye Laser Using an External Stabilizer." Preprint, 1991.

[43] R. C. Dorf, *Modern Control Systems.* Addison-Wesley, 1974.

[44] D. Hils and J. L. Hall, "Response of a Fabry-Perot cavity to phase modulated light," *Review of Scientific Instruments*, vol. 58, p. 1406, 1987.

[45] Apex Microtechnology Corporation; Tuscon, Arizona.

[46] Hewlett-Packard Corporation; Palo Alto, California.

[47] D. N. Nikogosyan, "Beta Barium Borate (BBO)," *Applied Physics A*, vol. 52, p. 359, 1991.

[48] F. Zernike and J. E. Midwinter, *Applied Nonlinear Optics.* Wiley, 1973.

[49] G. D. Boyd, A. Ashkin, J. M. Dziedzic, and D. A. Kleinman, "Second Harmonic Generation of Light with Double Refraction," *Physical Review*, vol. 137, p. A1305, 1965.

[50] G. D. Boyd and D. A. Kleinman, "Parametric Interaction of Focused Gaussian Light Beams," *Journal of Applied Physics*, vol. 39, p. 3597, 1968.

[51] M. Boshier, P. Baird, C. Foot, E. Hinds, M. Plimmer, D. Stacey, J. Swan, D. Tate, D. Warrington, and G. Woodgate, "Laser spectroscopy of the 1S-2S transition on hydrogen and deuterium: Determination of the 1S Lamb shift and the Rydberg constant," *Physical Review A*, vol. 40, p. 6169, 1989.

[52] C. Zimmermann, R. Kallenbach, and T. W. Hänsch, "High Resolution Spectroscopy of the Hydrogen 1S-2S Transition in an Atomic Beam," *Physical Review Letters*, vol. 65, p. 571, 1990.

[53] H. Kogelnik and T. Li, "Laser Beams and Resonators," *Proceedings of the IEEE*, vol. 54, p. 1312, 1966.

[54] H. W. Kogelnik, E. P. Ippen, A. Dienes, and C. V. Shank, "Astigmatically Compensated Cavities for CW Dye Lasers," *IEEE Journal of Quantum Electronics*, vol. QE-8, p. 373, 1972.

[55] J. T. F. Johnston and T. J. Johnston, "Tunable single frequency 215-235-nm radiation by barium borate intracavity doubling in the stilbene-3 ring dye laser," in *CLEO 1989 Proceedings*, 1989.

[56] PMS Electro-Optics; Boulder, Colorado.

[57] T. W. Hänsch and B. Couillaud, "Laser frequency stabilization by polarization spectroscopy of a reflecting reference cavity," *Optics Communications*, vol. 35, p. 441, 1980.

[58] L. A. Bloomfield, *High Resolution Ultraviolet Laser Spectroscopy of Mercury and Helium.* PhD thesis, Stanford University, 1983.

[59] P. Camus, 1991. private communication.

[60] A. E. Siegman, *Lasers.* University Science Books, 1986.

[61] D. H. McIntyre, R. G. Beausoleil, C. J. Foot, E. A. Hildum, and T. W. Hänsch, "Continuous-wave measurement of the hydrogen 1S-2S transition frequency," *Physical Review A*, vol. 39, p. 4591, 1989.

[62] Opthos Instruments; Rockville, Maryland.

[63] J. D. Gillaspy and C. J. Sansonetti, "Absolute wavelength determinations in molecular tellurium: new reference lines for precision laser spectroscopy," *Journal of the Optical Society of America B*, vol. 8, p. 2414, 1991.

[64] Emerson & Cuming, Incorporated; Woburn, Massachusetts.

[65] Acheson Colloids Company; Port Huron, Michigan.

[66] Handy & Harmon, Incorporated; New York, New York.

[67] Johnson Matthey Catalog Company; Ward Hill, Massachusetts.

[68] Y. S. Touloukhian, R. K. Kirby, R. E. Taylor, and P. D. Desai, *Thermophysical Properties of Matter*, vol. 12 of *Thermal Expansivity.* IFI/Plenum, New York, 1976.

[69] Y. S. Touloukhian, R. K. Kirby, R. E. Taylor, and T. Y. R. Lee, *Thermophysical Properties of Matter*, vol. 13 of *Thermal Expansivity.* IFI/Plenum, New York, 1977.

[70] Vernitron Corporation; Bedford, Ohio.

[71] Galileo Electro-Optics Corporation; Sturbridge, Massachusetts.

[72] Janos Technology Incorporated; Townshend, Vermont.

[73] Valpey-Fisher Corporation; Hopkinton, Massachusetts.

[74] Optovac; North Brookfield, Massachusetts.

[75] W. N. Hardy, M. Morrow, R. Jochemsen, B. W. Statt, P. R. Kubik, R. M. Marsolais, and A. J. Berlinsky, "Magnetic-Resonance Studies of Gaseous Atomic Hydrogen Confined at 1 K and Zero Magnetic Field," *Physical Review Letters*, vol. 45, p. 453, 1980.

[76] W. Demtröder, *Laser Spectroscopy Basic Concepts and Instrumentation.* Springer-Verlag, 1982.

[77] F. Biraben, M. Bassini, and B. Cagnac, "Line-shapes in Doppler-free two-photon spectroscopy. The effect of finite transit time," *Le Journal de Physique*, vol. 40, p. 445, 1979.

[78] Y. Kagan and G. V. Shlyapnikov, "Bose-Condensation of Spin-polarized Hydrogen in a Highly Inhomogeneous Field," *Physics Letters A*, vol. 130, p. 483, 1988.